UNIVERSITY OF OKLAHOMA
GRADUATE COLLEGE

THE ROLES OF STRUCTURAL INHERITANCE IN REGIONS OF INDUCED SEISMICITY AND ACTIVE TECTONICS

A DISSERTATION
SUBMITTED TO THE GRADUATE FACULTY
in partial fulfillment of the requirements for the
Degree of
DOCTOR OF PHILOSOPHY

By

FOLARIN KOLAWOLE
Norman, Oklahoma
2020

THE ROLES OF STRUCTURAL INHERITANCE IN REGIONS OF INDUCED SEISMICITY AND ACTIVE TECTONICS

A DISSERTATION APPROVED FOR THE
SCHOOL OF GEOSCIENCES

BY THE COMMITTEE CONSISTING OF

Dr. Brett M. Carpenter, Chair

Dr. Ze'ev Reches

Dr. Kurt J. Marfurt

Dr. Xiaowei Chen

Dr. Zulfiquar A. Reza

Acknowledgements

First, I dedicate the achievement of my dissertation to God almighty. I could not have been able to make it through without His grace and favor.

I want to thank my charming, awesome, loving, and ever supportive wife, 'Lore, who had endured the long distance that graduate school and career pursuit had brought into our marriage. Her constant care and support provided an unending source of motivation for me to keep pursuing my career goals. This PhD award is also for you dear! I also thank my beautiful daughter, Foyinsola, for coming into our lives during the last year of my PhD, and totally overwhelmed us with her graciousness. Her smiles and feistiness always reminded me that there is more to life outside of my academic pursuits.

I also thank my mother, for her endless love and support for my education ever since my father passed away when I was 7 years old. I also thank my younger brother, Doyin Kolawole for the various academic chats we have had through the course of my PhD. I thank my two older brothers, Wale and Diran Kolawole and their families for their support through the long period of my graduate education in the U.S.

I would like to express my sincere gratitude to my committee chair and advisor Dr. B. M. Carpenter, and my committee members Dr. Ze'ev Reches, Dr. K. J. Marfurt, Dr. Xiaowey Chen, and Dr. Zulfiquar A. Reza for their support, guidance and mentorship throughout the course of my PhD education. There is no way I could have acquired all the knowledge and skillsets that guided the successful completion of my dissertation without their support.

I would also like to thank the other professors and administrative staff that I interacted with at the School of Geosciences, University of Oklahoma, for making the program an awesome place for

minority students like me to learn and grow. I thank Rebecca Fay, Ashley Tullius, Leah Moser, Ginger Leivas, Ginny Gandy-Guedes, Dr. Lynn Soreghan, Dr. Michael Soreghan, Dr. Jake Walter, Dr. Shankar Mitra, Dr. Michael Behm, Dr. Heather Bedle, and Dr. Nori Nakata. I thank all my friends, colleagues, and mentees that I interacted with me through the course of my stint in the program: Max Firkins, Roberto Clairmont, Dalila De Jesus, Chris Ramos Sanchez, Candace Johnston, Thuwaiba Al Wahaibi, Wijdan Al Jabri, Travis Vick, Aristides Costa, Jean-Joel Legre, Joy Foluso, Brittany Stroud, Peter Reilly, Lennon Infante, Gabriel Machado, Swetal Patel, Julian Chenin, Karelia La Marca, Javier Tellez, Greg Connock, Pranshu Ratre, Deepankar Dangwal, Yan Qin, Will Kibikas, Emillio Torres, Muizz Matemilola, Ifunaya Ekwunife, Tanner Shadoan, Christina Hamilton, Rafael Pires-De Lima, Paul Gilbert, David Lubo, David Duarte, Francis Oyebanji, Oluwatobi Olorunsola, Jing Zhang, Sai Sandeep Chitta, Abidin Caf, Cansu Demirel, Matt Hamilton, Raymond Ng, Colin Pennington, Tengfei Wu, Hannah Morgan, Angie Ortega, Edimar Perico, Clayton Silver, Lily Pfeifer, Carl Symcox, Tara Putri, Saurabh Sinha, Tengfei Wu, Zhuobo Wang, Jieweng Zhang, Chenxi Xu, Thang Ha, Peiyao Li… and many others (I'm deeply sorry if I forgot to mention your name). You guys made my PhD experience and awesome one.

Also, I would like to thank the collaborators and mentors who helped me in my Chapter 1 project: Dr. Z. Reches, Dr. K. Marfurt, C. S. Johnston, C. B. Morgan, Dr. J. C. Chang, and Dr. D. A. Lockner. I would like to acknowledge the USGS Induced Seismicity Project for providing financial support and laboratory expertise/time to conduct the experiments presented in the chapter. I thank Osage Nation and SpyGlass Energy, LLC for providing the seismic data used in the study. I also thank the Oklahoma Geological Survey for providing earthquake and focal mechanism data.

I thank my internship supervisor and friend, Molly Turko for her co-mentorship on the Chapter 3 of this dissertation. I thank TGS for providing access to the 3-D Seismic Reflection and well data used in the study. I appreciate Chesapeake Energy Corporation, Oklahoma City for an internship opportunity through which I was provided access to the computer software and hardware used to analyze and interpret the seismic data. I thank the Oklahoma Petroleum Information Center (OPIC), Norman, OK for providing access to the basement penetration borehole drill cuttings used in the study. Also, I thank the Chesapeake Energy Reservoir Technology Center for the photographs, X-ray diffraction and X-ray fluorescence analyses of the drill cuttings. I thank Laura Bellingar for assistance with basement well log synthetic modelling, Matthew Davis for assistance with the phase assessment of the seismic dataset, and Michael Horn for assistance with the seismic attribute computation.

I would like to thank Dr. Z. Reches for his co-mentorship on the Chapter 4 project in this dissertation. I thank the Center for Autonomous Sensing and Sampling (CASS), National Weather Center, University of Oklahoma, for assisting with the acquisition and processing of the drone datasets analyzed in the study. I thank the Geological Society of America (GSA) for the GSA Graduate Student Research Grant #11968-18 awarded to me, which provided the funds used for the acquisition of the drone datasets. I also thank Connor Mears, Max Firkins, Will Kibikas, and Brittany Stroud for help in making some of the field observations. I sincerely appreciate Deepankar Dangwal for assisting with the programming code that I used for the Discrete Fourier Analysis of the fracture distribution data.

I would like to thank my collaborators that helped me to complete the project presented in the Chapter 5 of this dissertation: Dr. E. A. Atekwana and Dr. D. A. Lao-Davila. I thank my mentees, Travis Vick and Aristides G. Costa, who assisted with different aspects of the study. Thanks to the

Geological Survey of Malawi for providing the 2013 aeromagnetic datasets used in the study. Thanks also to the South African Development Community (SADC) for providing both the 1985 aeromagnetic dataset and the regional aeromagnetic dataset used in the study. I also thank Geosoft for providing academic Oasis Montaj software licenses used in the study.

Table of Contents

List of Figures

List of Tables

ABSTRACT

The structural fabric of crystalline crustal rocks, commonly defined by fractures, metamorphic foliation, tabular intrusions, bedding planes, cleavage etc. represent mechanical anisotropy and structural weakness which are exploited by subsequent tectonic and anthropogenic stressing (induced seismicity) events. In this dissertation, two overarching questions are explored:

1.) What are the roles of inherited crustal deformation in the seismogenic release of elastic strain in areas of sporadic and widespread induced seismicity?

2.) What are the controls of structural inheritance on strain accommodation within contractional and multiphase extensional tectonic settings?

The first question is explored in the intraplate induced seismicity setting of the Central – Eastern United States (CEUS), and the second question in the Anadarko Basin, Oklahoma, U.S. and the Shire Rift, Southern Malawi, Eastern African Rift System. In this dissertation, field observations, 3-D seismic reflection data, earthquake data, potential field (aeromagnetic & gravity) datasets, and experimental rock mechanics testing are integrated to address the research questions in the different study areas where appropriate.

Among several interesting findings, the results of this dissertation work can be summarized as follows:

1.) In areas of sporadic basement-hosted induced seismicity, the geometry, structure, and mechanical stability of the basement faults make them critically susceptible to seismic reactivation. Furthermore, the presence of a regional-scale structural fabric in an area of anthropogenic stress perturbation facilitates the production of widespread regional-scale induced seismicity.

2.) In juvenile multiphase continental rift settings, the structures that are inheritance from the pre-rift basement and the subsequent phases of extension may influence the patterns of lengthening, widening, bifurcation, and even the episodic termination of propagating rifts. Furthermore, the results show that magmatic structures and basement fabrics represent sustained controls on multiphase rift development.

Overall, the various studies presented in this dissertation provide compelling evidences suggesting that pre-existing structures and tectonic conditions promote and sustain subsequent crustal deformation and the associated seismicity in regions of anthropogenic stress perturbations (induced seismicity) and active tectonics.

In summary,

INHERITED GEOLOGICAL STRUCTURES MATTER!

CHAPTER 1

INTRODUCTION

The structural fabric of crystalline crustal rocks is defined by fractures (joints and faults), metamorphic foliation, preferentially-orientated of mineral grains, xenoliths, tabular intrusions, bedding planes, cleavage etc. These fabrics represent mechanical anisotropy and structural weakness in the crust which are exploited by subsequent geological events, commonly referred to as "tectonic inheritance" or "structural inheritance" (e.g., Colletta et al., 1997; Vauchez et al., 1998; Thomas, 2006; Audet and Bürgmann, 2011). Essentially, the Wilson Cycle model of cyclical opening and closing of ocean basins is intrinsically dependent on tectonic inheritance (Wilson, 1966; Audet and Bürgmann, 2011).

Elastic tectonic stresses and strains accumulate in the Earth's crust, along active plate boundaries and within intraplate regions (Heidbach et al., 2018), where the built-up stresses and strains are released by sudden fault slip events which may be accompanied by seismicity (e.g., Bollinger et al., 2004; Bourgois et al., 2007). Anthropogenic stress perturbations, also known as 'induced seismicity', include industrial activities (surface and subsurface) that lead to the alteration of the in situ stresses in the shallow Earth's crust leading to the occurrence of earthquakes or tremors (e.g., Grigoli et al., 2017; Foulger et al., 2018). The most common earthquake-triggering industrial activities include shale gas exploitation, hydrocarbon storage and extraction, geothermal energy exploitation, mining operations, water impoundment (dams), and CO_2 sequestration (Grigoli et al., 2017; Foulger et al., 2018).

Of the six groups of activities, four (shale gas exploitation, hydrocarbon storage and extraction, geothermal energy exploitation, and CO_2 sequestration) involve the active injection of fluids into the subsurface (Grigoli et al., 2017). Therefore, I focus my dissertation research on fluid injection

induced seismicity. Favorable conditions during the subsequent natural and anthropogenic stress perturbation events may facilitate the reactivation of the earlier structures.

This dissertation explores the roles of inherited crustal deformations in 1.) the seismogenic release of elastic stresses and strains in areas of sporadic and widespread induced seismicity, and 2.) the accommodation of tectonic strain within contractional and multiphase extensional tectonic settings.

My research focuses on the Central – Eastern United States (CEUS) region, and more specifically, Oklahoma as a natural laboratory where the structural inheritance and its relationship to induced seismicity can be investigated. For the investigations of structural inheritance in tectonic settings, my research focuses on the Paleozoic contractional tectonics of the Anadarko Basin, Oklahoma, and the extensional tectonics of the currently active Eastern African Rift System.

In Chapter 2, we utilize a combination of 3-D seismic reflection data interpretation, earthquake data, field structural geology, and experimental rock friction experiments to investigate the controls of the inherited basement structure on the sporadic and widespread induced seismicity of Oklahoma. The results reveal that that the geometry, structure and mechanical stability of Oklahoma's basement faults make them critically susceptible to seismic reactivation.

In Chapter 3, we explore the basement control on the propagation of deformation through the sedimentary cover in the Anadarko Basin of Oklahoma, an intracratonic foreland basin that accommodated Late Paleozoic contraction and transpression. We integrate an analyses of high-quality 3-D seismic reflection dataset with basement penetration well data (wireline logs, drilling cuttings, and geochemical analysis). The results reveal that pre-existing basement-rooted faults were reactivated and propagated up-section into the Phanerozoic sedimentary sequences in

different structural patterns. Also, we find that the basement-driven propagation of faulting resulted in the vertical partitioning of the fault structure across the basement-sedimentary interface which poses important implications for the current induced seismicity of the basin.

In Chapter 4, we analyze the detailed structure of a brittle damage zone in the outcrops of Precambrian granite in southern Oklahoma. First, we show that the damage zone is characterized by a multi-scale hierarchical zonation that represent a distributed domino-style strike-slip deformation. We show that the damage likely represents the shallow extension of an immature or buried strike-slip fault, herein named the "Mill Creek Fault Zone". Further, we demonstrate that the characteristics of this damage zone is consistent with that of the recently reactivated faults in the buried basement of central Oklahoma. The results suggest that the analyzed structural pattern of fracturing and slip zonation poses important implications for shallow basement fluid circulation and basement-hosted seismicity.

In Chapter 5, we investigate the spatio-temporal relationships between basement fabrics, magma-plumbing structures, and faulting in the multiphase Shire Rift, one of the least understood active segments of the East African Rift System. We integrate aeromagnetic, satellite Digital Elevation Model (DEM), and field data to delineate the fault segments, igneous intrusions, and pre-rift metamorphic fabrics, and estimate the along-fault distribution of throw. Among several interesting findings, we show how the continuous inheritance of structures influence rift lengthening and widening, bifurcation and episodic termination through the course of multiphase continental extension. The observations demonstrate that magmatic structures and basement fabrics represent sustained controls on multiphase rift faulting.

In the Appendix 1, we expand on the analysis in Chapter 2 to cover the entire extents of the Mesoproterozoic Granite-Rhyolite Provinces of the United States Mid-Continent to which the

Oklahoma basement belongs. The results show that prominent NE-SW and NW-SE (with minor N-S and E-W) trends characterize the structural fabric of this Mesoproterozoic basement. These prominent structural trends represent inherent weaknesses in the igneous basement of the U.S. Mid-Continent which influenced the Phanerozoic tectonic deformation in the region. Furthermore, the results suggest the inheritance of this regional-scale structural fabric by anthropogenic stress perturbations facilitates the production of widespread regional-scale induced seismicity.

In Appendix 2, we explore the spatial relationships between the seismicity of Oklahoma, and collocated fault intersection and basement contacts, using aeromagnetic and gravity datasets. We investigate this relationship in the Fairview area of Oklahoma where a Mw5.1 earthquake occurred in 2016 in relation to wastewater injection in the area. We argue that the collocation of the intersection of critically-oriented faults and faulted contacts acted as a stress concentrator that enabled the localization of seismogenic fault rupture

In Appendix 3, We investigate the patterns formed by mafic sheet intrusions emplaced in fractured granite basement in the outcrops of Troy Granite in the Mill Creek area of southern Oklahoma. We show evidence suggesting that the inherited fracture patterns in granitic basement influenced the emplacement of the diabase dikes and sills.

Finally, I summarize all the results of my dissertation work in Chapter 6, the Conclusion chapter.

REFERENCES

Audet, P. and Bürgmann, R. (2011). Dominant role of tectonic inheritance in supercontinent cycles. Nature Geoscience, 4(3), 184-187.

Bollinger, L., Avouac, J. P., Cattin, R., & Pandey, M. R. (2004). Stress buildup in the Himalaya. Journal of Geophysical Research: Solid Earth, 109(B11).

Bourgois, J., Bigot-Cormier, F., Bourles, D., Braucher, R., Dauteuil, O., Witt, C. and Michaud, F., 2007. Tectonic record of strain buildup and abrupt coseismic stress release across the northwestern Peru coastal plain, shelf, and continental slope during the past 200 kyr. Journal of Geophysical Research: Solid Earth, 112(B4).

Colletta, B., Roure, F., de Toni, B., Loureiro, D., Passalacqua, H., & Gou, Y. (1997). Tectonic inheritance, crustal architecture, and contrasting structural styles in the Venezuela Andes. Tectonics, 16(5), 777-794.

Foulger, G. R., Wilson, M. P., Gluyas, J. G., Julian, B. R., & Davies, R. J. (2018). Global review of human-induced earthquakes. Earth-Science Reviews, 178, 438-514.

Grigoli, F., Cesca, S., Priolo, E., Rinaldi, A. P., Clinton, J. F., Stabile, T. A., Dost, B., Fernandez, M. G., Wiemer, S., & Dahm, T. (2017). Current challenges in monitoring, discrimination, and management of induced seismicity related to underground industrial activities: A European perspective. Reviews of Geophysics, 55(2), 310-340.

Heidbach, O., Rajabi, M., Cui, X., Fuchs, K., Müller, B., Reinecker, J., Reiter, K., Tingay, M., Wenzel, F., Xie, F., & Ziegler, M. O. (2018). The World Stress Map database release 2016: Crustal stress pattern across scales. Tectonophysics, 744, 484-498.

Thomas, W. A. (2006). Tectonic inheritance at a continental margin. GSA today, 16(2), 4-11.

Vauchez, A., Tommasi, A., & Barruol, G. (1998) Rheological heterogeneity, mechanical anisotropy and deformation of the continental lithosphere. Tectonophysics 296, 61–86.

Wilson, J. T. (1966). Did the Atlantic close and then re-open? Nature 211, 676–681.

CHAPTER 2

THE SUSCEPTIBILITY OF OKLAHOMA'S BASEMENT TO SEISMIC REACTIVATION

ABSTRACT

Recent widespread seismicity in Oklahoma is attributed to the reactivation of pre-existing, critically-stressed, and seismically unstable faults due to decades of wastewater injection. However, the structure and properties of the reactivated faults remain concealed by the sedimentary cover. Here, we explore the major ingredients needed to induce earthquakes in Oklahoma by characterizing basement faults in the field, in seismic surveys and via rock-mechanics experiments. Outcrop and satellite mapping reveal widespread fracture/fault systems with trends that display a marked similarity to the trends of recent earthquake lineaments. Our 3D seismic analyses show steeply-dipping basement-rooted faults that penetrate the overlying sedimentary sequences, representing pathways for wastewater migration. Experimental stability analysis indicates that Oklahoma's basement rocks become seismically unstable at conditions relevant to the dominant hypocentral depths of the recent earthquakes. These analyses demonstrate that the geometry, structure and mechanical stability of Oklahoma's basement faults make them critically susceptible to seismic reactivation.

INTRODUCTION

The dramatic increase in widespread seismicity in Oklahoma since 2009 (Figure 1a), which has been attributed to large-scale wastewater injection, exceeded the seismicity level of other areas of wastewater injection in Central and Eastern United States, and Canada(Ellsworth, 2013; Keranen et al., 2014; Walsh and Zoback, 2015; Schultz et al., 2017). The majority of Oklahoma earthquakes have occurred on previously unknown fault segments within the Precambrian crystalline basement (Keranen et al., 2014); yet, the nature of basement structure is largely unknown. For example, the largest earthquake in Oklahoma, the 2016 Mw5.8 Pawnee event (Figure 1a), ruptured an unmapped fault trending WNW-ESE (now called the Sooner Lake Fault). Similarly, the 2016 Mw5.1 Fairview earthquake (Figure 1a) ruptured a previously unmapped segment of the Galena Township Fault (Chen et al., 2017; Goebel et al., 2017).

Wastewater injection can induce earthquakes along pre-existing faults via various triggering mechanisms that include direct increase of pore-pressure within fault-zones (McGarr and Barbour, 2016), and elastic stress transfer from injection sites to remote faults (Goebel et al., 2017). While these mechanisms may induce fault slip, it is also known that the induced fault slip may occur either as stable creep or as unstable rupture, and that the seismic stability of a fault-zone depends strongly on its composition and the loading conditions. Although much is known about the stability of faults in common crystalline rocks (Blanpied et al., 1991), the seismic stability of the Granite-Rhyolite Provinces of the U.S. mid-continent, which have undergone multiple phases of tectonic deformation and hydrothermal alteration (Bickford et al., 2015; Lidiak et al., 2014; Denison, 1981; Denison et al., 1984), are not known. Further, the fact that significant wastewater injection in some parts of Oklahoma has induced only limited seismicity (Walsh and

Zoback, 2015) raises questions on (a) the physical linkage and hydraulic connectivity between injection zones and the basement, and (b) the rheology and stress state of the basement.

Oklahoma basement rocks form part of a Precambrian igneous province that extends across the U.S. mid-continent (Bickford et al., 2015) (Figure 1c). Thus, we envision that a better understanding of induced seismicity in Oklahoma and better knowledge of the nature of its basement faults can lead to injection strategies that mitigate the likelihood of damaging induced or triggered earthquakes. Such mitigating strategies can be applied to areas underlain by similar basement as Oklahoma in the Central U.S. and other parts of the world with active wastewater injection operations (Ellsworth, 2013).

Here, we address the above deficiencies in understanding the controlling mechanisms of the widespread induced seismicity in Oklahoma. We characterize the patterns of fracture/fault systems in the Precambrian basement exposures of southern Oklahoma, the structure of subsurface basement faults in the region of earthquake activity, and experimentally determine the seismic stability of the basement rocks at in-situ conditions. These analyses provide the first documented link between basement structure and the current earthquakes, show potential pathways between wastewater injection intervals and the deeper Precambrian basement, and explain the depth distribution of the earthquake hypocenters.

Geological Background

The Oklahoma basement is in the southern part of the 1.35-1.4 Ga Granite-Rhyolite province of the US mid-continent (Bickford et al., 2015), which extends from west Texas to western Ohio (Bickford et al., 2015) (Figure 1c). These provinces are dominated by siliceous igneous rocks of granites and rhyolites and their metamorphic derivatives (Bickford et al., 2015;

Shah and Keller, 2017). The Southern Granite-Rhyolite province (1.35-1.40 Ga) has undergone multiple phases of tectonic deformation that included Precambrian NNE-SSW rifting followed by reverse-faulting (Cannon, 1994), Early-Middle Cambrian NW-SE rifting, and the related Southern Oklahoma Aulacogen (Brewer et al., 1983). While the Late Paleozoic tectonic phases are best documented in the sedimentary sequence (Powers et al., 1928; Brewer et al., 1983; Denison, 1995; Keller and Stephenson, 2007), they certainly affected the underlying crystalline basement.

Most of the recent earthquake activity in Oklahoma occurs in the north-central region of the state (Figure 1a) where the crystalline Precambrian basement is covered by a 1-3 km thick veneer of sedimentary strata (Shah and Keller, 2017). Due to this cover, our field analysis of basement structure focuses on the only major basement outcrop in Oklahoma, which is a >300 km^2 region in Johnston County (Figures 1d, 2a-d). The exposed basement is composed of granites, granodiorites and gneisses, 1.36-1.39 Ga in age, that are locally intruded by sub-vertical diabase dikes of Precambrian and Cambrian ages (Denison, 1995; Lidiak et al., 2014). Common hydrothermal alterations include calcite and epidote veins (Lidiak et al., 2014). The NW-SE predominant trend of these dikes was influenced by pre-existing structural imprints of previous tectonic phases (Lidiak et al., 2014; Denison, 1995). Since the basement of Oklahoma has similar thermo-tectonic history as those of the other areas underlain by the Precambrian Granite-Rhyolite Provinces (Bickford et al., 2015), we envision that a better understanding of the structure of the Oklahoma basement would provide some insight into the dynamics of induced seismicity in the other areas.

DATA AND METHODS

Seismic Attributes

The seismic survey used in this study includes a post-stack time-migrated 3-D seismic volume with bin size of 20 x 20 m and an estimated limit of vertical resolution of 15 m. We utilize curvature and coherence seismic attributes (Chopra and Marfurt, 2007) to better resolve subsurface structures and basement fault-zones along the Top-Arbuckle Group surface map (the preferred unit for wastewater injection) (Kroll et al., 2017) and the Top-Basement surface map (zone of most frequent seismicity) (Schoenball and Ellsworth, 2017). Structural deformation such as flexural and stepped block-faulting are revealed by the positive and negative curvature seismic attributes, where the most-positive curvature (*k1*) highlights up-warped/up-thrown zones and most-negative curvature (*k2*) highlights down-warped/down-thrown areas along the seismic reflectors associated with the mapped surfaces (Figures 3a-c). These curvature attributes are sensitive to fault zones characterized by small vertical offsets and subtle structural flexures often typical of strike-slip faults. The edge-detection energy ratio similarity (coherence) attribute computes the ratio of the coherent energy of the data to the total energy of the traces within an analyses window. Energy Ratio Similarity attribute is sensitive to zones of discontinuity along a reflector, thus, revealing fault damage zones as lineaments of low energy relative to the surrounding intact rocks of higher energy (Figures 3a-b). In this study, we compute the volumetric seismic attributes in the Attribute Assisted-Seismic Processing and Interpretation (AASPI) software application from University of Oklahoma; then extract and co-render the generated attributes in Petrel Software application.

Earthquake Relocation

We obtain 10, 879 earthquake events (of Mw > the lowest magnitude of the catalog) for the period of 2010-2017 from the Oklahoma Geological Survey earthquake catalogue, and relocated the events by using HypoDD, and phase picking for 1-dimensional velocity modelling following the methods of Fielding et al. (2017) and Waldhauser and Ellsworth (2000). About 2-4% of the events in Oklahoma Geological Survey earthquake catalogue occurred in the period preceding the uptick in seismicity in Oklahoma (1882-2009). Since there are no phase picks in this old data, we could not include pre-2010 data in our relocated catalog. We manually digitize the lineaments defined by the earthquake epicenter clusters to delineate the traces of the causative faults.

We present frequency-azimuth plots of the structural trends obtained in the different datasets and compile the mean trends each of the modal sets (Figure 3d and Table 1).

Experimental Samples

We measure the mechanical behavior of five (5) basement rock samples obtained in Oklahoma (Table 2). Four of the samples are derived from core material collected in three wells that penetrated the top of the igneous basement in the north-central region of the state (Figure 4). The Jones 46 and SHADS 4 samples are from the Washington Volcanic Group, whereas the Kohpay sample is from the Osage County Microgranite (Denison et al., 1984). The MMA-1 sample is an outcrop sample from a Martin-Marietta Aggregates quarry in south-central Oklahoma and is derived from the Troy Granite ("Q" in Figure 1d). All borehole core samples are obtained from the Oklahoma Petroleum Information Center (OPIC) core repository in Norman, Oklahoma. Samples are collected as intact core or rubble. All samples are pulverized in a disc mill until all

material passed through a 150μm sieve. The resulting gouge is then wetted to make a paste that form a 1 mm experimental gouge layer.

Friction Tests

We perform the experiments in a standard triaxial apparatus (Figure 5a). The 1 mm gouge layer is sandwiched within the sawcut of 19 mm diameter granite forcing blocks. The sawcut, inclined at 30° (Figure 5b), is roughened with 100 grit abrasive to ensure distributed deformation within the gouge layer (Moore et al., 2011). The top forcing block had a hole drilled through it to allow pore pressure communication with the gouge layer. Conditions for the experiments are chosen to represent depth conditions (confining pressure, pore pressure, and temperature) within the crust (Table 3). Temperature calculations are based on a 23°C/km (Harrison et al., 1982), which is a reasonable approximation for the Precambrian crust of the midcontinent. Pore pressure is set to be hydrostatic, 10 MPa/km and effective confining pressure is set to be 17.5 MPa/km. All samples are saturated with a solution of DI water that was allowed to equilibrate with granite rubble for 24 hours. All experimental conditions are shown in Table 3.

Samples are jacketed in a lead jacket for isolation from confining fluid. A greased Teflon shim is placed between the piston and the sample assembly to allow for lateral slip of the lower driving block during shear. A shear strength correction, due to the stretching of the lead jacket, is applied to the measured shear stress. Also, we correct for shear and normal stresses for the reduction in contact area as the two sample halves slide past each other. Axial load is measured with an internal load cell. Confining and pore pressures are measured at a rate of 1 Hz. Shear and normal stress resolved on the fault surface are computed in real time from the axial stress,

confining pressure and axial shortening. Confining pressure is modified in real time to maintain a constant resolved normal stress on the experimental fault plane. Axial stress, confining pressure and pore pressure have accuracies of at least 0.03 MPa. Sample strength is reported as the coefficient of friction (Figure 6). Within a single experiment, changes in the coefficient of friction have a precision of ±0.001. After correcting for true contact area and jacket strength, the determined coefficient of friction has an accuracy of ±0.01.

Samples are sheared to a total of ~4.5 mm axial shortening. Axial shortening rates are stepped in the following sequence to determine the dependence of friction on shear velocity: 1.0-0.3-0.1-0.03-0.1-0.3-1-0.5 μm/s. Due to the 30° sawcut, slip and slip rate on the inclined fault surfaces are 15% higher than the corresponding axial values.

The friction rate parameter is determined by manually measuring the change in friction ($\Delta\mu$) due to a velocity step from a de-trended friction-displacement curve. De-trending is necessary to remove long-term strain hardening trends. The measured $\Delta\mu$ values are then used to calculate the friction rate parameter (a-b) via:

$$(a\text{-}b) = (\Delta\mu)/\ln(V/V_0)$$

where V_0 is the velocity before the velocity step and V is the velocity following the step (Dieterich, 1979; Ruina, 1983). Where samples are failing by stick-slip, ($\Delta\mu$) is measured between the average friction before/after the velocity step.

RESULTS

Exposed Fault and Fracture Systems

In our fieldwork we characterize the fault and fracture systems in basement outcrops of the Tishomingo, Troy and Blue River granites (Figure 1d). The exposures display multiple networks of sub-vertical fracture that locally control the hummocky surface morphology and stream directions (Figures 2a, 7a-b). The clear majority of the fractures show tensile features, including rough surfaces, en-echelon segmentation, and rare mineralization (Figures 7a, 8a-b). These tensile indicators are common in coarse-grained granites (Barton and Choubey, 1977; Martin and Stimpson, 1994), and the grain size of the studied granites ranges 1-3 cm. The examination of hundreds of fractures revealed only a small number of strike-slip faults with minor displacements of 2-36 cm, and sporadic occurrences of slickenlines (Figures 8a-b).

While most fractures are widely spaced, we found several discrete zones of intense damage with multiple, closely-spaced fractures (e.g., Figures 2a, 7b), exhibiting the following features: (1) a predominant fracture set with a cross-cutting minor set that together form rhombohedral blocks (Figure 2b); (2) systematic increase of fracture density toward the core of the zone (Figures 2a-b); (3) multi-scale, dense pattern of anastomosing fractures with local gouge (pulverized zone) (Figures 2b-c); and (4) partial control of the local drainage system (Figures 2a, Figure 7b). We interpret these damage-zones as the upper portions of deeper immature strike-slip fault zones. The interpretation is based on documented observations and analyses of fault-zones in crystalline rocks that revealed similar features of sub-parallel arrays of steeply-dipping fractures with small (cm-scale) strike-slip displacements (Segall and Pollard, 1983). Further, both field and subsurface observations have also shown that the intensity of fracturing and damage is highest at the fault core and decreases with distance from the fault zone (Barton and Zoback, 1992; Sagy et al., 2001), this pattern is similar to the present observation.

A striking feature of the fractures in the granite exposures is the consistent trends of both tensile fractures and small faults with predominant trends of NW-SE (317°±6.4°) and NE-SW (241°±2°), and a minor ~N-S trend (Figures 2d, 7, 8a-b). These trends also fit the NW-SE and NE-SW trends of the regional pegmatite and diabase intrusions (Denison, 1995) (Figure 8c). We extended the scale of the field analyses by mapping fracture systems on satellite images of the granite exposures (Figure 7b). The mapped 745 fracture segments, which range 3-200 m in length with a cumulative length of 17.3 km, reveal two dominant sets of NW-SE (308°±3.6°) and NE-SW (234°±3.7°) (Figure 7c). In summary, the exposed Precambrian basement displays a multi-scale consistency of the fracture/fault systems that generate a tectonic grain of two prominent trends (Figures 2d, 7c). Geochronological and structural analyses of the igneous intrusions that utilized these prominent fracture trends indicate that the fractures are Precambrian in age (Lidiak et al., 2014; Denison, 1995).

Earthquakes and Subsurface Fault Structures

As mentioned above, the recent earthquakes occur in north-central Oklahoma (Figure 1a) where the crystalline basement is covered by 1-3 km of sedimentary strata (Shah and Keller, 2017). We examined the seismicity pattern via the relocation of 10,879 earthquakes of Mw ≥0 covering the period of 2010-2017. The relocated epicenters display spatial clusters that form 717 distinct lineaments (e.g., Figure 1b) with two prominent trends of NW-SE (297°±3.6°) and NE-SW (239°±2.9°) (Figure 9a). These lineaments are reasonably interpreted as traces of reactivated faults (Fielding et al., 2017). We further examined the focal-plane solutions of 6,253 earthquakes of Mw ≥3 for the period of 2010-2018 (source: Oklahoma Geological Survey). These solutions revealed

two dominant trends of seismic slip planes: 307°±1.6° and 226°±1.6° (Figure 9b) that are consistent with the trends of the epicenter lineaments (Figure 9a).

To determine the subsurface basement structure in the seismically active area, we use 3-D seismic reflection data that covers 114 km^2 area in Osage County, northern Oklahoma, located at distance of about 18 km from 2016 Mw5.8 Pawnee earthquake epicenter (Figure 1a). The analysis reveals 16 sub-vertical fault-zones, some of which (black arrows in Figures 3a-b) cut through the upper-basement, disrupting intra-basement reflectors, into the top of the Arbuckle group. These intra-basement reflectors, which are most-likely related to mafic igneous sheet intrusions, have been observed in other parts of north-central Oklahoma (Elebiju et al; 2011). Some of the mapped faults branch out into strands that offset the sedimentary formations above the Arbuckle group (Figures 3a-c), and exhibit 230-500 m-wide zone of splays (Figure 3c) that depict the typical 'flower structures' of strike-slip faults. These basement faults range in length from 1.5 km to 7 km with variable trends (Figures 3a-b) (Table 1), and their implications for Oklahoma's earthquakes are discussed below.

Seismic Stability of Basement Material

As noted above, fluid injection can induce fault slip, but this slip may be manifested by either stable creep or seismic events (McGarr and Barbour, 2017; McGarr and Barbour, 2018), depending on the fault's seismic (i.e. frictional) stability at the given temperature/pressure conditions (Blanpied et al., 1991). We experimentally (Moore and Lockner, 2011) analyzed the frictional stability of basement rocks using four samples of cores from north-central Oklahoma, and one outcrop sample from south-central Oklahoma (Figures 4a-c, Table 2). These samples are

representative of common crystalline rocks as one might find anywhere in the exposed shield (Lidiak et al., 2014; Denison, 1981; Denison et al., 1984), where multiple phases of deformation are ubiquitous (Bickford et al., 2015). The experiments were performed at conditions relevant for the dominant seismicity depth range of 1.5 - 9.0 km. For the in-situ conditions of both temperature and confining pressure, we used a geothermal gradient of 23 °C/km (Harrison et al., 1982), and a pore-fluid pressure gradient of 10 MPa/km to produce an effective confining pressure gradient of 17.5 MPa/km (Table 3).

Frictional stability, as related to earthquake nucleation, is typically presented by the (a-b) parameter of the rate- and state- friction law, for which negative values indicate the likelihood of earthquake nucleation (Dieterich, 1979; Marone, 1998; Ikari et al., 2011) (Figure 10a). All tested samples display dominantly stable frictional behavior [(a-b) > 0] at shallow depths of 1.5 - 3 km followed by a transition to unstable frictional behavior at greater depths (Figure 10a). The unstable behavior frequently resulted in stick-slip sliding during the experiments for all samples (Figures 6a-d). The sample of the partially dolomitized carbonate vein (Figure 4c) transitioned to unstable behavior at shallower depths (3 km), and displayed the largest intensity of frictional instability, with large stick-slips by 6 km depth. The granite and rhyolite samples transitioned to fully unstable behavior at greater depth (4-6 km), consistent with previous experimental behavior of granite under hydrothermal conditions (Blanpied et al., 1991). The observed transition from stable to unstable slip of the Oklahoma basement samples at depths (3 - 6 km) corresponds well to the depth distribution of the earthquake hypocenters and major increase in cumulative moment release (Figure 10b). Our results indicate that extensive hydrothermal alteration, observed in many parts of Oklahoma (Lidiak et al., 2014; Denison, 1981; Denison et al., 1984) could result in seismically unstable fault zone material at shallower depths. Further, we view the stability determinations as

a conservative estimate considering the observation of a sub-hydrostatic gradient in Oklahoma (Nelson et al., 2015), and previous experimental results in granite which show increased instability with lower loading velocities (Blanpied et al., 1998), both of which would result in a shallower transition to unstable behavior.

DISCUSSION & SUMMARY

Oklahoma's Susceptibility to Seismic Reactivation

The results of the present analyses shed light on the basic mechanics that control the recent Oklahoma earthquakes. Our analyses explain why the Oklahoma basement faults are susceptible to reactivation by wastewater injection in such a way that has led to the widespread, intense seismicity within the current stress field (Keranen et al., 2013, 2014). We discuss here our three main discoveries and their implications for the observed seismicity.

First, we show a remarkable relationship between the dominant basement fabric and recent earthquake characteristics in Oklahoma. We document these relations via five independent methods (Supplementary Table 1): (1) field-mapping of fracture and fault networks (Figures 2a-d, 7a, 8a-b); (2) satellite-scale mapping of fracture systems (Figures 7b-c); (3) subsurface mapping of fault-zones (Figures 3a-c); (4) delineation of earthquake cluster lineaments (Figure 1b, 9a); and (5) compilation of nodal planes from earthquake focal-mechanism solutions (Figure 9b). The observations indicate the existence of a tectonic fabric with dominant discontinuity zones within the Precambrian basement that trend NE-SW and NW-SE (Figure 3d). These preexisting faults are weak zones waiting to be reactivated, similar to previously documented reactivation of basement faults in the New Madrid area of the central United States[35]. Further, the reactivation of faults can

even occur under unfavorably-oriented stresses (Reches, 1978) or after long periods (>2 Ga) of inactivity (Heesakkers et al., 2011). In Oklahoma, the faults trending NE-SW and NW-SE are favorably oriented relative to the maximum horizontal compression that strikes ~080° in the mid-continent United States, determined prior to the recent seismic activity (Zoback and Zoback, 1991). Therefore, the preexisting faults documented in the present study are critically stressed for strike-slip motion, and are thus expected to be reactivated, even by stress or pore pressure perturbations of 2 MPa and less (Walsh and Zoback, 2016; Barbour et al., 2017).

Second, a crucial observation of the subsurface analysis is that the basement fault-zones cut into the Arbuckle Group and shallower units (Figures 3a-c). This is the first direct observation of physical linkage between the Arbuckle Group, which is the main unit for wastewater disposal in Oklahoma, and underlying basement faults (Figure 3c). The existence of such fluid migration pathways is an essential component for fast earthquake triggering by waste-water injection. For example, the foreshocks leading up to the 2016 Mw5.8 Pawnee earthquake (Figure 1a) were near-instantaneous response to variations in injection rates at disposal wells within 20 km radius of the mainshock (Chen et al., 2017; Barbour et al., 2017).

Third, our rock-mechanics analysis of Oklahoma basement rocks and hydrothermal alteration products (Table 2) show that these rocks become seismically unstable under in-situ depth conditions (temperature, pressure and water-saturation) of 3 - 6 km (Figure 10a). Thus, fault-zones composed of these rocks are likely to nucleate earthquakes, rather than creep, at depths >3 km. This transition to unstable slip well explains the depth distribution of the hypocenters and moments with concentration at 3 - 6 km depth interval (Figure 10b), and further explains the relatively small number of earthquakes at the wastewater injection depths of <3 km below surface[6].

Our analyses provide the essential ingredients for understanding the current induced seismicity by wastewater injection in Oklahoma. We show that Oklahoma is prone to wide-spread seismicity by reactivation of preexisting basement structures facilitated by the key properties of these structures. It is suspected that other regions of intense wastewater injection, e.g., Texas and South Dakota, which display significantly lower levels of induced earthquakes lack one or more of the needed ingredients highlighted in this study.

Contributors to this project: F. Kolawole, C. S. Johnston, C. B. Morgan, J. C. Chang, K. J. Marfurt, D. A. Lockner, Z. Reches, and B. M. Carpenter.

Acknowledgments: Thanks to the USGS Induced Seismicity Project for providing financial support and laboratory expertise/time to conduct the experiments. Thanks to Nick Beeler, Andrew Barbour, and two anonymous reviewers for their helpful reviews. Thanks to the Osage Nation and SpyGlass Energy, LLC for providing the seismic data used in this study. Thanks to the Oklahoma Geological Survey for providing earthquake and focal mechanism data.

Publication of the results: Kolawole, F., Johnston, C. S., Morgan, C. B., Chang, J. C., Marfurt, K. J., Lockner, D. A., Reches, Z., & Carpenter, B. M. (2019). The Susceptibility of Oklahoma's Basement to Seismic Reactivation. *Nature Geoscience, 12(10), 839-844*.

CHAPTER 2 FIGURES

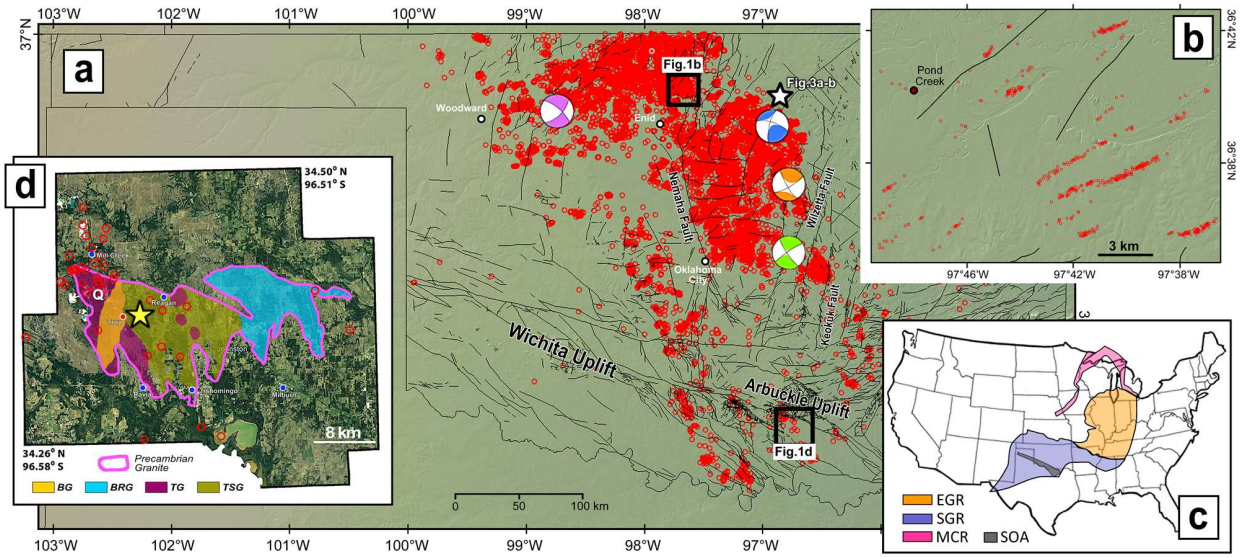

Figure 1. Earthquakes and basement lithology in Oklahoma. (a) Earthquakes in Oklahoma for 2010 – 2017; red circles = earthquake epicenters (Oklahoma Geological Survey catalogue); thin, black lines = mapped faults (Marsh and Holland, 2016); focal mechanism solutions of Mw >5.0 events = 2011 Mw5.7 Prague (green), 2016 Mw5.1 Fairview (purple), 2016 Mw5.8 Pawnee (blue), and 2016 Mw5.0 Cushing (orange); black squares and white star indicate location of stated figures. (b) Close-up of region marked "Figure 1b" in Figure 1a showing a discrepancy between lineaments of relocated earthquakes (red circles) and previously mapped faults. (c) Precambrian Terranes in US Mid-continent (Bickford et al., 2015); EGR = Eastern Granite-Rhyolite Province, SGR = Southern Granite-Rhyolite Province, MCR = Mid-Continent Rift. SOA = Southern Oklahoma Aulacogen (Cambrian). (Bickford et al., 2015). (d) Close-up satellite image (source: Google, Landsat/Copernicus) of region marked "Figure 1d" in Figure 1a, showing Precambrian basement exposures (Lidiak et al., 2014), Johnston County, southern Oklahoma; Q = Martin Marietta Quarry; BG = Burch Granodiorite, BRG = Blue River Granite, TG = Troy Granite, TSG = Tishomingo Granite.

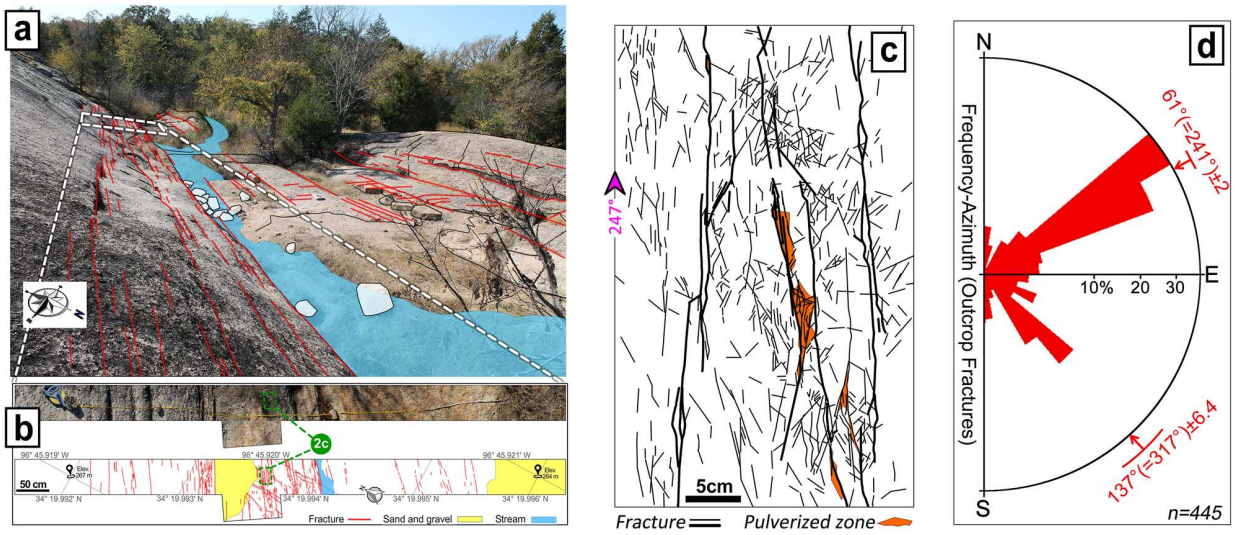

Figure 2. Outcrop fractures. (a) Precambrian basement outcrop with a 241° trending zone of fracture clusters, interpreted as the upper portions of a deeper immature strike-slip fault zone (location: yellow star in Figure 1d). (b) Close-up photograph of the zone of fracture clusters with structural mapping. (c) Close-up view with dense fracture network and gouge at the core of a fracture cluster (dashed green boxes and line in Figure 2b). (d) Frequency-azimuth distribution of 445 fracture segments from Figure 1d. Structural trends are described as "mean trend (=mean trend+180º) ± standard deviation".

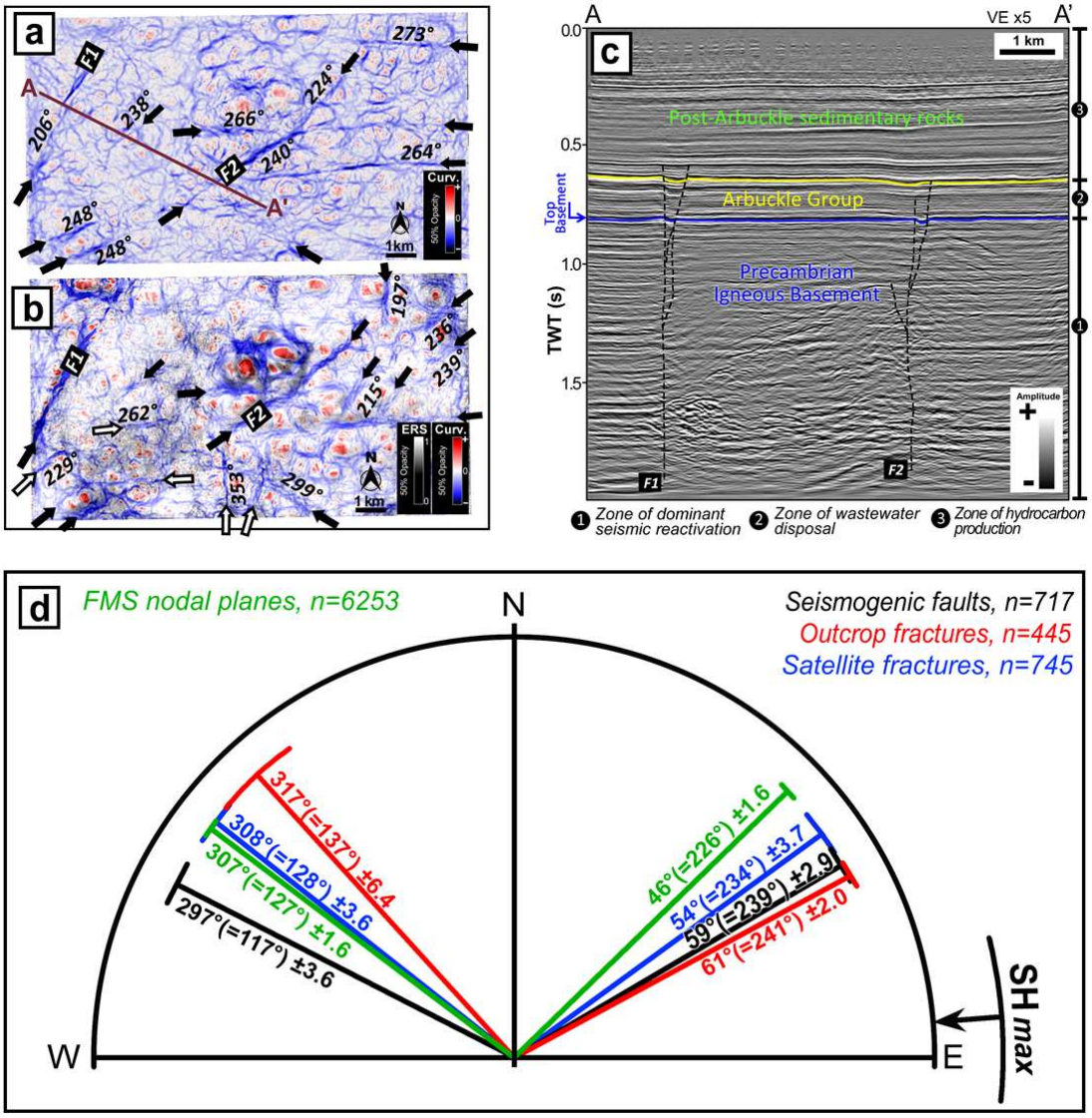

Figure 3. 3D seismic data and structural data compilation. Subsurface structure at location marked in Figure 1a (white star) based on 3D seismic survey showing time-structure map of Top-Basement (a) and Top-Arbuckle (b) co-rendered with curvature and energy-ratio-similarity (ERS) seismic attributes. Black arrows = lineaments detected in both Figures 3a and b; white arrows = lineaments detected only in b; these lineaments are interpreted as fault-zones. (c) Seismic cross-section along A-A' (in Figure 3a) overlaid with interpretations. F1 and F2 are faults with associated flower structures. Data courtesy: Osage Nation and SpyGlass Energy. (d) Overlays of frequency-azimuth rose diagrams for satellite-scale fractures, outcrop-scale fractures, seismogenic faults (Figure 1b; see text) and focal-plane mechanism solution (FMS) nodal planes. Structural trends are described as "mean trend (=mean trend+180º) ± standard deviation". Arrow represents estimated SHmax orientations for Oklahoma (Zoback and Zonack, 1991; Qi, 2016; Alt and Zoback, 2016).

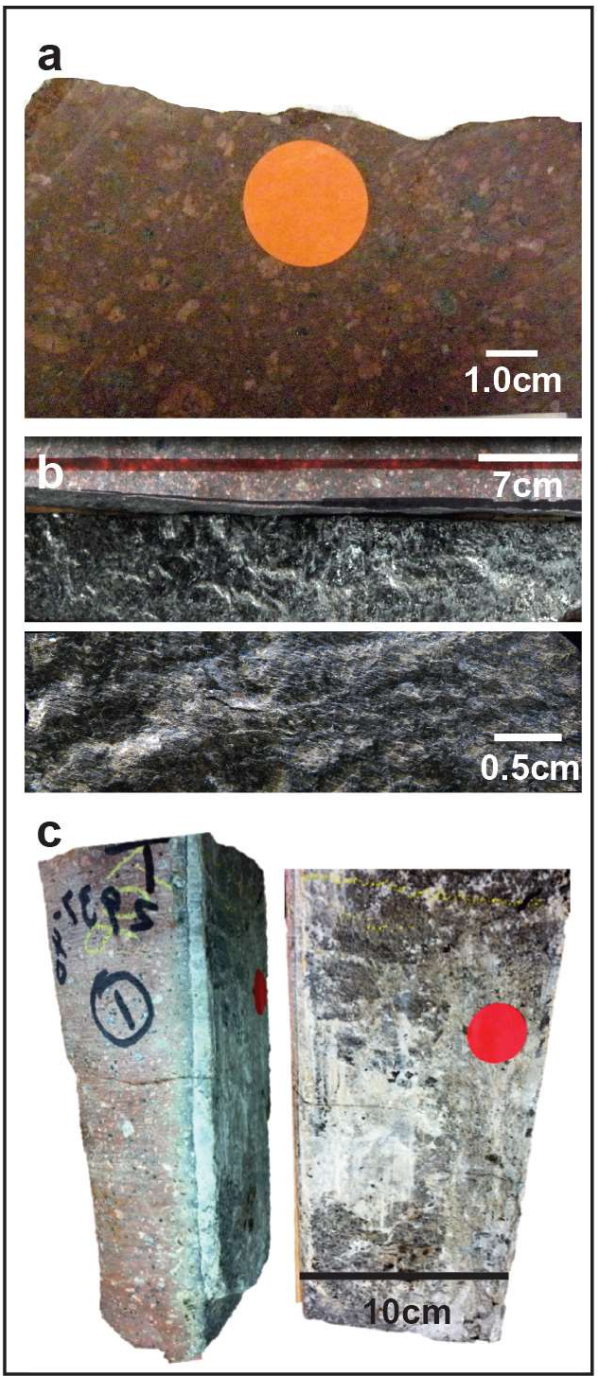

Figure 4. Experimental samples. Experimental borehole samples, and their depths, from north-central Oklahoma. (a) Kohpay, 0.86 km, Osage Microgranite. (b) SHADS 4-1, 0.99 km material from sub-vertical, epidote coated fracture. (c) Jones 46-1 (left), and Jones 46-5 (right), 0.90 km, partially dolomitized calcite vein in rhyolite.

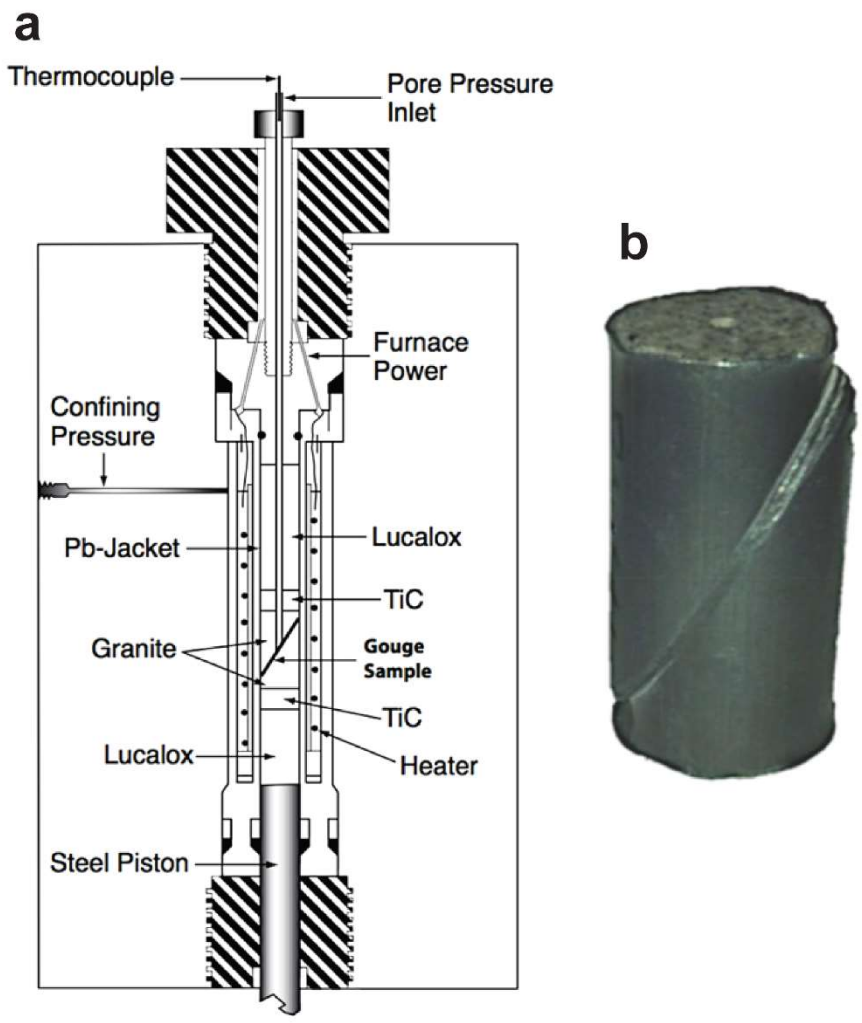

Figure 5. Experimental apparatus. a, Schematic of the triaxial deformation apparatus used in this study. b, Jacketed, post-experimental sample.

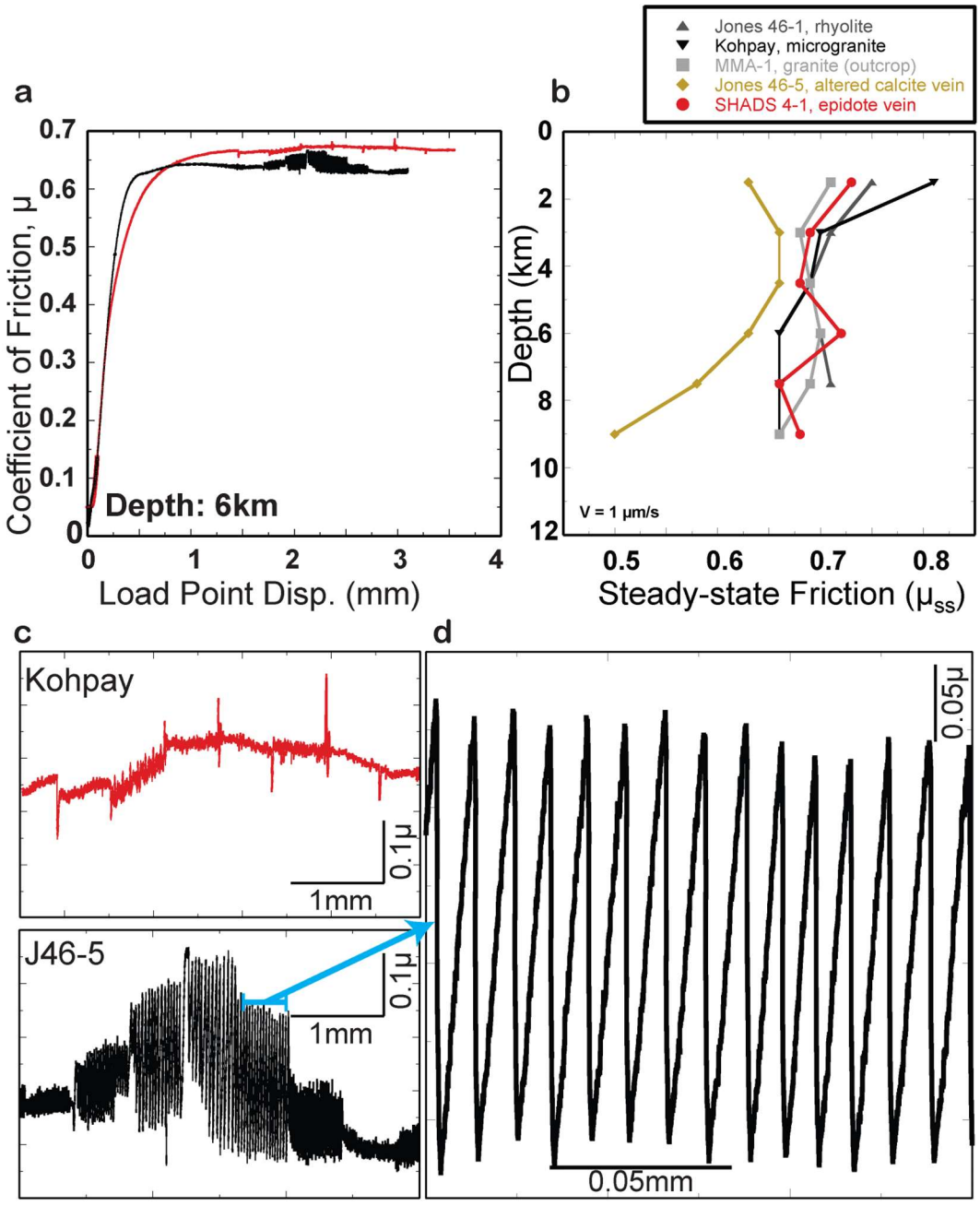

Figure 6. Experimental friction data. (a) Experimental data for Kohpay and Jones 46-5 at experimental depth conditions of 6 km. (b) Steady-state friction, at v = 1 μm/s, as a function of experimental depth for all samples in this study. (c) Zoom of the velocity step portion of the experiments in A showing stable sliding in the Kohpay sample and stick-slip behavior in the Jones 46-5 sample. (d) Additional zoom showing stick-slip sliding in the J46-5 sample.

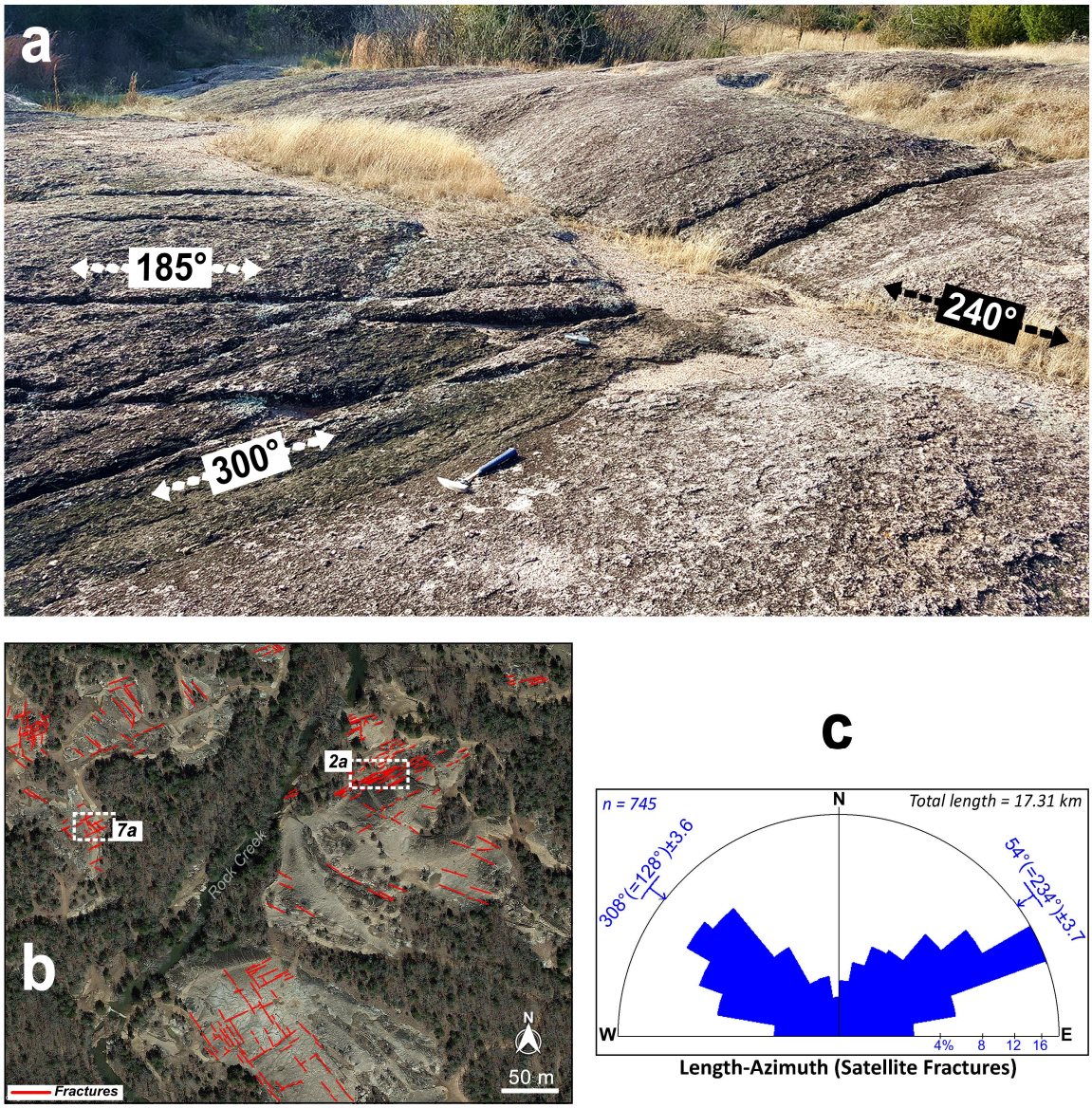

Figure 7. Outcrop exposures. (a) Hummocky granite exposure in southern Oklahoma (location in Figure 7b) showing an intersection zone of the dominant fracture trends in the Precambrian basement outcrops. (b) Fracture systems in Tishomingo granite exposures (location: yellow star in Figure 1d), mapped on satellite image (satellite data source: Google, Landsat/Copernicus). (c) Length-azimuth distribution for the satellite-scale fractures in Figure 1d. Structural trends are described as "mean trend (=mean trend+180º) ± standard deviation".

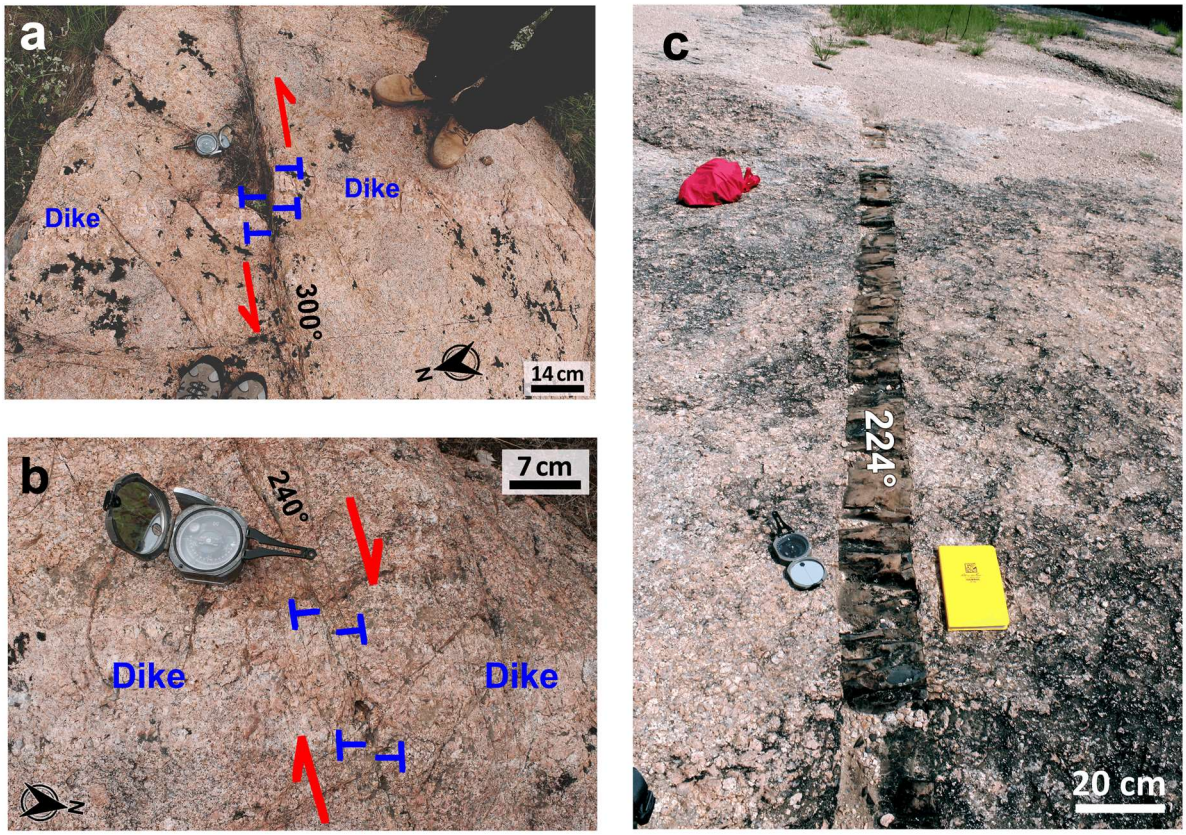

Figure 8. Outcrop deformation details. (a) 300° left-lateral strike-slip fault with 10 cm offset on a pegmatite dike (Blue River Granite). (b) 240° right-lateral strike-slip fault with 2 cm offset on a pegmatite dike (Blue River Granite). (c) 224° -striking diabase dike (Tishomingo Granite).

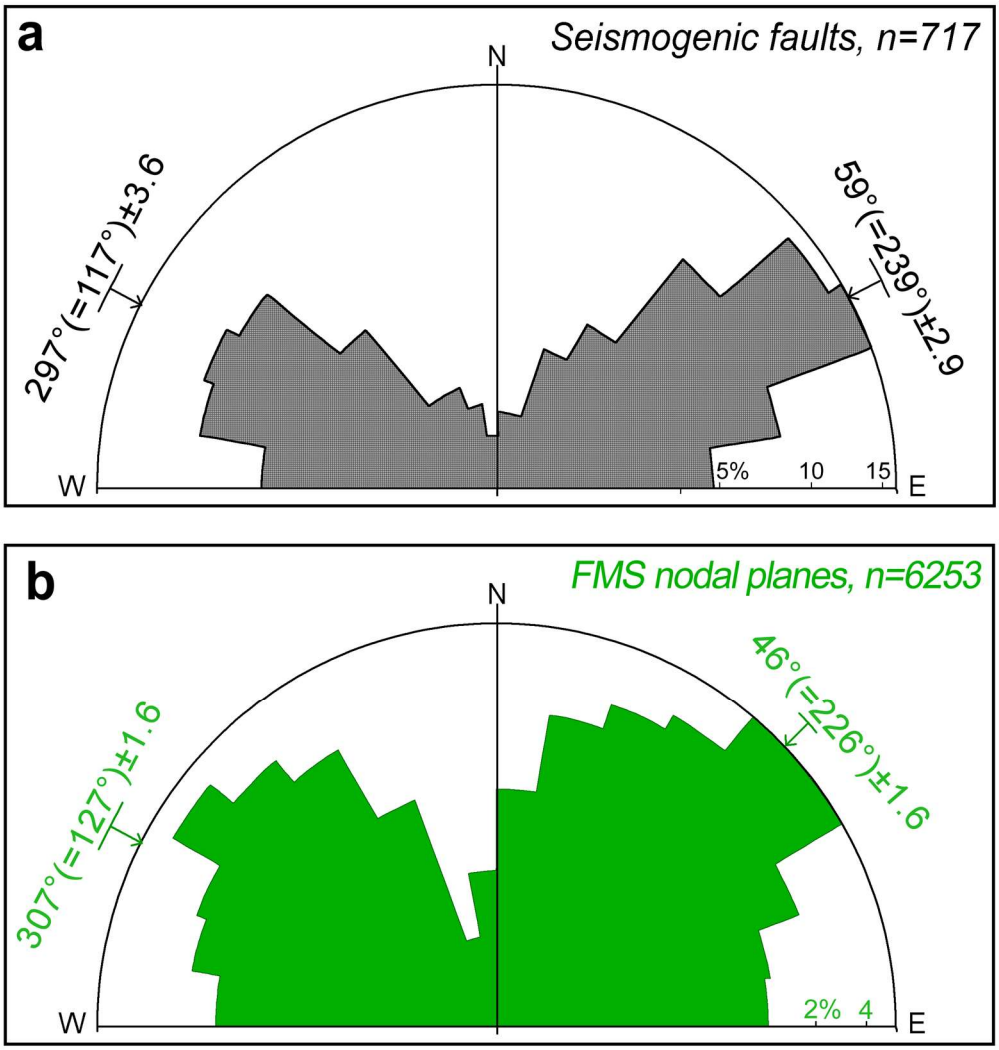

Figure 9. Seismologically determined fault orientations (a) Frequency-azimuth distribution of the seismogenic faults (lineaments formed by earthquake clusters e.g., Figure 1b). (b) Frequency-azimuth distribution of nodal planes from focal mechanism solutions for Oklahoma earthquakes (Source: *Oklahoma Geological Survey*). Structural trends are described as "mean trend (=mean trend+180º) ± standard deviation".

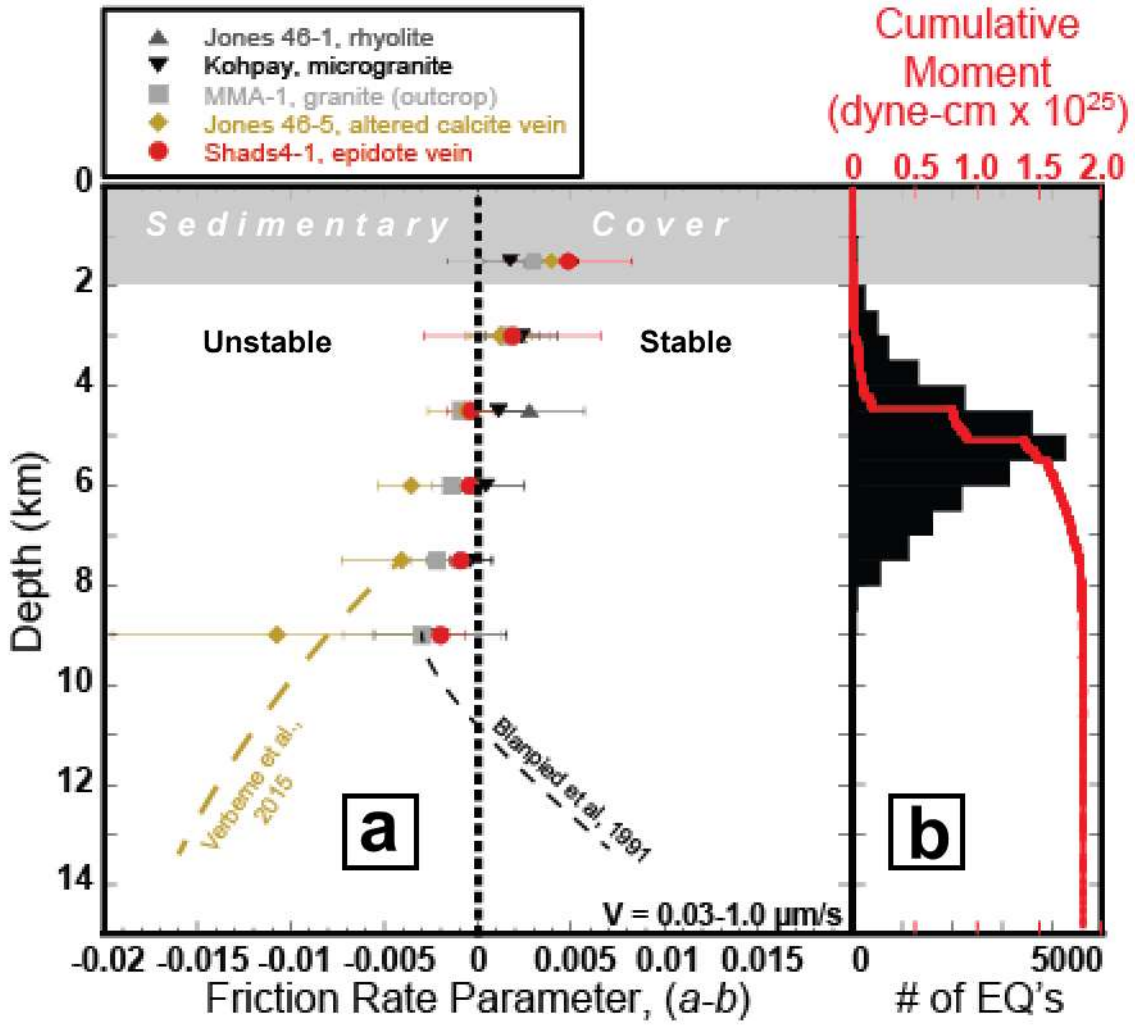

Figure 10. Depth distribution of seismic stability and earthquakes in Oklahoma. (a) Seismic stability of Oklahoma basement samples as represented by the rate- and state-friction parameter (*a*-*b*). The symbol shows the average of the velocity steps tested and the error bars show the range of values for each experimental sample and depth. Gold and black dashed lines represent projection of data for pure calcite (Verberne et al., 2015) and Westerly granite (Blanpied et al., 1991) respectively. (b) Histogram and cumulative moment (Kanamori et al., 1983) with depth for the relocated Oklahoma earthquakes (this study) for the period 2010-2017.

TABLE 1. Summary of structural trends of basement fractures/fault systems and seismic trends in Oklahoma.

Independent Sources	Mean trend NE Set	Mean trend NW Set
Outcrop Fractures	241° (±2.0)	317° (±6.4)
Satellite Fractures	234° (±3.7)	308° (±3.6)
Seismogenic Faults	239° (±2.9)	297° (±3.6)
Focal-mechanism solution	226° (±1.6)	307° (±1.6)
95% confidence interval of mean trend in bracket		

TABLE 2. Lithology and location of samples used in this study.

Sample	Material	Sample Depth (km)	Location
Jones 46-1	Unaltered rhyolite	0.90	36.277°, -96.472°
Kohpay	Osage Microgranite	0.86	36.621°, -96.460°
MMA-1	Troy Granite	Outcrop	34.358°, -96.809°
Jones 46-5	Partially (10%) dolomitized calcite vein	0.90	36.277°, -96.472°
Shads 4-1	Epidote vein fill	0.99	36.266°, -95.759°

Table 3. Experimental conditions for the triaxial testing of the seismic stability of the 5 analyzed basement samples. P_c' = Effective Confining Stress, P_c = Confining Stress, P_p = Pore Pressure, T = Temperature.

Depth (km)	P_c' (MPa)	P_c (MPa)	P_p (MPa)	T (°C)
1.5	26.25	41.25	15	35
3.0	52.5	82.5	30	70
4.5	78.75	123.75	45	105
6.0	105	165	60	140
7.5	131.25	205.25	75	175
9.0	157.5	247.5	90	210

REFERENCES

Alt, R. C. & Zoback, M. D. (2016). In situ stress and active faulting in Oklahoma. Bull. Seis. Soc. Amer. 107, 216-228.

Barbour, A. J., Norbeck, J. H., & Rubinstein, J. L. (2017). The effects of varying injection rates in Osage County, Oklahoma, on the 2016 Mw 5.8 Pawnee earthquake. Seis. Res. Lett. 88, 1040- 1053.

Barton, N. & Choubey, V. The shear strength of rock joints in theory and practice. Rock Mech. 10, 1-54 (1977).

Barton, C. A., & Zoback, M. D. (1992). Self-similar distribution and properties of macroscopic fractures at depth in crystalline rock in the Cajon Pass scientific drill hole. J. Geophys. Res. 97, 5181–5200.

Bickford, M. E., Van Schmus, W. R., Karlstrom, K. E., Mueller, P. A., & Kamenov, G. D. (2015) Mesoproterozoic-trans-Laurentian magmatism: A synthesis of continent-wide age distributions, new SIMS U–Pb ages, zircon saturation temperatures, and Hf and Nd isotopic compositions. Precamb. Res. 265, 286-312.

Blanpied, M. L., Tullis, T. E., & Weeks, J. D. (1998). Effects of slip, slip rate, and shear heating on the friction of granite. J. Geophys. Res. 103, 489–511.

Blanpied, M. L., Lockner, D. A., & Byerlee, J. D. (1991). Fault stability inferred from granite sliding experiments at hydrothermal conditions. Geophys. Res. Lett. 18, 609-612.

Brewer, J. A., Good, R., Oliver, J. E., Brown, L. D. & Kaufman, S. (1983). COCORP profiling across the Southern Oklahoma aulacogen: Overthrusting of the Wichita Mountains and compression within the Anadarko Basin. Geol. 11, 109-114.

Cannon, W. F. (1994). Closing of the Midcontinent rift - A far-field effect of Grenvillian compression. Geol. 22, 155-158.

Chen, X., Nakata, N., Pennington, C., Haffener, J., Chang, J. C., He, X., Zhan, Z., Ni, S., & Walter, J. I. (2017). The Pawnee earthquake as a result of the interplay among injection, faults and foreshocks. Scientific Reports, 7(1), 1-18.

Chopra, S., & Marfurt, K. J. (2007). Seismic attributes for prospect identification and reservoir characterization. Soc. Expl. Geophys., Tulsa.

Denison, R. E. (1995). Significance of air-photograph linears in the basement rocks of the Arbuckle Mountains. Ok. Geol. Surv. Circ. 97, 119-131.

Denison, R. E. (1981). Basement rocks in northeastern Oklahoma. Ok. Geol. Surv. Circ. 84, The Univ. of Oklahoma Printing Services, Norman.

Denison, R. E., Lidiak, E. G., Bickford, M. E. & Kisvarsanyi, E. B. (1984). Geology and geochronology of Precambrian rocks in the central interior region of the United States. U.S. Geol. Surv. Prof. Pap. 1241-C, C1-C20.

Dieterich, J. H. (1979). Modeling of rock friction 1. Experimental results and constitutive equations. J. Geophys. Res. 84, 2161-2168.

Elebiju, O. O., Matson, S., Keller, G. R., & Marfurt, K. J. (2011). Integrated geophysical studies of the basement structures, the Mississippi chert, and the Arbuckle Group of Osage County region, Oklahoma. AAPG Bull. 95, 371-393.

Ellsworth, W. L. (2013). Injection-induced earthquakes. Science 341, 1225942.

Fielding, E. J., Sangha, S. S., Bekaert, D. P., Samsonov, S. V. & Chang, J. C. (2017). Surface deformation of north-central Oklahoma related to the 2016 Mw 5.8 Pawnee earthquake from SAR interferometry time series. Seis. Res. Lett. 88, 971-982.

Goebel, T. H. W., Weingarten, M., Chen, X., Haffener, J., & Brodsky, E. E. (2017). The 2016 Mw5.1 Fairview, Oklahoma earthquakes: Evidence for long-range poroelastic triggering at >40 km from fluid disposal wells. Ear. Plan. Sci. Lett. 472, 50-61.

Harrison, W. E., Luza, K. V., Prater, M. L., Cheung, P. K., & Ruscetta, C. A. (1982). Geothermal resource assessment in Oklahoma. No. DOE/ID/12079-71-Vol. 1; ESL-98-Vol. 1; CONF-820491 1-12.

Heesakkers, V., Murphy, S., Lockner, D. A., & Reches, Z. (2011). Earthquake Rupture at Focal Depth, Part II: Mechanics of the 2004 M2.2 Earthquake Along the Pretorius Fault, TauTona Mine, South Africa. Pur. Appl. Geophys. 168, 2427–2449.

Hurd, O., & Zoback, M. D. (2012). Regional stress orientations and slip compatibility of earthquake focal planes in the New Madrid seismic zone. Seis. Res. Lett. 83, 672-679.

Ikari, M. J., Marone, C., & Saffer, D. M. (2011). On the relation between fault strength and frictional stability. Geol. 39, 83-86.

Kanamori, H. (1983). Magnitude scale and quantification of earthquakes. Tectonophys. 93, 185-199.

Keller, G. R., & Stephenson, R. A. (2007). The southern Oklahoma and Dniepr-Donets aulacogens: a comparative analysis. Geol. Soc. Amer. Mem. 200, 127.

Keranen, K. M., Savage, H. M., Abers, G. A., & Cochran, E. S. (2013). Potentially induced earthquakes in Oklahoma, USA: Links between wastewater injection and the 2011 Mw 5.7 earthquake sequence. Geol. 41, 699-702.

Keranen, K. M., Weingarten, M., Abers, G. A., Bekins, B. A. & Ge, S. (2014). Sharp increase in central Oklahoma seismicity since 2008 induced by massive wastewater injection. Science 345, 448-451.

Kroll, K. A., Cochran, E. S., & Murray, K. E. (2017). Poroelastic properties of the Arbuckle Group in Oklahoma derived from well fluid level response to the 3 September 2016 Mw 5.8 Pawnee and 7 November 2016 M w 5.0 Cushing earthquakes. Seis. Res. Lett. 88, 963-970.

Lidiak, E. G., Denison, R. E. & Stern, R. J. (2014). Cambrian (?) Mill Creek Diabase Dike Swarm, Eastern Arbuckles: a glimpse of Cambrian rifting in the Southern Oklahoma Aulacogen. Ok. Geol. Surv. Guidebook 38, 105-122.

Marone, C. (1998). Laboratory-derived friction laws and their application to seismic faulting. Ann. Rev. Ear. Plan. Sci. 26, 643–696.

Marsh, S. & Holland, A. (2016). Comprehensive fault database and interpretive fault map of Oklahoma. Ok. Geol. Surv. Open-File Rep. OF2-2016 15.

Martin, C. D. & Stimpson, B. (1994). The effect of sample disturbance on laboratory properties of Lac du Bonnet granite. Canad. Geotech. J. 31, 692-702.

McGarr, A. & Barbour, A. J. (2017). Wastewater disposal and the earthquake sequences during 2016 near Fairview, Pawnee, and Cushing, Oklahoma. Geophys. Res. Lett. 44, 9330-9336.

McGarr, A. & Barbour, A. J. (2018). Injection-induced moment release can also be aseismic. Geophys. Res. Lett. 45, 5344–5351.

Moore, D. E. & Lockner, D. A. (2011). Frictional strengths of talc-serpentine and talc-quartz mixtures. J. Geophys. Res. Sol. Ear. 116, B01403.

Nelson, P. H., Gianoutsos, N. J. & Drake, R. M. (2015). Underpressure in Mesozoic and Paleozoic rock units in the Midcontinent of the United States. AAPG Bull. 99, 1861–1892.

Powers, S. (1928). Age of the Folding of the Oklahoma Mountains—the Ouachita, Arbuckle, and Wichita Mountains of Oklahoma and the Llano-Burnet and Marathon Uplifts of Texas. Bull. Geol. Soc. Amer. 39, 1031-1071.

Qi, W. (2016). Stress analysis of recent earthquakes in Oklahoma. Thesis, University of Oklahoma, Norman, OK.

Reches, Z. (1978). Analysis of faulting in three-dimensional strain field. Tectonophys. 47, 109-129.

Ruina, A. (1983). Slip instability and state variable friction laws. J. Geophys. Res. 88, 10359–10370.

Sagy, A., Reches, Z. E., & Roman, I. (2001). Dynamic fracturing: field and experimental observations. J. Struct. Geol. 23, 1223-1239.

Segall, P., & Pollard, D. D. (1983). Nucleation and growth of strike slip faults in granite. J. Geophys. Res. Sol. Ear. 88, 555-568.

Schoenball, M., & Ellsworth, W. L. (2017). Waveform-Relocated Earthquake Catalog for Oklahoma and Southern Kansas Illuminates the Regional Fault Network. Seis. Res. Lett. 88, 1252-1258.

Shah, A. K., & Keller, G. R. (2017). Geologic influence on induced seismicity: Constraints from potential field data in Oklahoma. Geophys. Res. Lett. 44, 152-161.

Schultz, R., Wang, R., Gu, Y. J., Haug, K., & Atkinson, G. (2017). A seismological overview of the induced earthquakes in the Duvernay play near Fox Creek, Alberta. J. Geophys. Res. Sol. Ear. 122, 492–505.

Verberne, B. A., Niemeijer, A. R., De Bresser, J. H. P., & Spiers, C. J. (2015). Mechanical behavior and microstructure of simulated calcite fault gouge sheared at 20–600°C: Implications for natural faults in limestones. J. Geophys. Res. Sol. Ear. 120, 8169–8196.

Waldhauser, F., & Ellsworth, W. L. (2000). A double-difference earthquake location algorithm: Method and application to the northern Hayward fault, California. Bull. Seis. Soc. Amer. 90, 1353–1368.

Walsh III, F. R., & Zoback, M. D. (2015). Oklahoma's recent earthquakes and saltwater disposal. Science advances 1, p.e1500195.

Walsh III, F. R., & Zoback, M. D. (2016). Probabilistic assessment of potential fault slip related to injection-induced earthquakes: Application to north-central Oklahoma, USA. Geol. 44, 991-994.

Zoback, M. D., & Zoback, M. L. (1991). Tectonic stress field of North America and relative plate motions. Neotect. Nor. Amer. 1, 339-366.

CHAPTER 3

BASEMENT-CONTROLLED DEFORMATION OF SEDIMENTARY SEQUENCES, ANADARKO SHELF, OKLAHOMA

ABSTRACT

Structures rooted in the crystalline basement frequently control the deformation of the host bedrock and the overlying sedimentary sequences. Here, we elucidate the structure of the ~2 km-deep Precambrian granitic basement in the Anadarko Shelf, Oklahoma, and how the propagation of basement faults deformed the sedimentary cover. Although the basin is foreland in origin, the gently-dipping shelf sequences experienced transpressional deformation in the Late Paleozoic. We analyze a 3-D seismic reflection dataset and basement penetrating well data in an area of 824 km^2. We observe: (1) pervasive deformation of the basement by basement-bounded interconnected mafic sills, and a system of sub-vertical discontinuity planes (interpreted as faults) of which some penetrate the overlying sedimentary cover, (2) three large (>10 km-long) through-going faults, with relatively small (<100 m) vertical separation (Vsep) of the deformed stratigraphic surfaces, (3) upward propagation of the large faults characterized by faulted-blocks near the basement, and faulted-monoclines in the deeper sedimentary units that transition into open monoclinal flexures up-section, (4) cumulative along-fault deformation of the stratigraphy exhibits systematic trends that varies with offset accrual, (5) two styles of Vsep - Depth distribution which include a unidirectional decrease of Vsep from the basement through the cover rocks (Style-1), and a bi-directional decrease of Vsep from a deep sedimentary unit toward the basement and shallower sequences (Style-2). We find that the basement-driven propagation (Style-1) shows greater efficiency of driving the fault deformation to shallower depths compared to the intrasedimentary-

driven fault nucleation and propagation (Style-2). Our study demonstrates an evolution of cumulative Vsep trends with offset accrual on the faults, and the partial inheritance of the heterogeneous intrabasement deformation by the sedimentary cover. This contribution provides important insight into the upward propagation of basement-driven faulting associated with structural inheritance in contractional sedimentary basins.

INTRODUCTION

Contractional basement-involved structures in sedimentary basins have been studied both in the field, geophysical datasets and through modelling experiments (e.g., Coward, 1983; Naylor et al., 1986; McClay & Ellis, 1987; Hardy & Ford, 1997; Harper et al., 2001; McClay, 2011; Lacombe & Bellahsen, 2016). The nucleation and development of contractional structures are often found to be controlled by structural inheritance from the underlying crystalline basement, typically in the form of faults and fracture networks (e.g., Lowell, 1995; Lihou & Allen, 1996; Turner & Williams, 2004; Keller & Stephenson, 2007; Iaffa et al., 2011), magmatic intrusions (Gwon & Kim, 2016; Lee & Kim, 2018), metamorphic foliation and ductile shear zones (e.g., Collanega et al., 2018). Zones of structural weakness in the basement may preferentially localize strain such that their tectonic reactivation can influence the structural architecture and deformation of the sedimentary sequences within a basin (e.g., Yonkee, 1992; Erslev & Koenig, 2009; Kolawole et al., 2018, 2019a).

Contractional basement-involved structures are most common in foreland basins where they occur between major fold and thrust belts and the undeformed craton (e.g., Rodgers, 1987; Mitra & Mount, 1998; Lacombe & Bellahsen, 2016). This category of basement-involved structures is typically characterized by a major basement-rooted fault that is overlain by a long chain of

anticlinally-folded sedimentary sequences with steepened (to overturned) forelimbs and gently-dipping backlimbs (e.g., Mitra & Mount, 1998). The associated fault may be steeply-dipping in the basement, but more shallowly-dipping in the sedimentary cover (anticlinal fault bend; e.g., Berg, 1962; Prucha et al., 1965). In other cases, the fault may be steeply-dipping at shallow basement depths, but less steep (synclinal fault bend; Mitra & Mount, 1998) or very gentle at deeper depths (thrust; Berg, 1962; Brown, 1983; Stone, 1993). Also, the structures may develop by reverse slip, strike-slip, or a combination of both kinematics (transpression), commonly associated with flexural slip in the sedimentary cover (e.g., Stearns, 1975, 1978; Reches, 1978; Suppe, 1983; Tindall & Davis, 1999). Additionally, the deeper sedimentary units may or may not be welded to the underlying crystalline basement, each case producing distinct structural styles of predictable mechanical deformation (Mitra & Mount, 1998).

Above a propagating contractional basement-rooted fault, a major fault-propagation fold develops with a triangle deformation field that converges downwards towards the tip of the basement fault trace (e.g., Erslev, 1991; Hardy & Ford, 1997; Mitra & Mount, 1998; Hardy & Allmendinger, 2011). This triangular deformation field above the basement fault represents a 'halo zone' of fault influence within which intense penetrative contractional deformation may be expected (e.g., Mitra & Mount, 1998; Burberry & Lowe, 2019). Furthermore, the associated styles of deformation may be influenced by a combination of position relative to the basement fault trace (i.e. height of the unit above the basement) and the mechanical behavior of the various rock units (Reches, 1978).

Most studies of contractional basement-involved deformation of sedimentary sequences have focused on faults that accommodate dominant thrust kinematics. There is limited understanding of the strain distribution and structural styles associated with those that accommodate transpressional kinematics (e.g., Schmidt & Hendrix, 1981, Tindall & Davis, 1999). Although these little-

understood faults have accommodated a minor component of reverse slip, the net slip is dominated by a larger component of strike-slip. A few attempts to address this problem employed a numerical modelling of the geometrical modification of stratigraphic surfaces resulting from transpressional fault displacement (Anderson et al., 2015). Nevertheless, robust numerical models should incorporate detailed observations of the structural and mechanical controls.

Here, we will investigate intrabasement deformation, and structural inheritance of the basement by analyzing the overlying sedimentary sequences in the transpressionally-deformed Anadarko Shelf, Oklahoma (Figure 11a). We will first analyze intrabasement deformation, and subsequently, show how components of the deformation are propagated up into the sedimentary cover. Our study will reveal a pervasive deformation of the granitic basement by: (a) basement-bounded mafic igneous sills; and (b) sub-vertical discontinuity planes interpreted as faults, some of which penetrate into the overlying sedimentary cover. We will show that deformation along the basement fault is propagated up over three structural domains: 1) basal faulted-block, 2) faulted-monocline that transitions into 3) monoclinal flexure. Also, our analyses will reveal two styles of Vertical Separation - Depth relationships, which include a basement-driven unidirectional fault propagation (Style-1), and an intrasedimentary-driven fault nucleation and bi-directional propagation (Style-2). Further, we will demonstrate that along-fault deformation of affected stratigraphic surfaces exhibits systematic trends that varies with offset accrual. We will show that the basement-driven fault propagation has greater efficiency of propagating the fault-related deformation to shallower depths compared to the intrasedimentary-driven nucleation and propagation. Overall, this contribution will show that the sedimentary deformation of the Anadarko Shelf represents a partial inheritance of the heterogeneous intrabasement deformation. The results presented here will

provide insights into the upward propagation of basement-driven faulting associated with structural inheritance in contractional sedimentary basins.

Geological Setting

The Precambrian basement

The Precambrian basement of Oklahoma is part of the 1.35-1.4 Ga Southern Granite-Rhyolite Province of central U.S. (Figure 11a inset; Thomas et al., 1984; Bickford et al., 2015). Studies in Oklahoma indicate that it is dominated by granitic and rhyolitic rocks (Figure 11b; Denison, 1981; Denison et al., 1984; Shah & Keller, 2016). In southern Oklahoma, where this basement is most extensively exposed, there is a pervasive occurrence of mafic sheet intrusions in the granites (Denison, 1995; Lidiak et al., 2014). The intrusions have a dominant NW-SE strike (Denison, 1995; Lidiak et al., 2014), parallel to a prominent trend of fracturing in the granitic basement (Kolawole et al., 2019b). Geochronological investigations suggest Mesoproterozoic to Cambrian ages for the intrusions (Denison, 1995; Lidiak et al., 2014).

By 1109-1094 Ma, the North American craton began to split apart (Cannon, 1994) along the Keweenawan Rift (Mid-Continent Rift) where the NNE-SSW-striking western arm of the rift propagated southwards from Lake Superior all the way through north-central Oklahoma (Figures 11a inset, 11b; Van Schmus & Hinze, 1985; Stein et al., 2018). By 1100 Ma, west-directed compressive tectonic stresses from the Grenville Orogeny in the east led to the closing of the rift with reverse-faulting of the previously extended crust (Cannon, 1994). The closing of the rift was followed by the widespread erosion of the basement surface in the Late Proterozoic, which resulted in the hummocky morphology pattern of the basement surface (Elebiju et al., 2011; Kolawole et al., 2019b).

The Anadarko Basin

The Anadarko Basin is one of the deepest basins in the United States (> 12 km of sedimentary fill), and its complex subsidence history can be divided into three major phases: (1) Late Proterozoic to Mid-Cambrian aulacogen development, (2) Late Cambrian through Early Mississippian post-rift thermal subsidence (the southern Oklahoma trough), and (3) Late Mississippian to Early Permian tectonic contraction associated with development of the Anadarko intracratonic foreland basin on the northwestern flank of the trough.

In the Late Proterozoic to Middle Cambrian, a NW-SE -trending rift system developed in southern Oklahoma and is associated with the voluminous emplacement of intrusive and extrusive igneous rocks (e.g., Figure 12a; Brewer et al., 1983). This is the last igneous tectonic event that affected the south-central United States region (e.g., Whitmeyer & Karlstrom, 2007). Through the Ordovician to the Mississippian, the Oklahoma basement subsided, allowing for the deposition of thick sedimentary sequences, marking the onset of Anadarko Basin development (e.g., Figures 12a-c; Johnson, 2008). By the Late Mississippian through the Pennsylvanian, SW-directed compressive stresses from the Appalachian Orogeny in the east led to crustal shortening and folding in southern Oklahoma. This tectonic compressional event caused an inversion of the NW-SE Cambrian rift system in south and SW Oklahoma, and the development of a NE-trending fold thrust belt in SE Oklahoma (e.g., Figures 11a, 12a, c; Powers, 1928; Brewer et al., 1983; Keller & Stephenson, 2007; Simpson, 2015). The inverted rift system is known as the Southern Oklahoma Aulacogen, SOA (Wichita and Arbuckle Uplifts), and the fold thrust belt is known as the Ouachita Mountains (Figures 11a, 12c).

The crustal loading from the accelerated uplift of the SOA and Ouachita domains in the Pennsylvanian resulted in the syn-tectonic down-warping of the basement in SW and SE Oklahoma, forming the present-day Anadarko and Arkoma foreland basins (Figures 11a, 12c; e.g., Brewer et al., 1983; Johnson, 2008; Simpson, 2015). As the Anadarko basin foredeep subsided in the south, a broad, gently dipping shelf area developed in the central and northern Oklahoma, known as the Anadarko Shelf (Figure 11a). As the shelf area developed, the tectonic stresses induced widespread transpressional deformation in central and northern Oklahoma, which include the development of several NE, NW, and ~N -trending sub-vertical strike-slip and reverse faults that root into the basement and penetrate the Paleozoic sedimentary sequences (Dolton & Finn, 1989; McBee, 2003a, 2003b; Gay, 2003; Gay, 1999; Liao et al., 2017). Among these transpressional strike-slip structures, the Nemaha Fault (and Uplift), Wilzetta Fault, Whitetail Fault, Keokuk Fault, El Reno Fault, Galena Township Fault, Stillwater Fault are most prominent (Figure 11a; Gay, 2003; McBee, 2003a, 2003b; Liao et al., 2017; Chopra et al., 2018a).

The stratigraphy of the Anadarko Shelf and its regional significance

The stratigraphy of the Anadarko Shelf (Figures 12a-c) consists of the basal Precambrian basement with an erosional top (Benson, 2014), above which Ordovician to Mississippian carbonate, shale and sandstone sequences were unconformably deposited (e.g., Johnson, 1989; Van der Pluijm & Catacosinos, 1996). These units generally thicken southwestwards towards the Anadarko Foredeep (Figure 12c), and due to multiple episodes of subaerial exposure of the units, several unconformities exist between the packages. Within the deeper sedimentary sections of the study area, the Arbuckle Group is thickest and lies directly on the Top-Basement erosional surface (Figures 12a-b). Recently, the Anadarko Shelf had been in the spotlight for two reasons. First, the

area hosts the occurrence of sporadic and widespread wastewater injection-induced seismicity (e.g., Kolawole et al., 2019b). The Arbuckle Group is the primary zone of wastewater disposal, and the Precambrian Basement hosts most of the resulting induced seismicity (e.g., Kolawole et al., 2019). Second, the shelf area hosts the STACK ("Sooner Trend, Anadarko, Canadian and Kingfisher") and Mississippi Lime Plays, which are currently some of the most active unconventional hydrocarbon exploration plays in North America (e.g., Yee et al., 2017). Exploration target zones include the Woodford, Hunton, Morrow, Oswego, Mississippian and Osage stratigraphic intervals (Figure 12a-b; Droege & Vick, 2018).

DATA AND METHODS

Seismic data set and fault interpretation

To investigate subsurface faulting in the Anadarko Shelf, Oklahoma, we utilize a post-stack time migrated 3-D seismic reflection survey covering an area of 824 km^2 in Kingfisher County, Oklahoma (Figures 11a-b, 13a; courtesy of TGS). The seismic dataset has a dominant frequency of 65 Hz in the sedimentary cover and ~56 Hz within the crystalline basement. For the sedimentary section, we assume a reasonable average velocity of ~5300 ms^{-1} (well log dynamic velocity for the Mississippian Meramec Fm., 2 – 2.5 km deep). Experimentally constrained P-wave velocity for the Oklahoma basement at effective confining pressure relevant for the interval of interest (50 - 60 MPa) is 6000 ms^{-1} (Kibikas et al., 2019). These frequencies and velocities imply a vertical resolution of ~21 m (sedimentary section) to ~27 m (in the basement) for the dataset. Through a student academic subscription to the IHS well database, we obtain access to raster wireline logs for basement penetration Well-KF1 which we digitize in the IHS Petra Software prior to integration with the seismic data. We perform a well log to seismic tie using the digitized Well-

KF1 logs and logs from other basement well penetrations within the study area for the log to seismic tie, we first create a velocity model approximation from the wells, which we then use to convert the seismic amplitude volume from time to depth. The log to seismic tie process involves a statistical wavelet extraction around multiple wells. The comparison of the average wavelet from each of the wells with a zero-phase wavelet indicates the difference in the phase of seismic traces. The seismic data was initially found to be -95° out of phase and was zero-phased prior to stratigraphic interpretation. Due to proprietary data restrictions, most of the seismic images are here in presented in the minimum phase. Our interpretation workflow consists of a manual interpretation and gridding of the Top-Basement (~3.2 km depth) and Top-Arbuckle (~2.7 km depth) surfaces. Further, we interpret a surface along a broad (347 km^2) deep-seated (> 6 km depth) intrabasement reflector (IBR) within the survey. Studies of intrabasement reflectors in sedimentary basins of similar basement depth have used seismic reflection data to investigate structural inheritance (e.g., Reeve et al., 2014), thus validating the feasibility of our approach. We envision that fault mapping at the Top-Basement and Top-Arbuckle surfaces provide first order assessment of basement fault linkage with the sedimentary cover. Analysis of sub-vertical discontinuity planes and related lineaments along the IBR surface provide an assessment of the trends of brittle deformation in the basement, and the depth extent of the major Top-Basement faults. For our surface horizon mapping, we pick the zero-crossing of the seismic reflectors near the target stratigraphic surfaces.

To better resolve structural deformation along the interpreted surfaces, we compute structure-oriented seismic attributes (e.g., Chopra & Marfurt, 2005, 2006; Infante-Paez & Marfurt, 2017) from the seismic volume and extract the attributes onto the mapped surfaces. Primarily, we use 3-D Curvature and Similarity seismic attributes. The most-positive curvature (k1) resolves up-

warped zones/upthrown blocks and the most-negative curvature (k2) highlights down-warped areas/downthrown blocks. Thus, fault zones with small vertical offsets and subtle structural flexures, often typical of strike-slip faults, are well resolved on the interpreted surfaces. The Energy Ratio Similarity (a measure of coherence) attribute is an edge-detection attribute that resolves zones of discontinuity along reflectors. Thus, the Energy Ratio Similarity attribute reveals fault damage zones as lineaments of low coherence relative to flanking blocks of higher coherence (Chopra & Marfurt, 2005). We compute the seismic attributes with the Attribute Assisted-Seismic Processing and Interpretation (AASPI) software package from the University of Oklahoma. We perform the attribute extraction and co-rendering with Petrel Software application.

Additionally, we quantify lineament distribution on the Top-Arbuckle, Top-Basement and intra-basement reflector (Top-Intra-basement reflector) surfaces by calculating Areal Lineament Density (L_d) and Areal Lineament Intensity (L_I). L_d is the ratio of total lineament count to the area of the stratigraphic surface; and L_I is the ratio of sum total of lineament lengths to the area of the stratigraphic surface. We assess the extent of the deformation field above the basement faults, we assess the dip isogon patterns (Ramsay, 1967; Ramsay & Huber, 1987) along the large, through-going faults. Within the bounds of this deformation field, we measure the vertical separation of the deformed stratigraphic contacts.

Estimation of three-dimensional distribution of vertical separation (Vsep) along the faults

The low magnitude of the vertical component of fault offset and limited seismic resolution make it difficult to resolve the footwall and hanging wall cut off markers on the faults, and consequently, difficulty in assessing fault throw. Therefore, to quantify the magnitude and 3-D distribution of deformation along the large (> 10 km) through-going faults in the seismic dataset, we estimate the

variation of vertical separation of seismic reflectors along the faults (Figures 13a-c). Here, we define 'vertical separation (Vsep)' as the vertical difference between the depth to a horizon in the hanging wall of a fault and the depth to the same horizon in the footwall of the fault (Figures 13b-c). Likewise, this definition includes the vertical difference between the depth to a horizon in the anticlinal segment of a monocline and the depth to the same horizon in the associated syncline. Since the well log-to-seismic tie allows us to constrain the major stratigraphic packages, the similarity and continuation of reflection packages across the faults helped to ensure an interpretation of the same horizon either side of the fault. We assume that the measured Vsep values represent only the apparent vertical component of fault displacement and the associated stratigraphic flexure. Thus, we use this term, Vsep, to quantify vertical separation at faulted blocks, faulted monoclines and fault-controlled monoclinal flexures.

At 2 km intervals along two representative faults, we measure the Vsep of six (6) stratigraphic surfaces where the data quality permits (Figures 13a-b). These surfaces include the Top-Basement (Top-Precambrian), Top-Lower Ordovician (Top Arbuckle Group), Top-Devonian (Top Hunton Group), a Mississippian reflector (strong, laterally-continuous reflector within the Mississippian section), Top-Mississippian (Top-Chester Group), and a Pennsylvanian reflector (strong, laterally-continuous reflector within the Pennsylvanian section). For these measurements, we use the zero-crossing of the seismic reflectors along the mapped surfaces as offset markers. Due to proprietary data limitations, we do not have Vsep measurements at the structural depth levels of the IBRs that were cut by the faults. We have provided the spreadsheets of our Vsep measurements in the Appendices 4 and 5 of this dissertation.

Basement well penetration data

To constrain our interpretation of aspects of the structure of the crystalline basement, we obtain wireline logs (courtesy of TGS) and drill cuttings (courtesy of Oklahoma Petroleum Information Center) from the basement penetration well in Kingfisher County, here-in referred to as Well-KF2 (Figure 12b). Further, we utilize X-Ray Diffraction (XRD) and X-Ray Fluorescence (XRF) analyses of the drill cuttings to understand the mineralogical and chemical compositions of the drill cuttings (courtesy of the Chesapeake Energy Reservoir Technology Center), and thus, identify the associated lithological characteristics of the basement. Additionally, using standard techniques, we model a synthetic seismogram using the sonic and density wireline logs available from Well-KF2 and other basement penetration wells in the study area. Due to proprietary restrictions, both the sonic and density logs used are not shown here. We have provided the spreadsheets of the XRD and XRF geochemical data as an appendix of this dissertation.

RESULTS

Below, we present our results in a bottom-up sequential manner, from the deep intrabasement domain, up through the Top-Basement, Top-Arbuckle, and shallower sedimentary formations.

The intrabasement reflectors (IBR)

Geophysical and geological observations

The 3-D seismic dataset shows distinct, systematic patterns of reflection packets within the crystalline basement, here-in referred to as intrabasement reflections (IBR) (see representative seismic section in Figure 14a). The original seismic dataset (minimum phase) shows that each of the IBRs are characterized by a reflection packet consisting of a trough–peak–trough wave-train (top panel in Figure 14b). However, the zero-phase seismic volume (lower panel in Figure 14b)

show that the IBR reflection packet consists of a peak–trough–peak wave-train. The IBRs comprise of gently-dipping systematic sets of relatively high amplitude reflectors that appear to cross-cut, but not offset, other intra-basement reflections. Through-out the seismic volume, the IBRs interconnect, commonly terminate at the Top-Basement interface (e.g., yellow X-symbols in Figure 14a), and show prominent trends along NNE-SSW (ESE-dipping), E-W (N- and S-dipping), NW-SE and NE-SW (SE-dipping). Visible in the uninterpreted representative seismic section (Figure 15a) and shown in the interpreted version (Figure 14a), we observe distinct geometrical interactions between the IBR segments. These interactions include: 1) simple truncation and/or vertical juxtaposition of the segments by sub-vertical discontinuity planes (IBR step), some of which extend upward and offset the Top-Basement and shallower reflectors; 2) IBR bridge structures characterized by a deeper segment overtopped by an approaching segment in which the deeper segment terminates at a sub-vertical discontinuity plane; 3) faulted IBR bridge structures in which both the deeper and overtopping IBR segments are truncated or offset by a sub-vertical discontinuity plane. We delineate the vertical extents and geometry of the discontinuity planes by the vertical stacking of abrupt truncations of IBRs within the seismic sections.

The zero-phase seismic dataset (lower panel in Figure 14c), which by standard practice is ideal for geological interpretation, shows that the upper contact of the IBRs is defined by an increase in acoustic impedance contrast, suggesting a rock that is denser than the host granite. Wireline logs, drill cuttings and geochemical analyses from basement penetration Well-KF2 within the study area (Figures 15a-d) provide additional insight into the lithological composition of the IBRs. Overall, the 120 m-deep basement interval, the wireline logs (Figure 14a) show high Gamma ray, high Resistivity, moderate Neutron and Density Porosity, and low P.E. baseline signatures. However, there exists two distinct intervals (17 m and 1.5 m-thick; yellow arrows in Figure 14a) that show

abrupt excursions from these baselines. The two intervals are characterized by very low Gamma ray and Resistivity values, high P.E. values, and Density - Neutron log crossovers. These two zones of abrupt excursions of the wireline logs clearly indicate distinct rock units within the crystalline basement.

A synthetic seismogram model of the intrabasement layer reflectivity show a strong positive reflection coefficient at the top contact of the 17-m thick layer (Figure 14a). Drill cuttings from a zone above (Sample A), within (Sample B), and below (Sample C) the intra-basement layers show that the distinct intrabasement unit is characterized by a rock that has a darker coloration compared to the host lighter-colored rock. XRD (Figure 14b) and XRF (Figures 14c-d) geochemical analyses of the three samples indicate that overall, the crystalline basement is dominated by a host rock that is rich in orthoclase feldspar and quartz (Samples A and C). Whereas, the intrabasement layer (Sample B) is dominantly made up of plagioclase feldspar, amphibole, illite, smectite and augite minerals, and is deficient in orthoclase feldspar and quartz (Figure 14b) and the associated elements (Figures 14c-d).

Structure of a mapped IBR

We carefully mapped the most extensive (347 km^2) IBR within the seismic survey, located between 6.5-8.5 km depth (Figures 16a-d). The surface is undulating, generally shallow in the west (< 6.9 km) and transitions across a N-S topographic gradient near the center of the survey to deeper depths (> 7.6 km) in the east. The deepest part of the IBR surface is a NW-trending narrow (2.8-6.5 km-wide) region that extends from the southeast corner of the mapped area towards the center (Figure 16a). An overlay of Top-Basement faults shows a striking coincidence of major fault F1 with the central N-S topographic gradient (red arrows in Figure 16a) and F3 with the NW-trending

deepest area along the IBR. An extraction of the Energy Ratio Similarity attribute onto the surface (Figure 16b) shows a high density of rectilinear discontinuity lineaments of low energy which show dominant NW-SE trend with 308°±7 mean trend, and a minor N-S (010°) trend (Figure 16c). We also observe that some of the rectilinear low energy attribute lineaments correspond to segments of the interpreted Top-Basement faults (Figures 16d, 17).

Faulting at the Top-Basement, Top-Arbuckle and shallower sedimentary sequences

The interpreted Top-Basement (Figures 18a) and Top-Arbuckle (Figures 18b) structure maps show marked resemblance in that the major fault traces and concentric structural highs are co-located. Both structure maps and their co-rendered seismic attributes show coincidence of major fault lineaments (red arrows in Figures 18a-b, 19a-c, 20a-b). Additionally, a major basement high on the eastern part of the Top-Basement surface (Figure 18a) is coincident with a structural dome at the Top-Arbuckle surface (Figure 18b). The two surfaces show three large faults (F1, F2 and F3) with lengths greater than 10 km. Fault F1 strikes 012° and dips west, F2 strikes 031° and dips NNW, and F3 strikes 296° and dips SSW. Along these faults, we do not observe any significant changes in thickness of stratigraphic packages within the intervals analyzed (i.e. no observed growth strata in the Pre-Pennsylvanian strata). The fault segments commonly show steeper dips in the sedimentary cover than in the basement. For example, F3 dips 68° in the basement, and 88° in the sedimentary cover (Figure 18c). An integration of the structural attribute maps allows us to better resolve the geometry of the large faults as well as smaller offset discontinuity lineaments at both the Top-Basement and Top-Arbuckle surfaces (Figures 19a-c, 20a-b).

As a first order approximation of propagation of brittle deformation from the basement through the sedimentary sequences, we first compare the density and intensity of discontinuity lineaments

observable on the mapped surfaces (Figure 18d). On the deep-seated IBR surface (~7.5 km depth), we estimate an areal lineament density of 0.458 km^{-2} and areal lineament intensity of 0.634 km^{-1}. Whereas, at the Top-Basement surface (~3.2 km depth), we estimate an areal lineament density of 0.145 km^{-2} and areal lineament intensity of 0.355 km^{-1}. At Top-Arbuckle surface (~2.7 km depth), we estimate an areal lineament density of 0.078 km^{-2} and areal lineament intensity of 0.256 km^{-1}. Overall, the deeper basement appears to host a larger density and intensity of discontinuity lineaments relative to the Top-Basement and Top-Arbuckle depth levels (Figure 18d).

A closer look at the co-rendered seismic attributes along the large faults (Figures 18c, 19a-c, 20a-b) provide insight into the vertical change in the geometry of fault deformation along the faults. The energy ratio similarity attribute map (Figure 19a) shows discontinuous lineaments that coincide with short segments of the large faults and a few other fault lineaments on the basement surface. The co-rendered *k1*-*k2* curvature maps of the Top-Basement surface (Figure 19b) show adjacent lineaments of upthrown and downthrown blocks that coincide with the large faults. Using F3 as a representative fault, Figures 18c and 19c show a fault structure that comprises of an upthrown block (*k1* lineament) adjacent and parallel to a downthrown block (*k2* lineament), both separated by a distinct discontinuity plane (low energy lineament). Similarly, at the Top-Arbuckle surface, each of the large faults show a lineament of up-warped/anticlinal flexure (*k1*) adjacent and parallel to a lineament of down-warped/synclinal flexure (*k2*) separated by a distinct fault plane (low-coherence lineament) (Figures 20b). Overall, the Top-Basement reflector shows simple offset and little to no folded geometry across the large faults, whereas the Top-Arbuckle shows both offset and strongly folded geometry (cross-sections in Figures 18c and 21a).

More interestingly, farther up-section of the Top-Arbuckle surface, we observe that the seismic reflectors show further transitions in geometry that is different from that of the Top-Basement and

Top-Arbuckle (Figure 21a). Again, using F3 as a representative fault, the dip isogon pattern (Figure 21b) describes a simple geometry between the Top-Basement and Top -Arbuckle surfaces primarily because of the lack of folding of the Top-Basement. However, the interval between the Top-Arbuckle and Top-Hunton surfaces show tightly-folded units with sub-parallel isogon contours that transition into less-tightly folded intervals between the Top-Hunton and Top-Chester surfaces. Above the Top-Chester, both the isogon contours and stratigraphic surfaces describe predominantly open to gentle folds (Figure 18b).

3-D distribution of vertical separation (Vsep) along the large faults

Vsep and cumulative Vsep versus distance along-strike of the large faults (Vsep-D and CVsep-D)

As shown in Figures 14-21, the three large faults in the dataset (faults F1, F2 and F3) deform the mapped broad IBR, Top-Basement surface and penetrate the sedimentary sequences. The zone of flexural curvature around these faults (i.e. the deformation field bounded by the 0° dip isogons) describes a triangular deformation zone that can be as large as 1.7 km^2 (fault F3, Figure 21b). Within this flexural zone, the distribution of vertical separation (Vsep) reveals important trends described below.

The Vsep-D plots along faults F1 and F2 show systematic variation of fault-related stratigraphic deformation along-strike of the faults (Figures 22a-b). Although the measured Vsep values along F1 are less than 100 m, they are highest in the north (96.1 m) and decreases southwards toward the intersection zone of the major faults (Figure 22a). At the intersection zone, there is little or no change in the continuity or geometry of the reflectors. To the south of the intersection zone, vertical separation is evident, although by only a small amount (<25 m, Figure 22a). Similarly, along F2, Vsep is highest in the north (~31 m) and decreases southwards along the fault towards the zone of

intersection with faults F1 and F3 (Figure 22b). Further, the distribution of cumulative Vsep with distance (CVsep-D) for both faults (Figures 22c-d, 23a-b) show spatial clustering of the curves. For both F1 and F2, The Top-Basement and Top-Arbuckle curves cluster tightly at relatively higher values, whereas the curves for the shallower stratigraphic surfaces cluster at relatively moderate to lower values ($<0.75 \cdot CVsep_{max}$) but the patterns differ markedly between the two faults. Along F1, most of the shallow strata curves cluster closely within the region between the $0.25 \cdot CVsep_{max}$ and $0.75 \cdot CVsep_{max}$ boundaries, although the Pennsylvanian reflector plots near the lower boundary (Figure 22c, 23a). Along F2, most of the shallow strata CVsep-D curves cluster within or just above the region below the $0.25 \cdot CVsep_{max}$ boundary (Figures 22d, 23b)

Vsep versus depth (Vsep-Z) along the large faults

The Vsep-Z plots for F1 and F2 (Figures 24a-b) show that overall, from the Top-Basement up through the Pennsylvanian units, Vsep decreases with shallowing depth. At all the measurement locations on F1 and F2, Vsep is highest at deeper depths (Top-Basement and Top-Arbuckle) and least at the shallowest depths (Top-Chester and Pennsylvanian reflector). Overall, the Vsep-Z distribution along these faults describes two styles, here in referred to as Style-1 and Style-2 (Figures 24c-d). Style-1 refers to a Vsep-Z distribution in which Vsep increases linearly with depth down through the Top-Basement surface (Figure 24c). We observe the Style-1 pattern of Vsep distribution at L1, L2 and L5 along fault F1, and L2, L4, L5 and L6 along fault F2. Style-2 consists of a Vsep-Z distribution in which Vsep is highest within the deeper sedimentary units and decreases upwards (through the shallower units) and downwards to the basement (Figure 24d). We observe the Style-2 pattern of Vsep distribution at L4, L6 and L10 along fault F1, and at L1 along fault F2.

Further, for both propagation styles, we assess the quantitative relationships between the magnitude of fault deformation at the inferred nucleation depths and the efficiency of upward propagation of the deformation. At all the measurement locations, the Top-Chester is the shallowest stratigraphic surface for which we have the most Vsep measurements along the two faults. Thus, for the Style-1 trends (in Figures 24a-b), the plot of Vsep at the Top-Basement ($Vsep_{TB}$) versus Top-Chester ($Vsep_{TC}$) surfaces (Figure 25a) describes the relationship:

$$\mathrm{Vsep_{TB}} = 2.21\ \mathrm{Vsep_{TC}} + 2.48 \quad (1)$$

Similarly, for the same Style-1 measurements, the plot of Vsep at the Top-Arbuckle ($Vsep_{TA}$) versus Top-Chester ($Vsep_{TC}$) surfaces describe the relationship:

$$\mathrm{Vsep_{TA}} = 1.81\ \mathrm{Vsep_{TC}} + 1.72 \quad (2)$$

Whereas, for the Style-2 measurements, the plot of Vsep at the Top-Arbuckle ($Vsep_{TA}$) versus Top-Chester ($Vsep_{TC}$) surfaces describe the relationship:

$$\mathrm{Vsep_{TA}} = 3.33\ \mathrm{Vsep_{TC}} + 4.72 \quad (3)$$

DISCUSSION

Intrabasement deformation and structural inheritance in the Anadarko Shelf

The analyzed seismic dataset shows distinct interconnected IBRs that commonly terminate at the Top-Basement erosional surface, giving the Anadarko Shelf basement a layered appearance (Figure 14a). This character is consistent with previous observations of enigmatic reflection packets in seismic reflection datasets from other parts of the basin (Elebiju et al., 2011; Chopra et al., 2018b; Kolawole et al., 2019b). Wireline logs and drill cuttings retrieved from a basement penetration Well-KF2 in our study area provide the first ground-truthing of the physical, mineralogical, and chemical composition of the IBRs (Figures 14c, 15b-c). The well data show

that the host granitic basement is layered by a distinct rock that is deficient in potassium feldspar, relatively more conductive and composed of dark-colored minerals (Figures 14c-d). Our geochemical analyses (XRD and XRF; Figures 15a-d) show mineral assemblages that indicate a host felsic (granitic) crystalline basement (Samples A and C) and a mafic (diabase/gabbro) intra-basement rock units (Sample B). These results provide, for the first time, physical and geochemical evidence of mafic origins for the intra-basement reflectors in north-central Oklahoma. It is possible that the granitic drill cuttings (Samples A and C) include pegmatitic sheet intrusions, however there is no strong evidence for this currently. Additionally, the zero-phased seismic data wavelet (Figure 14c) and synthetic seismogram model from wireline logs (Figure 15a) show increased impedance across the top-IBR contact, suggesting that the rock defining the IBR is denser than the host granite. Thus, the geometrical, geological and geophysical evidences presented here lead us to interpret that the IBRs beneath the Anadarko Basin are Precambrian gabbro and/or diabase sills that intruded the granite-rhyolite basement. Further, the basement-bounded character of the IBRs suggest that they most-likely intruded the granitic basement sometime between the Mesoproterozoic (emplacement of the host Granite-Rhyolite Province) and the Ordovician Arbuckle carbonate units.

As shown in Figures 12a-c, a Precambrian crystalline basement unconformably underlie the Phanerozoic sedimentary cover of the Anadarko Shelf. This basement is part of the 1.35 - 1.48 Ga Granite-Rhyolite Province of central and Eastern U.S. (CEUS), mapped as an extensive juvenile terrane which extends from southwestern United States through the mid-continent (e.g., Figure 11a inset; Thomas et al., 1984; Whitmeyer & Karlstrom, 2007; Bickford et al., 2015). Legacy deep seismic imaging also shows intrabasement reflectors (IBR) in the Cambrian basement of the Southern Oklahoma Aulacogen (SOA; Figure 11a; 12c), interpreted to be gabbro sills (Widess &

Taylor, 1959) or mylonitic segments of deep thrust detachment faults (Brewer et al., 1983). Similar features have been reported in the basement of other areas in CEUS of similar age and tectono-thermal history as the basement of the Anadarko Shelf. These include north Texas (e.g., Font, 2003), southwest Texas (Kim & Brown, 2019), and the Illinois Basin (McBride et al., 2016, 2018). However, due to the relatively deep burial of this basement in most of the places, its detailed structure and influence of its structural inheritance on the deformation of the phanerozoic cover sequences are poorly understood. Here, we present one of the first results showing a ground truthing evidence of the composition of the widely observed intrabasement seismic reflectors across the Mesoproterozoic Granite-Rhyolite Province of central-eastern US.

In addition to the intrusion of sills as a form of basement deformation, we also observe the pervasive occurrence of sub-vertical discontinuity planes that terminate or offset segments of the IBRs (e.g., Figures 14a, 15a). Some of these discontinuity planes extend up into the cover rocks, offsetting and deforming both the Top-Basement surface and the sedimentary sequences (e.g., Figures 14a, 15a, 16d, 21a,). However, we also find that although other segments of the discontinuity planes are well defined in the basement, they do not reach or deform the Top-Basement reflector (Figure 14a). We interpret these sub-vertical discontinuity planes as fault planes that constitute brittle deformation in the basement.

Some striking characteristics of these discontinuity planes are evident and may provide insight on their origin. First, although some of the discontinuity planes define IBR steps and offset IBR bridges (Figure 14a, 15a), we observe cases of IBR bridge interactions where the deeper segment terminates at a sub-vertical discontinuity plane and both of which are overtopped by an approaching IBR segment. An example of this interaction is labelled “IBR Bridge” in Figure 14a. Second, lineaments of these discontinuity planes that cut the mapped IBR surface (Figure 16b)

show a dominant trend of 308° (Figure 16c). This trend is remarkably consistent with: 1) the strike of one of the largest faults in the study area (Fault F3), 2) a prominent fracture trend (308°±3.6) in the outcrops of this basement in southern Oklahoma (Kolawole et al., 2019b), 3) the dominant trend of Proterozoic-Cambrian mafic dikes (300°) in the outcrops of the basement (Denison, 1995; Lidiak et al., 2014), and 4) a prominent trend of recent seismogenic basement faulting in the Anadarko Shelf (297°±3.6) (Schoenball & Ellsworth, 2017; Kolawole et al., 2019b). This common NW (~300°) trend, a conjugate NE (~240°) trend, and a secondary N-S trend has been interpreted to be dominant structural trends in the Precambrian basement of Oklahoma (Denison, 1995; Kolawole et al., 2019b).

Therefore, considering the character and trends of these sub-vertical discontinuity planes, our preferred interpretation is that they represent fault planes within the Precambrian basement that possibly predate the emplacement of the IBRs. Further, we interpret that the extension of some of the discontinuity planes up-section and the associated deformation of the Top-Basement and shallower stratigraphic surfaces represent a reactivation of this brittle structures during the Phanerozoic. Additionally, the comparison of lineament density and intensity between the depth levels (Figure 18d) suggest that fault linkage between the basement and the sedimentary section is defined by a relatively small proportion of the basement faults that are propagated up across the Top-Basement surface. Although pre-existing intrabasement mafic sheet intrusions can control faulting in contractional tectonic settings (Gwon & Kim, 2016; Lee & Kim, 2018), our seismic dataset does not show any evidence for this in the Anadarko Shelf. However, we do not rule out the possibility. Both sub-horizontal (sill) and sub-vertical (dike) mafic sheet intrusions occur in the outcrop exposures of the Oklahoma basement, where the sills commonly branch out from the dikes (e.g., Lidiak et al., 2014; Kolawole et al., 2019). However, the absence of dike-related

reflections in our seismic dataset may be explained by the inherent difficulty of seismic reflection imaging of dikes (e.g., Zaleski et al., 1997; Wall et al., 2010; Phillips et al., 2018). Overall, based on our dataset, we infer that at least the brittle component of the intrabasement deformation was inherited by the sedimentary sequences of the Anadarko Shelf.

Propagation of fault deformation into the sedimentary sequences

Implied kinematics of the large faults

The seismic sections do not show the presence of growth strata across the analyzed large faults. Along the mapped surfaces (Top-Basement and Top-Arbuckle; Figures 18a-b, 19, 20), the faults do not exhibit pervasive secondary faulting patterns (e.g., Reidel and flower structures) that may be used as fault kinematic indicators. Nevertheless, to understand the most probable sense of movement on the faults, the following should be emphasized:

(1) The geometry (N, NNE and WNW-ESE strikes, and sub-vertical dips) of the faults are consistent with those of previously studied large fault zones nearby on the Anadarko Shelf. Among these structures, the Nemaha Fault (and Uplift), Wilzetta Fault, Whitetail Fault, Keokuk Fault, El Reno Fault, Galena Township Fault, Stillwater Fault are most prominent (Figure 11a; Dolton & Finn, 1989; Gay, 2003; McBee, 2003a, 2003b; Liao et al., 2017; Chopra et al., 2018a; Castro Manrique, 2018). Our study area is located just north of the El Reno Fault and just west of the Nemaha Fault (Figures 11a-b). Seismic imaging (Liao et al., 2017; Chopra et al., 2018a) and analog modelling of these faults (Liao et al., 2017) show strong right-lateral strike-slip kinematics marked by the pervasiveness of NE-trending Reidel splay faults extending outwards from the primary ~N-S principal slip zones. The published seismic images were focused on the shallower and mechanically weaker Woodford Shale unit. Additionally, detailed structural interpretation of a

sub-vertical >12 km-long W- to WNW-trending fault system in Grady County, Oklahoma (south of the study area) suggest left-lateral strike-slip kinematics (Castro Manrique, 2018). Farther east of the study area, published interpretations of the Wilzetta, Whitetail, and the Keokuk Fault zones show mapped secondary faulting patterns and recent focal mechanism solutions consistent with strike-slip kinematics (e.g., McBee, 2003a; McNamara et al., 2015). The consensus is that these fault trends are associated with the major structural deformation of the Anadarko Shelf in a transpressional stress field. The stress field is related to SW- and W-directed compressional stresses from the southward propagation of the Appalachian-Ouachita-Marathon fold-thrust belt in the Late Paleozoic (e.g., McBee, 2003a).

(2) The generally small vertical separation (<100 m) on the large faults (Figures 22a-b) may imply a relatively larger lateral component of fault slip. However, the maximum Vsep value is not a conclusive evidence since limited coverage of the fault extents by our seismic dataset also makes it difficult to compare with any standard empirical throw-length relationships along faults of known kinematics (e.g., Scholz et al., 1993).

However, the large faults in our study area (F1, F2, F3) are not only in the proximity of these known faults, they also have similar geometries and deform the same stratigraphic units as the structures. Therefore, considering the tectonic history of the Anadarko Shelf and the kinematics of the known faults, we infer that the large faults in focus must have accommodated significant transpressional strain.

Structural domains of vertical fault propagation

We analyze three large (> 10 km-long) through-going faults that extend from the crystalline basement up into the sedimentary cover (faults F1, F2 and F3). These faults do not show any

significant growth section in the analyzed interval (Precambrian - Lower Pennsylvanian), suggesting that upward fault propagation into the sedimentary cover is largely post-depositional. The vertical changes in the geometrical character of the deformed stratigraphic surfaces in the seismic cross-sections (e.g., Figures 18c, 21a, 21b), seismic attribute expressions of the fault zone deformation (Figures 18c, 19a-c, 20a-b) suggest that fault deformation is propagated up over three distinct structural domains. These domains include: (1) basal block-faulting near (and within) the basement, that transitions through (2) a middle faulted-monocline, into (3) an upper monoclinal flexure (Figure 21b). To better understand the characteristics and drive of upward fault propagation through the deformed sequences, we focus on F1 and F2 as representative large faults and analyze the 3-D distribution of vertical separation (*V*sep) along the faults. Overall, we find that Vsep along the large faults generally diminishes toward the intersection zone of the faults (Figure 22a). More importantly, northwards of the intersection zone where significant Vsep is prominent, we assess the trends.

Vertical Separation versus Depth (Vsep-Z): Vertical fault propagation styles

The Vsep-Z relationships along the faults describe two broad patterns which we here-in describe as Style-1 and Style-2 (Figures 24a-d). Style-1 is characterized by a unidirectional, linear decrease of Vsep with shallowing of depth from the Top-Basement surface (Figures 24a and c). Style-2 is characterized by a bi-directional decrease of Vsep from a deep sedimentary unit (in this case, the Arbuckle carbonates) down toward the basement, and up through the shallower sequences (Figure 24b and d). We interpret that Style-1 involve a basement-driven propagation of faulting, whereas, Style-2 involve an intrasedimentary-driven fault nucleation and propagation.

Along many of the segments with Style-2 Vsep distribution, the faults significantly offset the intrabasement reflectors, but show relatively smaller offset of the Top-Basement and sedimentary cover reflectors (e.g., F1 in Figures 14a; F3 in Figures 16d, 21a). Also, we commonly observe an abrupt change in the dip of the large fault segments across the Top-Basement surface (up to 20° change; e.g., Figure 21a). These observations suggest a probable difference in growth history between the basement and sedimentary segments of the large faults. Thus, we interpret that the Style-1 faulting involves a reactivation of pre-existing basement faults. Although Style-2 propagation indicates fault nucleation above the basement, it appears that the pre-existing basement faults help to control where later faults nucleate in the sedimentary cover. Thus, the two styles of vertical fault propagation essentially involve significant or partial reactivation of pre-existing basement faults. Furthermore, the observation of both patterns of fault propagation at different segments of F1 and F2 suggests that the segments of the large fault do not have the same growth history prior to their linkage and coalescence. Mechanically, these styles of basement-controlled deformation may be explained by the relatively low stiffness of the basement fault rocks compared to the rigid host basement and directly overlying carbonate-dominated sedimentary units (e.g., Griffith et al., 2009). Such pre-existing zones of relatively lower cohesion and shear strength are more susceptible to stress localization and shear reactivation, compared to the relatively more-intact rocks.

However, these patterns of vertical fault growth may not be unique to contractional or transpressional settings, as they have also been observed in extensional tectonic settings. For example, Collanega et al. (2018) found that normal fault segments that nucleated in the cover rocks show displacement profiles that are clearly distinct from those that physically root into the basement. Of particular interest are the intrasedimentary faults, which show a throw gradient with

either the maximum throw at the fault center that decreases towards the tips, or localization of greater throw near the upper tip line than the lower or lateral tips.

Efficiency of the vertical fault propagation styles

To better understand the relative efficiency of vertical propagation of fault deformation by the two propagation styles, we assess the quantitative relationships between Vsep at the nucleation depth levels (Top-Arbuckle and Top-Basement) and one of the shallowest analyzed strata (Top-Chester). For Style-1 propagation, the plot of Top-Basement Vsep ($Vsep_{TB}$) versus Top-Chester Vsep ($Vsep_{TC}$) shows that >2.5 m Vsep is required at Top-Basement to propagate deformation as high up as the Mississippian (Figure 25a). In addition, deformation at the Top-Basement could produce about half of its magnitude at depths as shallow as the Mississippian. Similarly, for this same basement-driven fault propagation style, deformation at the Top-Arbuckle will correspond to about half of its magnitude at the Mississippian level (Figure 25b). The plot also shows that only a minimum of 1.7 m Vsep is needed at the Top-Arbuckle level to propagate deformation up to the Mississippian level. However, when compared to faults that nucleate within the sedimentary cover (Style-2 propagation), deformation at the nucleation zone (Top-Arbuckle) may only produce about a third of its magnitude at the shallow strata (Figure 25b). Furthermore, the plot indicates that a minimum of ~5 m of Vsep is needed at the nucleation depth (Top-Arbuckle) to propagate deformation as shallow as the Mississippian. These estimates suggest that the basement-driven contractional fault propagation (Style-1) has a relatively greater efficiency of driving deformation to shallower depth levels in the sedimentary cover, compared to intrasedimentary-driven faults. We speculate that the greater efficiency of Style-1 may be associated with the combined influence

of basement stiffness (stiffer backstop for fault propagation) and the welded nature of the basement and the basement and deeper sedimentary units (Johnson, 1991).

Evolution of vertical separation with accrual of fault offset

Fault F1 has a Vsep max of 96.1 m suggesting a relatively larger offset fault than fault F2 which has a Vsep max of 30.64 m (Figures 22a-b). The comparison of the cumulative Vsep versus distance (CVsep-D) plots for the two faults show spatial and systematic clustering of the curves for the analyzed stratigraphic surfaces (Figures 23a-b, 22c-d). Based on the trends shown, we observe that for the larger offset fault F1, most of the shallow strata CVsep-D curves appear to cluster in the region between the $0.25 \cdot CVsep_{max}$ and $0.75 \cdot CVsep_{max}$ boundaries (Figure 22c, 23a). Whereas, for the smaller offset fault F2, most of the shallow strata CVsep-D curves cluster within or just above the region below the $0.25 \cdot CVsep_{max}$ boundary (Figures 22d, 23b). This is reasonable considering that with increase fault growth and upward propagation of the fault tip, more of the initially monoclinally-folded strata at shallower depths become faulted. The spacing of these curves may also indicate the relative intensity of strain accommodated by different faulted-monocline strata (same CVsep-D region), as well as between units that have accommodated only folding and those that have experienced both faulting and folding. Therefore, we infer that with increasing accrual of offset on these faults, more of the shallow strata CVsep-D curves transition from lower value regions ($<0.25 \cdot CVsepmax$) into the moderate and higher value regions. Thus, we present a simplified conceptual model of evolution of CVsep-D trends that vary with accrual of offset along basement-rooted contractional and transpressional faults (Figure 26a-c).

Implications for the structural inheritance and subsurface fluid migration

The geometry and shallow reaches of the deformation of the large faults our study area pose important significance for (1) basement-sedimentary and intrasedimentary fluid transport, and (2) modern seismic hazard in the Anadarko Shelf. The observations presented here demonstrate that only the brittle component of the intrabasement deformation is inherited by the sedimentary sequences. Thus, the fault linkage presents potential pathways for migration of basement-derived hydrothermal fluids into the sedimentary cover, source to reservoir migration of hydrocarbons, and downward migration of fluids from the cover rocks into the basement. This is supported by recent observations of hydrothermal alteration of carbonate reservoirs in the Anadarko Shelf (e.g., Mohammadi et al., 2017; Jaiswal et al., 2017). In other basins where basement-rooted transpressional faults exist, near-fault diagenetic hydrothermal alterations can localize "light-bulb" structures and influence the local petroleum system and metallic-ore mineralization trends (e.g., the Appalachian foreland basins of Eastern US, Evenick, 2006; Evenick & Hatcher, 2006; Smith Jr & Davies, 2006). Further, the structural inheritance of basement fault systems by the sedimentary sequences may explain the recent widespread seismogenic strike-slip reactivation in north-central Oklahoma, attributed to sedimentary-to-basement migration of fluids (e.g., Qin et al., 2018, 2019; Kolawole et al., 2019b).

Finally, on the timing of upward propagation of the inherited structures, based on the lack of significant growth strata along the analyzed faults, the post-Cambrian ages of the gently-dipping shelf sequences, and analyses of the character of the basement faults, we infer a Late Paleozoic age. If a thick mechanically compliant sedimentary unit had existed at the depth interval between the basement and sedimentary cover, the unit may have acted as a decoupling layer which could have facilitated the detachment of the basement and cover rocks and into which the intra-sedimentary faults could sole (Mitra & Mount, 1998). However, across the Anadarko Basin,

basement-penetration cores show that the sedimentary units that directly overlay the basement are the thick non-compliant Arbuckle Formation dolomites and Reagan Sandstone (Figure 12a; Johnson, 1991). Therefore, the welding of the deep sedimentary units to the basement represents a mechanically coupled structure which may have sustained the sub-vertical propagation of the pre-existing basement faults into the sedimentary cover.

We summarize the history of structural deformation of the Anadarko Shelf as follows (Figure 26d): Stage 1: development of steep basement faults associated with the southward propagation of the Mid-Continent Rift in the Precambrian (1.1 Ga; Dickas, 1986; Stein et al., 2018); Stage 2: Erosion of the Top-Basement and deposition of sedimentary sequences in the Early to Mid-Paleozoic (480 - 350 Ma; Johnson, 1989; Van der Pluijm & Catacosinos, 1996); and Stage 3: Late Paleozoic transpressional reactivation and upward propagation of the basement faults, leading to the folding and faulting of the cover rocks (350 – 300 Ma; Perry, 1989). We suggest that the systematic 3-D characterization of the distribution of deformation along basement-rooted transpressional faults, as presented in this study, could help provide more insight into the mechanics of inherited fault propagation in contractional tectonic settings.

CONCLUSIONS

Here, we characterize the intrabasement structure of the Precambrian basement of the Anadarko Shelf, Oklahoma and investigated how the brittle component of the basement structure is inherited by the overlying sedimentary sequences. Our study reveals pervasive deformation of the granitic basement by two major structures: (a.) basement-bounded mafic sills, and (b.) sub-vertical discontinuity planes interpreted as faults, some of which penetrate the overlying sedimentary cover. Overall, based on our dataset, we infer that at least the brittle component of the

intrabasement deformation was inherited by the sedimentary sequences of the Anadarko Shelf. We find that deformation along the basement fault is propagated up the cover over three structural domains: 1) basal faulted-block, 2) middle faulted-monocline that transitions into 3) monoclinal flexure. Our analyses reveal two styles of Vertical Separation - Depth relationships which include a basement-driven unidirectional propagation (Style-1), and an intrasedimentary-driven fault nucleation and bi-directional propagation (Style-2). Further, we show that the along-fault deformation of affected stratigraphic surfaces exhibits systematic trends that varies with offset accrual. Furthermore, we demonstrate that the basement-driven fault propagation has greater efficiency of propagating the fault-related deformation to shallower depths compared to the intrasedimentary-driven nucleation and propagation. Finally, we suggest that the through-going basement-rooted faults in the study area are likely Proterozoic and were later reactivated in transpression in the Late Paleozoic.

Using geophysical and geological data, we present one of the first results showing ground truthing evidence of the composition of the widely observed intrabasement seismic reflectors (IBRS) in the Mesoproterozoic Granite-Rhyolite Province of central-eastern US. Our study suggests that the IBRs are basement-bounded mafic sill intrusions. The Anadarko Shelf deformation represents only a partial inheritance of the observed heterogeneous intrabasement deformation by the sedimentary cover. The systematic characterization of basement deformation and its propagation as presented in this study contributes to the understanding of the mechanics of structural inheritance in contractional tectonic settings.

Contributors to this project: F. Kolawole, M. Simpson Turko, and B. M. Carpenter.

Acknowledgements: Thanks to TGS for providing access to the 3-D Seismic Reflection and well data used in this study. We thank Chesapeake Energy Corporation, Oklahoma City for providing access to the computer software and hardware used to analyze and interpret the seismic data. We thank the Oklahoma Petroleum Information Center (OPIC), Norman, OK for providing access to the basement penetration borehole drill cuttings used in this study. Also, we thank the Chesapeake Energy Reservoir Technology Center for the photographs, X-ray diffraction and X-ray fluorescence analyses of the drill cuttings. We thank Laura Bellingar for assistance with basement well log synthetic modelling, Matthew Davis for assistance with the phase assessment of the seismic dataset, and Michael Horn for assistance with the seismic attribute computation. We also thank the Editor Craig Magee, and reviewers Rebecca E. Bell and Alexander Peace for their constructive feedback.

Publication of the results: Kolawole, F., Simpson Turko, M., & Carpenter, B. M. (2020). Basement-controlled Deformation of Sedimentary Sequences, Anadarko Shelf, Oklahoma. *Basin Research, 00, 1– 23*.

CHAPTER 3 FIGURES

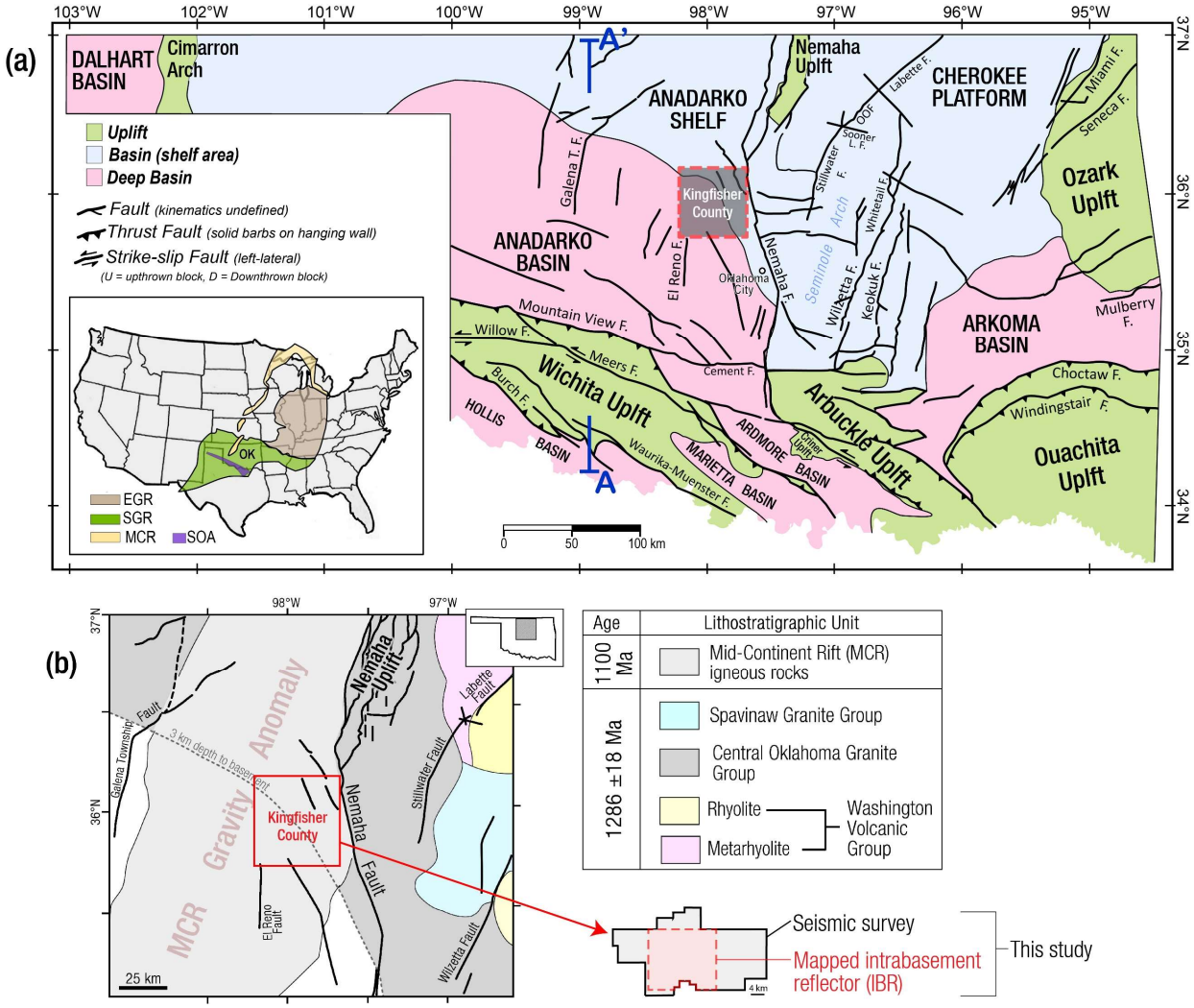

Figure 11. (a) Map of Oklahoma, showing the location of the study area (red dashed square), geologic provinces (after Northcutt and Campbell, 1995), and major faults (Marsh and Holland, 2016; Chase et al., 2018) area. *Inset:* Map showing the Precambrian igneous basement terranes in the central and eastern United States (after Thomas et al., 1984; Bickford et al., 2015). EGR = Eastern Granite-Rhyolite Province (1440-1480 Ma); SGR = Southern Granite-Rhyolite Province (1350-1400 Ma); MCR = Mid-Continent Rift (~1100 Ma); SOA = Southern Oklahoma Aulacogen (~520 Ma); OK = Oklahoma. (b) Basement geology of north-central Oklahoma (after Denison, 1966, 1981; Shah & Keller, 2016; Stein et al., 2018). Red arrow points to the outline of the 3D seismic survey used in this study.

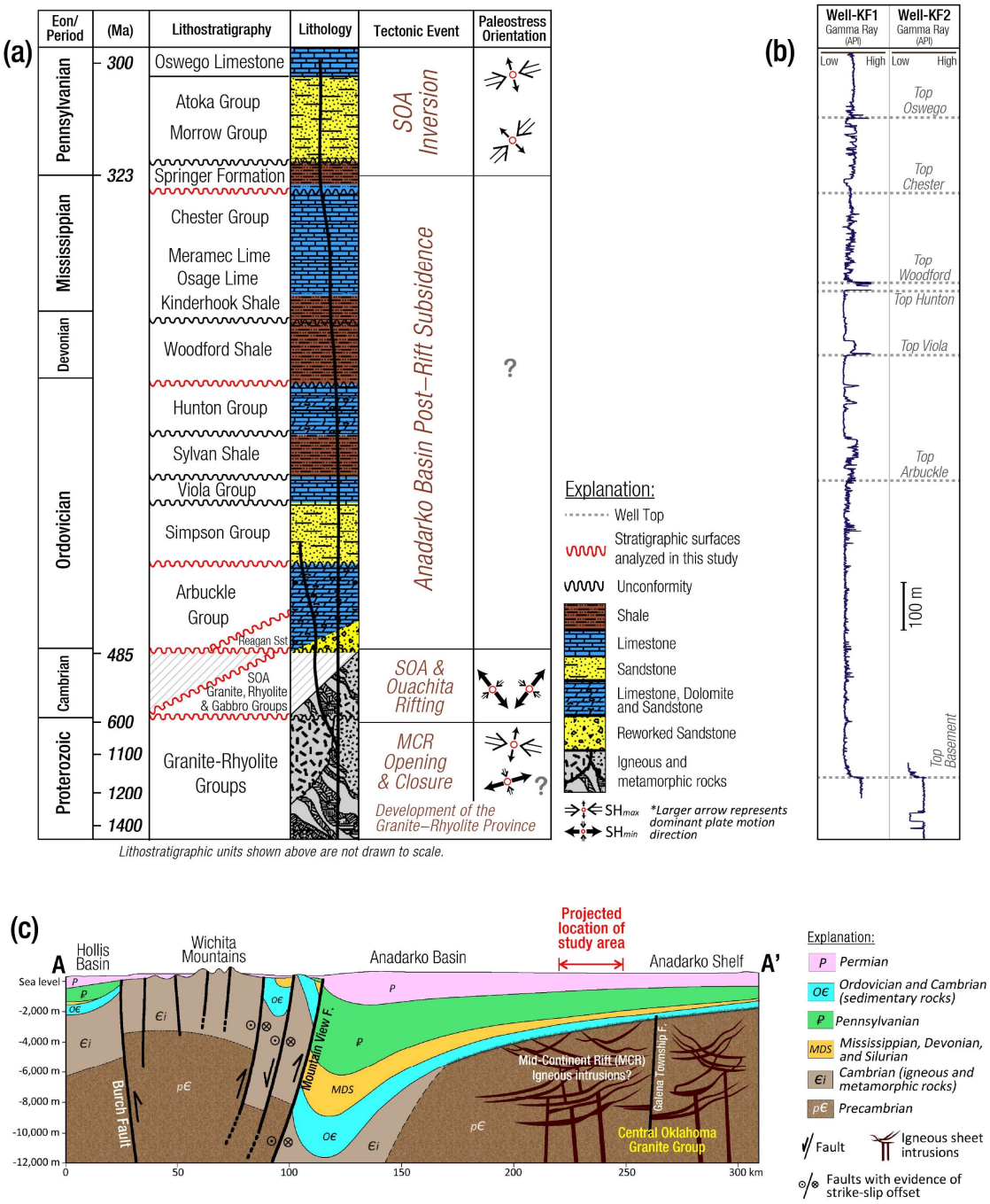

Figure 12. (a) Generalized stratigraphic column of the Anadarko Basin, Oklahoma (after Henry & Hester, 1995; Elebiju et al., 2011). (b) Gamma Ray logs and associated stratigraphic tops for two basement penetration well-KF1 and -KF2 within the study area. We used Well-KF1 for our seismic-well tie. See Figure 15 for more details on Well-KF2 (additional logs, drill cuttings, and geochemical analysis). (c) Cross-section A-A' (transect in Figure 11A) across the Anadarko Basin, Oklahoma, showing the subsurface configuration of the basin, associated stratigraphic units and basement features (after Brewer et al., 1983; Johnson, 2008; Simpson, 2015). The section also shows the projected location of the study area.

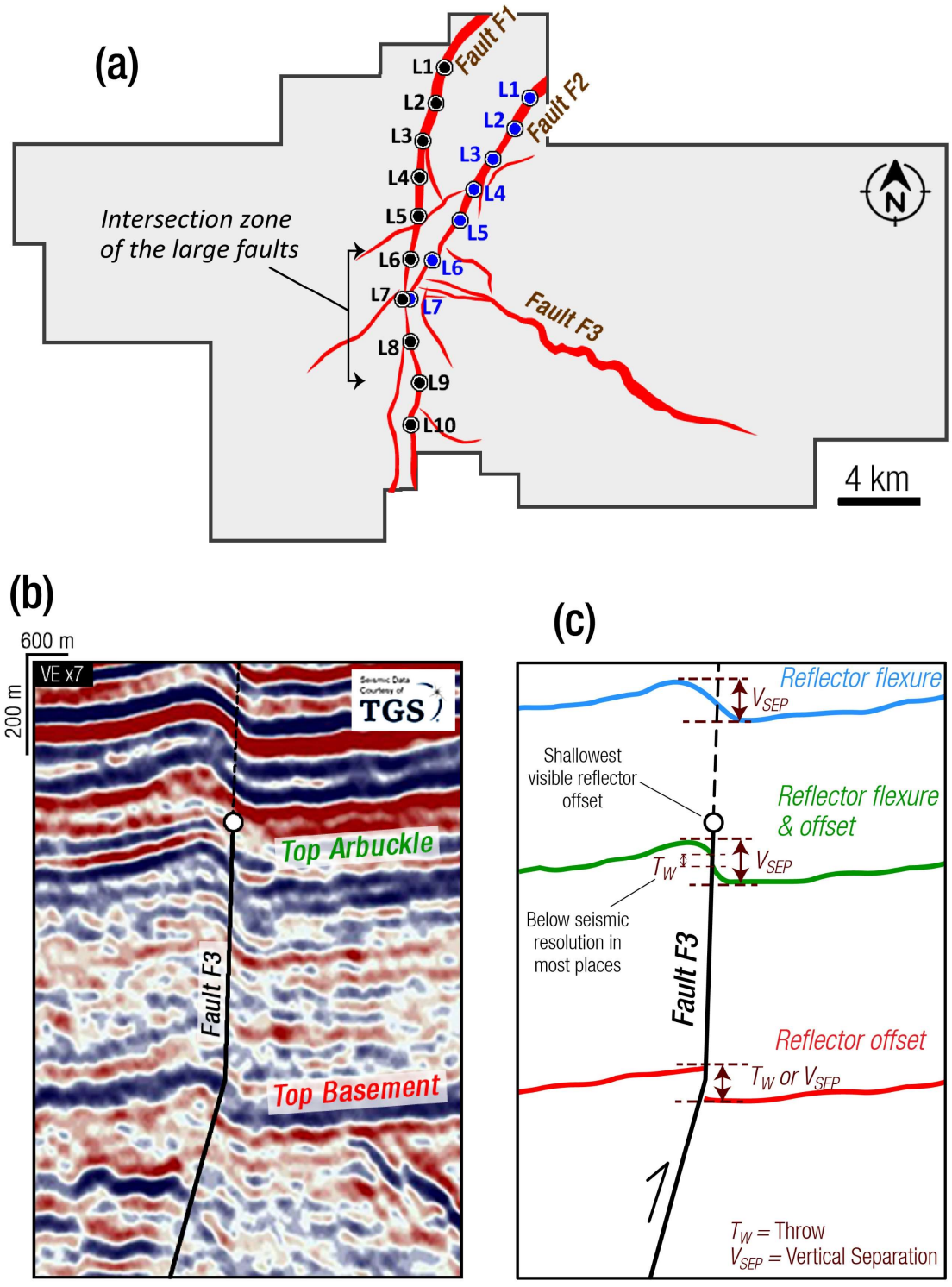

Figure 13. (a) A map of the seismic survey showing the large faults in the study area, and the 2 km interval locations at which vertical separation (Vsep) measurements were obtained (L1-L10 along F1; L1-L7 along F2). (b) Representative seismic section and (c) interpretation illustrating how the Vsep measurements were obtained at each of the locations.

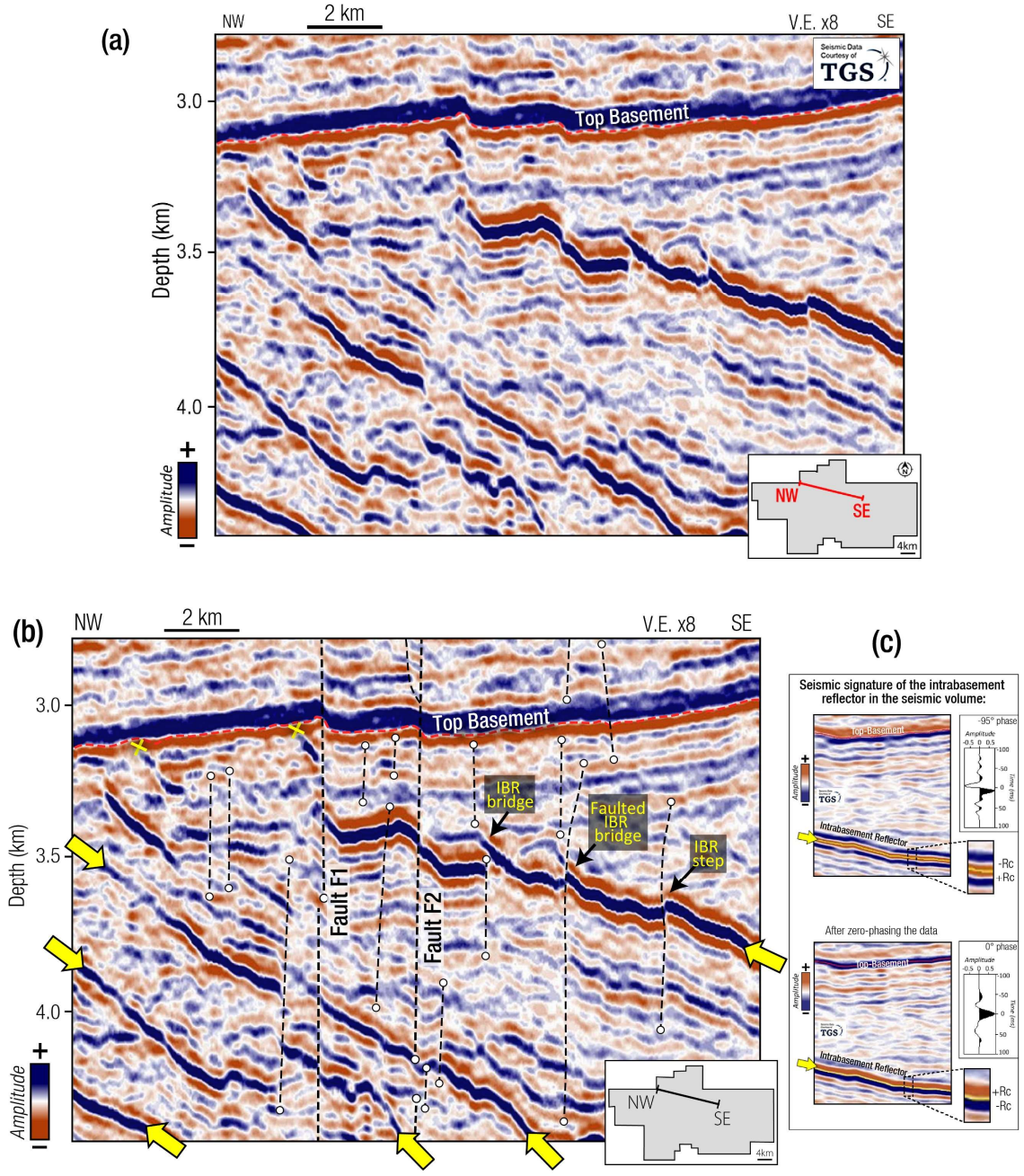

Figure 14. (a) Representative cross-section through the 3-D seismic dataset used in this study (transect in the bottom-right corner), and (b) interpretations showing distinct patterns of the intrabasement reflectors (IBR) in the area (yellow arrows) and geometry of interacting segments. The yellow "X-symbols" indicate the shallowest reaches of the IBRs terminating at the basement-sedimentary interface. Data courtesy of TGS. (c) *Top:* Representative seismic section and wavelet from the interpreted volume showing that the data is out of phase by -95° (erroneously suggests negative acoustic impedance for the Top-IBR contacts). *Bottom:* Same section and associated wavelet after the data is zero-phased, showing positive acoustic impedance for the Top-IBR contacts.

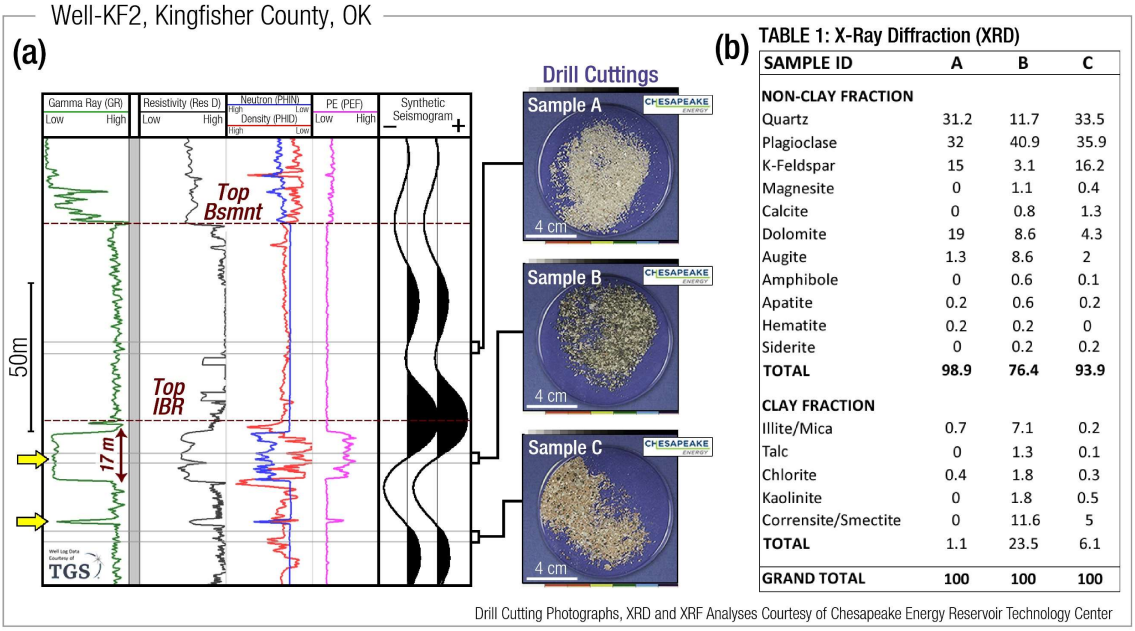

SAMPLE ID	A	B	C
NON-CLAY FRACTION			
Quartz	31.2	11.7	33.5
Plagioclase	32	40.9	35.9
K-Feldspar	15	3.1	16.2
Magnesite	0	1.1	0.4
Calcite	0	0.8	1.3
Dolomite	19	8.6	4.3
Augite	1.3	8.6	2
Amphibole	0	0.6	0.1
Apatite	0.2	0.6	0.2
Hematite	0.2	0.2	0
Siderite	0	0.2	0.2
TOTAL	**98.9**	**76.4**	**93.9**
CLAY FRACTION			
Illite/Mica	0.7	7.1	0.2
Talc	0	1.3	0.1
Chlorite	0.4	1.8	0.3
Kaolinite	0	1.8	0.5
Corrensite/Smectite	0	11.6	5
TOTAL	1.1	23.5	6.1
GRAND TOTAL	**100**	**100**	**100**

(c)

TABLE 2: X-Ray Fluorescence (XRF)

	Sample A	Sample B	Sample C
Mg wt%	1.8638	2.1592	BDL
Al wt%	4.1302	4.4637	5.0358
Si wt%	22.3335	13.7566	25.6265
P wt%	BDL	BDL	BDL
S wt%	BDL	BDL	BDL
K wt%	2.4284	0.8374	2.5593
Ca wt%	3.5491	4.8771	1.5094
Ba wt%	BDL	BDL	BDL
Ti wt%	BDL	0.47	0.121
V wt%	BDL	BDL	BDL
Cr wt%	0.0058	0.0028	0.0063
Mn wt%	0.038	0.0671	0.0453
Fe wt%	0.5935	4.6826	1.3172
Ni wt%	0.0053	0.0026	0.0061
Cu wt%	BDL	0.0033	BDL
Zn wt%	0.0151	0.0079	0.0131
Th wt%	BDL	BDL	BDL
Rb wt%	BDL	BDL	BDL
U wt%	BDL	BDL	BDL
Sr wt%	BDL	0.0167	BDL
Y wt%	0.0027	0.0021	0.0022
Zr wt%	0.0099	0.0071	0.0081
Nb wt%	0.0012	0.0005	0.0009
Mo wt%	0.0043	0.0059	0.0045

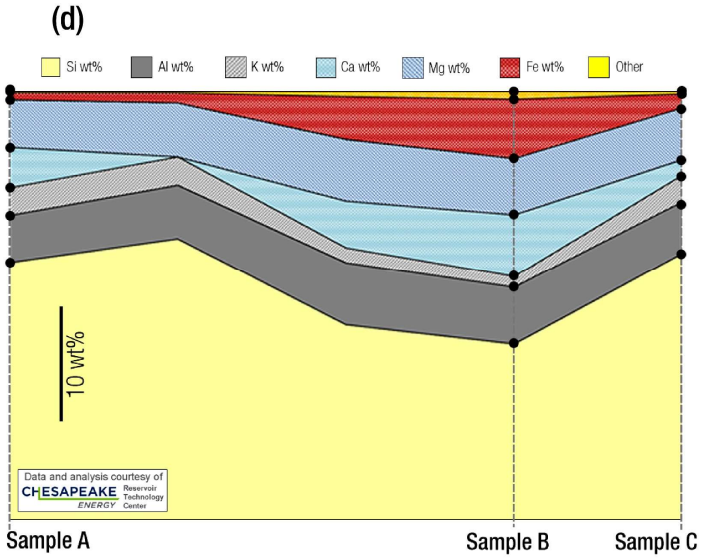

Figure 15. (a) Left: Wireline logs from basement well penetration Well-KF2 (Data courtesy of TGS) and modeled synthetic seismogram from density and sonic logs (not shown here) from Well-KF2 and other basement wells within the study area. Right: Photographs of drill cuttings from the indicated basement depth intervals (Courtesy of the Oklahoma Petroleum Information Center and Chesapeake Energy Reservoir Technology Center). (b) Table 4 showing the results of X-Ray Diffraction (XRD) analysis of the drill cuttings. (c) Table 5 and (d) Plot showing X-Ray Fluorescence (XRF) analyses of the drill cuttings. The XRF and XRD data are courtesy of the Chesapeake Energy Reservoir Technology Center.

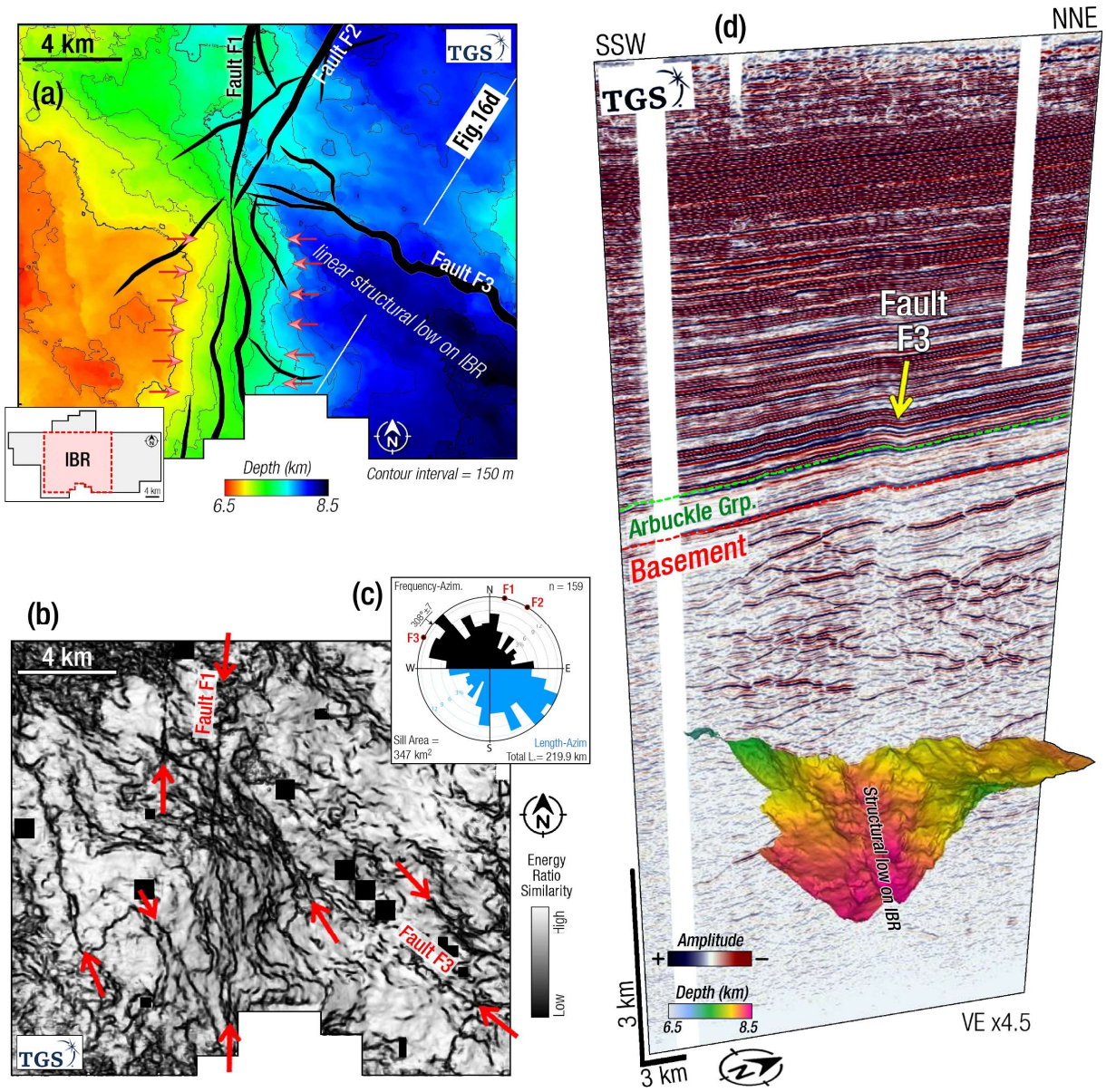

Figure 16. (a) Structure map of the mapped extensive deep-seated (6.5-8.5 km depth) intra-basement reflector (IBR) within the seismic survey, overlaid with major Top-Basement faults (black polygons). Red arrows point at N-S topographic gradient near the center of the survey, coinciding with fault F1. (b) Structure map of the IBR (same as 16a) co-rendered with Energy Ratio Similarity (ERS) seismic attribute. The low ERS lineaments represent sub-vertical discontinuity planes at deeper basement depths in the area. Red arrows point at the more rectilinear lineaments which include Fault F1. Black squares represent no-data zones. (c) Rose diagram showing azimuthal and length distribution of the Top-IBR lineaments. Overall, the dominant orientations of the lineaments (NW-SE and N-S) trend parallel to faults F1 and F3. (d) Representative seismic section (looking NW; see 5a for transect) showing the extents and 3D geometry of the IBR surface and relationship between Fault F3 and pronounced NW-SE structural-low on the IBR.

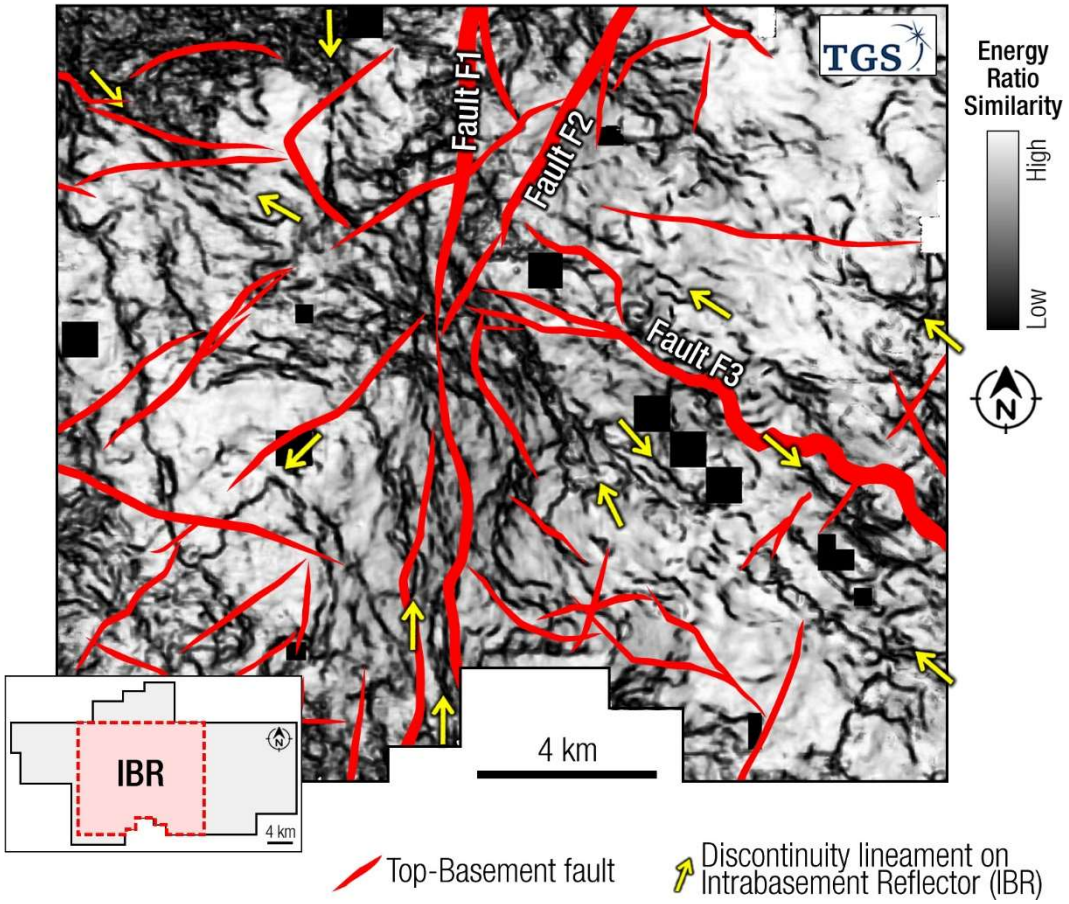

Figure 17. Surface map of the mapped intrabasement reflector (IBR) rendered with the Energy Ratio Similarity seismic attribute. Red polygons represent interpreted Top-Basement fault lineaments. Yellow arrows point at rectilinear discontinuity lineaments.

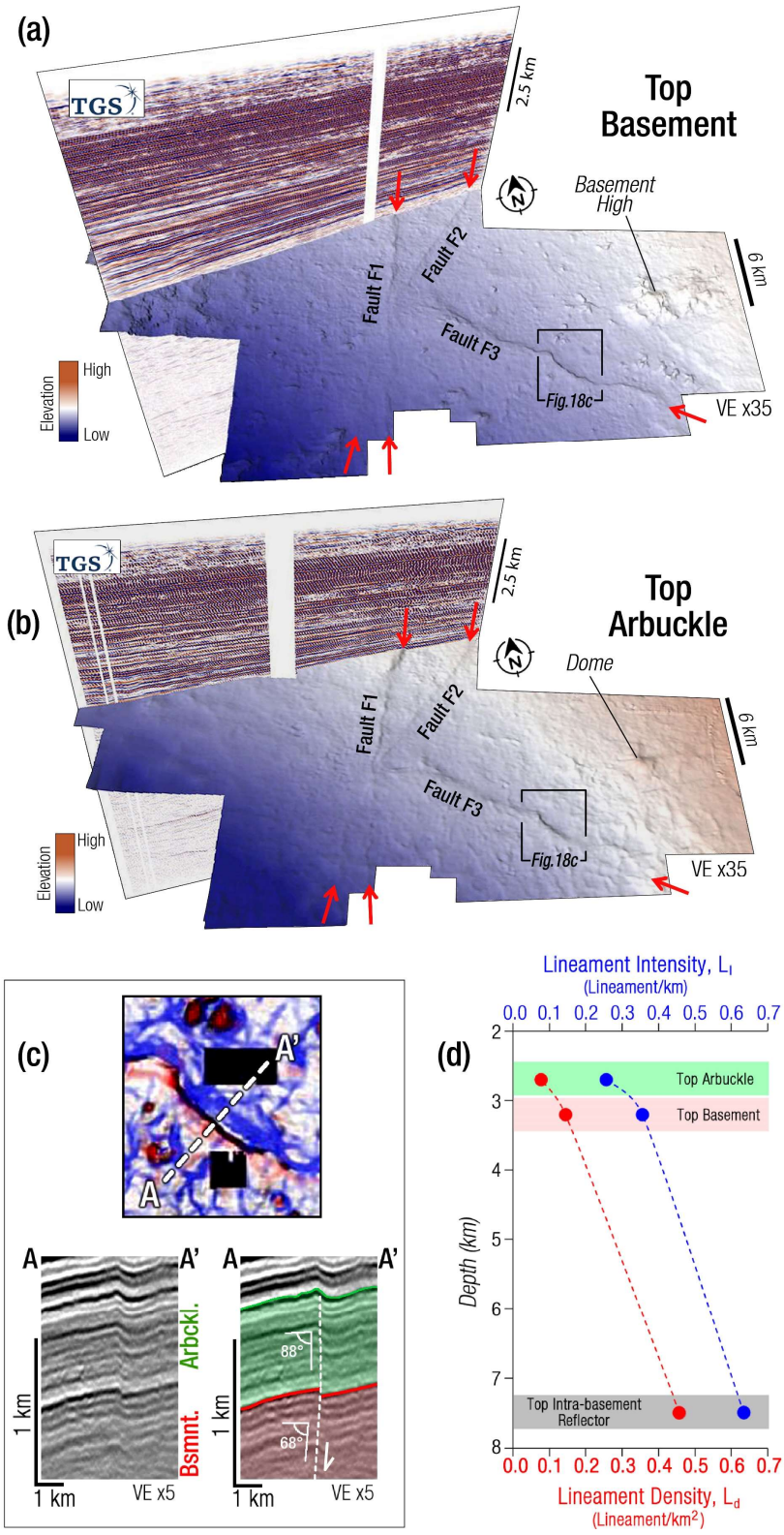

Figure 18. (a) Top-Basement structure map with a seismic cross-section showing the large (>10 km-long) faults within the study area (faults F1, F2, and F3). (b) Top-Arbuckle structure map with seismic cross-section. Red arrows point to the same large faults observed at the Top-Basement surface. (c) Structure-oriented attribute map (see Figure 19 for details) of a segment of Fault F3 at the Top-Basement surface, and associated seismic cross-section and interpretation. The map and sections show a change in geometry of deformed reflectors from the Top-Basement into the sedimentary cover. (d) Comparison of the intensity and density of discontinuity lineaments at the Top-Arbuckle (~2.7 km depth), Top-Basement (~3.2 km depth) and Top-Intra-basement reflector (~7.5 km depth) surfaces. This plot shows relatively greater predominance of the sub-vertical discontinuity planes at depth in the basement compared to the Top-Basement and Top-Arbuckle domains.

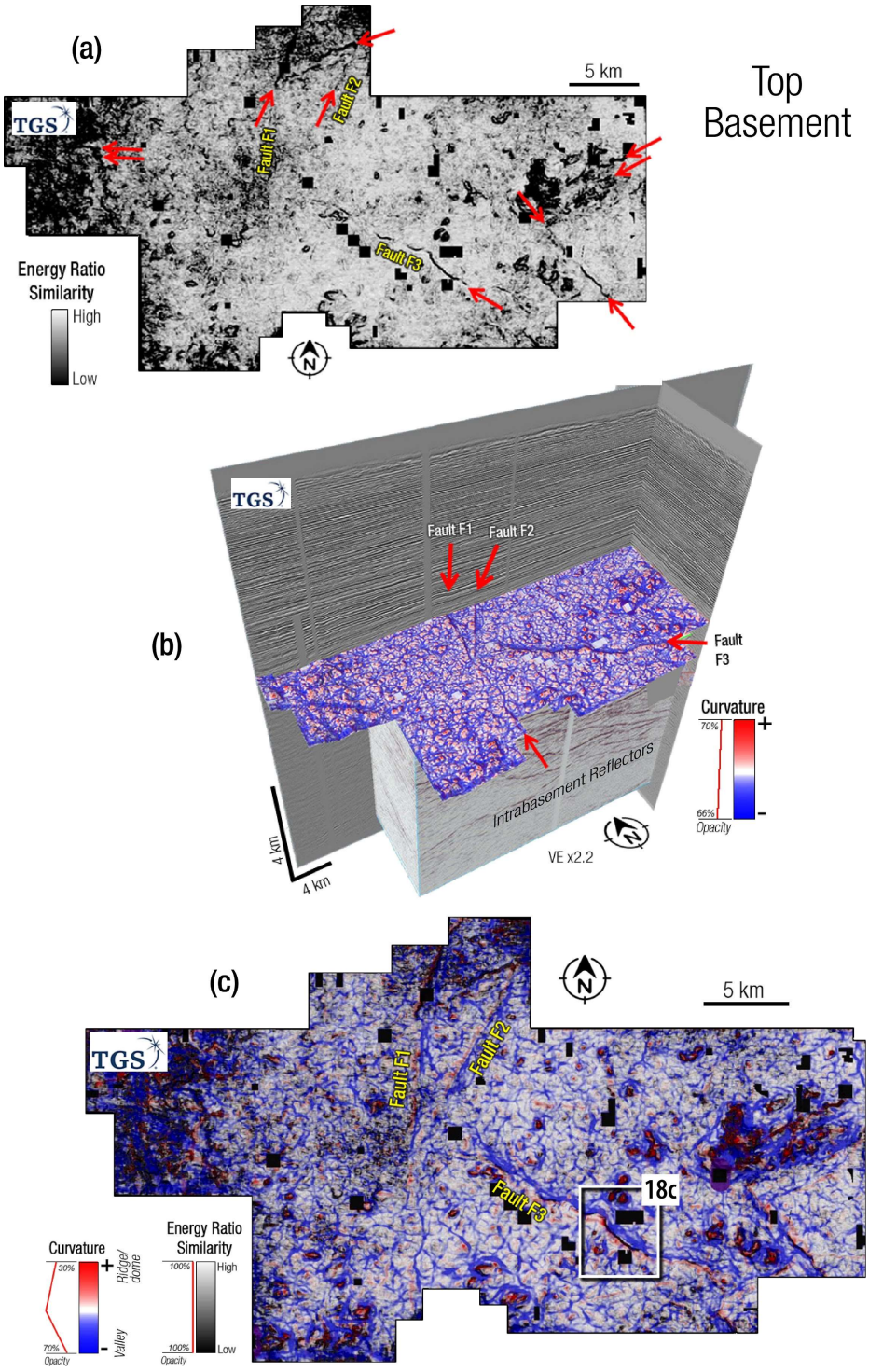

Figure 19. (a) Top-Basement surface rendered with Energy Ratio Similarity attribute. (b) Chair display showing Top-Basement rendered with most-positive (*k1*) and most-negative (*k2*) curvature attribute. (c) Top-Basement surface rendered with Energy Ratio Similarity and curvature attributes. Red arrows point at fault lineaments.

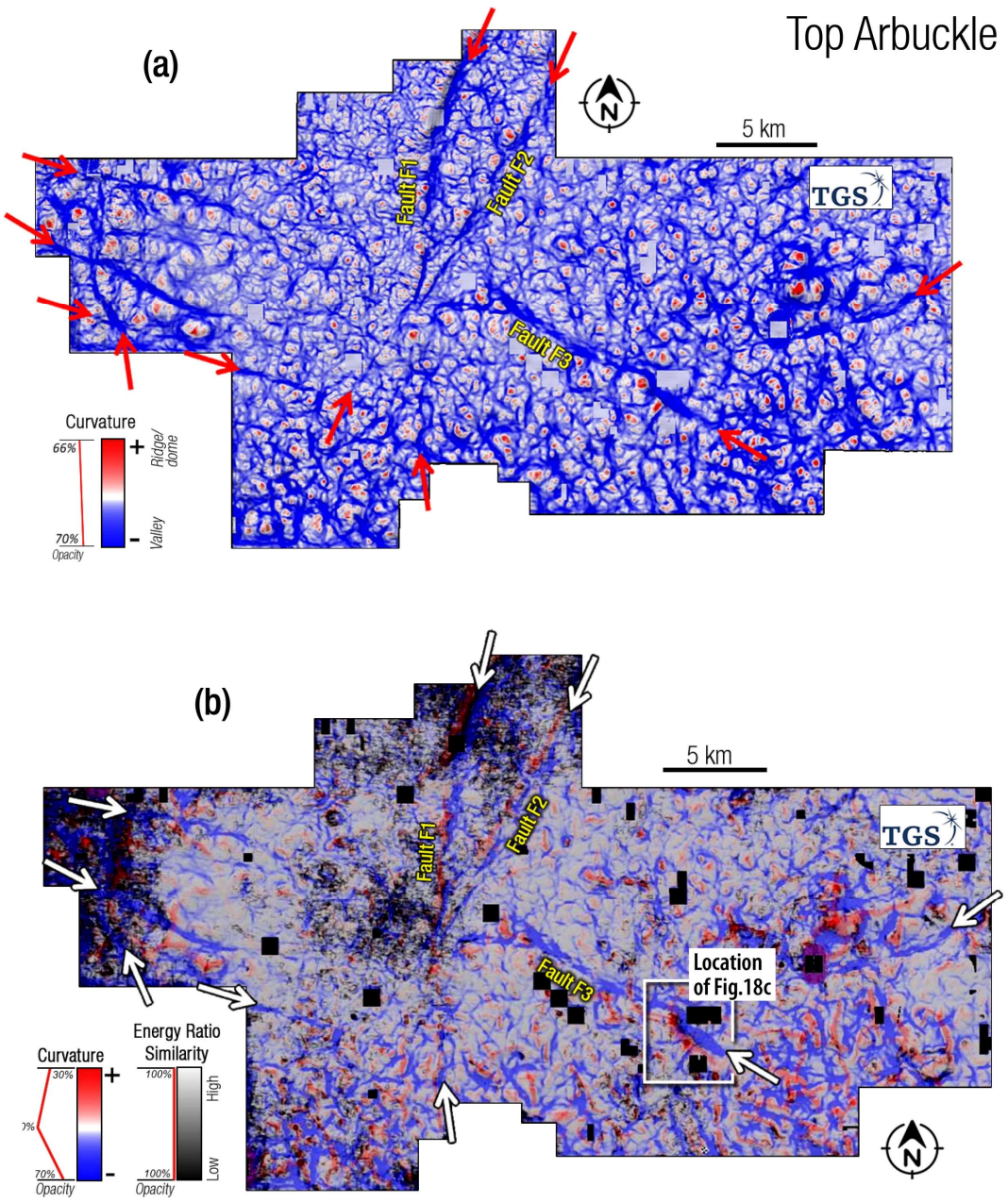

Figure 20. (a) Top-Arbuckle surface rendered with most-positive (*k1*) and most-negative (*k2*) curvature seismic attributes. Red arrows point at fault lineaments. (b) Top-Arbuckle surface rendered with most-positive (*k1*), most-negative (*k2*) curvature and energy ratio similarity attributes.

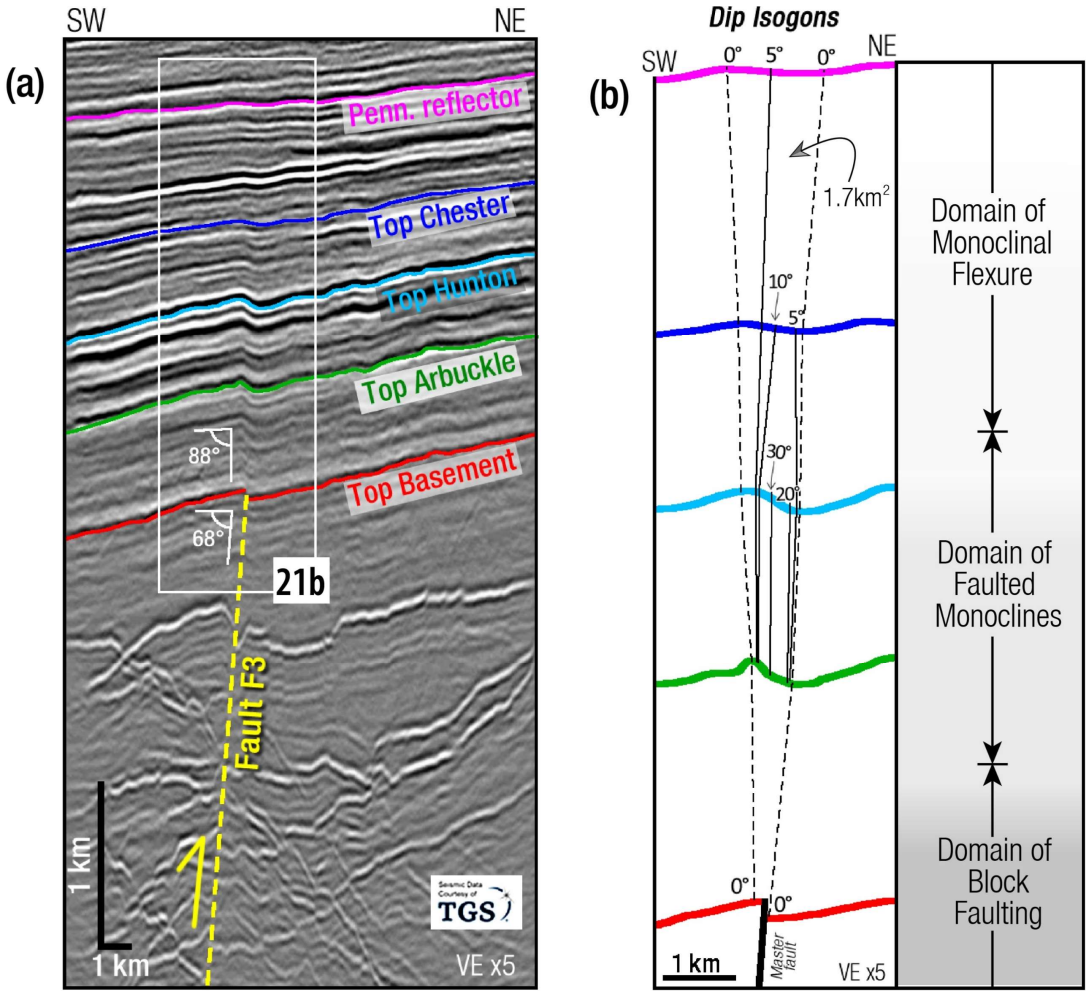

Figure 21. (a) Representative seismic section across fault F3 showing the Precambrian to Pennsylvanian interval (same transect as in Figure 18c). (b) Left: Dip isogon pattern for the faulted sequence along fault F3 showing the vertical changes in the geometrical character of the deformed stratigraphic surfaces. The indicated dip values on the dip isogon panel are exaggerated i.e. measured reflector dips at x5 vertical exaggeration. Right: Interpreted vertical zonation of structural domains above the large basement faults.

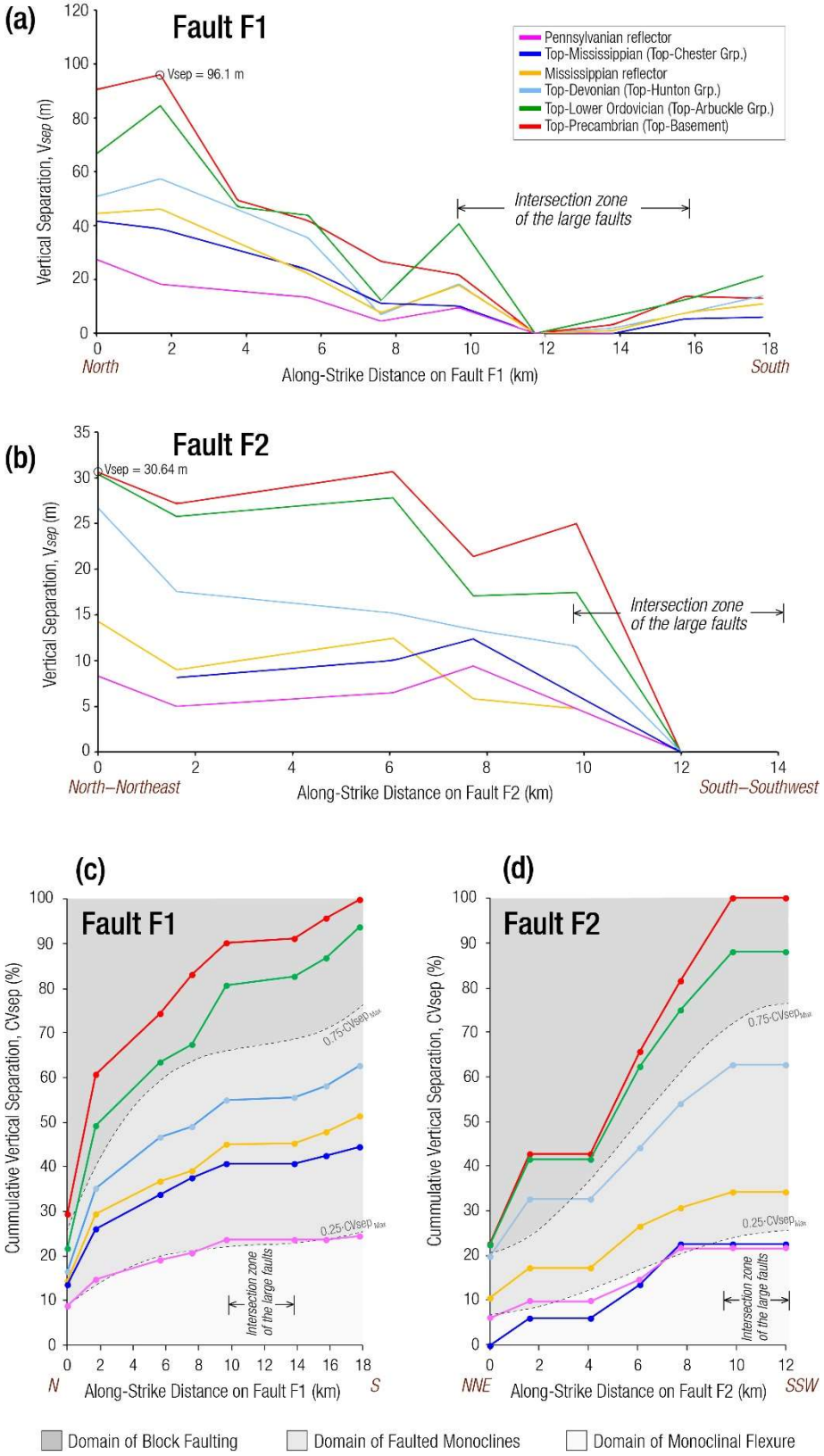

Figure 22. Distribution of Vsep versus distance (Vsep-D) along (a) fault F1, and (b) fault F2. Distribution of cumulative Vsep versus distance (CVsep-D) along (c) fault F1, and (d) fault F2. The CVsep-D values are plotted as percentages of the maximum CVsep value of each fault. The greyscale zonation of the plots is based on the 3rd order polynomial fitting curves for the 25% $CVsep_{max}$ and 75% $CVsep_{max}$ at each measurement location.

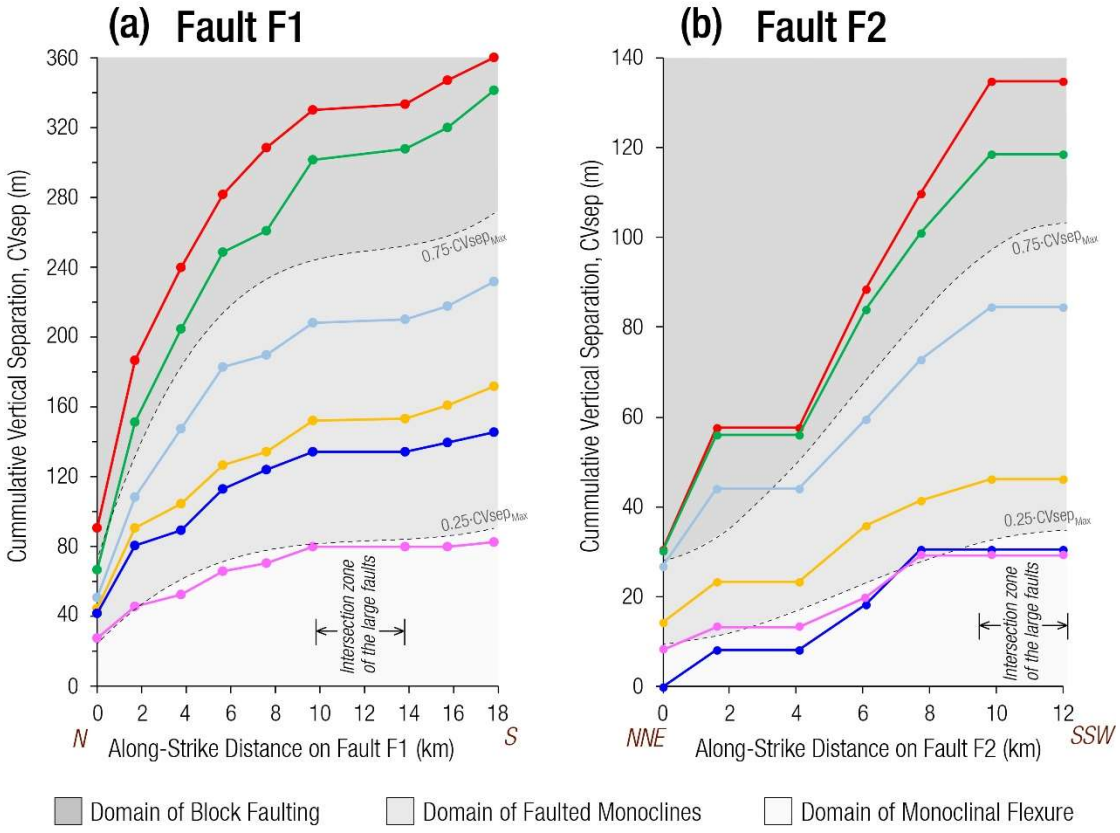

Figure 23. Distribution of cumulative Vsep versus distance (CVsep-D) along (c) fault F1, and (d) fault F2. The greyscale zonation of the plots is based on the 3rd order polynomial fitting curves for the 25% $CVsep_{max}$ and 75% $CVsep_{max}$ at each measurement location.

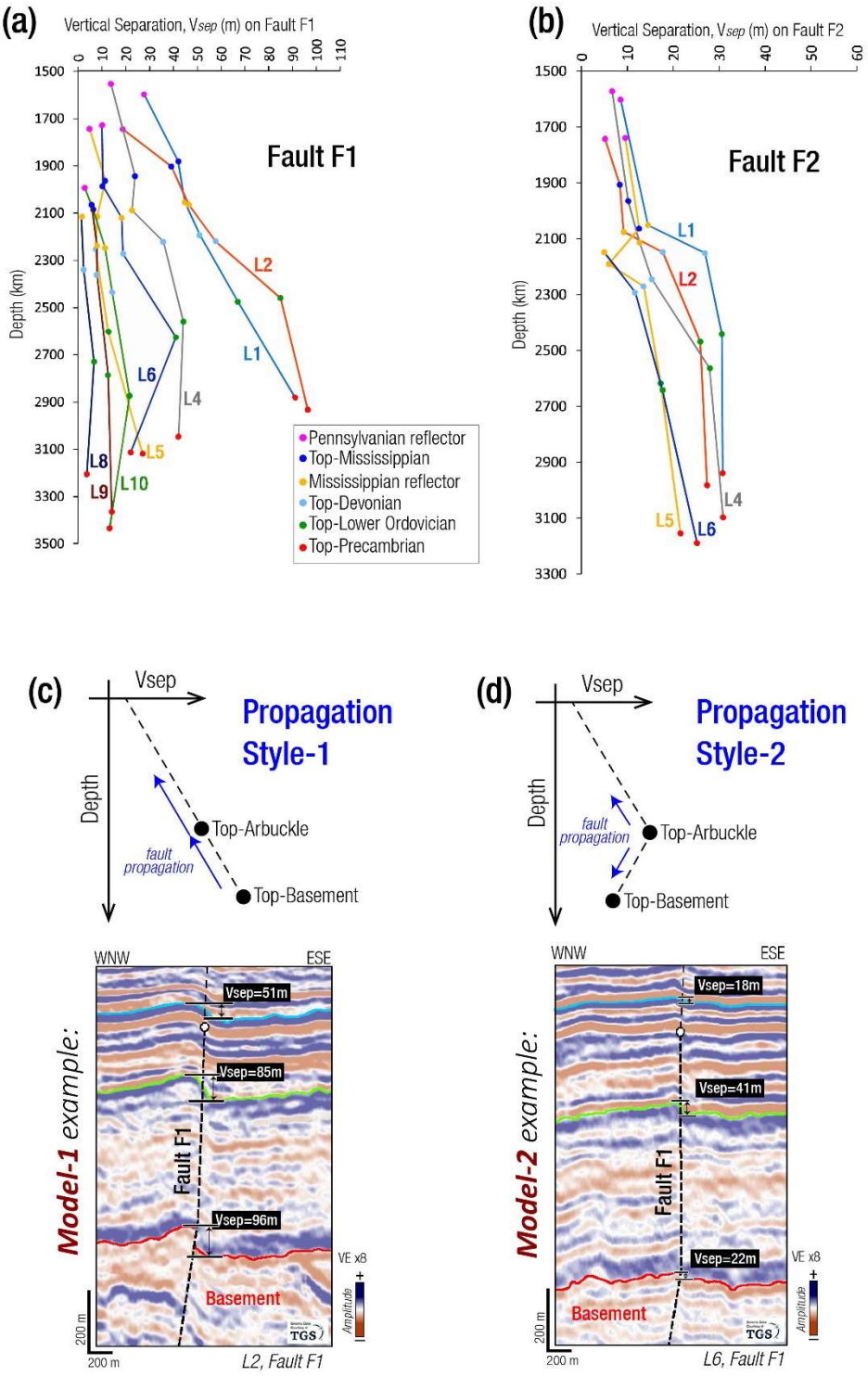

Figure 24. Vertical separation versus Depth (Vsep-Z) distribution along (a) fault F1, and (b) fault F2. See Figure 18c for the measurement locations. Vsep-Z models inferred from the observed trends in Figures 24a-b, in which (c) Style-1 describes basement-driven propagation of fault deformation, and (d) Style-2 describes intrasedimentary-driven nucleation and propagation of fault deformation. The associated seismic sections show an example of each propagation style.

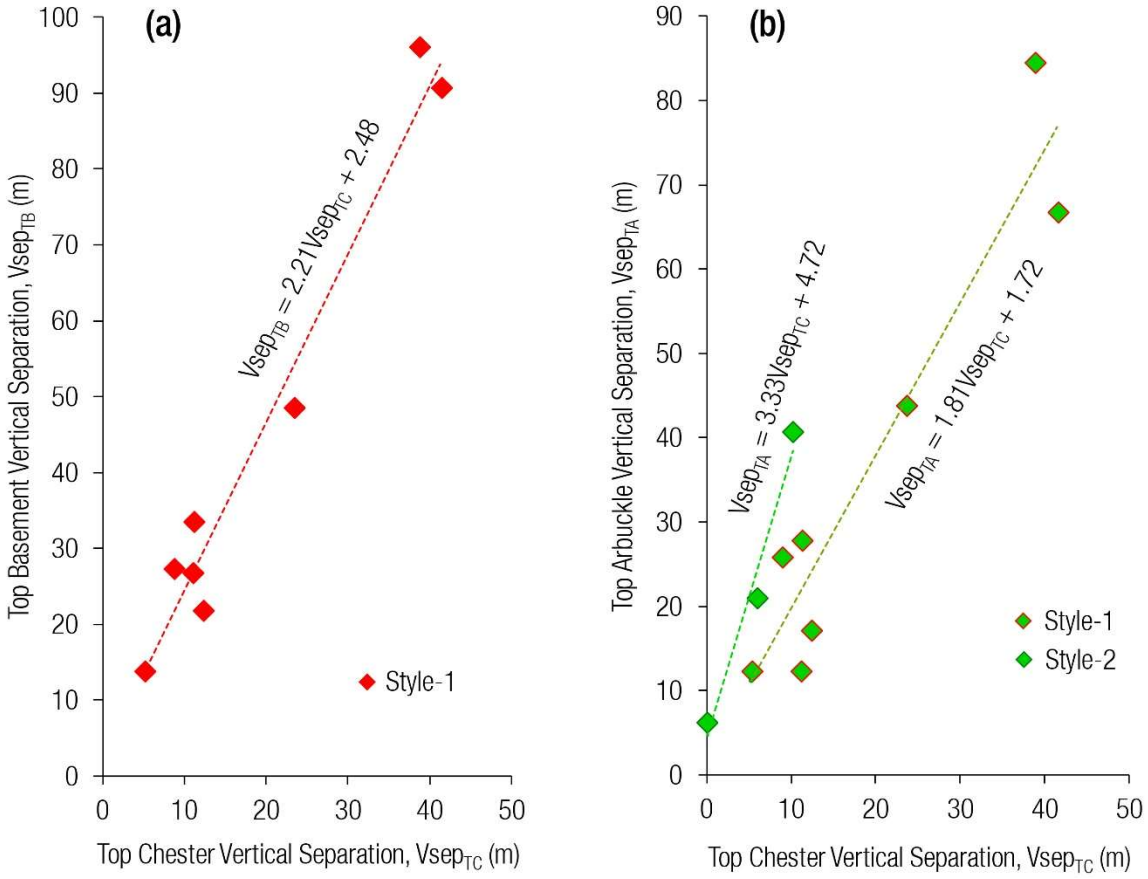

Figure 25. Efficiency of the vertical fault propagation styles. (a) Plot of Top-Basement Vertical Separation (Vsep$_{TB}$) versus Top-Chester Vertical Separation (Vsep$_{TC}$) for Style-1 trend. (b) The plots of Top-Arbuckle Vertical Separation (Vsep$_{TA}$) versus Top-Chester Vsep$_{TC}$ for Style-1 and Style-2 trends. The plots suggest that basement-driven propagation of deformation (Style-1) has a relatively greater efficiency of propagating deformation to shallower depths compared to sedimentary-driven deformation (Style-2).

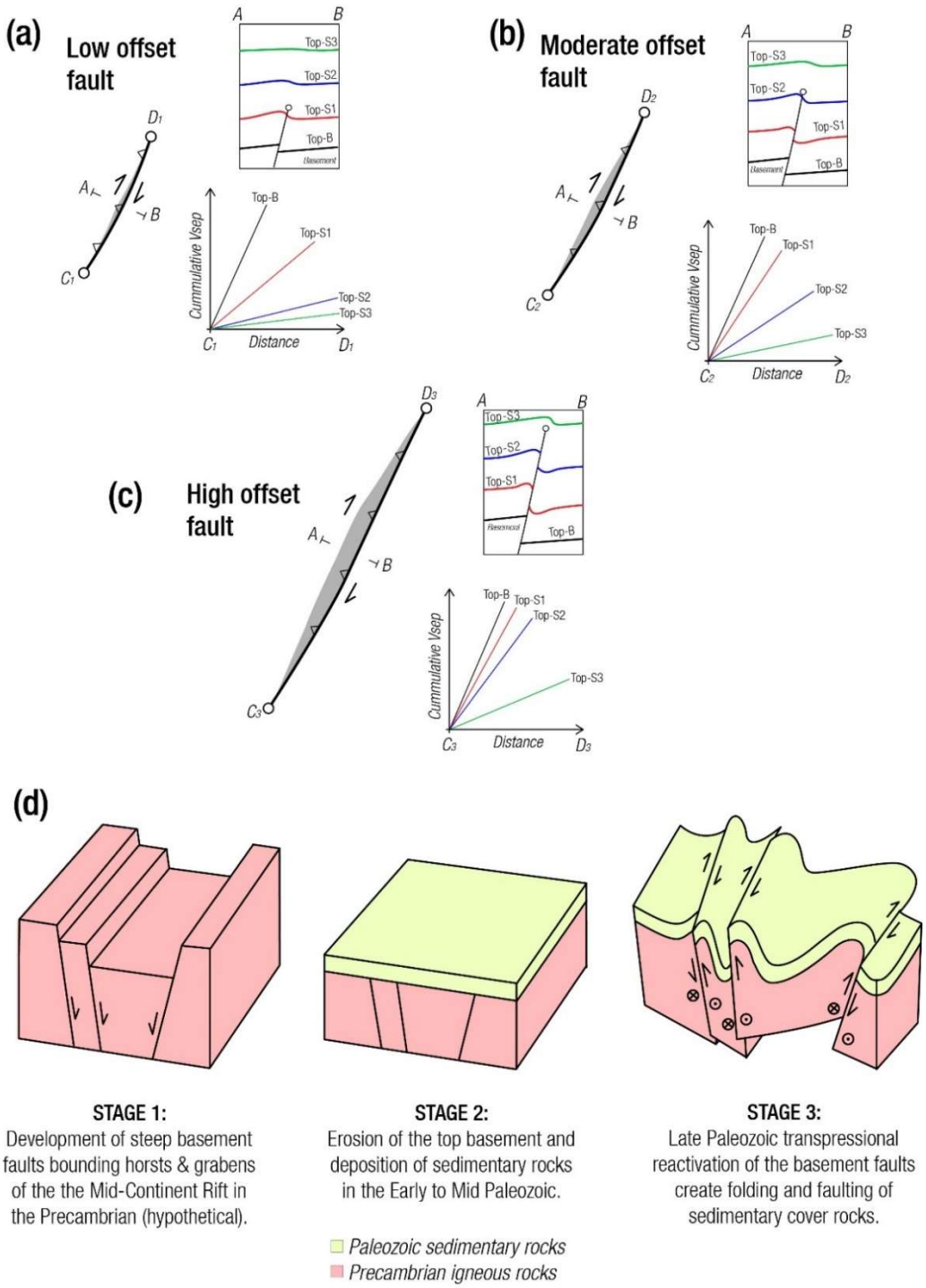

Figure 26. (a-c) Schematic models based on the observed distribution of cumulative vertical separation with distance (CVsep-D) along faults F1 and F2 (see Figures 22c-d). The plan-view fault traces represent the deepest stratigraphic surfaces (e.g. Top-B and Top-S1). The figures describe how the clustering of the CVsep-D curves changes with the accrual of offset on a propagating basement-rooted transpressional fault. (d) Cartoons summarizing a hypothesized evolution of the basement-involved deformation of the sedimentary cover of the Anadarko Shelf, Oklahoma.

REFERENCES

Anderson, H., Ellis, J. F., Muir, R., & Macaulay, E. (2015). September. 3-D Trishear: Parameters and Possibilities. AAPG-SEG International Conference and Exhibition, Melbourne, Australia 13-16 September 2015 (525-525).

Benson, W. A. (2014). The Spavinaw Granite (Proterozoic), Mayes County, Oklahoma. *The Shale Shaker*, *65*, 258-264.

Berg, R. R. (1962). Mountain flank thrusting in Rocky Mountain foreland, Wyoming and Colorado. AAPG Bulletin, 46, 2019–2032.

Brewer, J. A., Good, R., Oliver, J. E., Brown, L. D., & Kaufman, S. (1983). COCORP profiling across the Southern Oklahoma aulacogen: Overthrusting of the Wichita Mountains and compression within the Anadarko Basin. Geology, 11, 109-114.

Brown, W. G. (1983). Sequential development of the fold-thrust model of foreland deformation, In Lowell, J. D. ed., Rocky Mountain foreland basins and uplifts, Denver, Colorado. Rocky Mountain Association of Geologists, 57–64.

Burberry, C. M., & Lowe, J. B. (2019). Analog Modeling of Penetrative Strain Around Laramide Structures: Similarities and Differences Between Thick and Thin-Skinned Styles of Deformation. AAPG Annual Convention and Exhibition 2018, poster # 420-P55.

Cannon, W. F. (1994). Closing of the Midcontinent rift - A far-field effect of Grenvillian compression. Geology, 22, 155-158.

Castro Manrique, B. J. (2018). Structural Geology of the Woodford Shale in the Southeastern Anadarko Basin, Grady County, Oklahoma. MS Thesis, University of Oklahoma, Norman.

Chase, B., Atekwana, E. A., Kolawole, F., Turko, M. S., Carpenter, B. M., Evans, R. L. & Finn, C. (2018). December. The Southern Oklahoma Aulacogen: New Insights from Aeromagnetic, Seismic Reflection and Magnetotelluric Data Analyses. In AGU Fall Meeting Abstract #G51E-0523.

Chopra, S., & Marfurt, K. (2006). Seismic Attributes–a promising aid for geologic prediction. CSEG Recorder, 31, 110-120.

Chopra, S., & Marfurt, K. J. (2005). Seismic attributes — A historical perspective. Geophysics, 70, 3SO-28SO.

Chopra, S., Marfurt, K., Kolawole, F., & Carpenter, B. M. (2018a) Nemaha Strike-Slip Fault Expression on 3-D Seismic Data in SCOOP Trend. AAPG Explorer, Search and Discovery Article #42235.

Chopra, S., Infante-Paez, L., & Marfurt, K. J. (2018b). Intra-Basement Intrusions in the STACK Area of Oklahoma. AAPG Geophysical Corner, AAPG Search and Discovery #42229.

Collanega, L., Suida, K., Jackson, C. A.-L., Bell, R. E., Coleman, A. J., Lenhart, A., Magee, C., & Breda, A. (2019). Normal fault growth influenced by basement fabrics: the importance of preferential nucleation from pre-existing structures. Basin Research, 31, 659–687.

Coward, M. P. (1983). Thrust tectonics, thin skinned or thick skinned, and the continuation of thrusts to deep in the crust. Journal of Structural Geology, 5, 113-123.

Denison, R. E. (1981). Basement rocks in northeastern Oklahoma. Oklahoma Geological Survey Circular 84. Norman, OK.

Denison, R. E. (1995). Significance of air-photograph linears in the basement rocks of the Arbuckle Mountains. Oklahoma Geological Survey Circular 97, 119-131.

Denison, R. E., Bickford, M. E., Lidiak, E. G., & Kisvarsanyi, E. B. (1987). Geology and geochronology of Precambrian rocks in the central interior region of the United States. U.S. Geological Survey Professional Paper 1241-C.

Dickas, A. B. (1986). Comparative Precambrian stratigraphy and structure along the mid-continent rift. AAPG Bulletin, 70(3), 225-238.

Dolton, G. L., & Finn, T. F. (1989). Petroleum geology of the Nemaha uplift, central mid-continent. Dept. of the Interior, US Geological Survey, No. 88-450-D.

Droege, L., & Vick, H. (2018). Redefining the STACK Play from Subsurface to Commercialization: Identifying Stacked Pay Sweet Spots in the Northern Anadarko Basin. AAPG ACE 2018 Annual Convention & Exhibition, Salt Lake City, Utah. Search and Discovery Article #11104.

Elebiju, O. O., Matson, S., Keller, G. R., & Marfurt, K. J. (2011). Integrated geophysical studies of the basement structures, the Mississippi chert, and the Arbuckle Group of Osage County region, Oklahoma. AAPG Bulletin, 95, 371-393.

Erslev, E. A., & Koenig, N. V. (2009). Three-dimensional kinematics of Laramide, basement-involved Rocky Mountain deformation, USA: Insights from minor faults and GIS-enhanced structure maps. Geological Society of America Memoirs, 204, 125-150.

Evenick, J. C., 2006, Potential subsurface structures and hydrocarbon reservoirs in the southern Appalachian basin beneath the Cumberland Plateau and eastern Highland Rim, Tennessee, Kentucky, and southwestern Virginia. University of Tennessee, Ph.D. Dissertation, 402.

Evenick, J. C., & Hatcher, R. D. Jr. (2006). Trenton-Black River suggested as common nomenclature across Appalachian basin. Oil and Gas Journal, 104, 31-36.

Font, R. G. (2003). Layered basement, basement truncated wedges, structural patterns, tectonic evolution, and seismic expression of Montague County, West of Muenster Arch in North Texas, USA. The Professional Geologist, 40, 2-7.

Frohlich, C., DeShon, H., Stump, B., Hayward, C., Hornbach, M., & Walter, J. I. (2016). A historical review of induced earthquakes in Texas. Seismological Research Letters, 87, 1022-1038.

Gay Jr, S. P. (2003). The Nemaha Trend-a System of Compressional Thrust-Fold, Strike-Slip Structural Features in Kansas and Oklahoma, (Part 2, Conclusion). The Shale Shaker, 54, 39-49.

Gay Jr., S. P. (1999), Strike-slip, compression thrust-fold nature of the Nemaha system in eastern Kansas and Oklahoma, in D.F. Merrian (ed.) Transactions of the 1999 AAPG Midcontinent section meeting: Kansas Geol. Surv. Open File Rep., 99–28.

Griffith, W. A., Sanz, P. F. and Pollard, D. D. (2009). Influence of outcrop scale fractures on the effective stiffness of fault damage zone rocks. Pure and Applied Geophysics, 166(10-11), 1595-1627.

Gwon, S., & Kim, Y. S. (2016). Interpretation of deformation history and paleostress based on fracture analysis exposed in a trench. The Journal of Engineering Geology, 26, 33-49.

Hardy, S., & Ford, M. (1997). Numerical modeling of trishear fault propagation folding. Tectonics, 16, 841 – 854.

Hardy, S., & Allmendinger, R. W. (2011). Trishear: A review of kinematics, mechanics, and applications, in McClay, K., Shaw, J., & Suppe, J., eds., Thrust fault-related folding. AAPG Memoir 94, 95-119.

Harper, T., Fossen, H., & Hesthammer, J. (2001). Influence of uniform basement extension on faulting in cover sediments. Journal of Structural Geology, 23, 593-600.

Henry, M. E., & Hester, T. C. (1995). Anadarko basin province (058), in Gautier, D. L., Dolton, G. L., Takahashi, K. I., and Varnes, K. L., ed., 1995 National assessment of United States oil and gas resources--Results, methodology, and supporting data: U.S. Geological Survey Digital Data Series DDS-30, Release 2.

Iaffa, D. N., Sàbat, F., Muñoz, J. A., Mon, R., & Gutierrez, A. A. (2011). The role of inherited structures in a foreland basin evolution. The Metán Basin in NW Argentina. Journal of Structural Geology, 33, 1816-1828.

Infante-Paez, L., & Marfurt, K. J. (2017). Seismic expression and geomorphology of igneous bodies: A Taranaki Basin, New Zealand, case study. Interpretation, 5, SK121-SK140.

Jaiswal, P., Gregg, J. M., Parks, S., Holman, R., Mohammadi, S., & Grammer, G. M. (2017). Evidence of fault/fracture “Hydrothermal” reservoirs in the southern midcontinent Mississippian carbonates. In Grammer, G. M., Gregg, J. M., Puckette, J. O., Jaiswal, P., Mazzullo, S. J., Pranter, M. J., & Goldstein, R. H., eds., Mississippian Reservoirs of the Midcontinent. AAPG Memoir 116.

Johnson, K. S. (1989). Geologic evolution of the Anadarko basin. Oklahoma Geological Survey Circular, 90, 3-12.

Johnson, K.S. (1991). Arbuckle group core workshop and field trip (No. 3). Oklahoma Geological Survey.

Johnson, K. S. (2008). Geologic history of Oklahoma. Earth sciences and mineral resources of Oklahoma. Oklahoma Geological Survey Educational Publication, 9, 3-5.

Keller, G. R., & Stephenson, R. A. (2007) The Southern Oklahoma and Dniepr-Donets aulacogens: A comparative analysis, in Hatcher, R. D., Jr., Carlson, M. P., McBride, J. H., & Martínez Catalán, J. R., eds., 4-D Framework of Continental Crust. Geological Society of America Memoir, 200, 127-143.

Kibikas, W.M., Carpenter, B. M., & Ghassemi, A. (2019) The Petrophysical and Mechanical Properties of Oklahoma's Crystalline Basement. In 53rd US Rock Mechanics/Geomechanics Symposium, American Rock Mechanics Association, August 2019.

Kim, D., & Brown, L.D. (2019). From trash to treasure: Three-dimensional basement imaging with "excess" data from oil and gas explorations. AAPG Bulletin, 103, 1691-1701.

Kolawole, F., Atekwana, E. A., Laó-Dávila, D. A., Abdelsalam, M. G., Chindandali, P. R., Salima, J., & Kalindekafe, L. (2018). Active deformation of Malawi rift's north basin Hinge zone modulated by reactivation of preexisting Precambrian Shear zone fabric. Tectonics, 37, 683-704.

Kolawole, F., Phillips, T. B., Atekwana, E. A., Jackson, C. A-L (2019a). Structural Inheritance Controls Strain Distribution During Early Continental Rifting, Rukwa Rift. EGU General Assembly Conference Abstract EGU2019-1849 (vol. 21).

Kolawole, F., Johnston, C. S., Morgan, C. B., Chang, J. C., Marfurt, K. J., Lockner, D. A., Reches, Z. & Carpenter, B. M. (2019b). The susceptibility of Oklahoma's basement to seismic reactivation. Nature Geoscience, 12, 839-844.

Lacombe, O., & Bellahsen, N. (2016). Thick-skinned tectonics and basement-involved fold–thrust belts: insights from selected Cenozoic orogens. Geological Magazine, 153, 763-810.

Lee, J., & Kim, Y. S. (2018). Deformation history based on the characteristics of dike-controlled faults and cross-cutting relationship between dikes and faults. In AGU Fall Meeting Abstracts #T23A-0326.

Liao, Z., Liu, H., Jiang, Z., Marfurt, K. J., & Reches, Z. E. (2017). Fault damage zone at subsurface: A case study using 3D seismic attributes and a clay model analog for the Anadarko Basin, Oklahoma. Interpretation, 5, T143-T150.

Lidiak, E. G., Denison, R. E., & Stern, R. J. (2014). Cambrian (?) Mill Creek Diabase Dike Swarm, Eastern Arbuckles: A Glimpse of Cambrian Rifting in the Southern Oklahoma Aulacogen. Oklahoma Geological Survey Guidebook 38, 105-122.

Lihou, J. C., & Allen, P. A. (1996). Importance of inherited rift margin structures in the early North Alpine Foreland Basin, Switzerland. Basin Research, 8, 425-442.

Lowell, J. D. (1995). Mechanics of basin inversion from worldwide examples. Geological Society, London, Special Publications, 88, 39-57.

Marsh, S. & Holland, A. (2016). Comprehensive fault database and interpretive fault map of Oklahoma. Oklahoma Geol. Survey Open-File Report, 15.

McBee, W. (2003a). The Nemaha and other strike-slip faults in the midcontinent USA. AAPG Mid-Continent Section Meeting Proceedings, Tulsa, OK., 1–23.

McBee, W. (2003b). Nemaha strike-slip fault zone, paper presented at AAPG Mid-continent section meeting, Oct. 13.

McBride, J. H., Leetaru, H. E., Keach, R. W., & McBride, E. I. (2016). Fine-scale structure of the Precambrian beneath the Illinois Basin. Geosphere, 12, 585-606.

McBride, J. H., William Keach II, R., Leetaru, H. E., & Smith, K. M. (2018). Visualizing Precambrian basement tectonics beneath a carbon capture and storage site, Illinois Basin. Interpretation, 6, T257-T270.

McClay, K. (2011). Introduction to thrust fault-related folding, in McClay, K., Shaw, J., & Suppe, J., eds., Thrust fault-related folding. AAPG Memoir 94, 1–19.

McClay, K. R., & Ellis, P. G. (1987). Geometries of extensional fault systems developed in model experiments. Geology, 15, 341-344.

McNamara, D. E., Rubinstein, J. L., Myers, E., Smoczyk, G., Benz, H. M., Williams, R. A., Hayes, G., Wilson, D., Herrmann, R., McMahon, N. D., & Aster, R. C. (2015). Efforts to monitor and characterize the recent increasing seismicity in central Oklahoma. The Leading Edge, 34, 628-639.

Mitra, S., & Mount, V. S. (1998). Foreland basement-involved structures. AAPG bulletin, 82, 70-109.

Mohammadi, S., Gregg, J. M., Shelton, K. L., Appold, M. S., & Puckette, J. O. (2017). Influence of late diagenetic fluids on Mississippian carbonate rocks on the Cherokee–Ozark Platform, NE Oklahoma, NW Arkansas, SW Missouri, and SE Kansas. In Grammer, G. M., Gregg, J. M., Puckette, J. O., Jaiswal, P., Mazzullo, S. J., Pranter, M. J., & Goldstein, R. H., eds., Mississippian Reservoirs of the Midcontinent. AAPG Memoir 116.

Naylor, M. A., Mandl, G. T., & Supesteijn, C. H. K. (1986). Fault geometries in basement-induced wrench faulting under different initial stress states. Journal of Structural Geology, 8, 737-752.

Perry, W. J. (1989). Tectonic evolution of the Anadarko Basin region, Oklahoma (No. 1866). Department of the Interior, US Geological Survey.

Phillips, T. B., Magee, C., Jackson, C. A. L., & Bell, R. E. (2018). Determining the three-dimensional geometry of a dike swarm and its impact on later rift geometry using seismic reflection data. Geology, 46, 119-122.

Powers, S. (1928). Age of the Folding of the Oklahoma Mountains—the Ouachita, Arbuckle, and Wichita Mountains of Oklahoma and the Llano-Burnet and Marathon Uplifts of Texas. Bulletin of the Geological Society of America, 39, 1031-1071.

Prucha, J. J., Graham, J. A., & Nickelson, R. P. (1965). Basement controlled deformation in Wyoming province of Rocky Mountain foreland. AAPG Bulletin, 49, 966–992.

Reeve, M. T., Bell, R. E., Jackson, C. A. L. (2014). Origin and significance of intra-basement seismic reflections offshore western Norway. Journal of the Geological Society, 171, 1-4.

Qin, Y., Chen, X., Carpenter, B. M., & Kolawole, F. (2018). Coulomb stress transfer influences fault reactivation in areas of wastewater injection. Geophysical Research Letters, 45, 11-059.

Qin, Y., Chen, X., Walter, J. I., Haffener, J., Trugman, D. T., Carpenter, B. M., Weingarten, M., & Kolawole, F. (2019). Deciphering the stress state of seismogenic faults in Oklahoma and southern Kansas based on an improved stress map. Journal of Geophysical Research: Solid Earth, 124.

Ramsay, J. G. (1967). Folding and fracturing of rocks. Mc Graw Hill Book Company, 568.

Ramsay, J. G., & Huber, M. I. (1987). The techniques of modern structural geology: Folds and fractures, volume 2. Academic Press.

Reches, Z. E. (1978), Development of monoclines: Part I. Structure of the Palisades Creek branch of the East Kaibab monocline, Grand Canyon, Arizona. Laramide folding associated with basement block faulting in the western United States. Geol. Soc. Amer. Mem., 151, 235-271.

Scholz, C. H., Dawers, N. H., Yu, J., Anders, M. H., & Cowie, P. A. (1993). Fault growth and fault scaling laws: preliminary results. Journal of Geophysical Research: Solid Earth, 98(B12), 21951-21961.

Shah, A. K., & Keller, G. R. (2017). Geologic influence on induced seismicity: Constraints from potential field data in Oklahoma. Geophysical Research Letters, 44, 152-161.

Simpson, M. (2015) A Structural Re-Evaluation of the Ardmore Basin. In Mid-Continent Section. Search and Discovery Article #10795. AAPG Mid-Continent Section meeting in Tulsa, Oklahoma, October 4-6, 2015.

Schoenball, M., & Ellsworth, W. L. (2017). Waveform-relocated earthquake catalog for Oklahoma and southern Kansas illuminates the regional fault network. Seismological Research Letters, 88, 1252-1258.

Smith Jr, L. B., & Davies, G. R. (2006). Structurally controlled hydrothermal alteration of carbonate reservoirs: Introduction. AAPG Bulletin, 90, 1635-1640.

Stearns, D. W., 1975, Laramide basement deformation in the Bighorn basin—the controlling factor for structures in the layered rocks. Geology and mineral resources of the Bighorn basin, Wyoming. Geological Association 27th Annual Field Conference Guidebook, 149–158.

Stearns, D. W., 1978, Faulting and forced folding in the Rocky Mountain foreland, in V. Matthews III, ed., Laramide folding associated with basement block faulting in the western United States. Geological Society of America Memoir 151, 1–37.

Stein, S., Stein, C. A., Elling, R., Kley, J., Keller, R., Wysession, M., Rooney, T., Frederiksen, A., & Moucha, R. (2018). Insights from North America's failed Midcontinent Rift into the evolution of continental rifts and passive continental margins. Tectonophysics. 744, 403-421.

Stone, D. S. (1993). Basement-involved thrust-generated folds as seismically imaged in the subsurface of the central Rocky Mountain foreland, In Schmidt, C. J., Chase, R. B., & Erslev, E. A. eds., Laramide basement deformation in the Rocky Mountain foreland of the western United States. Geological Society of America Special Paper 280, 271–318.

Subrahmanyam, D., & Rao, P. H. (2008). Seismic attributes–A review. In 7th International Conference & Exposition on Petroleum Geophysics, Hyderabad, 398-404.

Suppe, J. (1983). Geometry and kinematics of fault-bend folding. American Journal of Science, 283, 684–721.

Thomas, J. J., Shuster, R. D., & Bickford, M. E. (1984). A terrane of 1,350-to 1,400-my-old silicic volcanic and plutonic rocks in the buried Proterozoic of the mid-continent and in the Wet Mountains, Colorado. Geological Society of America Bulletin, 95, 1150-1157.

Tindall, S.E., and Davis. G.H. 1999. Monocline development by oblique-slip fault-propagation folding: The East Kaibab monocline, Colorado Plateau, Utah. Journal of Structural Geology, 21, 1303–1320.

Turner, J. P., & Williams, G. A. (2004). Sedimentary basin inversion and intra-plate shortening. Earth-Science Reviews, 65, 277-304.

Van der Pluijm, B. A., & Catacosinos, P. A. (1996). Basement and basins of eastern North America. Geological Society of America Special Paper, 308.

Van Schmus, W. R., & Hinze, W. J. (1985). The midcontinent rift system. Annual Review of Earth and Planetary Sciences, 13, 345-383.

Wall, M., Cartwright, J., Davies, R., & McGrandle, A. (2010). 3D seismic imaging of a Tertiary Dyke Swarm in the Southern North Sea, UK. Basin Research, 22, 181-194.

Whitmeyer, S. J., & Karlstrom, K. E. (2007). Tectonic model for the Proterozoic growth of North America. Geosphere, 3, 220-259.

Widess, M. B., & Taylor, G. L. (1959). Seismic reflections from layering within the pre-Cambrian basement complex, Oklahoma. Geophysics, 24, 417-425.

Yee, D., Johnston, G., Howard, D. and Ahmed, S., 2017, September. STACKing It Up: An Economic and Geological Analysis of the STACK. In Unconventional Resources Technology Conference, Austin, Texas, 24-26 July 2017, 2496-2501. Society of Exploration Geophysicists, American Association of Petroleum Geologists, Society of Petroleum Engineers.

Yonkee, W. A. (1992). Basement-cover relations, Sevier orogenic belt, northern Utah. Geological Society of America Bulletin, 104, 280-302.

Zaleski, E., Eaton, D. W., Milkereit, B., Roberts, B., Salisbury, M., & Petrie, L., (1997). Seismic reflections from subvertical diabase dikes in an Archean terrane. Geology, 25, 707-710.

CHAPTER 4

SCALE-DEPENDENT HIERARCHICAL COMPARTMENTALIZATION AND DOMINO-STYLE SLIP ZONATION OF A GRANITIC BASEMENT FAULT

ABSTRACT

The deformation in brittle, crystalline basement is manifested by multiscale fracturing and faulting that may control intra-basement and basement-sedimentary fluid circulation, and earthquake patterns at depth. We analyze the multiscale fracture distribution associated with a brittle damage zone in the outcrops of texturally homogenous Precambrian granite basement, southern Oklahoma, U.S. We combine satellite and multi-scale resolution (0.3 cm and 2.84 cm) drone images, and field mapping, to analyze the geometries, spacing, intensity, and cross-cutting relationships of a series of the fracture systems. The mapped fractures generally display sub-vertical geometries, and tensile features such as rough surfaces, en-echelon segmentation, and a dominant trend of NE-SW (245°±0.5), with a secondary NW-SE (318°±1.7) and minor ~N-S (189°±1.5) sets. Our results reveal a ~260 m-wide, at least 3 km-long NE-trending fracture cluster zone (FCZ), within which self-organized clusters of parallel ~245°-trending fractures with the common occurrence of iron-stains, epidote- and gouge-fill, and local spring branches are most predominant. The regional distribution of fracture density and intensity within the study area show that the highest values (>7 m^{-2} and >0.25 m^{-1} respectively) are collocated with the FCZ. Fourier transform of the FCZ fracture arrays and scanline distributions of fracture spacing show prominent fracture spacing groupings of <0.1 m, 0.1 – 0.99 m, 1 – 9.99 m, and >10 m, interpreted to respectively represent Near Slip Surface (NSS), Intra-Slip Zone (ISZ), Intra-Damage Zone (IDZ), and background damage compartments of the FCZ. Core samples obtained at one of the NSS fracture spacing locations

within the FCZ reveal gouge-fill and horizontal slicken lines, suggesting strike-slip movement along the FCZ in the past. We find that the structure of the FCZ is characterized by distributed parallel slip zones (domino-style) that confine slip surfaces (fault cores), separated by damage zones of relatively moderate fracturing. We also find that the boundaries of the FCZ are defined by slip zones that show a sharp transition into relatively undeformed granite country rock (country rock). Additionally, we show that the FCZ structure and its inferred stress state are similar to those of recent injection-activated basement faults in areas nearby. We interpret that the fault damage represents the shallow extension (i.e. distal part) of an immature or buried strike-slip fault, herein named the "Mill-Creek Fault Zone". We suggest that the analyzed structural pattern of fracturing and slip zonation poses important implications for shallow basement fluid circulation and basement-hosted seismicity.

INTRODUCTION

The deformation in brittle, crystalline basement is manifested by multiscale fracturing and faulting which produce common patterns of en echelon, conjugate, Reidel, and parallel cluster array configurations (e.g., Aydin and Reches, 1982; Segall and Pollard, 1983a; Schultz, 2019). The spatial organization of fracture patterns as a genetic mechanism of deformation in crystalline rocks have become of interest in the recent scientific literature (e.g., Faulkner et al., 2003, 2008; Mitchell and Faulkner, 2009; Gabrielsen and Braathen, 2014; Wang et al., 2019). Patterns of brittle deformation are known to play important roles in subsurface fluid circulation (e.g., Henriksen and Braathen, 2006; Singh et al., 2008; Questiaux et al., 2009).

In addition, the patterns of inherited discontinuity surfaces may influence the distribution of earthquakes (e.g., Rowe et al., 2018; Kolawole et al., 2019), thus, posing important implications for seismic hazard assessment in populated areas.

The major aim of this study is to investigate the structure of a fracture cluster zone (FCZ) in the outcrops of texturally homogenous granitic basement rocks of southern Oklahoma, to better understand fault-related deformation and relevance to basement-hosted seismicity in the region and other places. Recently, large-scale increase in fluid injection in Central and Eastern United States, related to oil and gas production activities in the region, has led to a spike in earthquake occurrences (e.g., Weingarten et al., 2015). This seismicity is most sporadic and widespread in Oklahoma (Figure 27a) where the earthquakes have reactivated previously unmapped pre-existing fault zones (Figure 27b, Kolawole et al., 2019).

The largest moment release is basement-hosted (Figure 27c) and is associated with strike-slip reactivation of ancient basement-rooted faults (e.g., see focal mechanism solutions in Figure 27a).

However, the primary zone of fluid injection is the sedimentary formation that directly overlies the crystalline basement (Figure 27d). Seismic imaging of basement-rooting faults in the area of seismicity reveals a portioning of the fault structural style across the basement-sedimentary interface (Figure 27d; Kolawole et al., 2020). This structural style features a dominance of brittle deformation in the basement and near the basement-sedimentary interface (BSI), which transition upwards into faulted monoclines and monoclinally-deformed sedimentary sequences (Figure 27d). The large-scale patterns of fracturing in the exposures of this basement, southern Oklahoma, are consistent with those of recently reactivated buried basement faults further north (Kolawole et al., 2019; Qin et al., 2019). Additionally, hypothetical models of fracture-controlled fluid diffusion between the deep sedimentary injection zones and the shallow basement show strong influence on the patterns of seismicity in the basement (Haffener et al., 2018). However, the detailed fault-zone structure at the BSI, and the associated patterns of fluid migration and seismicity are not known.

In this study, we analyze the multiscale fracture distribution associated with a prominent damage zone (FCZ) in the outcrops of the seismogenic basement. Our results show that the FCZ is characterized by an organized zonation of fracturing that is represents a genetic structure of distributed fault-related deformation in granitic basement. The inferred zonation features a configuration in which a fracture spacing of <0.1 m characterizes near slip surface (NSS) regions, 0.1 – 0.99 m Intra-slip zones (IDZ), 1 – 9.99 m Intra-damage zones (IDZ), and >10 m typifies background fracturing patterns. We interpreted that the fault damage represents the shallow extension (i.e. distal part) of an immature or buried strike-slip fault, herein named the “Mill-Creek Fault Zone”. Furthermore, we showed that the FCZ structure and stress state are similar to those of recent injection-activated basement faults in areas nearby. Finally, we suggest that the analyzed

structural pattern of fracturing and slip zonation poses important implications for shallow basement fluid circulation and basement-hosted seismicity.

Geological Setting

Our study area is the former Off-Road Park, located in the Mill Creek area of Johnston County, southern Oklahoma, United States (Figures 27a and 28b-c). Johnston County (Figure 28a) hosts the largest exposure of the Precambrian granitic basement in the region. The granitic rocks are a part of the Precambrian Granite-Rhyolite Provinces of Central U.S. which were emplaced during the Mesoproterozoic (1.50–1.34 Ga) accretion of the US Mid-continent (Bickford et al., 2015). The granitic rocks intruded a Paleoproterozoic terrane known as the Mazatzal Province (Whitmeyer and Karlstrom, 2007). The granitic intrusions of the granite-rhyolite province are generally unmetamorphosed (Bickford et al., 2015). In the Mill Creek area (Figure 28a), the granitic rocks are comprised of different ages of intrusive masses, consisting of the Burch Granodiorite (1390±7 Ma) as the oldest, followed by the Blue River Granite (1389±10 Ma), the Troy Granite (1368±3 Ma), and the Tishomingo Granite (1363±8 Ma). In the Late Proterozoic, these rocks were intruded by a complex of diabase dikes and sills that were emplaced in pre-existing fracture systems (Denison, 1995; Lidiak et al., 2014). The fracture systems in the granitic rocks dominantly trend NE-SW and NW-SE, with a minor overprint of a N-S -trending set, representing a structural fabric that extends across the region (Kolawole et al., 2019).

DATA & METHODS

Surface exposures of the granitic basement within the study area allow for the characterization of the spatial distribution of the brittle deformation in the rocks. It has been demonstrated that the combination of various data types with different imaging resolutions is most suitable for a reliable estimation of stable fractal dimensions of fracture distribution (Ehlen, 2000). Therefore, in this study, we employ a multi-scale approach which includes the integration of satellite images and drone images with detailed field mapping.

Satellite-scale Fracture Characterization

We utilize Google Earth© satellite images to map the satellite-sale fracture segments within the study area (Figure 28b), within which the satellite image is made up of a combination of Landsat and Copernicus satellite images, supplemented by aerial images. The resulting satellite image has a spatial resolution of ~50 cm. We manually digitize the observable penetrative (non-exfoliation related) fracture and obtain scanlines of the fracture distribution at selected locations.

Drone-scale Fracture Characterization

To obtain a higher resolution of the brittle deformation in the granite exposures with a coverage that is as wide as that of the satellite images, we performed a multi-resolution drone imaging of the study area. The acquired drone images consist of a wider coverage (~2 km^2) Tough Wing image covering the entire study area, and multiple smaller-coverage DJI Phantom drone images acquired at selected representative fracture zones within the area. The Tough Wing drone, flown

at 40 m ground clearance, produced an orthomosaic with a spatial resolution (ground sample distance) of 2.84 cm (Figure 28b). The Phantom images covering three selected locations (~800 m^2 each) have spatial resolutions (ground sample distances) that range between 0.23 cm and 0.31 cm (Figures 28c-e). The drone datasets were acquired and processed by the Center for Autonomous Sensing and Sampling (CASS), National Weather Center, University of Oklahoma. Similar to the analysis of the satellite image, we manually digitize the penetrative fractures observable in the drone images and obtain scanlines of the fracture distribution at the selected locations.

Outcrop-scale Fracture Characterization

We obtain scanlines of fracture distribution across the outcrops of selected fracture zones within the study area. The selected locations include the southeastern boundary, northwestern boundary, and the southwestern part of a ~260 m-wide fracture cluster zone (FCZ, Figures 29a, 29b, and 29c). The scanline of the southeastern boundary of the FCZ is 227 m-long, that of the northwestern boundary is 85 m-long, and that of the southern part of the FCZ is ~13 m-long.

Quantification of Fracture Pattern and Reactivation Tendency

We utilize the FracPaQ© MATLAB^{TM} -based program (Healy et al., 2017) to analyze the drone fracture maps and quantify the spatial distribution of areal fracture density (P_{20}) and intensity (P_{21}) (Dershowitz and Herda, 1992), and fracture strike (Figure 29c). The areal fracture density (P_{20}, m^{-2}) is expressed as the number of fractures within a scan window per unit area of the window (Figures 30a and 30b). However, in areas of limited outcrops such as our study area, fracture density is less useful as it is related to presence of exposures and their quality. The areal fracture

intensity (P_{21}, m^{-1}) is expressed as the total length of fractures within a scan window per unit area of the window (Figures 30c and 30d). Here, for both the areal density and intensity calculations, a circular scan window is used, with a specified diameter of 50 m (Figure 30a). We choose this window size based on the consideration of the overall average width of outcrops and drone-scale fracture clusters within the entire ~2 km^2 study area, and the computation run time required for the analysis.

Furthermore, we assess the reactivation tendencies of the mapped fracture sets within the current regional Oklahoma stress field. To estimate this, using the FracPaQ program, we calculate the estimates of Normalized Slip Tendency (T_s, Morris et al., 1996) and Dilation Tendency (T_d, Ferrill et al., 1999) for the fracture cluster sets. For these estimates, we use 2-D stress field configuration of $\sigma1$ = 155.41 MPa, $\sigma3$ = 155.41 MPa, and θ ($\sigma1$ orientation at 5-6 km depth) = 85° (Walsh and Zoback, 2016; Alt and Zoback, 2017).

Fourier Analysis of Fracture Scanline Data

We utilize classic 1-D discrete Fourier analysis of the fracture arrays mapped along the scanlines to identify the dominant spatial wavelengths of fracture clustering (dominant fracture spacing) within the FCZ fracture arrays. More specifically, we perform the analysis on the distribution of fracture locations along a scanline. Since the field outcrop scanline has the most measurements compared to the collocated scanlines obtained from the satellite and drone fracture maps, we perform the Fourier analysis on the field outcrop scanline data. The 1-D discrete Fourier transform (X) of vector (x) is expressed as:

$$X(k) = \sum_{j=1}^{n} \mathrm{x}(j)\, W_n^{(j-1)(k-1)}$$

Where *k* is the spatial frequency index, *j* is spatial index, x is the spatial vector representing fracture distribution along the scanline, n is the total number of elements in x, and *W* is the Fourier kernel, defined as:

$$W_n = e^{(-2\pi i)/n}$$

RESULTS

General Characteristics of the Mapped Fractures

From the satellite image of the study area, we map a total of 384 fracture traces (Figure 29a), consisting of 411 fracture segments. Whereas, in the drone images we map a total of 2,048 fracture traces (Figure 29a), consisting of 5,881 segments (Figure 29b). Overall, our observations in the field show that the fractures generally display tensile features such as rough surfaces, en-echelon segmentation, and sub-vertical geometries (e.g., Figures 31a-d). Mafic and felsic igneous dikes in the outcrops show sharp contacts that trend parallel to nearby open fractures (e.g. Figure 31e). In places where the dikes have been offset by non-colinear open fractures, the offsets are generally <10 cm (e.g., Figure 31f).

Dominant Fracture Trends, Spatial Clustering, and Distribution of Fracture Alteration

The frequency-azimuth distribution of the mapped drone fractures shows a dominant trend of NE-SW (245°±0.5), with a secondary NW-SE (318°±1.7) and minor ~N-S (189°±1.5) sets (Figures 29a-b). Although these fracture sets are present in most of the outcrops, the map of fracture strike

(Figure 29c) shows that the most dominant trend (~245°) is most abundant within a ~260 m-wide NE-trending fracture cluster zone (FCZ). The regional distribution of fracture density within the area (Figures 30a-b) show that the peak fracture density (>7 m^{-2}) is collocated with the FCZ. Similarly, the highest fracture intensity values (>0.25 m^{-1}) are located within the FCZ (Figures 30c-d).

Field observation of fracturing near the southeastern boundary of the FCZ show systematic sets of highly dense, self-organized clusters of ~245°-trending fractures that transition abruptly into relatively undeformed granitic rocks (Figures 32a-d). This boundary zone is characterized by a narrow linear valley surface morphology within which a spring point feeds a spring branch which itself is locally controlled by the fracture clusters (Figures 32b-c). Also, segments of the fractures show infilling with pulverized material, herein referred to as "gouge zones" (Figure 32d). Core samples of some of the gouge zones reveal horizontal slicken lines on polished gouge-coated fracture surfaces (Figure 32e). Also, we observe the occurrence of epidote veins and iron-stains along fracture clusters, more commonly at or near the southeastern boundary of the FCZ (e.g., Figures 32f-5h).

Similarly, the northwestern boundary of the FCZ is characterized by a sharp transition from dense fracture clusters to relatively undeformed granite (Figures 33a-e). Although the NW boundary zone is also characterized by a linear narrow valley (Figure 33b-c) as observed along the SE boundary zone, we observe the pervasiveness of a set of cross-fractures that are bounded by the NE-trending dominant fracture set (Figure 33c). These cross-fractures exhibit sigmoid-shaped geometry which produces rhomb-shaped granite blocks within the fractured zone (Figures 33d-e).

Field observations in the southwestern (Figures 34a-d) and northeastern extensions of the FCZ (Figures 34e-g) show common occurrence dense clustering of parallel NE-trending sub-vertical fractures, gouge-zones, and fracture-controlled spring points and streamflow. In the southern part of the FCZ, we observe the occurrence of 270°-striking fracture sets that form Reidel patterns with the dominant ~240° clusters (Figure 34c). A closer observation shows gouge zones along a 240°-striking fracture and the associated obliquely-trending wedge-shaped cavities (Figure 34d). Furthermore, to delineate the overall length of the FCZ, we follow the fracture clusters along strike, beyond the bounds of the study area. Sparseness of outcrops to the southwest of the study area limits our estimation of the southwestern extent of the FCZ. However, we are able to trace the continuation of the fracture clusters for an additional ~1.2 km NE of the study area, resulting in a total subaerial length of at 3 km for the FCZ.

Representative Fourier Analysis of Fracture Clustering within the Fracture Cluster Zone (FCZ)

The Fourier analysis of the outcrop scanline fracture spacing data (Figures 35a-b) shows distinct spatial frequency peaks with corresponding wavelengths that generally range between 10^{-2} and 10^{1} m (Figure 35c). These wavelength groupings represent categories of fracture clustering within the FCZ. Thus, we herein refer to each of the clustering categories as Near Slip Surface (NSS, <0.1 m), Intra-Slip Zone (ISZ, 0.10 – 0.99 m), Intra-Damage Zone (IDZ, 1.0 – 9.99 m), and Background (undeformed wall rocks, >10 m).

Fracture Spacing

Southeastern Boundary of the FCZ

The distribution of fracture spacing along the satellite-scale scanline shows fracture clusters within the FCZ that exhibit 2.0 - 2.49 m average spacing, which transition sharply into < 10 m across the southeastern boundary of the FCZ (Figure 36a). The fractures dominantly trend 240° – 260° (lower panel of Figure 36a). Based on the categories revealed in the Fourier transform of the FCZ fracture array (Figure 35c), the deformation of the FCZ detectable in the satellite-scale data is limited to the IDZ and background signatures of fracturing. Whereas, the Drone-scale scanline (Figure 36b) shows clusters within the FCZ with average spacings as low as 0.17 to 0.23 m (ISZ), a cluster between 1m and ~7 m (IDZ), and others >10 m (background). The region of most intense fracture clustering in the FCZ is collocated with a spring branch (Figures 36a and 36b). We also observe the occurrence of N-S fractures within this zone of most intense clustering.

Further, the outcrop-scale scanline (Figure 37a) shows more clusters of fracturing within the FCZ with values ranging between 0.06 m (NSS) and 0.35 m (ISZ), which transition abruptly into 1 – 10 m (IDZ) fracture spacings, and subsequently into >10 m (background) fracture spacing values. Similar to the drone and satellite data, the spring branch is collocated with the location of the most intense clustering, and the occurrence of N-S fractures (Figure 37a). Furthermore, we observe the pervasive occurrence of iron-stains along an ISZ (0.15 m average spacing) fracture cluster within the FCZ (Figure 32g).

In addition to outcrop-scanline, we obtain a shorter, but more detailed scanline (damage zone-scale scanline) focused on the region of most intense fracture clustering near the southeastern FCZ boundary (Figure 37b, 37c, and 37d). This scanline reveals a pervasive occurrence of isolated fracture clusters with <0.1 m average fracture spacing, corresponding to NSS clustering (Figure 37d). The NSS clusters are associated with gouge zones along strike (Figure 37b and 37d). We note that the annotated gouge zones in the scanline photograph (Figure 37b) as the same points at

which core samples show horizontal slicken lines (Figures 32d-e). Interestingly, all the fracture spacing values are less than 10 m, indicating the absence of background fracturing within the damage of the FCZ. The photograph and interpretation of the damage zone-scanline (Figures 37b-c) show the occurrence of N-S trending cross-fractures that terminate at and are bounded by the ~240°-trending clusters.

Northwestern Boundary of the FCZ

Although the satellite- and drone-scale scanlines have fewer data points compared to those of the SE FCZ boundary, the measurements show a clear sharp transition from 1.76 m average fracture spacing values (IDZ) within the FCZ, to background values in the relatively undeformed granitic basement (Figure 38a). However, the outcrop-scale scanline (Figure 38b) reveals the presence of at least three fracture clusters within the FCZ with average fracture spacing that range between 0.07 (NSS) and 0.12 m (ISZ) clustering patterns. The delineated ISZ fracture cluster is associated with iron-stained fracture segments (Figure 38b). Furthermore, we observe that although the fractures within the FCZ dominantly trend ~240°, near the NW FCZ boundary ~300° fracture trends are abundant, consistent with observations in the outcrops (Figures 33b-c). Also, we note the occurrence of an isolated fracture cluster zone (0.02 m average spacing) within the relatively undeformed granite wall rocks farther northwest of the northwestern FCZ boundary (Figure 38b).

Southwestern Extension of the FCZ

In the southwestern parts of the FCZ, both the satellite- and drone-scale scanlines show fracture spacings that occur primarily in the 1 – 10 m range (1.13 m average spacing), indicating Intra-damage Zone (IDZ) patterns (Figure 39a). The outcrop-scale scanline further reveals multiple

isolated clusters of 0.02 (NSS) to 0.06 m (ISZ) average fracture spacings (Figure 39b). The fractures dominantly strike ~240° with the rare occurrence of iron-stained segments (Figure 39b). We note that similar to the satellite- and drone-scale scanlines, the outcrop-scanline does not show any fracture spacing that corresponds to background signature.

Normalized Slip and Dilation Tendencies of the Fracture Trends

Our results show that the most dominant 210 - 250° -trending fracture sets, and the secondary 280 - 320° sets in the study area show the highest slip tendencies (0.85 – 1), whereas the minor ~N-S trending set shows the lowest slip tendencies (Figures 40a-b). In summary, the most prominent fracture populations in the area are well oriented for shear reactivation in the current stress field of Oklahoma. The 240 - 290° fracture orientations show the highest dilation tendencies (0.85 – 1), whereas the NW-trend show very low values (<0.4) and the ~N-S and NNW-trending fractures show the least dilation tendencies (<0.1).

DISCUSSION

Structure of the Analyzed Fracture Cluster Zone (FCZ)

Kinematics of the Deformation

We observe that the density and intensity of the regional fracture distribution are much higher in the FCZ compared to its relatively undeformed flanking granitic rocks (Figures 30a-d). Although the dominant fracture trends within the FCZ is NE-SW (Figures 29c and 30b), regional distribution of fracture strike shows that the FCZ hosts the most abundant concentration of other fracture trends (Figure 30b). The regional localization of fracture density along the FCZ is consistent with published observations along fault zones where the density of microscale and mesoscale fracturing

increases from the flanking country rock into the fault zone (e.g., Faulkner et al., 2003, 2008; Mitchell and Faulkner, 2009). In addition, the presence of epidote veins and iron stains along the FCZ fracture clusters (e.g., Figures 32f -h) suggests that the FCZ is, in fact, a deep-reaching structure that was permeable to the circulation of crustal fluids in the past. The control of the FCZ on the locations of spring points and flow trends of their spring branches (Figures 32c, 34a, and 34e-f), and the structural control on the NE-trending segment of the Rock Creek (e.g., Figure 29a) indicate the present-day permeability of the FCZ to fluid flow in the shallow basement.

The homogenous texture of granitic rocks makes it challenging to find reliable offset markers for kinematic interpretations. Although several of the fracture segments within the FCZ only exhibit tensile (opening mode) characteristics, the occurrence of shear indicators in the form of slickensides and chatter marks (Figures 32d-e, 34b ad 34d) provide additional insight into the kinematics of deformation along the FCZ. The collocation of gouge zones and slicken lines along well-developed fracture surfaces at the locations of most intense fracture clustering (Figures 32d, 32e, and 37b-d) indicate that the FCZ has experienced strike-slip movement(s) in the past. These past strike-slip events are accommodated along distinct isolated parallel surfaces. Consistent with Mohr-Coulomb criterion of faulting, the sub-vertical dips of the FCZ fractures (e.g., Figures 32e, 34b, and 34g) are compatible with strike-slip kinematics (e.g., Sibson, 1985; Schultz, 2019).

Furthermore, we observe the presence of subsidiary obliquely oriented tail- and cross-fracturing in different parts of the FCZ. At both the boundary and internal areas of the FCZ, we observe ~E-W (Figures 34c-d), NW-SE (Figures 33b-c), and ~N-S (Figures 33b-c, 37b-c) trending subsidiary fracture sets. These sets are commonly bounded by the dominant NE-trending clusters (e.g., Figures 37b-c). In other places, the cross-fractures are also cross-cut by the NE-trending clusters (e.g., Figure 34c). A holistic assessment of these subsidiary trends with respect to the 245° (±0.5)

may be interpreted to represent Reidel pattern in some places, and conjugate patterns in others; both configurations suggesting a strike-slip shear system. The northwestern boundary of the FCZ (Figure 33a-e) shows an excellent cross-fracture pattern bounded by distinct segments of the NE-trending FCZ fractures. The development of NW-trending sigmoidal fracture geometries bounding rhomb-shaped granite blocks between the major NE-trending fracture surfaces (Figure 33d-e) suggest strike-slip shear deformation with associated rigid body block rotations. Following the convention of Schultz and Balasco (2003) and Schultz (2019), the sigmoidal fractures are passive shear markers whose backward-breaking geometries suggest right-lateral shear on the bounding parallel NE-trending FCZ fractures. The kinematics imply a counterclockwise rotation of the fault-bounded blocks. This structure is characteristic of domino-style strike-slip faults along which displacement is distributed on multiple parallel slip surfaces (Nixon et al., 2011).

In addition, the development of right-stepping pull-apart structure on an ~E-W-trending fracture and right-splaying tail fractures on a NE-trending fracture near the southeastern boundary of the FCZ (Figures 41a-b) are consistent with the inferred right-lateral kinematics of the FCZ. Based on the structural observations and analyses above, we hereby name the analyzed FCZ deformation zone “Mill-Creek Fault Zone”.

Hierarchic Structural Zonation of Fracture Compartments and Slip Surfaces

The distinct clustering of fractures within the Mill-Creek Fault Zone demonstrates the hierarchical compartmentalization of the deformation in the texturally homogenous granitic basement rocks (e.g., Figures 35 to 42). We show that the fault zone has a large-scale average fracture spacing (1 - 10 m) that can be described as indicative of fault damage. This Intra-damage (IDZ) fracturing may be detected by low-resolution remote sensing (>50 cm spatial resolution, e.g., satellite

images). The relatively undeformed host rock is characterized by a fracture spacing >10 m (background).

However, within the fault zone, the distribution of parallel slip zones with associated slip surfaces produces other distinct fracturing patterns that may only be detectable on high resolution (<1 cm resolution) imaging (Figure 42). One of such patterns is the Intra-Slip Zone fracturing (ISZ , 0.1 – 1 m fracture spacing) which is characteristic of areas within which at least one slip surface is located, and areas between two closely spaced slip surfaces (e.g., Figures 37b-d). Furthermore, we find a tighter cluster pattern that commonly occurs at the local vicinity of the slip surfaces (near Slip Surface, NSS) with fracture spacing <0.1 m. Thus, the detection of NSS fracture spacing patterns may suggest the proximity to a slip surface. The distribution of estimated imaging resolution with the observed ranges of fracture spacing for each of the scales (outcrop, drone, and satellite) of fracture imaging used in this study (Figure 42) shows a logarithmic trend. The fitting curve and vertical max-min bars show that the drone imaging technique is comparable to the traditional outcrop fracture mapping techniques.

Across the Mill-Creek Fault Zone, we do not observe the typical configuration of deformation that is characteristic of well-developed fault zones (Figures 43a and 43b, e.g., Caine et al., 1996; Mitchell and Faulkner, 2009). What we observe is a ~260 m-wide zone of parallel fracture clustering that is bounded by to by narrow slip zones that transition sharply into the background fracturing (>10 m fracture spacing). Although it is possible that an intermediate zone of damage may exist at the micro-scale, outboard of the inferred local boundaries of the Mill-Creek Fault Zone (Mitchell and Faulkner, 2009). Nevertheless, we suggest that the intense clustering of tensile fractures (NSS fracturing) at the proximity of shear surfaces indicates an increase in strain from the intra-damage zone (IDZ) areas into the core of the slip zones where the slip surfaces are located

(Figure 43c). Essentially, the structure can be attributed to fracture saturation leading to shear localization as the rock progressively accommodates strain. This occurs in a more coherent form within well-developed fault zones (i.e. increase in fracture intensity and density towards the fault core e.g., Childs et al., 2009, Lindanger et al., 2007).

Overall, the distributed slip zonation of the Mill-Creek Fault Zone generally represents a multi-stranded slip fault zone structure, however, the fault zone does not exhibit anastomosing slip zone (or surface) pattern typical of the conventional models of distributed (multi-strand) slip fault zones (Mitchell and Faulkner, 2009; Rowe et al., 2018; e.g., Figure 43b). Rather, the Mill-Creek Fault Zone is characterized by arrays of sub-vertical parallel slip zones containing the slip surfaces (Figure 43c).

Gabrielsen and Braathen (2014) analyzed fracture clusters in outcrops of crystalline basement rocks within an area of tectonic extension. The authors identified that unlike the nearby well-developed fault zones, the structure of the damage lacks the presence of a fault core, and demonstrated that fracture cluster zones essentially represent the distal portions of a deeper immature fault zone, such that with progressive strain accommodation, the fracture cluster will temporally transgress into the classic core-damage zone-country rock fault structure. Therefore, we interpret that the analyzed deformation of the Mill-Creek Fault Zone represents the shallow extension (i.e. distal part) of an immature or buried strike-slip fault. Furthermore, consistent with our observations in this study, Gabrielsen and Braathen (2014) also identified that the zonation of damage within the fracture cluster zones are detectable in fracture intensity measurements. Here, we go further to demonstrate how the fracture cluster zonation is related, not just to the resolution of the imaging technique, but the structural architecture of the fault-related deformation zone (Figure 42).

The consideration of the mechanical development of the sub-parallel pattern of fracture arrays associated with the Mill Creek Fault Zone (pervasive tensile fractures with rare shear fractures) presents interesting complexities. In the context of previous studies, the pattern may appear to be consistent a temporal change in the stress field, following inferences made on fracture arrays of similar patterns in the Sierra Nevada granodiorite outcrops (Segall and Pollard, 1983a). An earlier stress field condition that favored development of joint (tensile fracture) clusters in the basement rocks such that multiple long joints initially nucleates, and the elastic interactions between the joints allows for the growth and early stagnation of shorter joints in the area in between the joints controlled by the larger crack extension force of the longer joints (Segall and Pollard, 1983b). At a later time, the rotation of regional stresses into an orientation that is oblique to the pre-existing tensile fracture clusters could begin to selectively reactivate the tensile fractures in shear mode (Segall and Pollard, 1983a). However, a problem with this mechanism is the increased tensile fracture clustering adjacent to the slip surfaces (Near Slip-Surface clustering) which suggests either 1.) an initial emplacement of parallel tensile fracture clusters in which there exists localized zones of intense fracture saturation within which slip localizes at a later time when the stress field rotates, or 2.) a contemporaneous shear kinematics on the slip surfaces with the local saturation of tensile fracturing in the vicinity of the slip surfaces. However, we recommend further investigation (experimental and modelling studies) into the mechanisms of brittle deformation that allow for the observed fracture patterns.

Implications for Fluid Flow Along Basement Faults with Distributed Slip Patterns

Here, we observe the hierarchical clustering of parallel planar fractures within a strike-slip deformation field in the granitic basement. Deformation associated with fracture clusters has been

observed in sedimentary formations where it influences the permeability of groundwater aquifers and hydrocarbon reservoirs (e.g., Henriksen and Braathen, 2006; Singh et al., 2008; Questiaux et al., 2009). Similarly, systematic clustering of parallel tensile fractures has been highlighted to pose important implications for fluid flow in crystalline basement rocks (e.g., Wang et al., 2019). Thus, the hierarchical arrangement of fracturing and the associated zonation of slip surfaces presented in our analysis present possibilities for fluid flow and fluid sealing in the shallow parts of the crystalline basement, near the basement-sedimentary interface (BSI in Figure 27d).

Storti et al. (2003) showed that the permeability structure of mature fault zones is quite distinct from that of the immature fault segments, thus influencing the 4-D evolution of permeability structure along an evolving fault zone. Immature fault zones are typically characterized by a country rock-to-damage zone-to-country rock structure, such that the low strain rates and absence of a well-developed core allow for great efficiency of fluid circulation. Whereas, for mature faults, the development of a core that is flanked by damage zones presents a lower efficiency of fluid circulation due to the high comminution of materials at the fault core, such that the core represents a barrier to fluid flow separating highly permeable damage zones (Caine et al., 1996).

Therefore, similar to the permeability structure of distributed slip fault zones with anastomosing slip zone strands (Faulkner et al., 2003), we are able to speculate on that of the Mill-Creek Fault. The parallel strands of slip zones along the Mill-Creek Fault present a case whereby the higher efficiency of fluid flow is confined to the areas between the slip zones, such that the near slip surface (NSS) regions will exhibit the highest efficiency of fault-parallel fluid flow due to its tightest clustering of fracture segments. The presence of comminution material (gouge) along the slip surfaces suggest a low potential for fault-perpendicular fluid circulation, with the exception of

a few areas where cross-fracturing occur along the fracture cluster zones (e.g., Figures 37b-c and 33b-c).

It is well known that the ambient in-situ stress field is one of the factors that determine the fluid conducting capacity of a fracture system (e.g., Henriksen and Braathen, 2005). However, in the present-day regional stress field of Oklahoma, the high dilation tendency and sparseness of mineralization fill of the Mill-Creek fracture clusters (Figures 40c-d) suggests that the fractures may currently be in opening-mode and have high hydraulic conductivity. This inference may also be supported by the observation of spring points within the fracture cluster zone (e.g., Figures 32c and 34e-f).

Implications for Basement-Hosted Seismicity

Our analysis of dilation and slip tendencies in Figures 40a-d shows that the Mill-Creek Fault Zone is critically oriented for displacement reactivation in both opening mode (Mode-I) and strike-slip shear (Mode-II). This observation indicates a similarity between the inferred stress state of the Mill-Creek Fault Zone and the estimated stress state of recently reactivated buried basement faults further north in central Oklahoma (Figures 27a and 27b). The lineament clusters of the buried seismogenic faults in central Oklahoma show dominant trends of NE-SW (239° ±2.9) and NW-SE (297° ±3.6) (Kolawole et al., 2019). Of these two trends, the NE component show marked consistency with the mean strike of the Mill-Creek Fault Zone fracture clusters (Figures 29b and 29c). Furthermore, the width of the Mill-Creek Fault Zone is consistent with the range of widths of major earthquake clusters that ruptured the shallower extents of basement faults in central Oklahoma (Mw5.7 Prague and Mw4.1 - 4.3 Woodward earthquake sequences; Figures 44a-c).

Additionally, the Mill-Creek Fault Zone width is within the range of widths of the pre-existing basement-rooted fault zones mapped in 3-D seismic reflection dataset (Liao et al., 2017, 2019).

We identify two other zones of fracture clustering in the study area with facture patterns that look similar to that of the Mill-Creek Fault Zone ("NE-trending and NW-trending isolated clusters" in Figure 29b). On a regional-scale, these isolated clusters make a fault-mesh pattern with the Mill-Creek Fault Zone. This mesh pattern is similar to the fault structure delineated by the Guthrie seismicity cluster in central Oklahoma as demonstrated by the analysis of Chen et al. (2018).

Furthermore, we assess the stress states of the well-known basement-rooting strike-slip faults in Oklahoma (Figures 44d-f), and we observe that among these faults, those trending NE and WNW are critically-oriented to the regional stress field and have been seismically-active in recent times. These set of structural trends show the highest slip tendencies in the current stress field (Figure 44f). These seismically-active faults and several other faults in the region (Figure 1a) are being reactivated by pore-pressure perturbations related to fluid injection into the deep sedimentary units (e.g., Keranen et al., 2013; Qin et al., 2018; Chen et al., 2018). A comparison of the first-order geometry and stress conditions on these faults with those of the Mill-Creek Fault Zone fractures (Figures 40a-b and 44f) shows consistency. Therefore, we suggest that the configuration of deformation within the fault zone presents important implications for buried basement fault zones of similar structure in the areas of induced seismicity in central Oklahoma (Figure 27a). More specifically, we suggest that the Mill-Creek Fault Zone represents an outcrop analog for the shallow extensions of the buried seismically-active basement faults that reach the basement-sedimentary interface (e.g., Figure 44g).

Thus, the analyzed fracture networks and structure of the Mill-Creek Fault Zone may be relevant for understanding basement-sedimentary fluid flow pathways leading to basement-hosted

seismicity. We suggest that wastewater injection into the deep sedimentary units in the vicinity of such faults may result in a multi-strand linear pattern of fluid channeling and focusing into the deeper basement sections of the faults. The basement rock composition and depth-distribution of temperature and pressure promote velocity-strengthening conditions near the basement-sedimentary interface where the injected fluids migrate into the basement faults (Kolawole et al., 2019). Also, it has been shown that accelerated fluid pressures and the associated dilation tendencies in the local region of high rate fluid injection promote strengthening behaviors, leading to aseismic reactivation of faults (Cappa et al., 2019; Eyre et al., 2019). The possible linear channelized pattern of fluid flow-focusing across the basement-sedimentary interface poses direct implications for local pressure distribution along the shallow extents of the fault zones, thus potentially influencing the evolution of aseismic reactivation of the basement-rooting faults. Fault creep (aseismic slip) is typically manifested in the form of low-frequency seismicity (e.g., Frank and Brodsky, 2019). Thus, for future studies, first, we recommend detailed seismological investigations into the influence of the fault permeability structure on the patterns of seismic and aseismic reactivation of the basement-rooting faults.

The induced seismicity of central Oklahoma inherited the fracture networks along the reactivated pre-existing basement faults. It has been shown that in areas of prolonged induced seismicity (such as the north-central Oklahoma), seismic rupture often continue within previously activated fault patches as new patches become activated (Schoenball and Ellsworth, 2017; Qin et al., 2018). The repeated shear and dilation reactivation of the fractures may lead to changes in the fault zone-fracture network typically represented by the linkage and flushing of the fractures (i.e. permeability enhancement; Zhang et al., 2017). Therefore, we further suggest that future studies should investigate the coupling and feedback mechanisms (in spatio-temporal scales) between the

interactions of inherited basement fault structure and persistent fluid injection-induced basement seismicity.

CONCLUSIONS

In this study, we analyzed the multiscale fracture distribution associated with a brittle damage zone (FCZ) in the outcrops of texturally homogenous Precambrian granite basement, southern Oklahoma. On a regional scale, compared to its bounding areas, the FCZ is hosts the highest fracture density and intensity, and localization of gouge-filled, iron-stained, and epidote-veined fractures. We showed that the FCZ is characterized by a zonation of fracturing that represents a genetic structure of the damage zone. The inferred zonation features a configuration in which a fracture spacing of <0.1 m characterizes near slip surface (NSS) regions, 0.1 – 0.99 m Intra-slip zones (IDZ), 1 – 9.99 m Intra-damage zones (IDZ), and >10 m typifies background fracturing patterns. We interpreted that the fault damage represents the shallow extension (i.e. distal part) of an immature or buried strike-slip fault, herein named the "Mill-Creek Fault Zone". Furthermore, we showed that the FCZ structure and stress state are similar to those of recent injection-activated basement faults in areas nearby. Finally, we suggest that the analyzed structural pattern of fracturing and slip zonation poses important implications for shallow basement fluid circulation and basement-hosted seismicity. We recommend further investigation (experimental and modelling studies) into the mechanism(s) of brittle deformation that allows for the observed fracture patterns.

Contributors to this project: F. Kolawole, Z. Reches, D. Dangwal, and B. M. Carpenter.

Acknowledgements: Thanks to the Center for Autonomous Sensing and Sampling (CASS), National Weather Center, University of Oklahoma, for assisting with the acquisition and processing of the drone datasets analyzed in the study. This project is supported by Geological Society of America (GSA) Graduate Student Research Grant #11968-18 awarded to Folarin Kolawole. Thanks also to Connor Mears, Max Firkins, Will Kibikas, and Brittany Stroud for help in making some of the field observations.

CHAPTER 4 FIGURES:

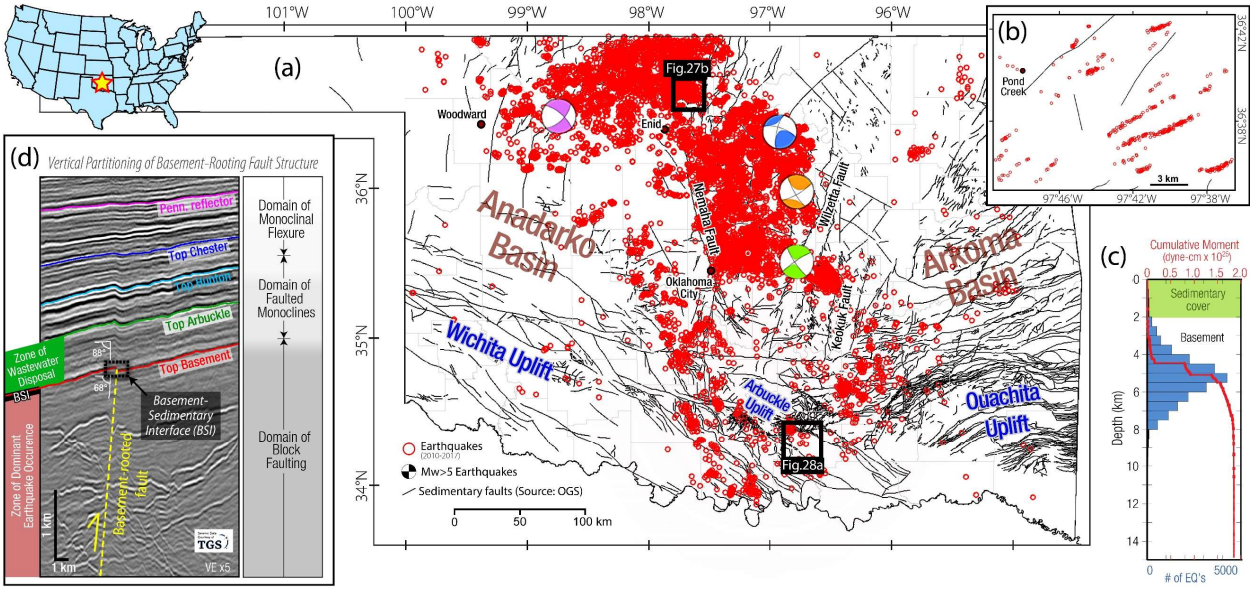

Figure 27. (a) Fault map of Oklahoma overlaid with relocated 2010 – 2017 earthquake epicenters (source: Oklahoma Geological Survey earthquake catalog). Beach balls represent Mw>5 earthquakes (Source: US Geological Survey earthquake catalog). (b) Zoomed-in map showing an example of the commonly observed discrepancies between known faults and relocated earthquakes in Oklahoma. (c) Hypocenter depth vs number of earthquakes and cumulative seismic moment for all the earthquakes in Figure 27a. (d) Depth-section of seismic reflection data from north-central Oklahoma (Kolawole et al., 2020), showing the vertical partitioning of structural styles along the basement-rooted faults in the Anadarko Basin. Also, the figure highlights the main interval of wastewater injection (Arbuckle Formation), the zone of dominant seismicity (crystalline basement; see Figure 27c), and the basement-sedimentary interface (BSI) separating the two domains.

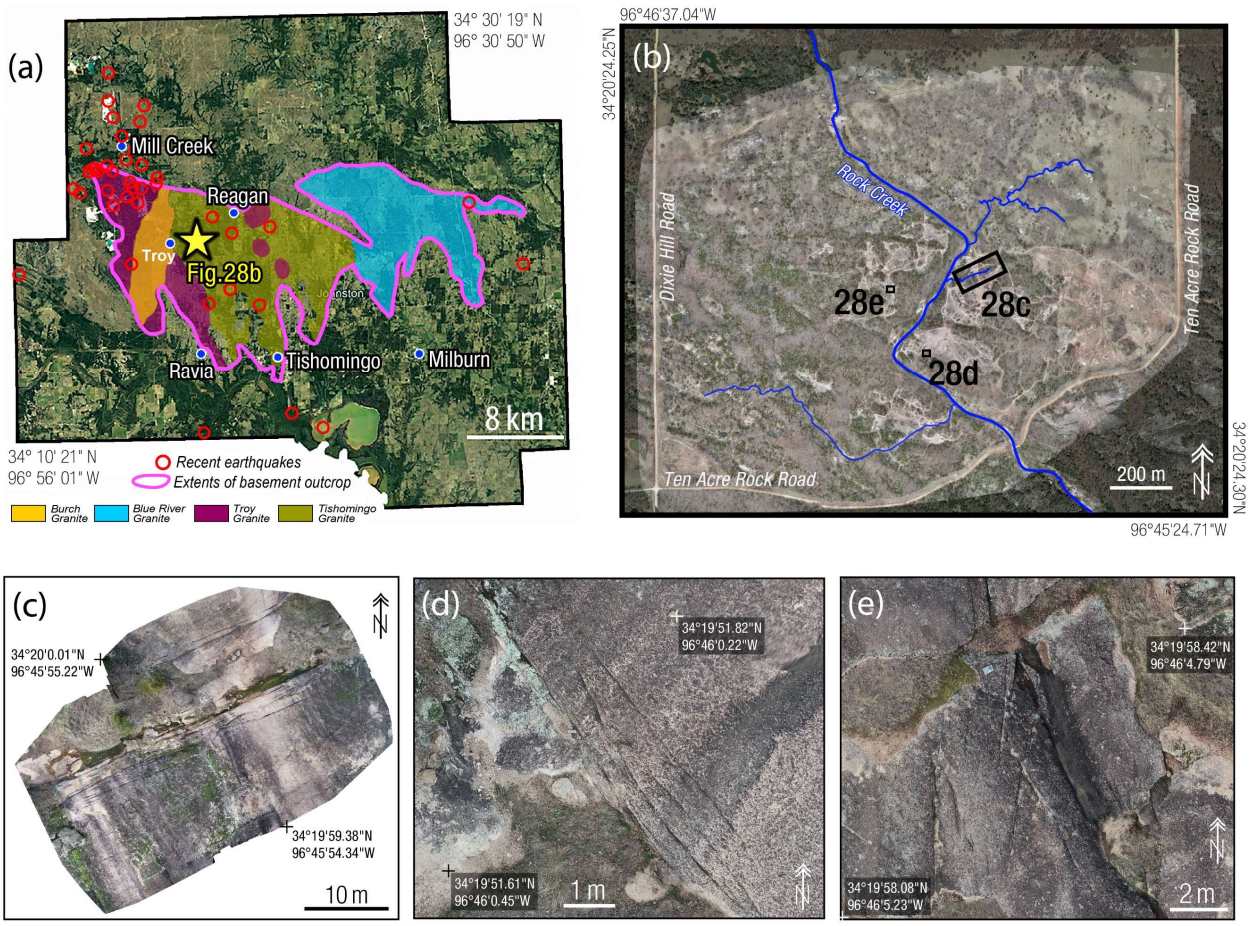

Figure 28. The Exposed Granitic Basement of Southern Oklahoma. (a) Google Earth© satellite image of the Johnston County, southern Oklahoma, showing the 300 km^2 area of Precambrian granite basement exposures (see location in Figure 27a) (modified after Lidiak et al., 2014). Yellow star = study area (location of Figure 28b). (b) Wide coverage drone image (2.84 cm spatial resolution) of the study area, overlaid on Google Earth© satellite image. (c - e) Smaller-scale drone images (0.23 cm for 28c, 0.31 cm for 28d, and 0.30 cm for 28e) of granite outcrops within the study area, showing clusters of fracture sets (2c and 2d) and the intersection zone of the fracture sets (Figure 28e).

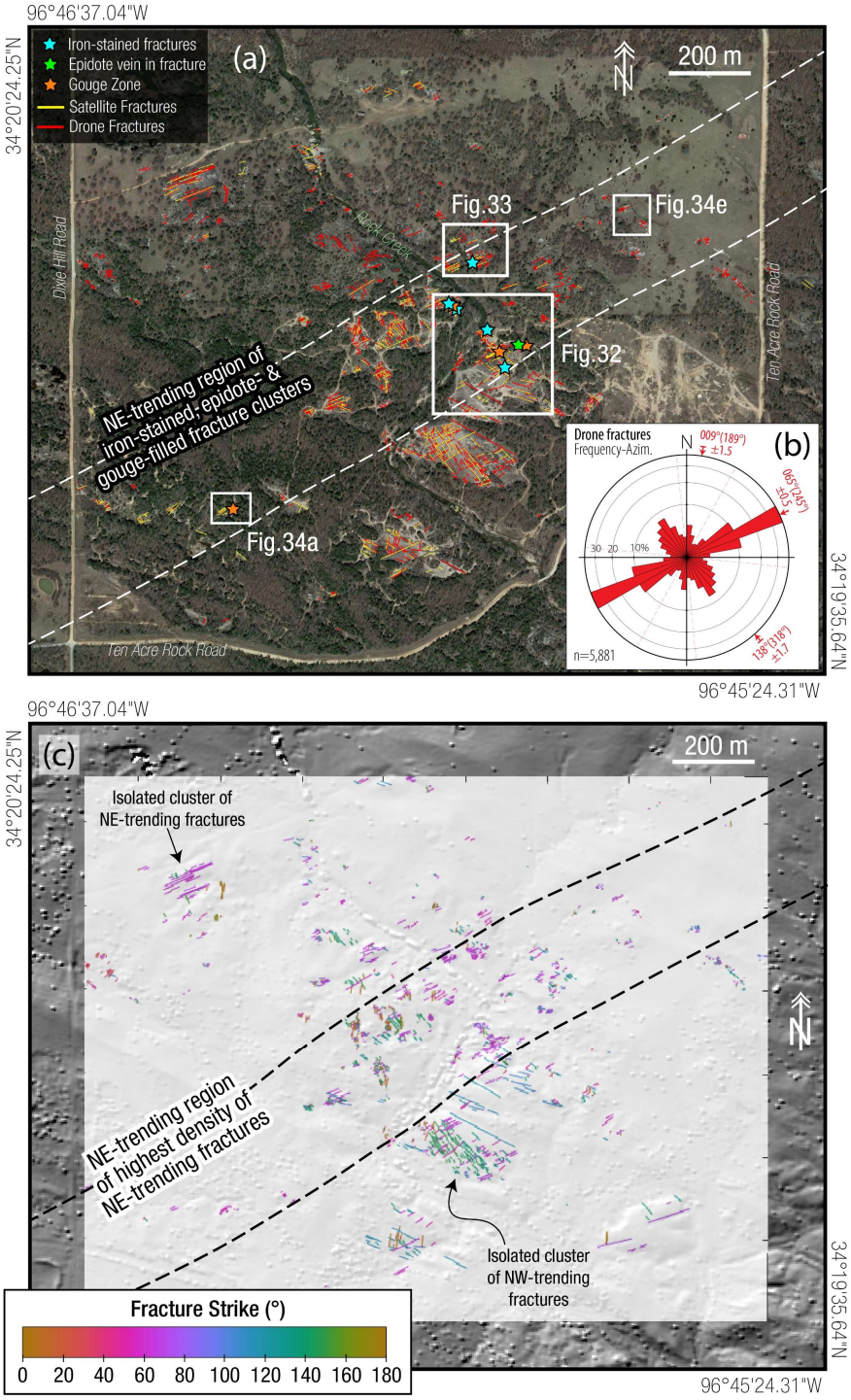

Figure 29. Fracture Trends in the Granite Outcrops. (a) Google Earth© satellite image of the study area, showing the satellite-scale (interpreted from the satellite image) and drone-scale fracture segments (interpreted from the drone images in Figures 28b-e). (b) Area-weighted frequency-azimuth distribution of the drone-scale fractures shown in 29a. (c) Map of color-coded fracture strike for the drone-scale fractures, overlaid on 4m-resolution Lidar Digital Elevation Model (DEM) hillshade map of the study area.

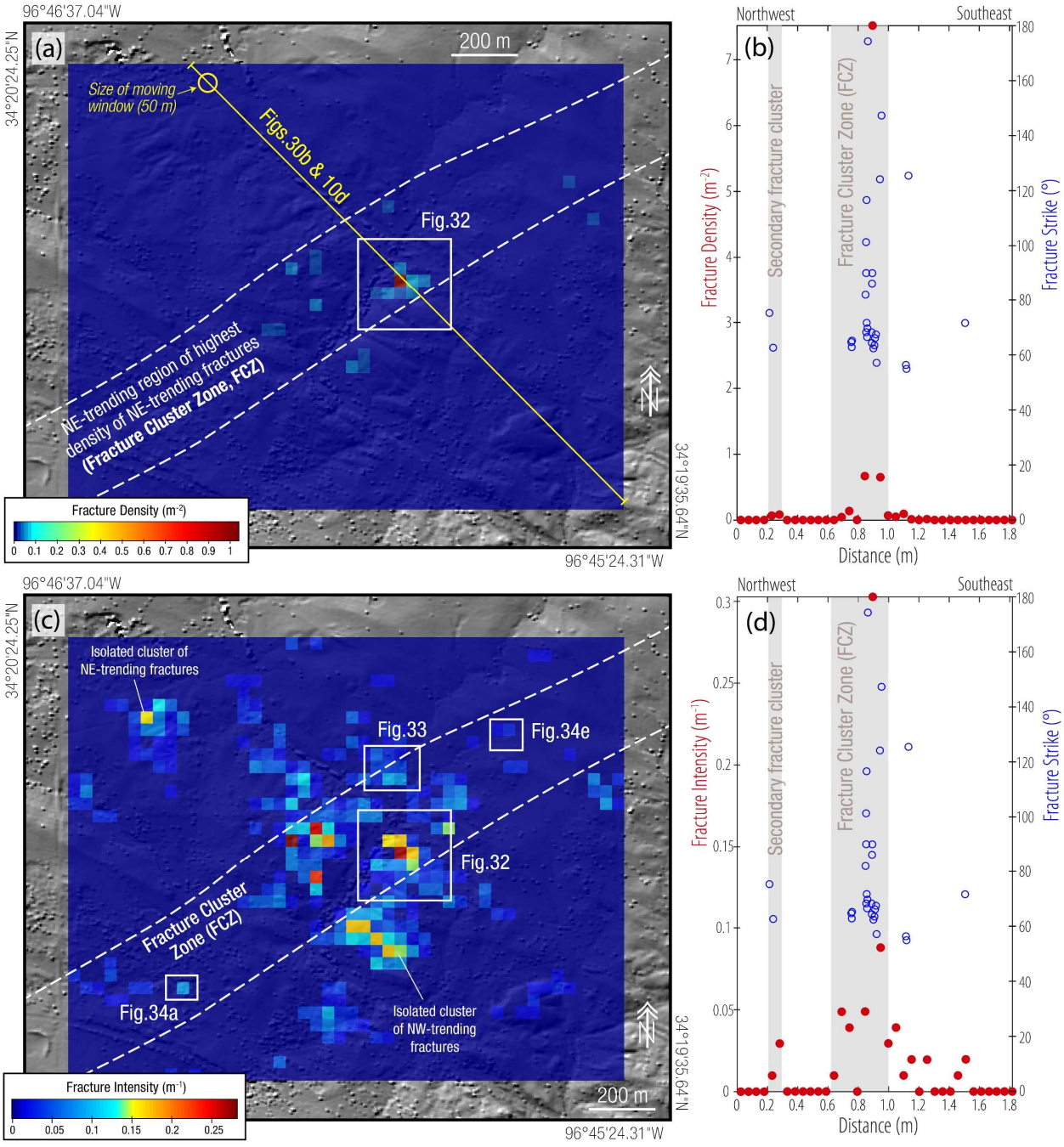

Figure 30. Spatial Distribution of Fracture Density and Intensity in the Granite Outcrops. (a) Fracture density map of the drone fractures overlaid on a 4m-resolution Lidar Digital Elevation Model (DEM) hillshade map of the study area. (b) Distribution of fracture density and the associated fracture strike along NW-SE profile line in Figure 30a. Note that due to limited outcrops, fracture density is less useful as it is related to presence of exposures and their quality. (c) Fracture intensity map of the drone fractures overlaid on the Lidar DEM hillshade map of the study area. (b) Distribution of fracture intensity and the associated fracture strike along NW-SE profile line in Figure 30a.

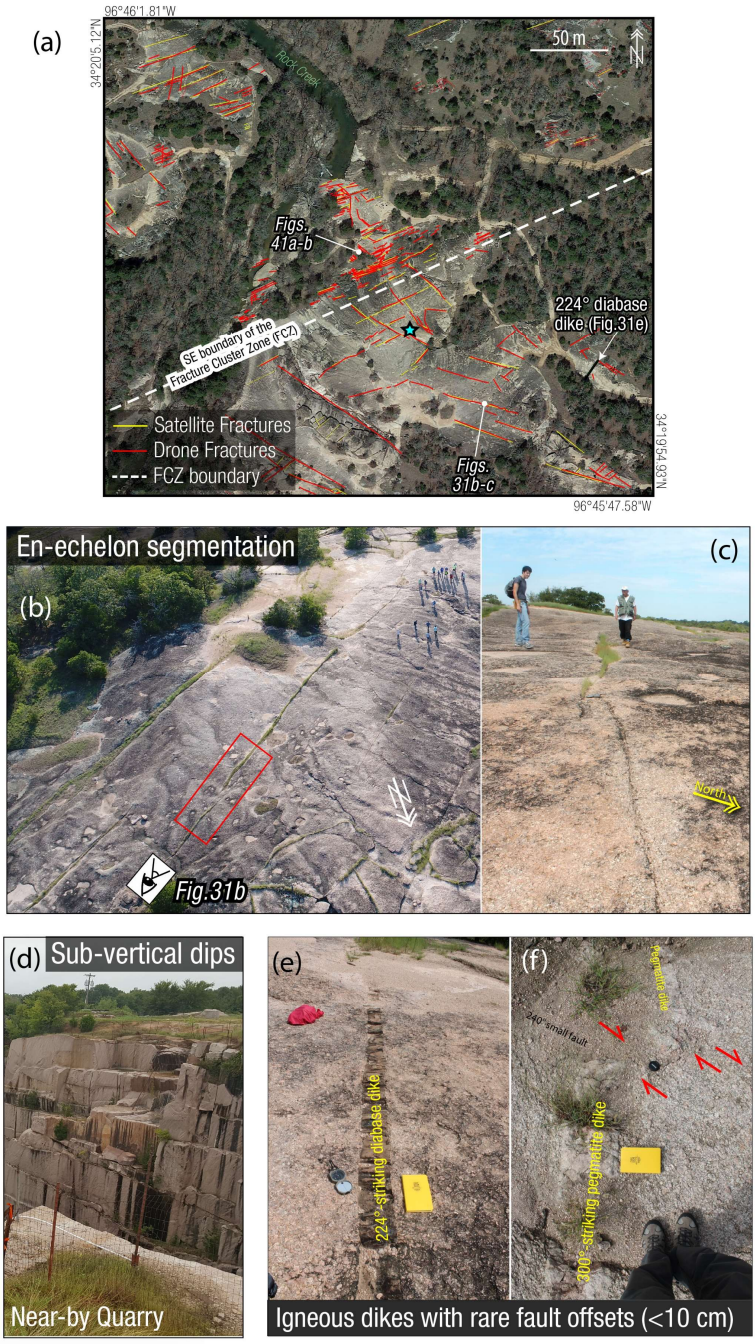

Figure 31. General characteristics of the fractures within the area. (a) Google Earth© satellite image of the study area, showing the satellite-scale (interpreted from the satellite image) and drone-scale fracture segments (interpreted from the drone images in Figures 28b-e). (b) Drone and (c) outcrop photographs of en echelon fracture patterns commonly observed in the study area. (c) Photograph of excavation at a nearby quarry (Martin Marietta Quarry) showing the sub-vertical geometries of the fracture systems in the exposed granitic basement rocks. (d) Photographs of fracture-filled igneous dikes and the observed small-offset faulting of some of the dikes.

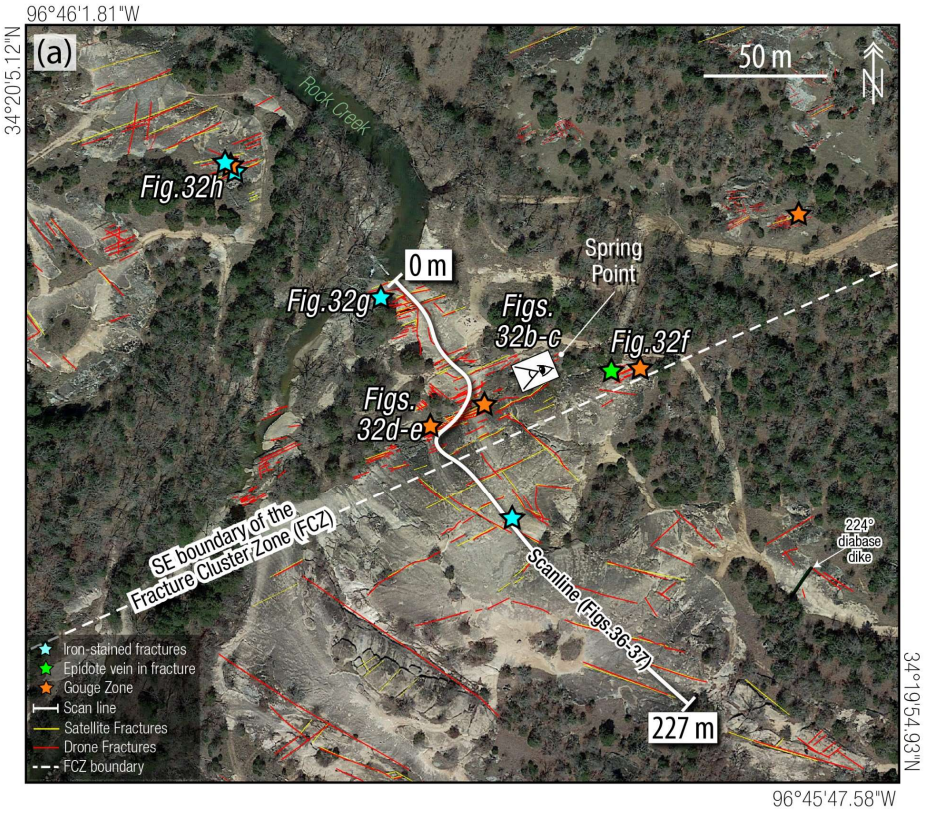
96°46'1.81"W
34°20'5.12"N
(a)
50 m
N
Rock Creek
Fig.32h
0 m
Spring Point
Fig.32g
Figs. 32b-c
Fig.32f
Figs. 32d-e
SE boundary of the Fracture Cluster Zone (FCZ)
224° diabase dike
Scanline (Figs.36-37)
227 m
Iron-stained fractures
Epidote vein in fracture
Gouge Zone
Scan line
Satellite Fractures
Drone Fractures
FCZ boundary
34°19'54.93"N
96°45'47.58"W


(b)

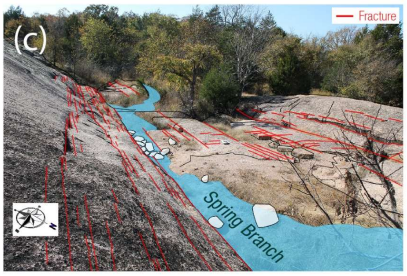
(c)
Fracture
~240°
Spring Branch

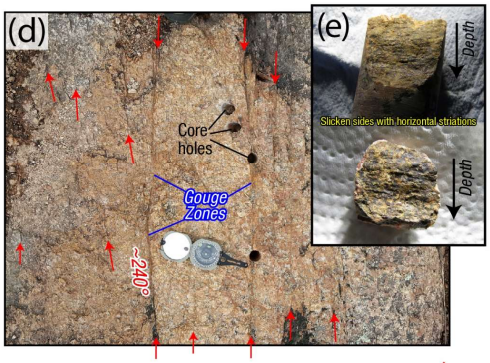
(d)
Core holes
Gouge Zones
~240°
(e)
Depth
Slicken sides with horizontal striations
Depth

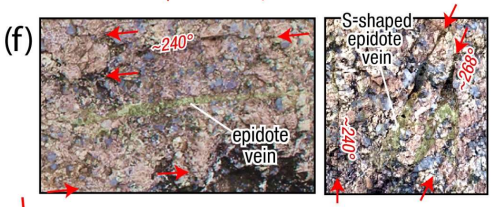
(f)
~240°
epidote vein
S-shaped epidote vein
~288°
~240°


(g)
Rock Creek
238°-striking iron-stained fractures

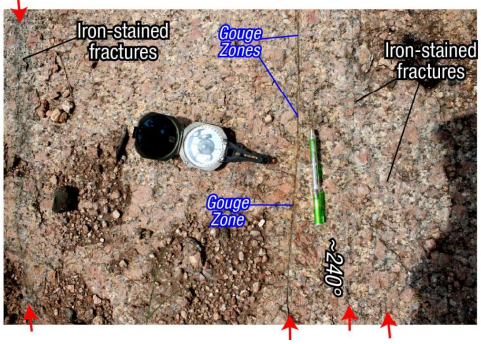
(h)
Iron-stained fractures
Gouge Zones
Iron-stained fractures
Gouge Zone
~240°

Figure 32. Deformation at the Southeastern Boundary of the Fracture Cluster Zone (FCZ). (a) Google Earth© image showing the mapped satellite-scale and drone-scale fractures, and locations of observed gouge-filled, epidote-filled, and iron-stained fractures, and scanline (see Figures 35-37). (b - c) Photograph and interpretation of pervasive fracturing and 'linear valley' morphology of the granite outcrops at the southeastern boundary of the FCZ. (d) Close-up photograph of the most deformed part of the southeastern boundary of the FCZ, showing gouge zones, and (e) horizontal slicken lines along fracture surfaces of drilled core samples. (f) Photographs of fracture-filled epidote veins observed along the fracture cluster. The S-shaped epidote vein is located at a breccia zone within the fracture clusters (photograph courtesy of Brittany Stroud). (g) Iron-stained cluster of fractures, and (h) gouge-filled fracture separating iron-stained fractures.

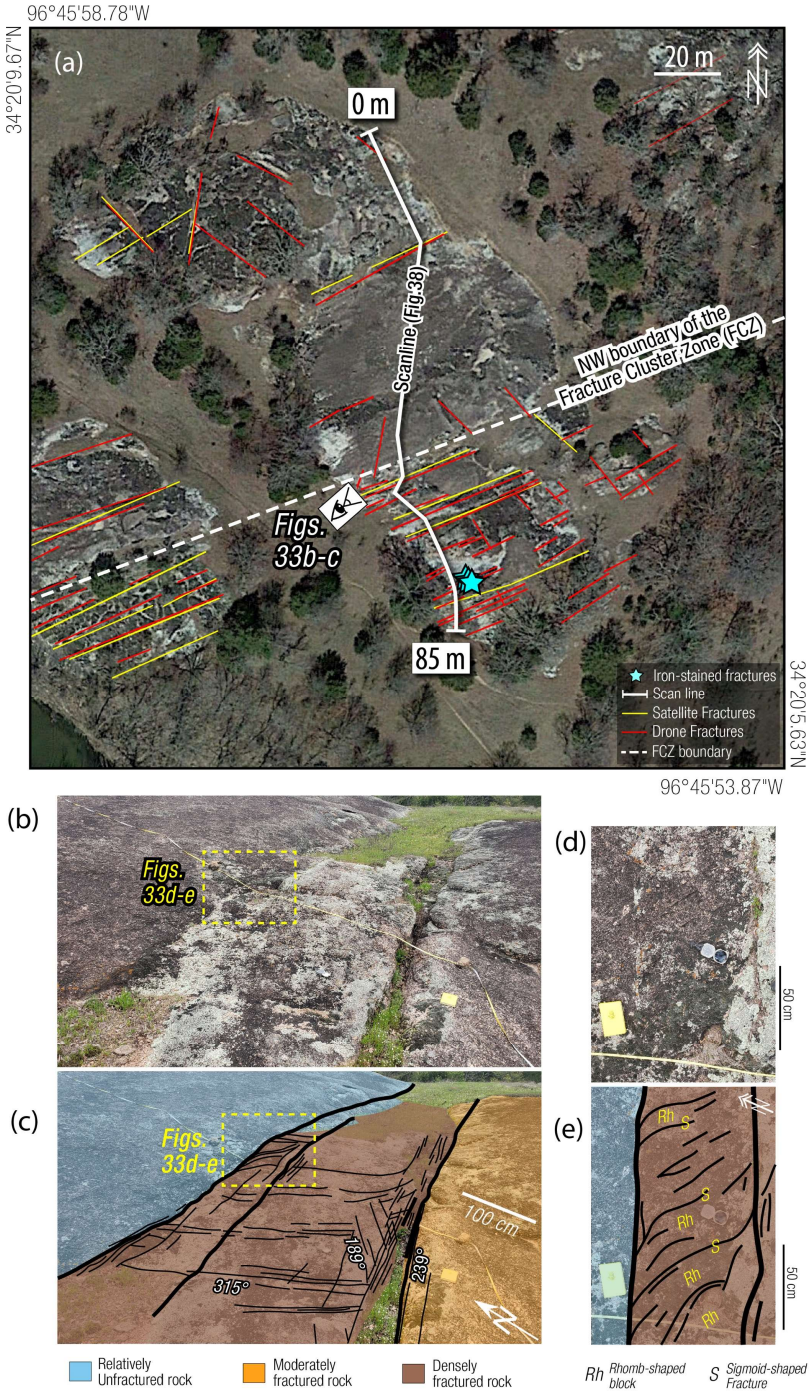

Figure 33. Deformation at the Northwestern Boundary of the Fracture Cluster Zone (FCZ). (a) Google Earth© image showing the mapped satellite-scale and drone-scale fractures, location of observed iron-stained fractures, and scanline (see Figure 38). (b - c) Photograph and interpretation of a 'linear valley' at the NW boundary of the FCZ, along which cross-fractures are bounded by NE-trending fracture clusters. (d - e) Close-up photograph and interpretation of the cross-fracture zone, showing rhomb-shaped blocks bounded by sigmoid-shaped fractures.

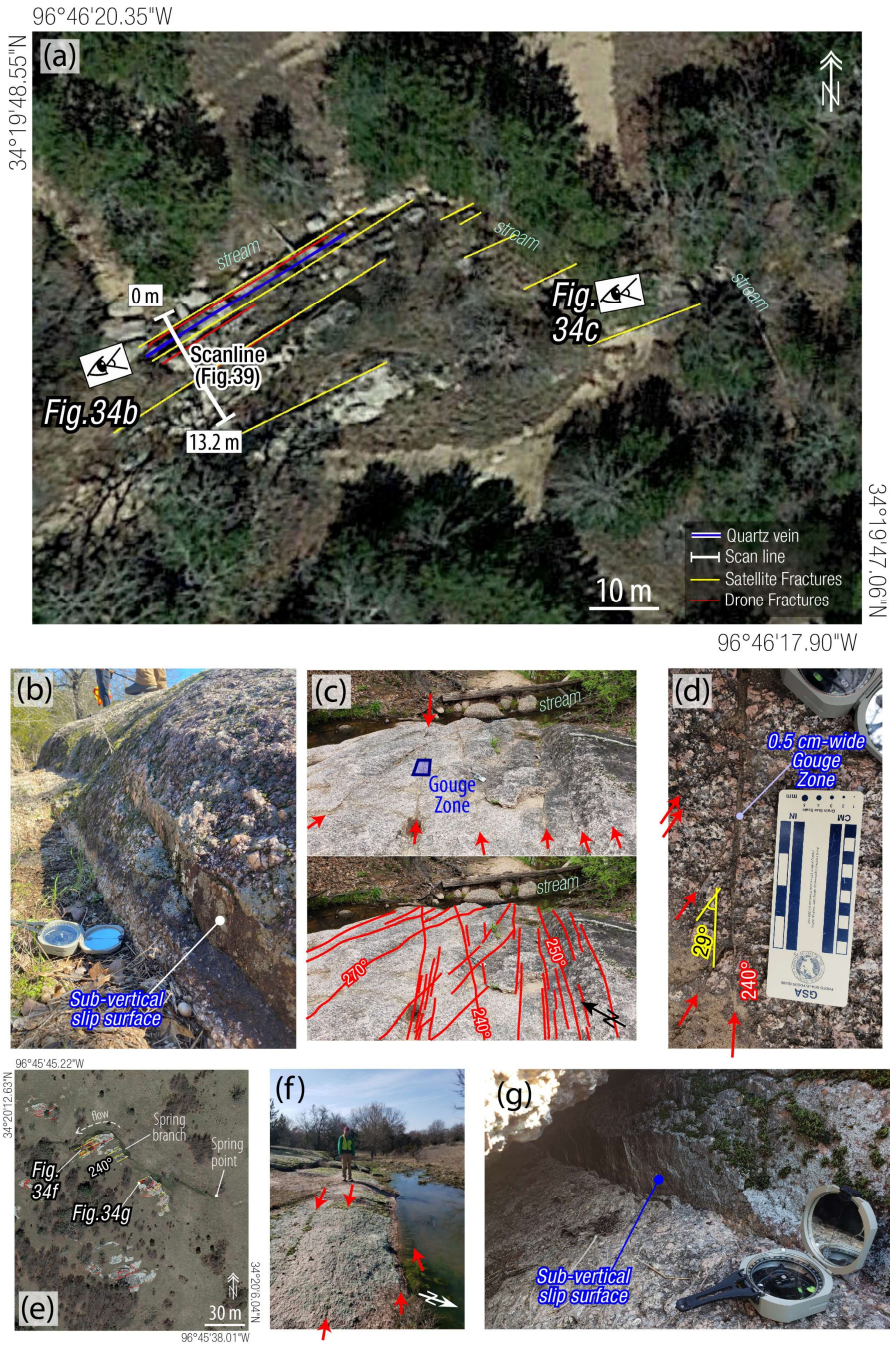

Figure 34. Deformation in the Southwestern and Northeastern Extensions of the Fracture Cluster Zone (FCZ). (a) Google Earth© image showing the mapped satellite-scale and drone-scale fractures, and scanline (see Figure 39) across an outcrop within the southwestern part of the FCZ. (b - c) Photographs showing (b) the sub-vertically dipping fracture surface with chatter marks (photograph courtesy of Connor Mears), (c) Reidel fracture patterns, and (e) gouge zones on 240°-striking fracture with wing fracturing. (e) Google Earth© image of an outcrop in the northeastern part of the FCZ, and photographs of (f) fracture-controlled stream, and (g) sub-vertically dipping fracture surface with chatter marks.

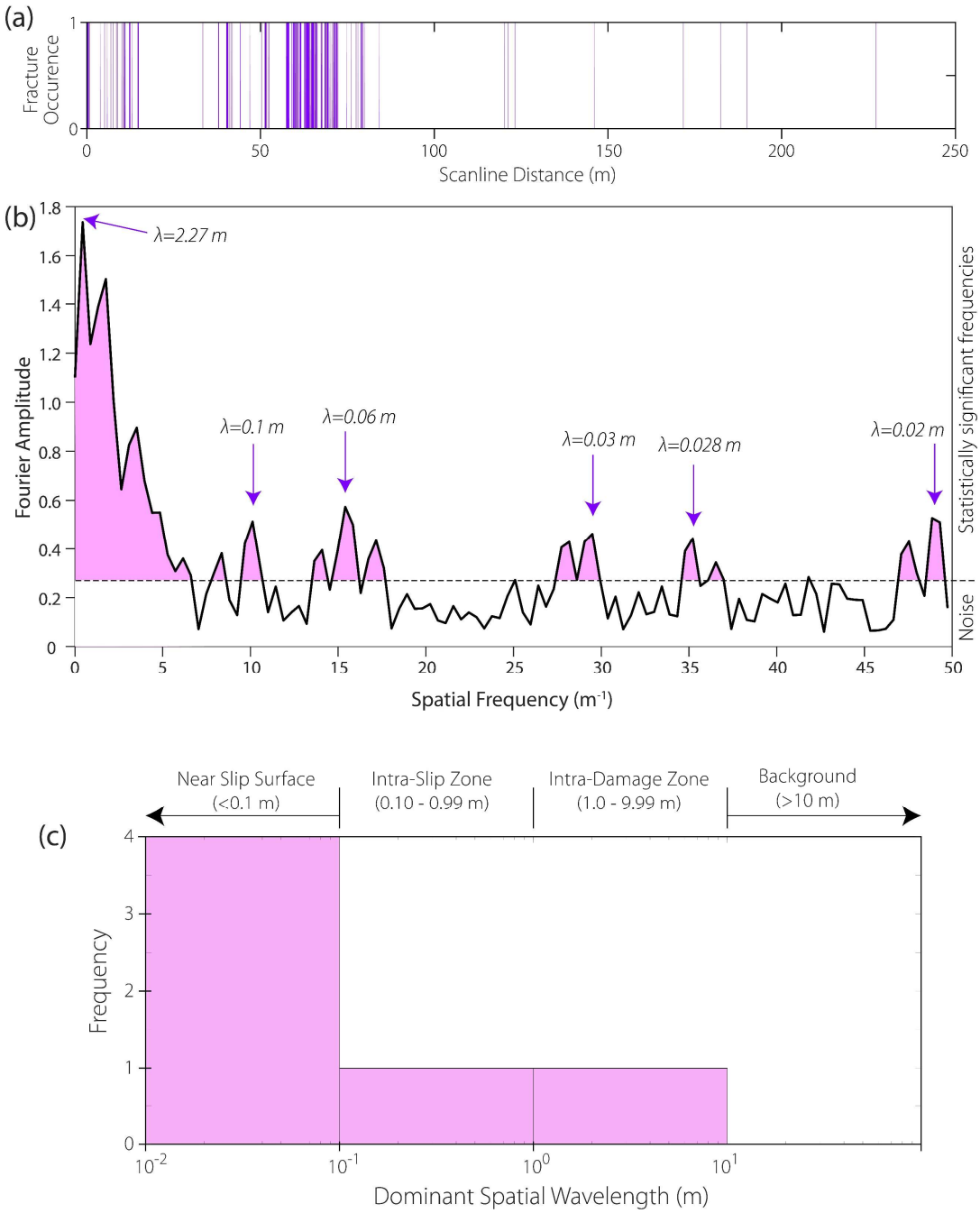

Figure 35. Representative Fourier Analysis of Fracture Distribution in the Fracture Cluster Zone (FCZ). (a) Distribution of fractures (outcrop-scale fractures) mapped along the NW-trending scanline at the southeastern boundary of the FCZ (see Figure 32a for transect). (b) Classic 1-D discrete Fourier transform of the fracture array in Figure 35a, showing the prominent peaks of the spatial frequency. λ = inverse of spatial frequency, corresponding to the spatial wavelength of each of the prominent peaks. The annotated peaks represent the dominant spatial wavelengths in the fracture distribution. (c) Histogram of the dominant spatial wavelengths revealed by the Fourier transform, plotted on a log-scale. The corresponding wavelength groupings are also observable in the detailed analysis of the scanline fracture distributions (see Figures 36-39).

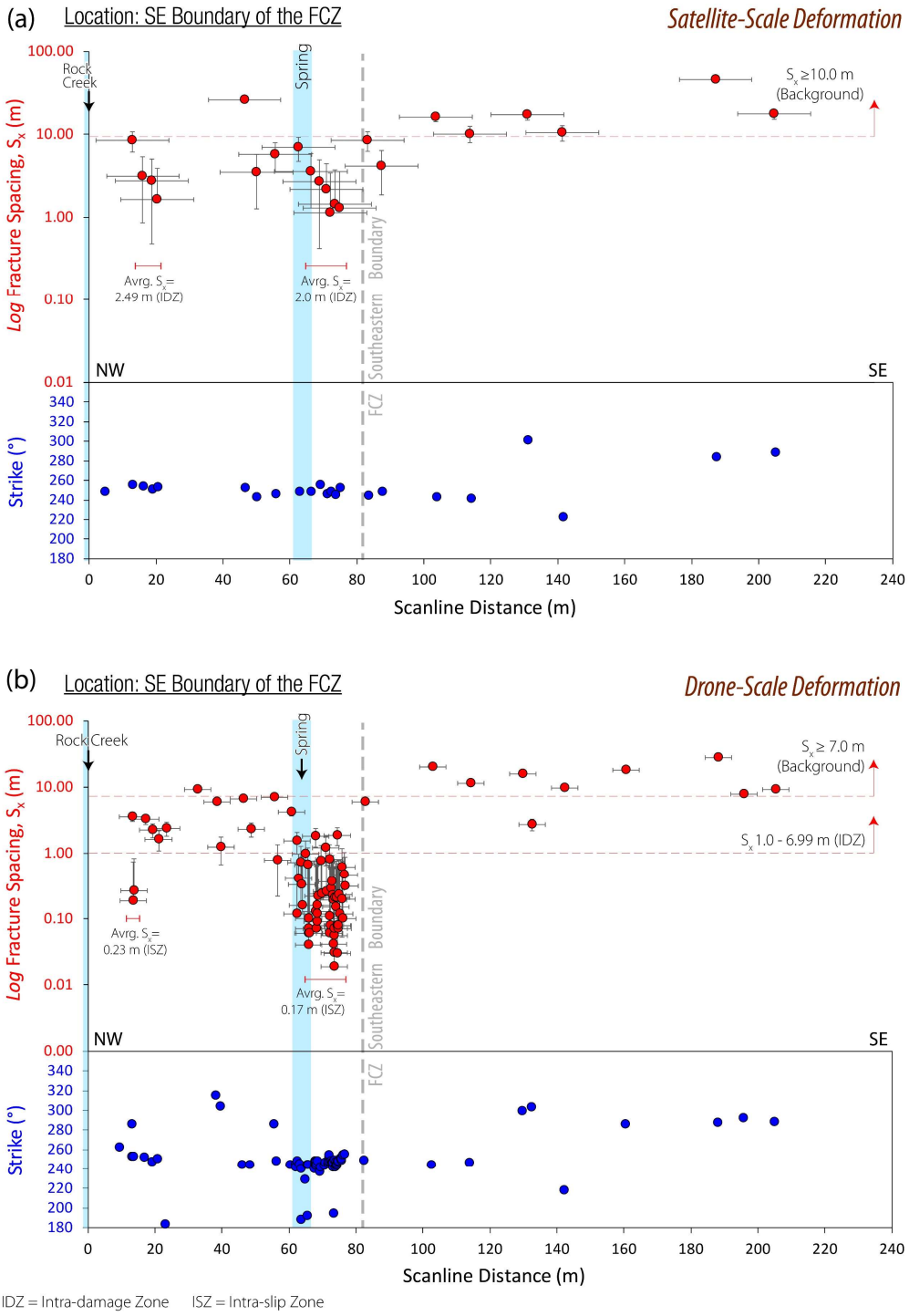

Figure 36. Satellite- and Drone-Scale Deformations at the Southeastern Boundary of the Fracture Cluster Zone (FCZ). See Figure 32a for transect. (a) Satellite-scale, and (b) drone-scale scanlines showing fracture distributions that are consistent with some of the wavelength groupings revealed in the Fourier analysis of the fracture array (Figures 35b-c).

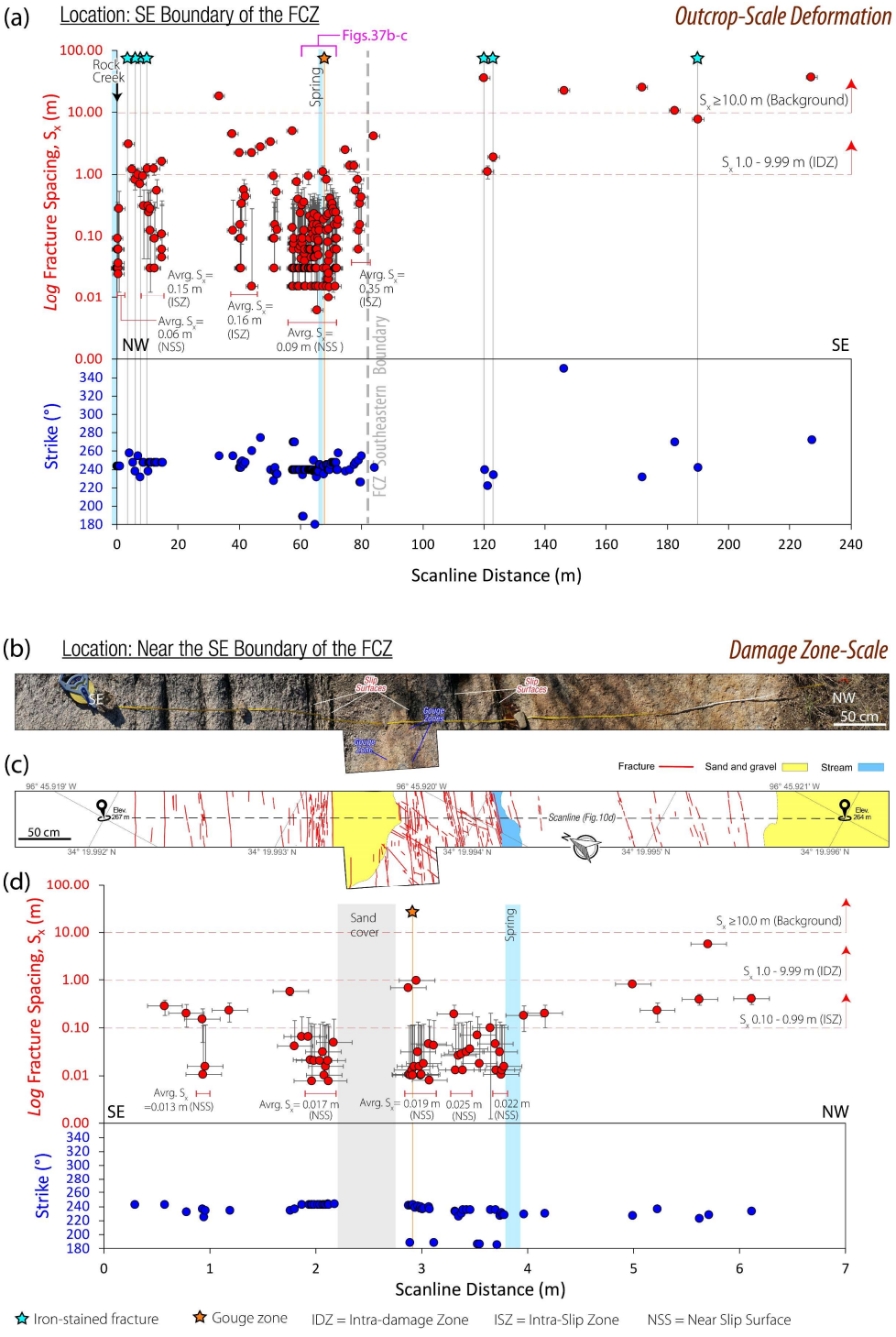

Figure 37. Outcrop- and Damage Zone-Scale Deformations at the Southeastern Boundary of the Fracture Cluster Zone (FCZ). See Figure 32a for transect. (a) Outcrop-scale, and (b) Damage Zone-scale scanlines showing variations in fracture clustering that that are represented in the Fourier analysis of the fracture array (see Figures 35b-c).

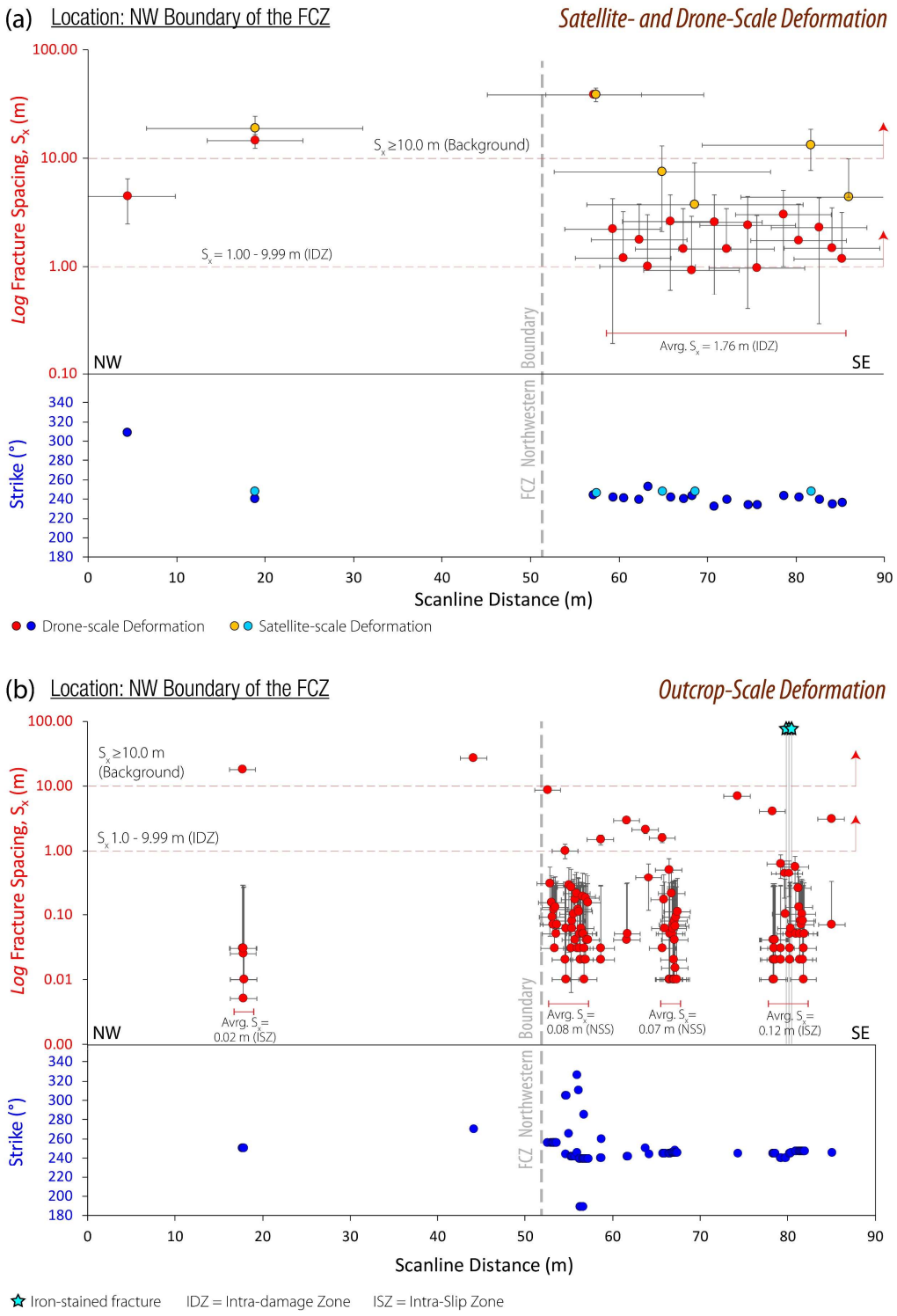

Figure 38. Satellite-, Drone-, and Outcrop-Scale Deformations at the Northwestern Boundary of the Fracture Cluster Zone (FCZ). See Figure 33a for transect. (a) Satellite-and drone-scale, and (b) outcrop-scale scanlines showing fracture distributions that are consistent with wavelength groupings revealed in the representative Fourier analysis of the FCZ (Figures 35b-c).

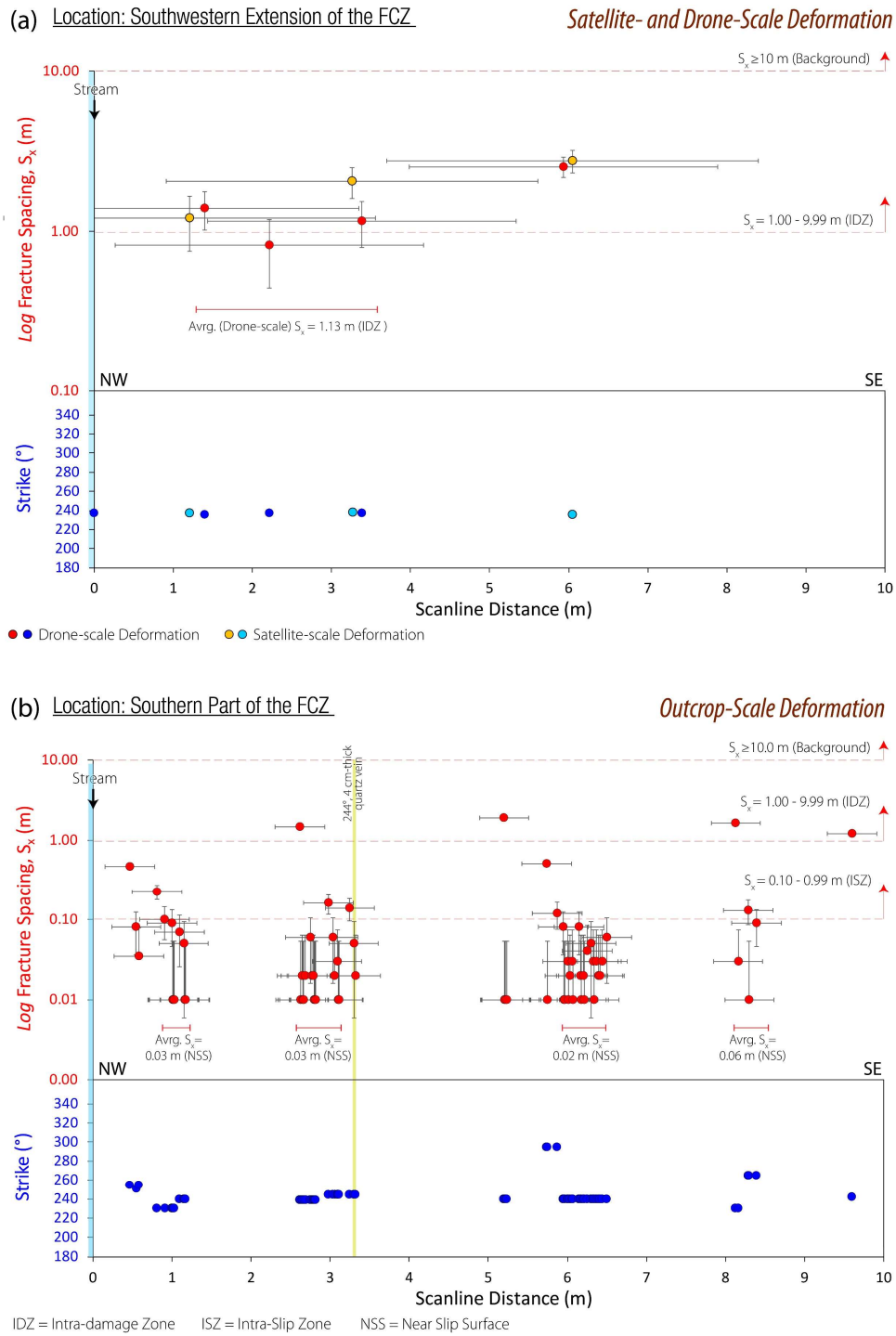

Figure 39. Satellite-, Drone-, and Outcrop-Scale Deformations in the Southwestern Extension of the Fracture Cluster Zone (FCZ). See Figure 32a for transect. (a) (a) Satellite- and drone-scale, and (b) outcrop-scale scanlines showing fracture distributions that are consistent with some of the wavelength groupings revealed in the representative Fourier analysis of the FCZ (Figures 35b-c). Note that no >10 m (background, i.e. off-fault signature) fracture spacing estimate is observable along the scanline.

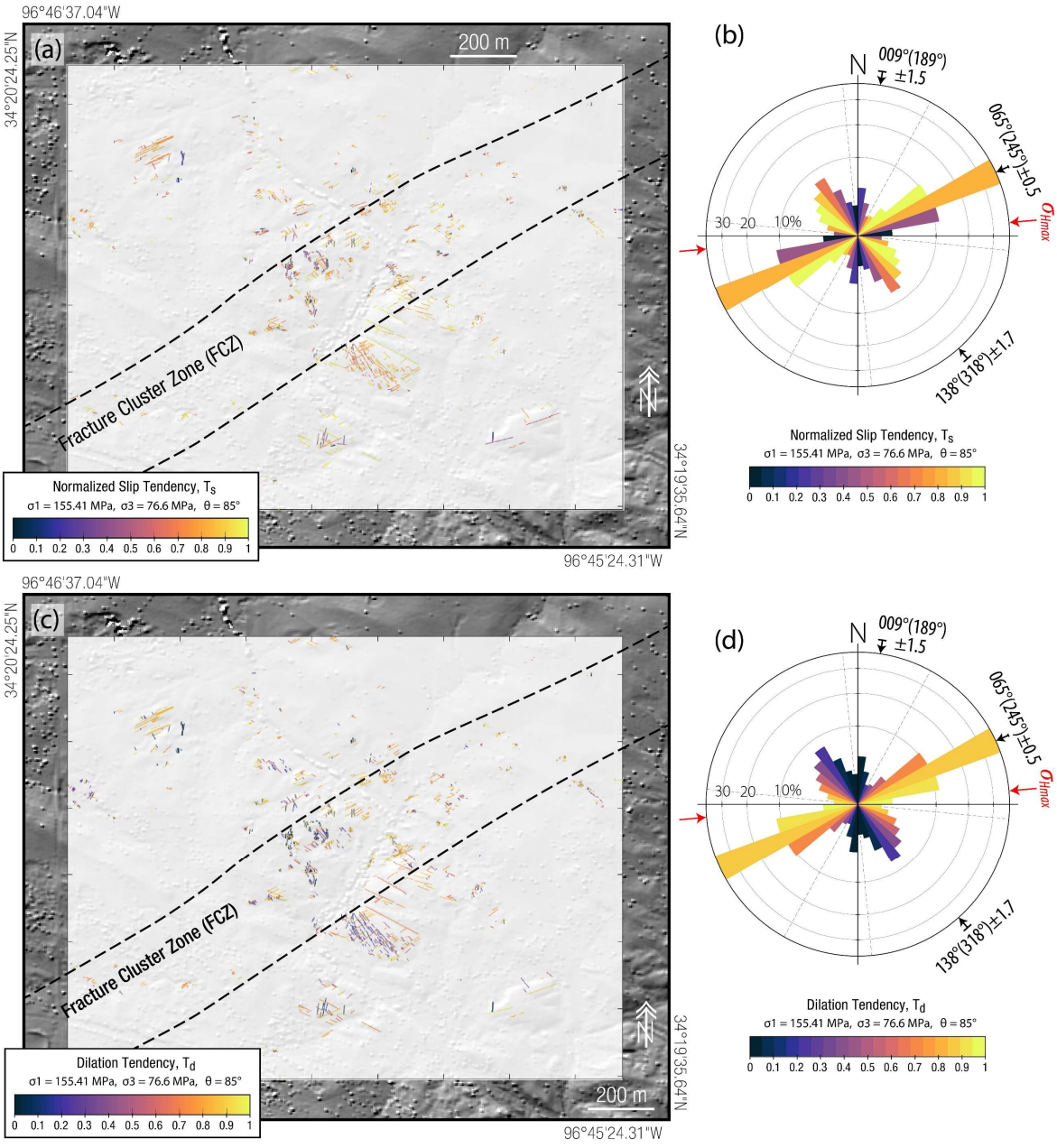

Figure 40. Reactivation tendency of the Fracture Cluster Zone (FCZ) in the current stress field. (a) 4m-resolution Lidar Digital Elevation Model (DEM) hillshade map overlaid with the fracture segments color-coded with the Normalized Slip Tendency (T_s) estimated using the convention of Morris et al. (1996). (b) Area-weighted frequency-azimuth distribution of the fractures, color-coded with the Normalized Slip Tendency estimates. (c) 4 m-resolution Lidar DEM hillshade map overlaid with the fracture segments, color-coded with Dilation Tendency (T_d) estimated using the convention of Ferrill et al. (1999). (d) Area-weighted frequency-azimuth distribution of the fractures, color-coded with the Dilation Tendency estimates.

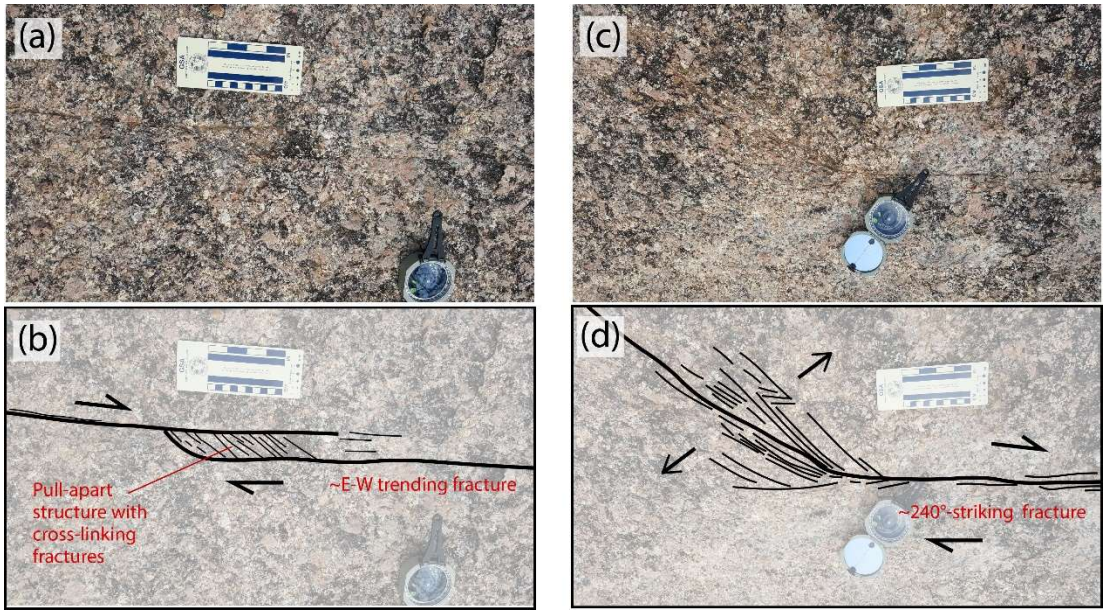

Figure 41. Kinematics of the Fracture Cluster Zone (FCZ). Photographs showing (a) Photograph and (b) interpretations of a pull-apart structure at a right step-over along an ~E-W-trending fracture. (c) Photograph and (d) interpretations of a splay fracture array at the tail of a ~240° -striking fracture.

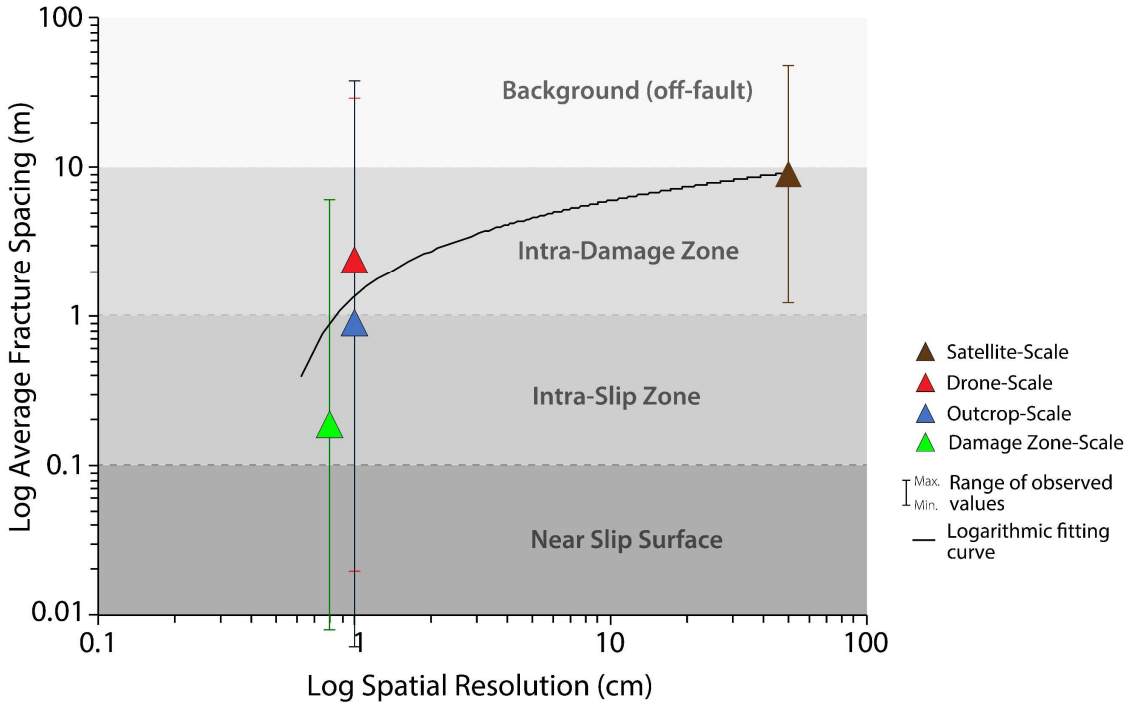

Figure 42. Resolution-Dependence of the Imaging of Fault Zone Damage Compartmentalization. Log-Log distribution of the observed fracture spacing and spatial resolution of imaging, based on the scanline data at the SE boundary of the Fracture Cluster Zone (FCZ) (i.e. scanline data in Figures 36-37). The triangles represent the plot of the global average of all the fracture spacing observed for the associated data type.

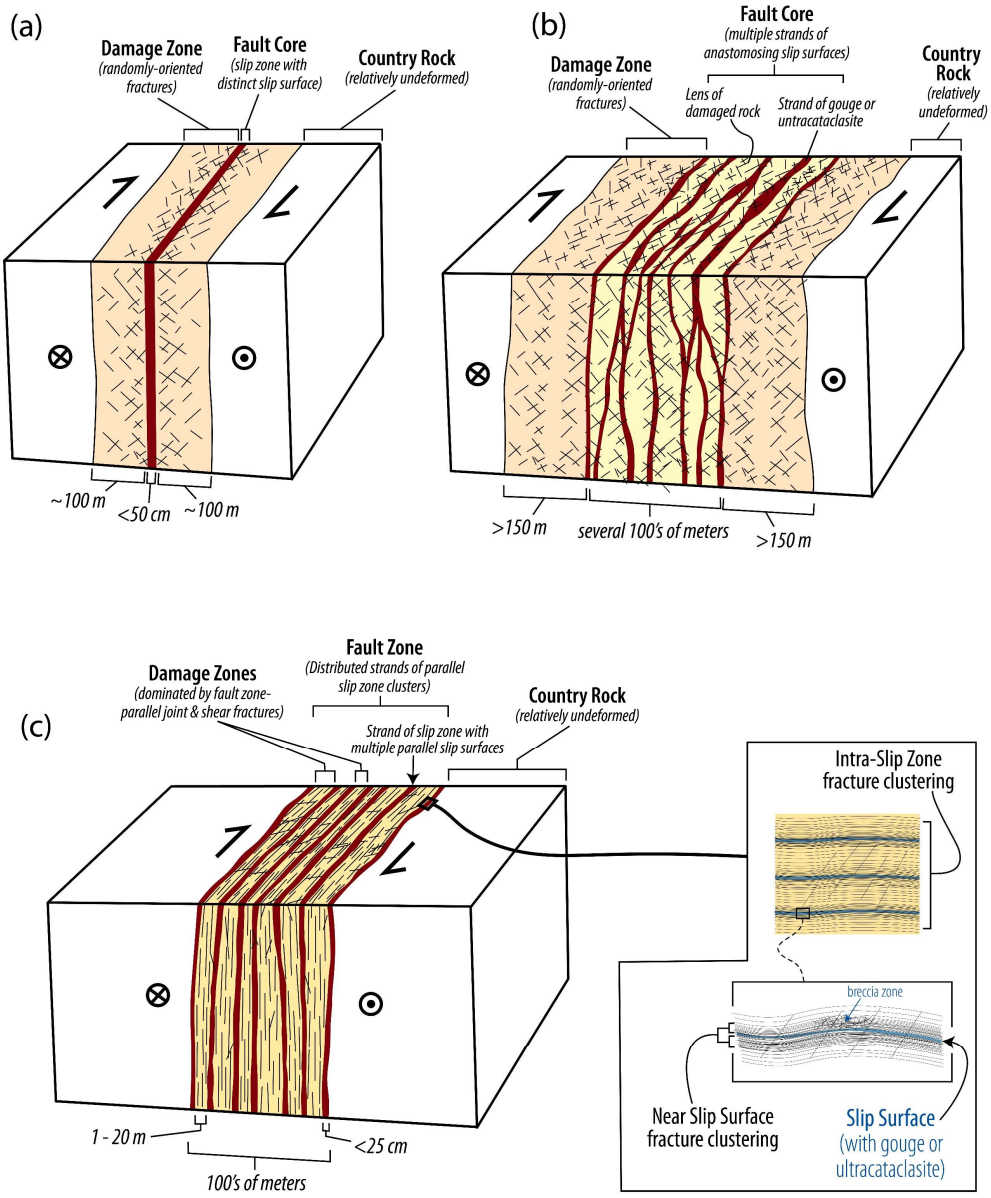

Figure 43. Localized and Distributed Slip Fault Zone Structure. Cartoons illustrating (a) Classic localized slip fault zone structure (modified after Caine et al., 1996; Faulkner et al., 2003; Mitchell and Faulkner, 2009), (b) Anastomosing distributed (multi-strand) slip fault zone structure (modified after Faulkner et al., 2003; Mitchell and Faulkner, 2009), and (c) Domino-style distributed (multi-strand) slip fault zone structure (this study).

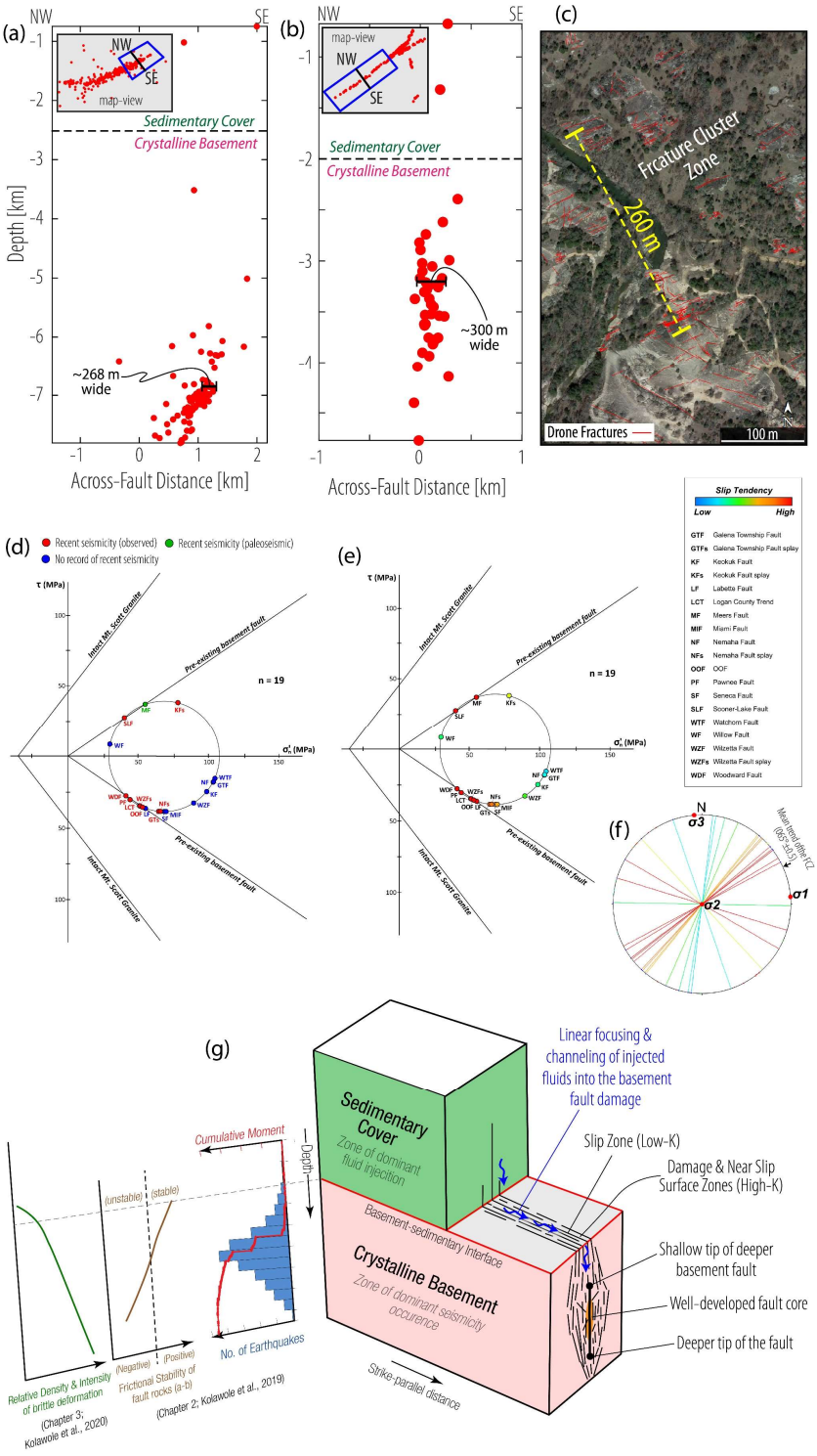

Figure 44. (a) Map and cross-section of the relocated events of the 2016 Mw4.1-4.3 Woodward Earthquake sequence (from Qin et al., 2018), showing ~268 m-wide event cluster near the shallow part of the cluster. Relative relocation error of 100 m (vertical) and 40 m (horizontal). (b) Map and cross-section of the relocated events of the 2011 Mw5.7 Prague Earthquake (from Kolawole et al., 2019), showing ~300 m-wide event cluster near the shallow part of the cluster. Relative relocation error of ~288 m (vertical) and ~200 m (horizontal). (c) Google Earth© image of the study area showing the ~260 m width of the Fracture Cluster Zone (FCZ; analyzed in this study). (d - e) Mohr-Coulomb and Slip Tendency plot for the major faults in the area of seismicity in central Oklahoma. (g) Cartoon illustrating the interpreted structure of the Mill Creek Fault Zone, based on outcrop observations and plausible subsurface structure.

REFERENCES

Caine, J. S., Evans, J. P., & Forster, C. B. (1996). Fault zone architecture and permeability structure. Geology, 24(11), 1025-1028.

Cappa, F., Scuderi, M. M., Collettini, C., Guglielmi, Y., & Avouac, J. P. (2019). Stabilization of fault slip by fluid injection in the laboratory and in situ. Science advances, 5(3), p.eaau4065.

Childs, C., Manzocchi, T., Walsh, J. J., Bonson, C. G., Nicol, A., & Schöpfer, M. P. (2009). A geometric model of fault zone and fault rock thickness variations. Journal of Structural Geology, 31(2), 117-127.

Alt, R. C., & Zoback, M. D. (2017). In Situ Stress and Active Faulting in Oklahoma. Bulletin of the Seismological Society of America, v. 107, 1–13.

Bickford, M. E., Van Schmus, W. R., Karlstrom, K. E., Mueller, P. A., & Kamenov, G. D. (2015). Mesoproterozoic-trans-Laurentian magmatism: A synthesis of continent-wide age distributions, new SIMS U–Pb ages, zircon saturation temperatures, and Hf and Nd isotopic compositions. Precambrian Research, 265, 286-312.

Denison, R. E. (1995). Significance of air-photograph linears in the basement rocks of the Arbuckle Mountains: Oklahoma Geological Survey Circular 97, 119-131.

Dershowitz, W. S., & Herda, H. H. (1992). Interpretation of fracture spacing and intensity. In 33rd US Symposium on Rock Mechanics, Santa Fe, NM, 757-766.

Eyre, T. S., Eaton, D. W., Garagash, D. I., Zecevic, M., Venieri, M., Weir, R., & Lawton, D. C. (2019). The role of aseismic slip in hydraulic fracturing–induced seismicity. Science advances, 5(8), p.eaav7172.

Faulkner, D. R., Lewis, A. C., & Rutter, E. H. (2003). On the internal structure and mechanics of large strike-slip fault zones: field observations of the Carboneras fault in southeastem Spain. Tectonophysics 367 (3–4), 235–251.

Faulkner, D. R., Mitchell, T. M., Rutter, E. H., & Cembrano, J. (2008). On the structure and mechanical properties of large strike-slip faults. In: Wibberley, C.A.J., Kurz, W., Imber, J., Holdsworth, R.E., Collettini, C. (Eds.), Structure of Fault Zones: Implications for Mechanical and Fluid-flow Properties. Geological Society, London, Special Publications, vol. 299, 139–150.

Ferrill, D. A., Winterle, J., Wittmeyer, G., Sims, D., Colton, S., Armstrong, A., & Morris, A. P. (1999). Stressed rock strains groundwater at Yucca Mountain, Nevada. GSA Today, 9(5), 1-8.

Frank, W. B., & Brodsky, E. E. (2019). Daily measurement of slow slip from low-frequency earthquakes is consistent with ordinary earthquake scaling. Science advances, 5(10), eaaw9386.

Gabrielsen, R. H., & Braathen, A. (2014). Models of fracture lineaments—Joint swarms, fracture corridors and faults in crystalline rocks, and their genetic relations. Tectonophysics, 628, 26-44.

Haffener, J., Chen, X., & Murray, K., 2018. Multiscale analysis of spatiotemporal relationship between injection and seismicity in Oklahoma. Journal of Geophysical Research: Solid Earth, 123(10), pp.8711-8731.

Healy, D., Rizzo, R. E., Cornwell, D. C., Farrell, N. J. C., Watkins, H., Timms, N. E., Gomez-Rivas, E., & Smith, M. (2017). FracPaQ: a MATLAB™ toolbox for the quantification of fracture patterns. Journal of Structural Geology, 95, 1-16.

Henriksen, H., & Braathen, A. (2006). Effects of fracture lineaments and in-situ rock stresses on groundwater flow in hard rocks: a case study from Sunnfjord, western Norway. Hydrogeology journal, 14(4), 444-461.

Keranen, K. M., Savage, H. M., Abers, G. A., & Cochran, E. S. (2013). Potentially induced earthquakes in Oklahoma, USA: Links between wastewater injection and the 2011 Mw 5.7 earthquake sequence. Geology, 41(6), 699-702.

Kolawole, F., Johnston, C. S., Morgan, C. B., Chang, J. C., Marfurt, K. J., Lockner, D. A., Reches, Z., & Carpenter, B. M. (2019). The susceptibility of Oklahoma's basement to seismic reactivation. Nature Geoscience, 12(10), 839-844.

Kolawole, F., Simpson Turko, M., & Carpenter, B. M. (2020). Basement-controlled deformation of sedimentary sequences, Anadarko Shelf, Oklahoma. Basin Research. 00, 1– 23.

Liao, Z., Liu, H., Jiang, Z., Marfurt, K. J., & Reches, Z. E. (2017). Fault damage zone at subsurface: A case study using 3D seismic attributes and a clay model analog for the Anadarko Basin, Oklahoma. Interpretation, 5(2), T143-T150.

Liao, Z., Liu, H., Carpenter, B. M., Marfurt, K. J., & Reches, Z. E. (2019). Analysis of fault damage zones using three-dimensional seismic coherence in the Anadarko Basin, Oklahoma. AAPG Bulletin, 103(8), 1771-1785.

Lidiak, E. G., Denison, R. E., & Stern, R. J. (2014). Cambrian (?) Mill Creek diabase dike swarm, eastern Arbuckles: a glimpse of Cambrian rifting in the Southern Oklahoma Aulacogen. Oklahoma Geological Survey, Guidebook, 38, 105-122.

Lindanger, M., Gabrielsen, R. H., & Braathen, A. (2007). Analysis of rock lenses in extensional faults. Norwegian Journal of Geology/Norsk Geologisk Forening, 87(4).

Morris, A., Ferrill, D. A., & Henderson, D. B. (1996). Slip-tendency analysis and fault reactivation. Geology, 24(3), 275-278.

Nixon, C. W., Sanderson, D. J., & Bull, J. M. (2011). Deformation within a strike-slip fault network at Westward Ho!, Devon UK: Domino vs conjugate faulting. Journal of Structural Geology, 33(5), 833-843.

Qin, Y., Chen, X., Carpenter, B. M., & Kolawole, F. (2018). Coulomb stress transfer influences fault reactivation in areas of wastewater injection. Geophysical Research Letters, 45(20), 11-059.

Qin, Y., Chen, X., Walter, J. I., Haffener, J., Trugman, D. T., Carpenter, B. M., Weingarten, M., & Kolawole, F. (2019). Deciphering the stress state of seismogenic faults in Oklahoma and southern Kansas based on an improved stress map. Journal of Geophysical Research: Solid Earth, 124(12), 12920-12934.

Questiaux, J. M., Couples, G. D., & Ruby, N. (2010). Fractured reservoirs with fracture corridors. Geophysical Prospecting, 58(2), 279-295.

Rowe, C. D., Ross, C., Swanson, M. T., Pollock, S., Backeberg, N. R., Barshi, N. A., Bate, C. E., Carruthers, S., Coulson, S., Dascher-Cousineau, K., & Harrichhausen, N. (2018). Geometric complexity of earthquake rupture surfaces preserved in pseudotachylyte networks. Journal of Geophysical Research: Solid Earth, 123(9), 7998-8015.

Schoenball, M., & Ellsworth, W. L. (2017). A systematic assessment of the spatiotemporal evolution of fault activation through induced seismicity in Oklahoma and southern Kansas. Journal of Geophysical Research: Solid Earth, 122, 189–10, 206.

Schultz, R. (2009). Geologic Fracture Mechanics. Cambridge University Press, Cambridge, UK.

Schultz, R. A., & Balasko, C. M. (2003). Growth of deformation bands into echelon and ladder geometries. Geophysical Research Letters, 30 (20).

Segall, P., and Pollard, D. D. (1983a). Nucleation and growth of strike slip faults in granite. Journal of Geophysical Research: Solid Earth, 88(B1), 555-568.

Segall, P., & Pollard, D. D. (1983b). Joint formation in granitic rock of the Sierra Nevada. Geological Society of America Bulletin, 94(5), 563-575.

Sibson, R. H. (1985). A note on fault reactivation. Journal of Structural Geology, 7(6), 751-754.

Singh, S. K., Abu-Habbiel, H., Khan, B., Akbar, M., Etchecopar, A., & Montaron, B. (2008). Mapping fracture corridors in naturally fractured reservoirs: an example from Middle East carbonates. First Break, 109.

Storti, F., Billi, A., & Salvini, F. (2003). Particle size distributions in natural carbonate fault rocks: insights for non-self-similar cataclasis. Earth and Planetary Science Letters, 206(1-2), 173-186.

Qin, Y., Chen, X., Carpenter, B. M., & Kolawole, F. (2018). Coulomb stress transfer influences fault reactivation in areas of wastewater injection. Geophysical Research Letters, 45(20), 11-059.

Walsh III, F. R., & Zoback, M. D. (2016). Probabilistic assessment of potential fault slip related to injection-induced earthquakes: Application to north-central Oklahoma, USA. Geology, v. 44, 9 91-994.

Wang, Q., Laubach, S. E., Gale, J. F. W., & Ramos, M. J. (2019). Quantified fracture (joint) clustering in Archean basement, Wyoming: application of the normalized correlation count method. Petroleum Geoscience, 25(4), 415-428.

Weingarten, M., Ge, S., Godt, J. W., Bekins, B. A., & Rubinstein, J. L. (2015). High-rate injection is associated with the increase in US mid-continent seismicity. Science, 348(6241), 1336-1340.

Whitmeyer, S. J., & Karlstrom, K. E. (2007). Tectonic model for the Proterozoic growth ofNorth America. Geosphere 3, 220–259.

Zhang, Q., Lin, G., Zhan, Z., Chen, X., Qin, Y., & Wdowinski, S. (2017). Absence of remote earthquake triggering within the Coso and Salton Sea geothermal production fields. Geophysical Research Letters, 44(2), 726-733.

CHAPTER 5

STRUCTURAL INHERITANCE AND FEEDBACK BETWEEN METAMORPHIC FABRICS, MAGMA-PLUMBING, AND FAULTING IN A MULTIPHASE RIFT: SHIRE RIFT BASIN, EAST AFRICA

ABSTRACT

We investigate spatio-temporal relationships between basement fabrics, magma-plumbing, and faulting in the Shire Rift, one of the few segments of the East African Rift System that experienced Permo-Jurassic (Phase-1), Jurassic-Cretaceous (Phase-2), and Cenozoic (Phase-3) rifting. We integrate aeromagnetic, satellite Digital Elevation Model (DEM), and field data to delineate the fault segments, igneous intrusions, and pre-rift metamorphic fabrics, and estimate the along-fault distribution of throw. First, we present an updated structure of the Shire Rift featuring six sub-basins with magmatic and non-magmatic groupings, associated with different rift episodes. Our results indicate that through the Phase-1 to -3 episodes, the pre-rift basement fabrics controlled border fault locations and geometries, and influenced locations of rift bifurcation, and the episodic termination, renewed propagation (rift lengthening), and widening of the rift tips. We observe that the Phase-1 and -2 igneous dikes and magmatic centers were structurally-controlled by basement fabrics and early phase faults. Further, we identify deformation that demonstrates static feedback between inherited early-phase dikes and long-lived normal faults. The observed relationships between pre-rift fabrics, magmatic structures, and the evolution of fault geometry and segmentation demonstrate the continuous influence of progressively inherited structures through the early stages of continental extension.

INTRODUCTION

Passive margins record multiple phases of tectonic extension in which inherited structures and magmatism influence the continued localization of strain and crustal weakening, leading to the final continental break-up. Studies in syn-rift sections of passive margins, failed continental rifts, and actively evolving rift segments demonstrate the widespread influence of structural inheritance on rift evolution (e.g., Hill, 1994; Katumwehe et al., 2015; Phillips et al., 2016; Rotevatn et al., 2018; Vasconcelos et al., 2019; Wright et al., 2020). The control of structural inheritance on rift and fault nucleation, their geometries, segmentation, and continued growth is well documented (e.g., Wheeler and Karson, 1989; Morley, 2010; Dawson et al., 2018; Hodge et al., 2018; Kolawole et al., 2018; Heilman et al., 2019; Osagiede et al., 2020). The influence of inherited structures, although multi-scale (e.g., Daly et al., 1989; Kirkpatrick et al., 2013), is known to be highly relevant at the early stages of continental extension (e.g., Kinabo et al., 2007, 2008; Manatschal et al., 2015; Kolawole et al., 2019).

However, there remains limited understanding of the evolution of strain localization and distribution during the earliest stages of continental rifting, and how these are influenced by structural inheritance. Here, we explore the Shire Rift segment of the East African Rift (Figure 45a), which is one of the segments of the rift system that experienced all the known phases of Phanerozoic extensional tectonics that affected the region. The Shire Rift is located between the southern tip of the Malawi Rift, the Zambezi Rift, and Urema Graben, and extends across the state boundary between Malawi and Mozambique (Figure 45a). The rift records both magmatic and non-magmatic phases of rifting (Castaing, 1991), thus providing an excellent location and opportunity to study the inheritance interactions between both magma-related and non-magma-related structures through the various rifting phases. Although several studies have explored the

influence of magmatism on normal faulting and rift structure (e.g., Phillips et al., 2018; Muirhead et al., 2019), there is little understanding of the intricate dynamic and static feedback processes associated with inheritance interactions between the two categories of geologic structures.

We integrate aeromagnetics, satellite radar digital elevation model, and a combination of published and ground-truthed field data to investigate the multiphase interactions between pre-rift basement metamorphic fabrics, syn-rift magmatism, and rift faulting, and how these interactions impact the evolution of the Shire Rift. First, we present an updated structure of the Shire Rift, revealing six sub-basins with magmatic and non-magmatic groupings, associated with different phases of rifting. We demonstrate that through the rifting episodes, the pre-rift basement fabrics strongly controlled the border fault development, influenced location of rift bifurcation and the episodic termination, renewed propagation (rift lengthening) and widening of the rift tips. Further, we identify deformation that demonstrates static feedback between the inherited structures, with associated fault dislocation that is preserved in the along-fault distribution of throw. The observed relationships between pre-rift fabrics, magmatic structures, and the evolution of fault geometry and segmentation demonstrate the continuous influence of progressively inherited structures through the early stages of rifting. We suggest that both magmatic structures and basement fabrics represent sustained controls on multi-phase rift faulting as continental extension advances.

Geological Setting

The Precambrian Basement

The Shire Rift extends along the tectonic boundaries separating four distinct Precambrian mobile belts and terranes (Figure 45b), which includes the Southern Irumide Belt (1060 - 950 Ma), Zambezi Belt (1830 - 795 Ma), the Unango Complex (1060 - 950 Ma), and the Nampula Complex

(1025-1075 Ma) (Hargrove et al 2003; Fritz et al., 2013). These mobile belts are primarily composed of Paleoproterozoic-Mesoproterozoic crust which have been reworked and overprinted by contractional structures and igneous intrusions of the Neoproterozoic Pan African Orogeny. Overall, the mobile belts are dominated by schists, amphibolite and granulitic gneisses, and deformed granites, granodiorites, syenites, gabbro, and anorthosites (e.g., Barr and Brown, 1987; Fritz et al., 2013). Several field studies have revealed the presence of prominent crustal and lithospheric scale shear zones and sutures separating these terranes. This includes the ~E-W-trending Sanangoe Shear Zone separating the Southern Irumide Belt and Zambezi Belt (e.g., Barr and Brown, 1987; Kröner et al., 1997), and the NE-trending Lurio Shear Zone (Bingen et al., 2009; Sacchi et al., 2000) which defines the boundary between the Unango and Nampula Complexes (Figures 45a and 45b).

Phanerozoic Rifting

The NW-trending Shire Rift structure is defined by a complex >300 km-long system of grabens and half grabens attaining total widths of ~140 km in the southeast and ~18 km at the current northwest tip (Figure 46a). The rift has undergone three distinct phases of extension in post-Precambrian times (Figure 46a; Castaing, 1991). The first episode of rifting (Phase-1), popularly known as the "Karoo" rifting episode, began in the Permian and ended in the Lower Jurassic (Castaing, 1991; Delvaux, 1991). This phase of extension established large >150 km-long border faults which includes the SW-dipping Mwanza-Namalambo Fault System to the northeast and the NE-dipping fault to the southwest, here in named the Tete Fault System (Figure 46a). The rift-related siliciclastic sediments were deposited in fault-bounded grabens and half grabens (Figure

46a; Choubert et al., 1988). Among these sub-basins, only the Lengwe and Mwabvi domains have been studied in detail (Castaing, 1991).

The Karoo phase of extension was concluded by the emplacement of igneous centers and diabase dike swarms across the basin in the Early Jurassic, known as the Stormberg vulcanicity (e.g., Monte Muambe Caldera in Figure 46a; Habgood et al., 1973; Woolley et al., 1979). Studies on the kinematics of Karoo rifting in the region of the study inferred contrasting SHmin orientations (Figure 46a inset) which includes NE-SW (Versfelt, 2009), E-W (Daly et al., 1989), and NW-SE (Castaing, 1991) orientations.

The second phase of extension (Phase-2) was short-lived, occurring between the Middle Jurassic and the Cretaceous (Castaing, 1991). The Phase-2 extension was magmatic with voluminous expulsion of volcanic material and minor clastic deposition, primarily within the western part of the basin (Lupata Volcanic Province; Figure 46a). The Cretaceous extension emplaced alkaline igneous centers and dike swarms both along the rift axis and in off-rift domains (e.g., Salambidwe Igneous Structure and Chilwa Igneous Province; Cooper and Bloomfield, 1961; Nyalugwe et al., 2019a).

The third phase of rifting (Phase-3) is thought to have begun in the Late Tertiary (Delvaux, 1991) or Quaternary (Castaing, 1991), and is associated with widespread deposition of Quaternary sediments in the Ngabu area of southern Malawi (Figure 46a; Castaing, 1991; Chisenga et al., 2019) and Chiuta area of Mozambique (Figure 46a; Choubert et al., 1988; Castaing, 1991). Although Phase-1 and Phase-2 episodes of extension in the Shire Rift were magmatic, the current Phase-3 extension is non-magmatic. During this phase, a system of synthetic SW-dipping faults developed on the eastern flank of the basin, consisting of the Thyolo, Muona, and Camacho Faults (Figures 46a and 46b). These relatively newer faults currently serve as the active eastern border

faults of the basin. In the Chiuta area, the west-bounding fault (here in named the Chiuta Fault) represents the border fault of the basin (Figure 46a). The ongoing Phase-3 rifting is associated with the East African Rift System and is responsible for several >Mw4 earthquakes in the basin (Figure 46a). Geodetic velocity solution for the Shire Rift area show strain rates of ~2 mm/year (Figure 46a; Stamps et al., 2018), and mechanical analysis show that the Phase-3 border faults are well oriented for activation within an ENE-WSW to E-W extension direction (Williams et al., 2019). Although the broad geologic history of the Shire Rift has been identified in these previous studies, the detailed structure, basin compartmentalization, and influence of structural inheritance on the multiphase deformation remain unknown.

DATA AND METHODS

Shuttle Radar Topography Mission (SRTM) Digital Elevation Model (DEM)

We utilize 1 arc second (30 m spatial resolution) Shuttle Radar Topography Mission (SRTM-1) Digital Elevation Model (DEM) maps to delineate surface traces of normal faults in the Shire Rift. Sub-aerial exposures of fault scarps are often well expressed as prominent linear zones of abrupt changes in elevation observable in high resolution topographic hillshade maps of tectonically active regions (e.g., Engelkemeir and Khan, 2008; Arrowsmith and Zielke, 2009). We obtain measurements of the cumulative scarp height along the trend of the border fault traces in the SRTM elevation data. In areas where subsurface data is sparse (e.g., NW and SE termination of Shire Rift), we map the linear topographic trends of basement outcrops as supporting independent data on the basement metamorphic fabric trends.

Aeromagnetic Data

Aeromagnetic datasets are useful for imaging the metamorphic fabrics of crystalline basement rocks (e.g., Ma et al., 2012; Kolawole et al., 2017) and estimating depths to the crystalline basement source where the basement is buried beneath less magnetic sedimentary sequences (e.g., Thurston and Smith, 1997; Smith et al., 1998). For our subsurface structural analysis, we utilize three aeromagnetic datasets, two of which cover the Malawi section of the Shire Rift (Figures 47a and 47b), and the third is regional aeromagnetic data which extends over both the Malawi and western Mozambique sections of the basin (Figure 48a). The Malawi aeromagnetic data includes two vintages, acquired in 1984/1985 (source: South Africa Development Community, SADC) and 2013 (source: Geological Survey Department of Malawi; Nyalugwe et al., 2019b). The 1984/1985 data (Figure 47a) was acquired with 120 m terrane clearance along NE-SW lines at a spacing of 1 km, resulting in ~250 m spatial resolution. The 2013 data (Figure 47b) was acquired with 80 m terrane clearance along NE-SW lines with a line spacing of 250 m, thus ~62 m spatial resolution. In the Mozambique section of the Shire Rift, we utilize a very-low resolution (2 km spatial resolution) regional-scale aeromagnetic data (Figure 48a) which consists of a grid of merged aeromagnetic field data acquired in the 1970s and 1980s from countries in southern Africa (source: South Africa Development Community, SADC). These datasets allow us to delineate the pre-rift basement fabrics, rift-related sub-aerial and subsurface faults, and mafic dike lineaments across the extents of the Shire Rift.

Field Data

We use a combination of ground truthing (this study) and published (Habgood et al., 1973) field measurements of strike of metamorphic foliation and exposed mafic dikes along the footwall of

the Thyolo Fault. Additionally, during the field work, we investigated the structure of the dike contacts and associated brittle deformation.

Lineament Interpretation

In this study, we utilize the high-resolution 2013 Malawi dataset and the very low-resolution regional SADC dataset for all aeromagnetic lineament interpretations. Following standard practice, to correct for the skewness of the magnetic field at low latitudes, we first pole-reduce (RTP) each of the aeromagnetic datasets (Baranov, 1957; Arkani-Hamed, 1988), after which we apply mathematical filters to better resolve the gradients in the trends of the magnetic field. We utilize the vertical derivative filter to resolve edges and lineaments associated with fault displacement, basement metamorphic fabrics, and mafic dikes (Figures 47c-h) (e.g., Ma et al., 2012; Kolawole et al., 2017; 2018; Heilman et al., 2019). Following a systematic characterization of the aeromagnetic fabrics observable in the 2013 Malawi aeromagnetic grid (Figures 47d-47h), we identify distinct fabric patterns herein referred to as aeromagnetic facies, which allow a better interpretation of the source character. Further, we manually digitize the aeromagnetic lineaments, and calculate the frequency-azimuth distribution of the facies groups within the relevant segments of the rift. For multimodal distributions, we divide the data into their modal sets using the frequency minima. For both unimodal and multimodal plots, we calculate the circular vector mean and 95% confidence interval for the modal sets using the method of Mardia and Jupp (2009). All frequency-azimuth plots present in this study are area-weighted.

Estimation of Top-Basement Fault Throw

To assess the history of fault growth associated with the influence of inherited structures, we quantify the distribution of cumulative fault throw (Top-Basement) along two representative border fault systems, the Mwanza-Namalambo Fault and Thyolo-Muona-Camacho Fault Systems (Figures 46b and 47c). To achieve this, we quantify and combine the sub-aerial component (scarp height; Figures 49a-b) and the subsurface component (depth-to-magnetic basement) of fault offset.

Sub-aerial Cumulative Fault Offset: Scarp Height

For the sub-aerial component of cumulative Top-Basement fault offset, we manually quantify fault scarp morphology along the target fault segments in 30 m resolution SRTM-1 grid maps, obtained from the U.S. Geological Survey data archive (http://earthexplorer.usgs.gov). SRTM-1 elevation data has an absolute vertical accuracy of ±5.6 m and horizontal accuracy of ±11.9 on the African continent (Rodriguez et al., 2006). We extract fault-perpendicular topographic profiles at 1 km intervals along the Mwanza-Namalambo Fault (180 profiles), Thyolo Fault (79 profiles), Chisumbi Fault (5 profiles), Muona Fault (31 profiles), and the Camacho Fault (39 profiles). On each of these profiles, following standard convention (Caskey, 1995; Hornsby et al., 2020), we estimate the vertical height (H) of the steepest local slope (e.g., Figures 49a-49b). In addition to scarp height, we assess the spatial distribution of the footwall uplift by estimating the maximum footwall elevation within 3 km of the fault base-scarp (Figure 49c) (e.g., Laó-Dávila et al., 2015; Wedmore et al., 2019).

Subsurface Cumulative Fault Offset: Depth-to-Magnetic Basement

For depth-to-magnetic basement calculations, we utilize the 1985 Malawi aeromagnetic dataset due to its moderate resolution and lack of high frequency anomalies related to shallow mafic dikes

(Figure 47a). We utilize the Source Parameter ImagingTM (SPITM) transform of the aeromagnetic grid (Thurston and Smith, 1997; Smith et al., 1998) to perform an automatic calculation of depth to the top of magnetic basement (D_{MB}; Figure 49b) within the study area. The SPITM technique assumes a step-type source model and produces spatially distributed source depth-solutions that are independent of magnetic declination, inclination, strike, dip, and remanent magnetization. Essentially, the transform first computes the tilt derivative, and the total horizontal gradient of the tilt derivative (local wavenumber, K). For a step source model, the $Kmax^{-1}$ represents the depth to the magnetic source where K_{max} is the peak value of the local wavenumber based on a simple Blakely test (Blakely and Simpson, 1986). In order to minimize the noise from shallow sources (e.g., intrasedimentary mafic dikes), we apply an upward continuation filter to the aeromagnetic grid and Hanning filter to the K grid before calculating the source depths. Source depth estimations from aeromagnetic data have an accuracy of about ±20% (Gay, 2009); therefore, we show this percentage vertical error on the graphical plots of extracted basement depths. Note that the along-fault depth-to-magnetic basement (D_{MB}) estimates were extracted at ~1 km basin-ward from the adjacent fault base-scarp (Figures 49a and 49b).

Finally, to obtain the minimum fault throw for the Top-Basement along the analyzed faults, we sum the scarp height (H), base-scarp height (H_b), and the depth-to-magnetic basement (D_{MB}) of the hanging wall (Figure 49b). Along buried fault segments, we also obtain depth-to-footwall of the magnetic basement using the 0° tilt derivative to delineate the location and trend of the footwall cutoff (e.g., Salem et al., 2007; Kolawole et al., 2018). Due to the limitations imposed by erosion and weathering on fault escarpments, and the limited resolution of depth-to-source estimates from magnetic data, we assume that these measurements only represents a minimum estimate of the cumulative throw of the Top-Basement surface (Figure 49b).

RESULTS

Structure and Morphology of the Shire Rift

To understand how the multiphase evolution of the Shire Rift is influenced by continuous structural inheritance, we first re-assess the rift structure and identify the first-order characteristics of basin compartmentalization relevant to the research problem. Based on the distribution and ages of rift-related sedimentary and volcaniclastic units, and geometry of basin-bounding faults in the compiled geologic map (Figure 46a), we identify six sub-basins (Figure 50a). These include four magmatic sub-basins (Lengwe, Mwabvi, Moatize, and Monte-Muambe) which host Permo-Jurassic (Phase-1) and Late Jurassic-Cretaceous (Phase-2) sedimentary and igneous deposits; and two non-magmatic sub-basins (Ngabu and Chiuta) which host mainly Cenozoic (Phase-3) sedimentary deposits (Figure 50a). The Lupata Volcanic Province (LVP) appears to overlay the southern sections of the Moatize and Monte-Muambe sub-basins, and western section of the Mwabvi sub-basin (Figures 46a, 48a-b, 50a,).

Along-rift basin-scale topographic profiles (profiles P1 to P3; Figure 50b) show that the most-prominent highs along the rift are the western and eastern flanks of the Chiuta sub-basin, the Salambidwe Igneous structure, the eastern flank of the Lengwe sub-basin, and the eastern flank of the Ngabu sub-basin. The along-rift distributions of rift shoulder-to-basin axis elevation difference (numbers in blue, Figure 50b) show that the estimate is largest in the Chiuta sub-basin (731 m on the west, 742 m on the east) and at the eastern margin of the Ngabu sub-basin (708 m). However, the rift shoulder-basin axis elevation difference is lowest in the western margin of the Lengwe sub-basin (50 m) and the western margin of the Lupata Volcanic province (66 m).

At the northwestern tip of the rift (profile P1, Chiuta sub-basin), the rift morphology can be characterized as an asymmetric graben geometry in which the basin tilts gently towards the western border fault (Chiuta Fault). At the central part of the rift (profile P2), the morphology shows western (Moatize sub-basin) and eastern (Lengwe sub-basin) grabens, separated by a basement block (here in named the Cana-Cana Horst). The southeastern part of the rift (profile P3) is characterized by a ~130 km-wide basin in which the western and central domains (LVP and Mwabvi sub-basins) are structurally higher than the far eastern domain (Ngabu sub-basin). The Ngabu sub-basin surface topography reflects a half-graben rift morphology in which the basin tilt eastwards towards the Thyolo-Muona-Camacho border fault system. The active depocenter of the Ngabu sub-basin is dominated by a >600 km^2 permanent wetland, Elephant Marsh. Overall, along the entire rift, the border faults with the greatest elevation difference are the Chiuta Fault and the Thyolo-Muona Fault.

Further, we present an updated and comprehensive structural map of the basin, showing the previously mapped features and those mapped in this study (Figure 50c). Surficial geology and topography shows that the Mwanza Fault scarp disappears at the region of overlap with the Thyolo Fault (Figure 46a), however, the filtered aeromagnetic grids (Figures 47c, 48a, 50c) reveal a NW-trending abrupt magnetic gradient (ABT) that extends further southeast beneath the Cenozoic cover, and links up with the exposed Namalambo Fault scarp. Additionally, beneath the Cenozoic cover on the Thyolo Fault hanging wall, the aeromagnetic map reveals an ABT that extends northeastwards from the NE sub-aerial termination of the Muona Fault (Figures 47c and 50c), representing a buried (non-surface-breaking) segment of the Muona Fault.

Basement Metamorphic Fabrics

One of the common aeromagnetic facies in the areas of exposed basement (similar to those observed in other metamorphic basement areas in the region e.g., Kinabo et al., 2007; Kolawole et al., 2017, 2018; Heilman et al., 2019) are the wide packets of long parallel distributed magnetic lineaments (Figure 47d). We refer to these aeromagnetic facies as the 'basement metamorphic fabrics' or 'basement fabrics'. Below, we summarize the results of frequency azimuth distribution of the basement fabrics observed along the Shire Rift.

The Mwanza and Thyolo-Muona Border Faults and Environs

Along the Mwanza Fault footwall, the frequency-azimuth distribution of the basement fabrics (Figures 51a and 51b) shows a dominant NW-SE trend with a 140°±1.9° mean trend. In the Thyolo-Muona Fault footwall, the mapped aeromagnetic metamorphic fabrics also show a prominent NW-SE trend with a mean of 123°±4.3°, consistent with published field measurements (129°±6.4°; Habgood et al., 1973). However, the NW tip of the Thyolo Fault exhibits a deviation from the NW-trend into NNW-trend near the axis of the adjacent South Malawi Rift (Figure 51a). The filtered aeromagnetic grid over the NNW-trending tip of the Thyolo Fault reveals a complex metamorphic fabric pattern, within which the fault trace is collocated with a linear transition zone between NW-trending tight folds to the west and N-NE trending open folds to the east (Figure 52a). Comparison with published field observations in the area (Morel, 1959) indicate that this transition zone represents the contact between amphibolite facies and granulite facies basement rocks (Figure 52b).

Cana-Cana Horst

In the absence of high-resolution aeromagnetic data over the Cana-Cana Horst, we map basement fabrics in both the filtered low-resolution SADC aeromagnetic data (Figures 48a-48b) and the SRTM hillshade DEM (Figure 51a). The frequency-azimuth distributions of the metamorphic fabric lineaments in both datasets (Figure 51d) show multimodal trends with consistent dominant sets along ENE-WSW to NE-SW (079° from aeromagnetics, 069° from DEM) and NW-SE (132° from aeromagnetics, 145° from DEM). The plots also show a secondary (minor) N-S set (011° from aeromagnetics, 018° from DEM).

The Northwest and Southeast Rift Termination Zones

Within the northwest rift termination zone (Chiuta sub-basin), the filtered SADC regional aeromagnetic grid (Figures 48a-b) shows that the basement fabrics is characterized by multimodal trends in which an ENE trend (079°±6.4° from aeromagnetics, 074°±5.1° from DEM) and NW-SE (134°±7.3° from aeromagnetics, 147°±4.3° from DEM) trend are most prominent (Figure 51e). Whereas at the southeast rift termination zone (SE tip of the Camacho Fault; Figure 51a) is dominated by NE-SW trending sets with a mean trend of 060°±10.3° (Figure 51f).

Magmatic Structures

In several parts of the Shire Rift, where high-resolution aeromagnetic data is available, the vertical derivative aeromagnetic grid reveals discrete high amplitude magnetic lineaments within the sedimentary rift-fill (e.g., Figure 47e), and in shallow or exposed basement (e.g., Figures 47e-f). In areas of shallow or exposed basement where metamorphic and dike -related lineaments are pervasive (mesh fabrics, e.g., Figures 47f-g), published field studies in the basin (Habgood, 1963; Habgood et al., 1973; Castaing, 1991), other similar geologic settings (e.g., Kolawole at el., 2017;

Heilman et al., 2019), and direct field observations in this study allow us to distinguish between the magnetic sources of the lineament sets. In addition, the SADC regional aeromagnetic data, although lower in spatial resolution, reveals possible buried magmatic centers in the Mozambique part of the basin where high-resolution magnetic data is absent.

Vicinity of the Mwanza and Thyolo-Muona Border Faults

On both the Mwanza and Thyolo-Muona Fault footwall blocks, the interpreted aeromagnetic dikes show a unimodal trend with a NE-SW dominant trend with mean trends of 045°±5.6° (Mwanza Fault footwall; Figure 51b), and 036°±2.4° (Thyolo-Muona Fault footwall; Figure 51c). Also, the Thyolo-Muona footwall trends are consistent with published field measurements (038°±0.6°; Figure 51c; Habgood et al., 1973).

Lengwe and Mwabvi Sub-Basins

Within the Lengwe sub-basin, the vertical derivative aeromagnetic grid reveals a more complex network of cross-cutting dike-related magnetic lineaments than the Mwabvi sub-basins (e.g., Figures 47c and 47e). The frequency-azimuth distribution of the Lengwe aeromagnetic dikes (Figure 51g) is multimodal with three dominant sets along N-S (000°±2.5°), NNE-SSW (028°±4.1°), and NW-SE (143°±4.1°). Whereas, in the Mwabvi sub-basin, the aeromagnetic dikes show only two dominant sets (Figure 51h) which include the N-S to NNW-SSE (176°±5.8°) and NE-SW (048°±5.5°).

Lupata Volcanic Province (LVP)

The filtered SADC regional aeromagnetic grid (Figure 48a) shows that both the Monte Muambe Volcano (MV) and Salambidwe Igneous Structure (SIS) are characterized by prominent ~10 km-wide ring-shaped magnetic-high anomalies. Over a distance of 140 km south-southeast from the Monte Muambe Volcano, we identify multiple ring-shaped high-amplitude magnetic anomalies that have similar diameter (7.5 – 19 km) as the Monte Muambe Volcano magnetic anomaly (white and red open stars in Figures 48a-48b). These identified ring-shaped anomalies do not correspond to any distinct surface topographic feature; however, the anomalies delineate a NW-trending belt that is parallel to the adjacent rift-bounding fault, the Tete Fault System (dotted yellow line in Figure 48b).

Distribution of Top-Basement Minimum Fault Throw

We present a map of depth-to-magnetic basement calculated from the aeromagnetic grid (Figure 53a), the distribution of sub-aerial and subsurface fault offset measurements for the Mwanza-Namalambo Fault (Figures 53b-c) and the Thyolo-Muona-Camacho Fault System (Figures 54a and 54b).

Mwanza-Namalambo Fault: Scarp Height and Footwall Elevation

Overall, the sub-aerial segment of the Mwanza Fault (A – C; Figure 53a) is characterized by a southeastward decrease in scarp height (max. ~200 m) and footwall elevation (max. ~700 min) up till a location 'B' (15 m scarp height, 137 m footwall elevation) beyond which the fault scarp is not visible (SDZ; Figure 53b). Over a distance of ~65 km further southeast, the surface topography gently decreases southeastwards up to a location 'C' at which the scarp of the Namalambo Fault (C – D; Figure 53a) rises abruptly and increases southwards attaining >300 m scarp height and

~700 m maximum footwall elevation. In the scarp height vs distance distribution, we identify three sub-aerial sub-segments along the analyzed portion of the Mwanza Fault (Mwanza-SA1 to -SA3) based on the locations of prominent minima. Whereas, the Namalambo Fault segment of the figure only shows two sub-aerial sub-segments which includes Namalambo-SA1 and -SA2.

Mwanza-Namalambo Fault: Depth-to-Magnetic Basement and Minimum Fault Throw

The distribution of depth-to-magnetic basement estimates along the Mwanza-Namalambo Fault (Figure 53c) shows maximum values along the buried Mwanza (~ 2.5 km) and exposed Namalambo Fault segments (~ 2.7 km). The location of the lowest basement depth estimate is collocated with the transition zone between the buried Mwanza Fault segment and the Namalambo Fault. The Top-Basement minimum fault throw distribution shows a trend that is similar to that of the depth-to-magnetic basement (Figure 53c). Based on the minima of the Top-Basement throw fitting curve, we identify a total of four subsurface sub-segments along the Mwanza Fault (Mwanza-1 to -4), and two along the Namalambo Fault (Namalambo-1 and -2).

A striking feature along the trend of the MFT datapoints and curve is the abrupt change in the throw values and curve gradient (throw-step) at about 5 km SE from location 'B', and 5 km NW of the location 'C'. Locations B and C are essentially the southern tip of the exposed Mwanza Fault segment and northern tip of the Namalambo Fault respectively. Along the buried segment of the Mwanza Fault, the highest throw, and thickest section of Cenozoic cover (1.5 km) occur at the Mwanza-3 sub-segment. The thickness of the Cenozoic cover decreases towards the locations B (~856 m at SSDZ) and C (~ 860 m at SSDZ).

Thyolo, Chisumbi, Muona, and Camacho Faults: Scarp Height and Footwall Elevation

The scarp height measurements along the Thyolo Fault (E – G; Figure 53a) describe two broad zones in which a western half show significantly low scarp (max. 52 m; Mwanza-SA1 to -SA3) and prominently high scarp on the Mwanza-SA4 (max. 91 m) and significantly lower scarp (max. 12 m) on the easternmost Mwanza-SA5 segment. The Thyolo Fault footwall elevation also shows a similar along-fault trend as the scarp height with the highest footwall elevation on the Thyolo-SA4 and -SA5 sub-segments, but relatively lower elevations along Thyolo-SA1 to -SA3. The Chisumbi Fault (F – I; Figure 53a) shows a steep southward increase in scarp height with a maximum value that is higher than that of the adjacent Thyolo Fault (52 m in the north and 127 m in the south). Also, we observe that the Chisumbi scarp height fitting curve show a south-facing 'half-bell' shape.

The Muona Fault scarp (I – J; Figure 53a) appear to show a peak value of ~100 m (similar to that of the Thyolo Fault) and three sub-aerial sub-segments (Muona-SA1 to -SA3). Interestingly, the moving average fitting curve of the Muona scarp height also delineates a west-facing 'half-bell' shape (facing the zone of intersection with Chisumbi Fault). The Camacho Fault (K – L; Figure 53a) scarp height and footwall elevation show values that are generally low (48 m maximum scarp height, 483 m maximum footwall elevation), similar to those of the western half of the Thyolo Fault. We identify three possible sub-aerial sub-segments along the Camacho Fault, which include Camacho-SA1 to -SA3. Overall, along the Thyolo-Muona-Camacho border fault system, the zones of highest scarp are collocated within the region of overlap between the Thyolo and Muona Faults (Figure 54a). This high-scarp region is collocated with the widest section of the Elephant Marsh (lower panel in Figure 54a) with boundaries that show abrupt increase in wetland width to the west, and abrupt decrease to the east.

Thyolo, Chisumbi, Muona, and Camacho Faults: Depth-to-Magnetic Basement and Minimum Fault Throw

The calculated Top-Basement minimum throw along the Thyolo-Chisumbi-Muona Fault (E – F – I – J; Figure 54b) shows a similar trend to that of the basement depth. Based on the distribution of major throw minima, we identify five distinct subsurface sub-segments along the fault system (Thyolo-Muona-1 to -5). The largest Top-Basement throw maximum (~1.4 km) occurs on the Thyolo-Muona-4 sub-segment (i.e. Muona segment of the system) which shows a smooth decrease across the Chisumbi Fault into the adjoining Thyolo Fault segment. The lowest throw maximum occurs on the Thyolo-Muona-3 sub-segment.

Further, we observe that the subsurface sub-segment with the overall maximum throw (Thyolo-Muona-4) is also collocated with the sub-aerial region of maximum scarp heights (Figures 54a-b). Additionally, the buried Muona Fault segment (H – I; Figure 54b) is characterized by westward asymmetric Top-Basement throw, but with significantly lower values than those of the exposed Muona segment. The composite throw curve (brown dashed curve in Figure 54b) indicates that the Thyolo-Muona-3 sub-segment is a distinct subsurface sub-segment along the fault system.

DISCUSSION

New Interpretation of the Shire Rift structure

Although the broad geologic history of the Shire Rift has been previously identified, only the Lengwe, Mwabvi, and Ngabu depocenters were distinguished while the rest of the basin is referred to as the Middle Zambezi Valley (Castaing, 1991, Chisenga et al., 2019). Thus, the detailed structure, complete basin compartmentalization and the associations with the phases of extension is not known.

The extent and distribution of fault-bounded Mesozoic and Cenozoic sedimentary and volcaniclastic deposits in the Shire Rift (Figure 46a) present a multiphase rift basin with distinct compartmentalization (Figure 50a) that is facilitated by complex brittle and thermomechanical deformation (Figure 50b). Based on the integration of surficial geology (Figure 46a) and the filtered aeromagnetic datasets, we identify seven structural domains in the basin, which include six sub-basins (Ngabu, Mwabvi, Lengwe, Monte Muambe, Moatize, and Chiuta) and a volcanic province (Lupata Volcanic Province). We consider the Lupata Volcanic Province (LVP) as an intrabasinal domain where syn-rift volcanism is super-imposed on older sedimentary units of the Moatize, Monte-Muambe, and Mwabvi sub-basins (Figure 50a). The surface morphology of the Shire Rift (Figure 50b) shows that the largest rift shoulder elevation gradients are located in the northwesternmost domain (Chiuta sub-basin; profile P1, Figure 50b) and the southeasternmost domain (Ngabu sub-basin; profile P2, Figure 50b). The Ngabu sub-basin sits on the buried (non-surface-breaking) southern segment of the Mwanza Fault (Figure 50c; Castaing, 1991; Chisenga et al., 2019).

Based on the distribution of magmatic intrusions, volcanic deposits, and timing of magmatic activities in the Shire Rift (e.g., Castang, 1991; Figures 46a and 50c), we characterize the sub-basins into magmatic and non-magmatic categories (Figure 50a). Also, previous stratigraphic and geochronologic studies on the Shire Rift (Castaing, 1991), age-distribution of surficial rocks (Figure 46a; Choubert et al., 1988), and the gravity study of a part of the basin (Chisenga et al., 2019) allow us to identify the rifting phase to which each sub-basin is associated. The observations suggest that the Lengwe, Mwabvi, Moatize, and Monte Muanbe sub-basins were established and most active during the Phase-1 rifting (Permian-Jurassic) (Figures 46a and 50a). Jurassic-age magmatic plumbing of the rift (Castaing, 1991; Figure 46a) indicates that these Phase-1 sub-basins

are magmatic. Phase-2 rifting (Middle Jurassic - Cretaceous) primarily focused rift-axial volcanism in the LVP and Lengwe sub-basin, and off-rift magmatism farther northeast, away from the evolving rift. The currently active Phase-3 rifting is non-magmatic and is associated with the northwestward propagation of the early phase rift tip into the Chiuta area (Chiuta sub-basin), and the widening of the SE termination of the rift (Ngabu sub-basin). Having identified the sub-basins and the rift-phase to which they're associated, we present evidence below that demonstrates the influence of continuous progressive structural inheritance on the evolution of the Shire Rift.

Phase-1 (Karoo, Permian – Early Jurassic) Rifting and the influence of inherited Structures

Border Fault Development

The Phase-1 sub-basins (Figure 50a) describe an overall rift-geometry that trends NW-SE. The Phase-1 rift-bounding faults (Mwanza-Namalambo, Tete, Moatize, and Salambidwe Faults; Figure 46a) and the surrounding pre-rift basement metamorphic fabrics show geometrical relationships that provide insight into the mechanics of early-stage rift faulting. Along the Mwanza Fault footwall, the pre-rift fabrics show a mean trend (140°±1.9) that is parallel to the trend of the Mwanza Fault (130° black arrows in Figure 51b). This fabric trend is consistent with the geometry of the easternmost segment of the Precambrian Sanangoe Shear Zone (SSZ, Figure 50a; Barr and Brown, 1987). The SSZ has been described as a crustal-scale south-dipping fault that juxtaposes different blocks of gabbro-anorthosite metamorphic complexes (Barr and Brown, 1987). Likewise, along the Salambidwe Fault footwall (NE margin of the Cana-Cana Horst), the aeromagnetic fabrics and DEM fabrics (Figures 48a, 51a) trend NW-SE, parallel to the Salambidwe Fault trend. Along the segments of the Tete Fault System, this same relationship is also evident in filtered aeromagnetic grid (Figure 48a) and published geologic maps (Choubert et al., 1988).

Although some of the border fault segments appear to cross-cut pre-rift metamorphic fabrics (Namalambo Fault and Moatize Faults; Figures 48a-b, 51a), our observations show that most of the Phase-1 cumulative border fault length align with the surrounding pre-rift basement fabrics. The uniform trends of the gneissic basement foliation along the border fault zones constitute alternating planes of high and low shear and tensile strengths (mechanical anisotropy) that are favorably-oriented for brittle reactivation in the Phase-1 tensional stress field (e.g., Donath, 1961; Youash, 1969; Ranalli and Yin, 1990; Morley, 1999, 2010). Such well-oriented planes of mechanical weakness in the host basement allow the early-stage rift faults to nucleate and easily propagate through the crust. This interpretation is consistent with previous observations in different parts of the Shire Rift (e.g., Cooper and Bloomfield, 1961; Castaing, 1991; Williams et al., 2019) and other rift segments of the East African Rift System (Kinabo et al., 2007; Morley, 1999, 2010; Wheeler and Karson, 1989, 1994; Kolawole et al., 2018; Heilman et al., 2019). Therefore, we infer that in the earliest episode of extension in the Shire Rift, the inherited Precambrian metamorphic fabrics largely controlled the location and geometry of the border fault systems.

Rift Bifurcation and Termination

The distribution of Permo-Jurassic rocks in the Shire Rift (Figure 46a) provides insights into the extent of the rift basin during the Phase-1 extension episode. To the northwest, the rift bifurcates around the Cana-Cana horst and splays into the Lengwe sub-basin and Moatize sub-basin segments, and terminates at the NNE-trending segment of the Sanangoe Shear Zone (Figures 48a-b, 50a). The eastern continuation of the SSZ is collocated with and trends parallel to the Machenga Transfer Zone (MTZ) which separates the Lengwe sub-basin from the Chiuta sub-basin (Figure

48b). To the SE, the phase-1 border fault (Mwanza Fault) deflects from a NW-SE trend into a N-S trend (Namalambo Fault) in the vicinity of dominantly NE-trending distributed basement fabrics (Figure 51f) and the associated NE-trending Precambrian Lurio Shear Zone (LSZ, Sacchi et al., 2000). Essentially, the Phase-1 SE rift termination occurs at its intersection with the Lurio Shear Zone (Figures 45a, 48a-b). The basement fabrics within the Cana-Cana Horst show multimodal azimuthal trends with dominant sets in the NE-ENE and NW orientations (Figure 51d). Also, the aeromagnetic fabrics within the Machenga Transfer Zone (Figures 48a-b) show dominantly NE trends.

In summary, these observations suggest that the presence of rift-oblique and -orthogonal fabric sets at the propagating tip of a young rift poses a potential mechanical barrier to rift lengthening at the earliest stage of rifting. This is consistent with observations in the Okavango Rift, a zone of nascent rift development, where the rift and its bounding faults terminate at the Precambrian Sekaka Shear Zone (Kinabo et al., 2007). The rift-oblique and -orthogonal fabrics represent misoriented planes of weakness, which may cause the rift to deflect or splay into multiple narrower segments that propagate around the block of misoriented fabric. The influence of isolated blocks of variable fabric orientation on rift bifurcation has also been observed in the Rukwa Rift where the basin bifurcates around the Mbozi Horst, a block of rift-oblique pre-rift fabric trends (Heilman et al., 2019).

Phase-2 Rifting (Middle Jurassic - Cretaceous) and the influence of inherited Structures

Structurally-Controlled Magma-Plumbing

The distribution of exposed and sub-aerial Mesozoic magmatic centers (Figures 46a, 48a-b, 50c) shows that Phase-2 rifting was associated with both rift-axial (e.g., LVP and Salambidwe Igneous

Structure) and off-rift magmatism (e.g., Zomba-Blantyre igneous centers). The associated mafic dikes are observable on the filtered high-resolution aeromagnetic grids covering the Lengwe sub-basin and Mwanza Fault hanging wall (Figure 55a) and the Mwabvi sub-basin and Namalambo Fault hanging wall (Figure 55b). In the Lengwe sub-basin, the mafic dike segments show multimodal azimuths with N, NE-NNE, and NW dominant trends (Figure 51g). Among these three trends, the NW set (143°±4.1) is parallel to the Mwanza Fault trend (130° black arrow in Figure 51g) and the surrounding basement metamorphic fabrics (140°±1.9, Figure 51b). In the Mwabvi sub-basin, the mafic dikes show dominant N-NNW (176°±5.8) and NE (048°±5.5) trends (Figure 51h). The bounding Namalambo Fault trends NNW-SSE (~170° black arrow in Figure 51h). The Nsanje Horst (Namalambo Fault footwall) is dominated by NE-trending basement metamorphic fabrics (field observations in Bloomfield, 1958), consistent with the trend of metamorphic fabrics in the adjacent SE rift termination zone (060°±10.3, Figure 51f).

Previous studies on the Shire Rift dikes (e.g., Habgood et al., 1973, Castaing, 1991) only observed the NE-SW and NW-SE dike orientations. The NE-trending dikes were inferred to be associated with both the Early Jurassic (Late Phase-1) and Late Jurassic-Cretaceous (Phase-2) magmatic rifting (Woolley et al., 1979). Castaing (1991) inferred that the NE and NW dikes sets were emplaced in different extensional stress regimes caused by stress rotation between the Late Karoo and Cretaceous episodes of rifting. The Karoo dikes are diabase in composition, whereas the Cretaceous dikes are mostly alkaline (e.g., Woolley et al., 1979; Castaing, 1991), and both dike categories are found in the same areas within the basin. Diabase and alkaline dikes typically have appreciable concentrations of magnetite and may be indistinguishable in aeromagnetic data (e.g., Ragland et al., 1983; Dutra et al., 2014). Thus, for convenience, we refer to the analyzed dike trends as the Phase-1-2 dikes.

Therefore, the proximity of location and trend of the N-NNE trending dikes to the Namalambo Fault scarp (Figure 55b) suggest that the inherited Phase-1 border fault segment influenced the propagation and emplacement of the Phase-1-2 mafic dikes in this part of the basin. Likewise, the similarity of orientation between the NE dike sets (border-fault oblique) and the surrounding basement metamorphic fabrics (Namalambo Fault footwall; Bloomfield, 1958) suggest that within the associated stress field, the inherited fabrics may have also influenced the propagation of the NE-trending dikes. The consistency of trend between the NW dikes in the Lengwe sub-basin, the adjacent Mwanza Fault (e.g., Dike-X in Figure 55a), and the surrounding basement fabrics provides additional evidence for the influence of the inherited pre-rift and early Phase-1 structures on the emplacement of the Phase-1-2 dikes. Faults and prominent basement fabrics often cause local stress rotations in the crust, thus locally controlling the patterns of active deformation and fluid flow (e.g., Morley, 2010; Kolawole et al., 2017). In addition to these findings, we observe that the mapped magmatic centers in the LVP (Figures 48a-b) show a NW-SE (~155°) axial trend that is parallel to the trend of the adjacent Tete Border Fault. This pattern of magmatism is reminiscent of previous observations in the Northern Malawi and the Kivu Rifts where magmatic centers form linear clusters that are collocated with intrabasinal faults that trend parallel to the adjacent border faults and basement fabrics (e.g., Fontijn et al., 2010; Smets et al., 2016; Heilman et al., 2019).

Therefore, we interpret that the inherited pre-rift basement metamorphic fabrics and early Phase-1 faults influenced the Phase-1-2 magma plumbing of the Shire Rift by serving as surfaces of reduced cohesion and reduced tensile strength that allow for tensile (dilation) or shear activation within the tensional stress field. The reactivated inherited structures thus may have served as

conduits for magmatic fluids to migrate up to intrabasinal vents and laterally across the basin into off-rift domains.

Phase-3 (Cenozoic) Rifting and the influence of inherited Structures

Rift Lengthening and Propagation of Previously Stagnated Rift Tip

The Chiuta sub-basin developed in the presently ongoing rifting episode further northeast of the earlier Lengwe sub-basin, separated by the Machenga Transfer Zone (Figure 50a). Surface topography and geology shows that the transfer zone is dominated by shallow Precambrian basement (Figure 46a) and the NE-trending fabrics of the SSZ (Figures 48a-b, 50a). Northwest of the SSZ, regional trends of basement metamorphic fabrics show ENE (074° – 079°) and NW-SE (134° - 147°) dominant sets (Figure 51e). However, locally, along the footwall and hanging wall of the Chiuta border fault, DEM and filtered regional aeromagnetic grid show distributed NE-trending basement fabrics (Figures 48a, 51a). At ~28 km SW of the Chiuta border fault, outcrop continuation of the SSZ shows a major NW-trending kink in the geometry of the shear zone (Barr and Brown, 1987; Figure 48b). This kink is parallel to the NE fabrics in the Chiuta sub-basin (Figure 48b).

On the eastern rift shoulder of the Chiuta sub-basin, the Mwanza Fault splays into two NW-trending segments that form a west-dipping synthetic border fault system. The basinward Mwanza splay trends across the eastern extension of the SSZ and the surrounding fabrics, but the craton-ward splay segment is collocated with and parallel to a bend and NW-trending segment of the SSZ (Figures 48a, 50a). Based on the observations above, we interpret that the nucleation of the Chiuta border fault and establishment of the Chiuta sub-basin was influenced by the brittle reactivation of NW-trending fabrics (favorably-oriented with respect to the stress field) within an isolated crustal

block near-field and colinear to the Machenga Transfer Zone. This reactivation style reflects an exploitation of the pre-rift fabrics by the Chiuta Fault. Overall, these observations demonstrate the influence of inherited pre-rift fabrics on the lengthening of propagating rift segments.

Rift Widening by the Development of New Synthetic Border Fault System

Previous studies (Casting 1991, Chisenga et al., 2019) have showed that the Ngabu sub-basin is a Cenozoic sub-basin, bounded by Cenozoic faults (Castaing et al., 1991). These faults are active in the current stress field, evidenced by the earthquake epicenters (and associated fault plane solutions) close to the Camacho and Thyolo Faults, and detailed geomechanical analysis (Williams et al., 2019). We observe that the Phase-3 lengthening of the Shire Rift in the NW is not observable in the SE termination of the rift; instead, a new depocenter (Ngabu sub-basin) opened up on the eastern flank of the rift, bounded by the Thyolo, Muona, and Camacho synthetic fault segments that form a staggered fault pattern (Figures 50a-b). Although the Quaternary sediments of the Ngabu sub-basin are largely bounded by the Cenozoic border fault system, there exists a region of Quaternary deposits extending along the scarp of the Mwanza Fault (Figure 46a; Habgood, 1963), thus indicating a partial reactivation of the Mwanza Fault in the Phase-3 rifting episode.

Along the Thyolo-Muona footwall, azimuthal distribution of the pre-rift basement metamorphic fabrics trend parallel to the Thyolo and Muona fault trends (Figure 51c). The northwestern segment of the Thyolo Fault bends from a NW trend into NNW trend at the transfer zone between the Shire Rift and the Southern Malawi Rift (Zomba Graben) (Figure 51a). The filtered aeromagnetic grid (Figure 52a) and published field observations (Figure 52b) reveal the collocation of the western Thyolo Fault segment with an exhumed Precambrian shear zone. Therefore, we interpret that the Phase-3 crustal extension is characterized by the widening of the Shire Rift, facilitated by: (1.)

retained stagnation of the SE rift termination at the Precambrian Lurio Shear Zone (Figure 48b), and (2.) exploitation of well-oriented (with respect to the current stress field) pre-rift basement fabrics by the relatively new synthetic border faults on the flanks of the early phase rift.

Hard- and Soft-Linkage of Newly Formed Synthetic Border Fault Segments

The term 'hard-link' refers to the overlap zones of interacting fault segments in which the faults are physically connected by a secondary fault; whereas, 'soft-link' refers to the case whereby the interacting faults are separated by a relay zone that lacks the presence of well-defined connecting faults (Fossen, 2010). The scarp and throw morphology of the Phase-3 border fault segments (Figures 54a-b) shows a striking collocation between the region with the largest scarp heights (Thyolo-SA4 – Chisumbi-SA – Muona-SA1 – Muona-SA2) and the region with the largest Top-Basement minimum throw (Thyolo-Muona-3). However, other segments of the fault system show interesting sub-aerial and subsurface segmentation of fault offset. To better understand the controls on offset distribution along the fault system, first, we assess the inherited basement structure along the Thyolo Fault footwall (Figures 56a-b).

We observe that the Thyolo-Muona-2 segment bounds a footwall crustal block of different magnetic character to those of the Thyolo-Muona-1 and -3 segments. Published field observations (Habgood et al., 1973) suggests that the Thyolo-Muona-2 segment propagated across a large block of Precambrian intrusion (deformed and overprinted by gneissic foliation) that outcrops in the Thyolo Mountain area (Figure 56a). We observe that the Thyolo-Muona-1 to -2 transfer zone is collocated with the western boundary of the magnetic anomaly associated with the intrusion, whereas, the Thyolo-Muona-2 to -3 transfer zone occurs near the eastern boundary of the magnetic anomaly. Additionally, these transfer zones are collocated with the change in the plan-view

geometry (curvilinearity) of the Thyolo Fault scarp (Figure 56b). These observations present a possible influence of the pre-rift basement structure on the segmentation of the Thyolo Fault.

More importantly, in the hanging wall of the Thyolo Fault, we identify a magnetic gradient representing a NW continuation of the synthetic Muona Fault (Figures 56c-d), separated from the exposed Muona Fault by the Chisumbi Fault which physically connects the Muona Fault to the Thyolo Fault (Figure 56d). Similarly, the Chisumbi separates the western Thyolo Fault hanging wall (with significant sedimentary cover) from the eastern part of the fault where there is little or no sedimentary cover; SDZ in Figure 54a). Interestingly, the region of sub-aerial linkage of the Thyolo, Chisumbi, and Muona Faults show the largest scarp height and Top-Basement throw. In fact, the minimum throw fitting curve shows continuous increase across the Chisumbi linking segment (projection of SDZ into Figure 54b). Whereas, the abandoned Muona Fault segment shows relatively low throw compared to the exposed Muona segment (Figure 54b), and the abandoned Thyolo segment shows lower scarp heights compared to the western segments (Figure 54a).

Therefore, based on the physical linkage of the exposed Muona Fault and the western Thyolo Fault through the Chisumbi Fault, and the localization of the largest sub-aerial and cumulative fault offset across the zone of linkage between the faults, we describe the Thyolo-Muona Fault as a hard-linked fault system. In addition, the relatively lower offsets on the abandoned segments suggest that although the Thyolo and Muona Faults initially formed as individual synthetic border faults, the hard-linkage of the faults most-likely occurred shortly after the establishment of the segments, such that the coalescence of the faults facilitated increased strain accommodation across the linked segments. This interpretation is supported by the variation in the along-rift trends of the width of the Elephant Marsh, a >600 km^2 wetland on the Thyolo-Muona Fault footwall (Figures

50a-b and 54a). Although the Elephant Marsh extends along most of the length of the Ngabu sub-basin, there is an abrupt widening of the marsh at the western boundary of the largest scarp height (and largest throw) region and abrupt narrowing at the eastern boundary of the region (lower panel of Figure 54a). Thus, the widest part of the wetland shows a marked collocation with the zone of largest fault offset along the synthetic border fault system. This observation is not surprising as the distribution of wetlands (lakes and swamps) along active continental rifts often provide insight into the distribution of extension. Common examples include the distribution of isolated lake bodies along the Okavango Rift (e.g., Shemang and Molwalefhe, 2011; Alvarez Naranjo, 2016), and the along-rift variation of Lake Malawi water depth (Laó-Dávila et al., 2015).

Aeromagnetic analysis and field data show that the Thyolo-Muona-Camacho border fault system is emplaced in a crust that has been pervasively intruded by NE-trending diabase dike swarms (Figure 51c) associated with Late Phase-1 rifting episode (Habgood et al., 1973). Integration of outcrop-mapped dike lineaments (from Habgood et al., 1973) with interpreted subsurface and sub-aerial dike lineaments from aeromagnetic and hillshade maps (Figure 56c) show that the NE-trending Chisumbi Fault is flanked to the west by buried NE-trending dike lineaments, and to the east by exposed NE-trending dikes. On the footwall of the Thyolo Fault, we observe NE-trending diabase dikes that cross-cut the NW-trending crystalline basement foliation (Figures 56e-f). We observe that the diabase dikes show sharp, discrete contacts with the host rocks, with clustering of en echelon dike-parallel fractures along or near the dike contacts (Figure 56e). We do not observe any mineralogical alteration along these en echelon fractures, thus implying fracture surfaces of relatively lower cohesion.

These field observations suggest that although the contacts of the mafic dikes may represent zones of lower shear strength (relative to the intact bounding rocks), the occurrence of colinear brittle

fracture planes with low cohesion near the contacts present additional zones of weakness where new faults may nucleate and propagate along the associated dike contact (Figure 57a). Therefore, based on the evidences presented above, we interpret that the Chisumbi Fault developed by the brittle exploitation of weak dike contacts in the hanging wall of the Muona Fault, leading to the dislocation of the Muona Fault (sub-surface fault dislocation zone, SSDZ in Figure 54b). Thus, the hard-linkage of the Thyolo-Muona synthetic border faults was strongly controlled by the inherited early dikes. Our interpretation of hard-linkage is consistent with recent field study along the Thyolo-Muona Fault (Wedmore et al., 2020).

Furthermore, we observe that to the east, both the Thyolo and Muona Fault segments terminate at a zone of conjugate dike clusters consisting of N and NW-trending dike sets (e.g., the Mulata Dike Cluster; Figures 56a-d). Likewise, the western tip of the Camacho Fault terminates at the Mulata Dike Cluster. Thus, we interpret that the inherited early phase dikes pose barriers to the development of a single Phase-3 border fault, resulting in the nucleation of multiple synthetic border fault segments that are soft-linked across the zone of conjugate dike cluster. This may also imply that at this initial stage of development, the maximum lengths of these border fault segments are delimited by the inherited dikes.

Dislocation of Long-lived Faults

Although the Mwanza-Namalambo Fault had been established since the first phase of extension in the Shire Rift, the partial reactivation of the Mwanza Fault in the ongoing phase exemplifies the long-lived activity of the fault. However, we observe that the central segment of the Mwanza-Namalambo system (South Mwanza Fault; Figure 53b) is buried, whereas the northern partially-reactivated segment, and the Namalambo segment are exposed (Figure 47c). Based on the spatial

confinement of the Mesozoic volcanic flows to the hanging wall of the Mwanza Fault, and absence of Mesozoic-age sedimentary rocks east of the Mwanza Fault, the Mwanza-Namalambo Fault is interpreted to be the eastern border fault of the Phase-1 and Phase-2 rifts (Castaing, 1991). Thus, the burial of the central segment of the fault system must have occurred in the early stages of the ongoing Phase-3 extension. To better understand the influence of the inherited early phase structures on the decoupling and burial of major segments of the long-lived Mwanza-Namalambo Fault, we first assess the distribution of throw along the fault, then we analyze the structure of the transition zone between the buried and exposed Mwanza-Namalambo Fault segments.

Two major throw-steps along the Mwanza-Namalambo Fault occur at the transition zones between the exposed and buried segments of the fault (SDZ-SSDZ; Figures 53b-c). Overall, based on the locations of throw minima, we observe that the Mwanza-2 and Namalambo-1 sub-segments extend across the transition zones into the buried segments of the fault. Essentially, the throw-distance curve describes basinward throw-steps which record the history of dislocation of the fault segment (subsurface fault dislocation zones, SSDZ). Such throw-steps define locations of interaction between an older fault and a younger propagating fault segment (Duffy et al., 2015).

The subsurface dislocation zone between the North and South Mwanza Faults is characterized by a northeastward side-stepping of the fault-related magnetic gradient (Figures 58a-c). Filtered aeromagnetic grid and satellite image (Google Earth©, Figure 47f, Figures 58a-b) show pervasiveness of NE-trending dikes on the Mwanza Fault footwall (Figure 51b) and the dislocation zone between the exposed and buried Mwanza segments (Figure 58c). We observe that the side-steps are collocated with segments of the NE-trending aeromagnetic dike lineament set that cross-cut the fault (Figures 51b and 53c). Likewise, the subsurface dislocation zone between the Namalambo and buried Mwanza Fault segments show northeastward side-stepping fault geometry

that is collocated with dike-bends along Namalambo Fault-controlled dikes ('dike-bends' in Figure 55b). In some cases, the dike-bend may occur at the coalescence of a NE dike with a Namalambo Fault-controlled dike (e.g., Dike Bend B in in Figure 55b). Therefore, as observed along the Muona Fault, we interpret that the brittle reactivation of the contacts of the NE-trending dike segments created the NE-stepping shear surfaces that accommodate relative slip between the exposed and buried fault segments, thus allowing the buried Mwanza Fault segment to subside beneath the Cenozoic sediments (Figure 57a).

We interpret that the throw-steps along both the Mwanza and Namalambo Faults indicate 'throw-starvation' related to the interactions with the faults that reactivated the dike contacts (e.g., Duffy et al., 2015). Although the dislocation faults appear to have accommodated oblique normal and/or strike-slip offsets (side-stepping of the fault in Figures 55b, 57a), the relative magnitude of the throw-steps may provide additional insight on the growth history of the faults. The Mwanza-2 throw-step shows considerable throw magnitude on its deeper section, whereas the Namalambo-1 throw-step does not, suggesting that the Mwanza-2 sub-segment has been reactivated after its dislocation. However, the significantly lower throw on the deeper section of the Namalambo-1 throw-step may have been driven by flexure in response to dislocation-induced displacement variations along-strike of the fault (Figure 57a).

Progressive Structural Inheritance and Feedback between Inherited Structures in the Early-Stages of Continental Rifting

Our observations in the Shire Rift demonstrate how the inheritance of the earlier-emplaced faults and magmatic intrusions continue to influence the localization and distribution of deformation in an evolving young continental rift. The Precambrian metamorphic fabrics were inherited by the

Phase-1 rifting episode, revealed in the influence on border fault location and geometry, and in a few locations (Mwabvi sub-basin) emplacement of the Phase-1 dikes (Figure 57b). However, the Late Phase-1 diking and the Phase-2 rifting episode inherited both the Precambrian fabrics and the Phase-1 faults, which influenced magma plumbing of the rift in the Jurassic and Cretaceous (Figure 57c). Similarly, in the ongoing Phase-3 episode, the Precambrian metamorphic fabrics, Phase-1 faults, and Phase-2 dikes influence the lengthening and widening of the Shire Rift, and dislocation of the long-lived faults (Figure 57d). Consistent with our findings, recent observations in the multiphase Northern North Sea Rift (Phillips et al., 2019) show that inherited pre-rift shear zones influenced the spatial distribution of depocenters, temporal variation and intensity of rift activity.

Continental rifting is thought to proceed by the nucleation of isolated rift segments that subsequently link-up, resulting in the lengthening of the rift (e.g., Nelson et al., 1992; Corti, 2012; Heilman et al., 2019). Segmentation of young continental rifts may be strongly influenced by inherited crustal and lithosphere-scale structures (e.g., Acocella et al., 1999; Corti, 2004; Corti et al., 2007; Heron et al., 2019). Here, we show that prior to rift segment linkage, the episodic termination and propagation of rift tips may be largely influenced by the distribution of inherited pre-rift and earlier rift phase structures. As such, rift lengthening may be replaced by transient phase of rift widening, influenced by rift-tip stagnation at mis-oriented inherited structures.

Furthermore, beyond the continuous inheritance of structures, we present one of the first observations of static feedback between the inherited structures along continental rifts. This is demonstrated by the dislocation of the long-lived Mwanza-Namalambo Fault by the reactivation of dike-contacts along the dike-bend segments of magmatic intrusions that were earlier controlled by the Namalambo Fault itself (Figure 57d). This static feedback between inherited structures,

although rarely observed, provides further insight into one of the processes by which structural inheritance controls the multiphase evolution of evolving rifts leading to continental break-up.

CONCLUSIONS

We have analyzed the pre-rift and rift structures of the Shire Rift, one of the few multiphase segments of the East African Rift System that experienced extensional tectonics in the Permian - Early Jurassic (Phase-1), Middle Jurassic – Cretaceous (Phase-2) and Cenozoic (Phase-3). The Phase-3 rifting is ongoing, thus allowing us to assess the influence of structural inheritance on the earliest stages of the rifting episode. We have analyzed the little understood Shire Rift structure and explored the continued influence of structures inherited by each phase of rifting on the progressive development of the rift. Among our findings, the following are most prominent:

1. The Shire Rift is characterized by a complex system of six (6) major sub-basins (depocenters) that were active at different phases of extension, among which four are magmatic and two are non-magmatic.
2. Phase-1 border fault geometries and locations were controlled by the exploitation of well-oriented pre-rift fabrics, and both rift bifurcation and termination are controlled by rift-oblique and -orthogonal pre-rift fabrics, likely mis-oriented to the Phase-1 stress field.
3. Clusters of Phase-2 intrabasinal magmatic centers and mafic dikes trend parallel to adjacent border fault segments and Precambrian basement fabrics, thus indicating the combined controls of pre-rift and Phase-1 structures on the Phase-2 magma plumbing.
4. Phase-3 rift lengthening in the NW facilitated by the exploitation of rift-parallel pre-rift fabrics located near-field of the previously-stagnated rift tip.

5. Phase-3 rift widening in the SE facilitated by the retained pinning of the rift at rift-orthogonal basement shear zone, and development of a synthetic border fault system by the exploitation of rift-parallel pre-rift fabrics located off-rift and adjacent to the Phase-2 rift.
6. Hard-linkage of the Phase-3 synthetic border fault system by the reactivation of rift-orthogonal Phase-1 dike contacts as breaching faults, and soft-linkage of the fault segments across a crustal block of conjugate earlier phase dike clusters.
7. Phase-3 dislocation of long-lived Phase-1 border faults by the brittle reactivation of the contacts of dike segments originally controlled by the dike; a character that suggests static feedback between the inherited structures, and is preserved in the throw-distance plot of the dislocation zones.
8. Overall, magmatic structures and basement fabrics represent sustained controls on multi-phase rift faulting.

Therefore, we suggest that the multiphase structural evolution of young continental rifts may be strongly influenced by the continuous and progressive inheritance of structures, leading to sustained lengthening and widening of the evolving rift system.

Contributors to this project: F. Kolawole, T. Vick, E. A. Atekwana, D. A. Laó-Dávila, A. G. Costa, and B. M. Carpenter.

Acknowledgements: Thanks to Geological Survey of Malawi for providing the 2013 aeromagnetic datasets used in this study. Thanks also to the South African Development Community (SADC) for providing both the 1985 aeromagnetic dataset and the regional aeromagnetic dataset used in this study. Thanks to Geosoft for providing academic Oasis Montaj software licenses used in this study. Thanks to Elias Chikalamo, Patrick R. N. Chindandali, Lois

Kamuyango, Wesley T. Prater, Amy R. Pritt, Alejandra Santiago-Torres, and Kevin Vélez-Rosado for collecting field structural data in southern Malawi. Thanks also to Jalf Salima and Leonard Kalindekafe for supporting the logistics of our fieldwork. This research was supported by the NSF Grant No. II-1358150.

Publication of the results: Kolawole, F., T. Vick, E. A. Atekwana, D. A. Laó-Dávila, A. G. Costa, & Carpenter, B. M. (2020). Structural Inheritance and Feedback between Metamorphic Fabrics, Magma-Plumbing, and Faulting in a Multiphase Rift. *Submitted to Journal of Structural Geology*.

CHAPTER 5 FIGURES

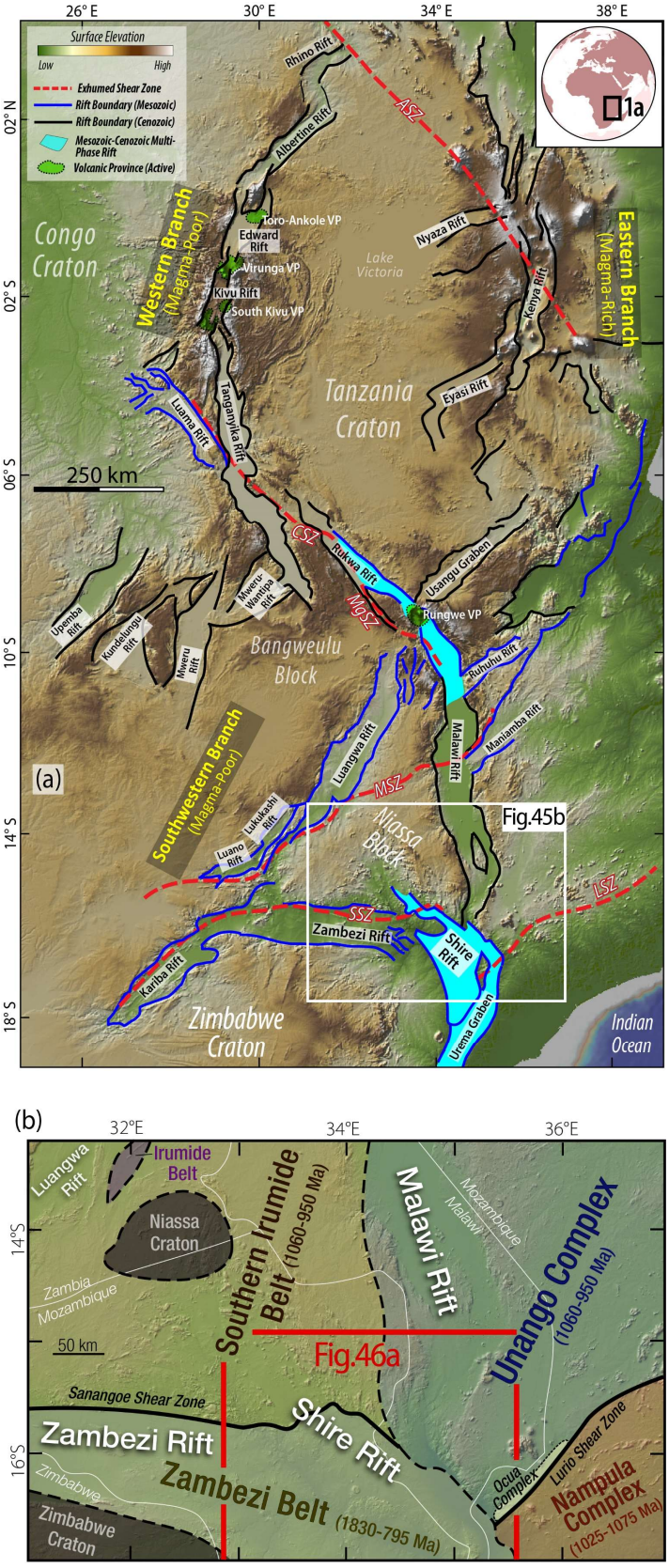

Figure 45. Regional tectonic setting. (a) Global Multi-resolution Topography (GMRT) digital elevation model (DEM) hillshade map of Eastern Africa showing the various segments of the East African Rift, and major Precambrian basement shear zones in the region (modified after Daly et al., 1989, Castaing, 1991; Delvaux, 1989; Fritz et al., 2013; Heilman et al., 2019). ASZ = Aswa Shear Zone, CSZ = Chisi Suture Zone, LSZ = Lurio Shear Zone, MgSZ = Mughese Shear Zone, MSZ = Mwembeshi Shear Zone, SSZ = Sanangoè Shear Zone. GMRT source: Ryan et al. (2009). (b) Generalized map of the Precambrian basement terranes in the sub-region of the Shire Rift (modified after Hargrove et al., 2003; Fritz et al., 2013).

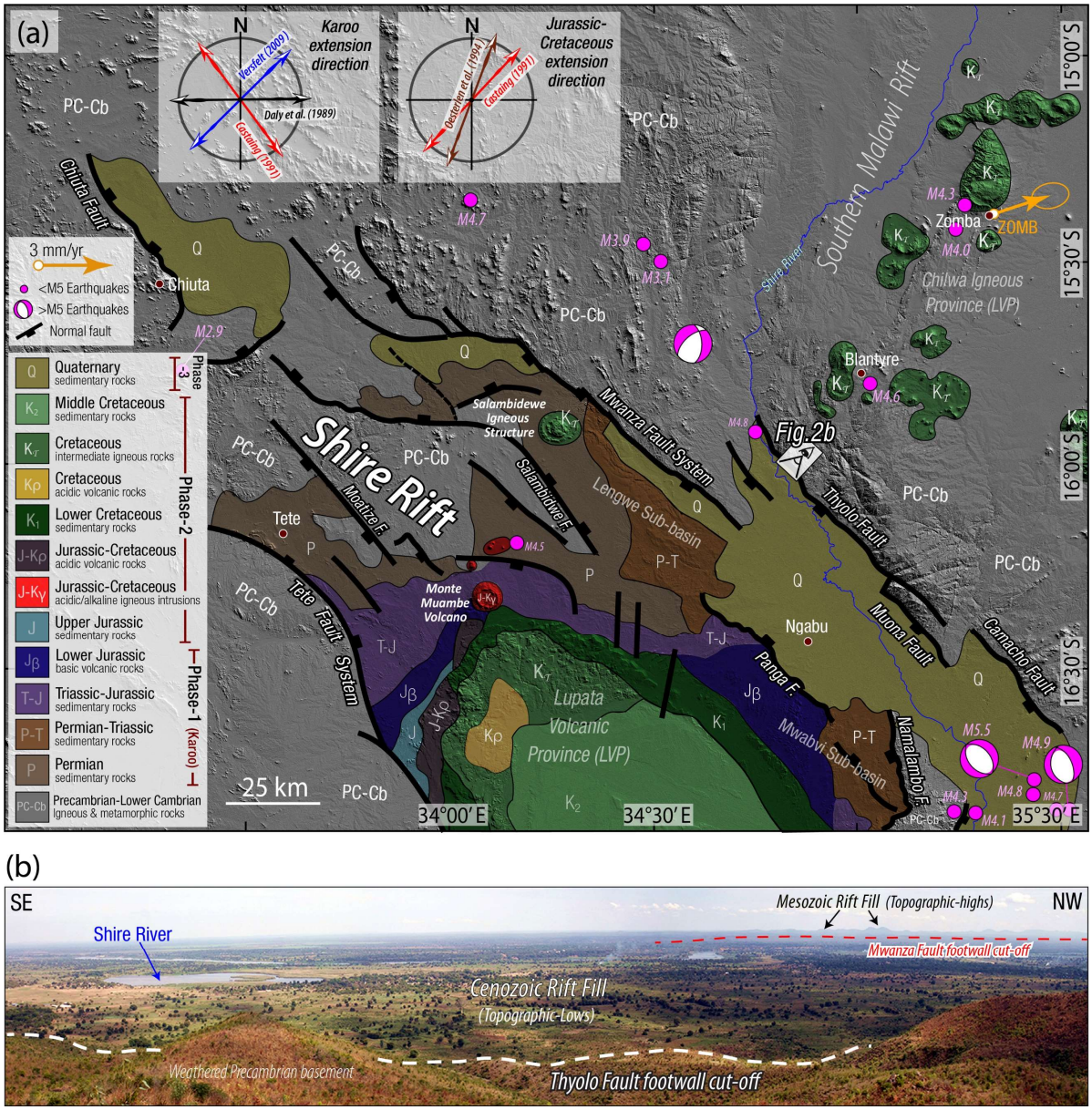

Figure 46. Geologic setting of the Shire Rift (a) Geologic Map of the Shire Rift, compiled from Habgood (1973), Habgood et al. (1963), Choubert et al., (1988), Bennett (1989), Castaing (1991), Chisenga et al. (2018), Nyalugwe et al. (2019a). Top insets show the inferred Mesozoic extension (SHmin) orientations for the region (Daly et al., 1989; Castaing, 1991; Oesterlen and Blenkinsop, 1994; Versfelt, 2009). (b) Landscape photograph of the Shire Rift, looking southwest from the Thyolo Fault escarpment (see location in Figure 46a). GNSS velocity solution with 95% uncertainty ellipse is from Stamps et al. (2018).

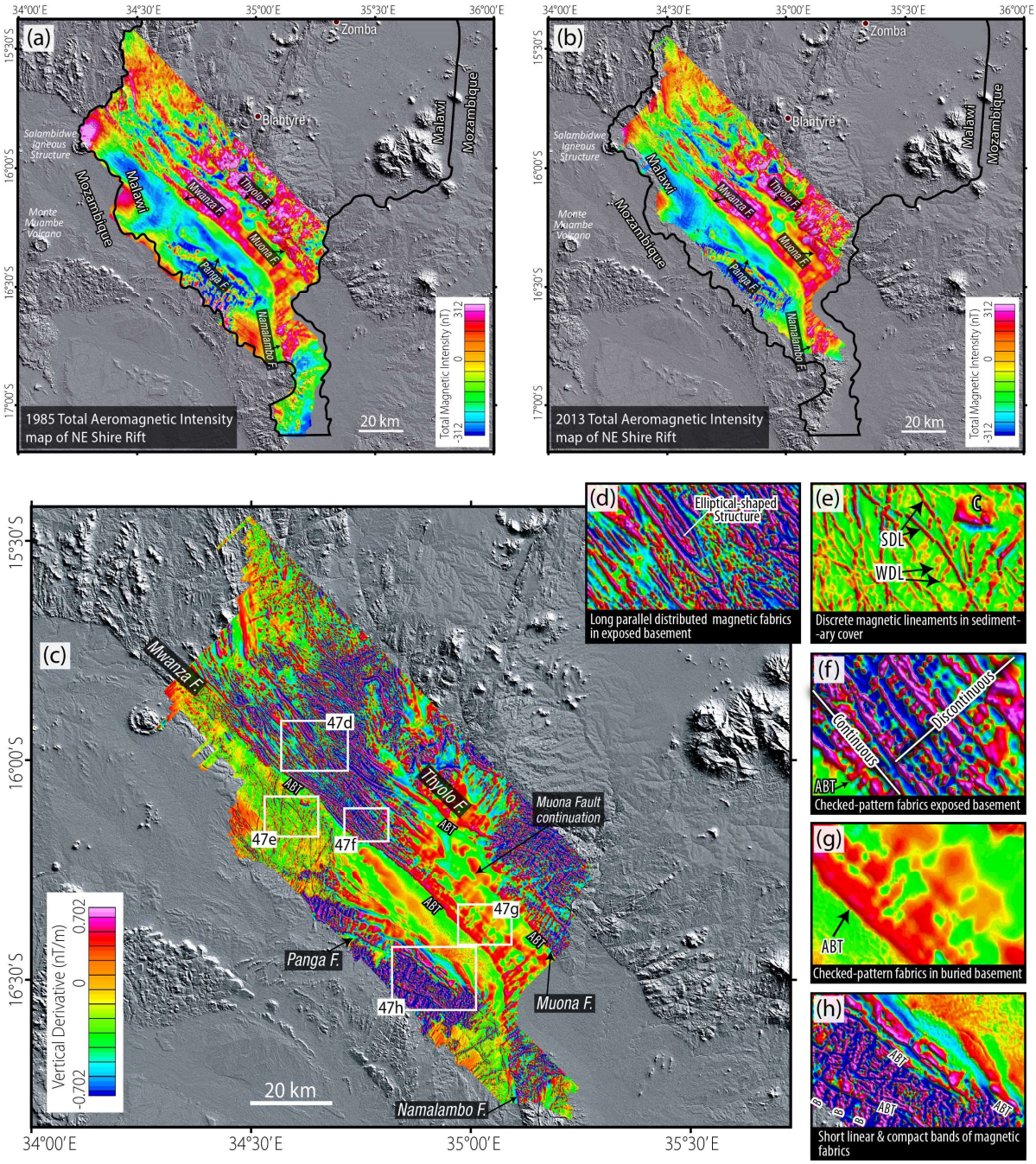

Figure 47. Aeromagnetic data and analytical methods. (a - b) Two vintages (1985 and 2013) of aeromagnetic data used in this study, overlaid on Shuttle Radar Topography Mission (SRTM) digital elevation model (DEM) hillshade map. Note that these high-resolution aeromagnetic datasets are only available for the Malawi part of the basin (see country boundary lines with Mozambique). (c) 1st vertical derivative of the 2013 aeromagnetic data overlaid on the SRTM DEM map, showing (d – h) five aeromagnetic fabric patterns (*aeromagnetic facies*) observable in the dataset and relevant to the study. ABT = abrupt magnetic gradient; SDL = Strong discrete lineament, WDL = Weak discrete lineament; B = Compact band.

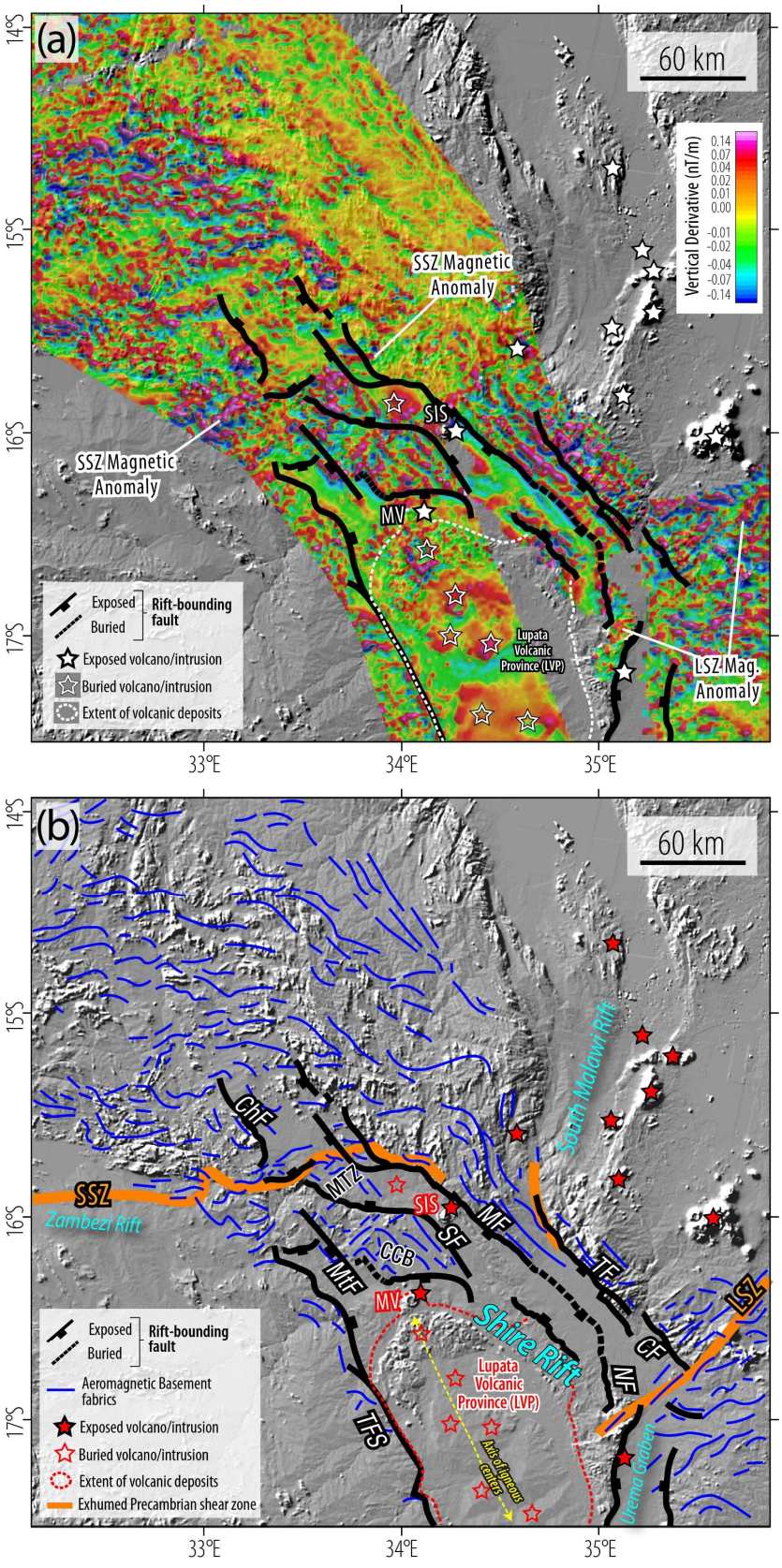

Figure 48. Regional trends of basement metamorphic fabrics. (a) Low-resolution 1st vertical derivative aeromagnetic map (from the SADC regional aeromagnetic Grid) overlaid on Global Multi-Resolution Topography (GMRT) hillshade DEM of the study area; (b) GMRT hillshade DEM overlaid with interpretations of the filtered regional aeromagnetic data. CCB = Cana-Cana Block, CF = Camacho Fault, ChF = Chiuta Fault, LSZ = Lurio Shear Zone, MF = Mwanza Fault, MtF = Moatize Fault, MV = Monte Muambe Volcano, NF = Namalambo Fault, SF = Salambidwe Fault, SIS = Salambidwe Igneous Structure, TF = Thyolo Fault, TFS = Tete Fault System. The location, geometry, and extents of the Lurio and Sanangoe Shear Zones are after Barr and Brown (1987); Sacchi et al. (2000), Kroner et al. (1997), Bingen et al. (2009), Fritz et al. (2013).

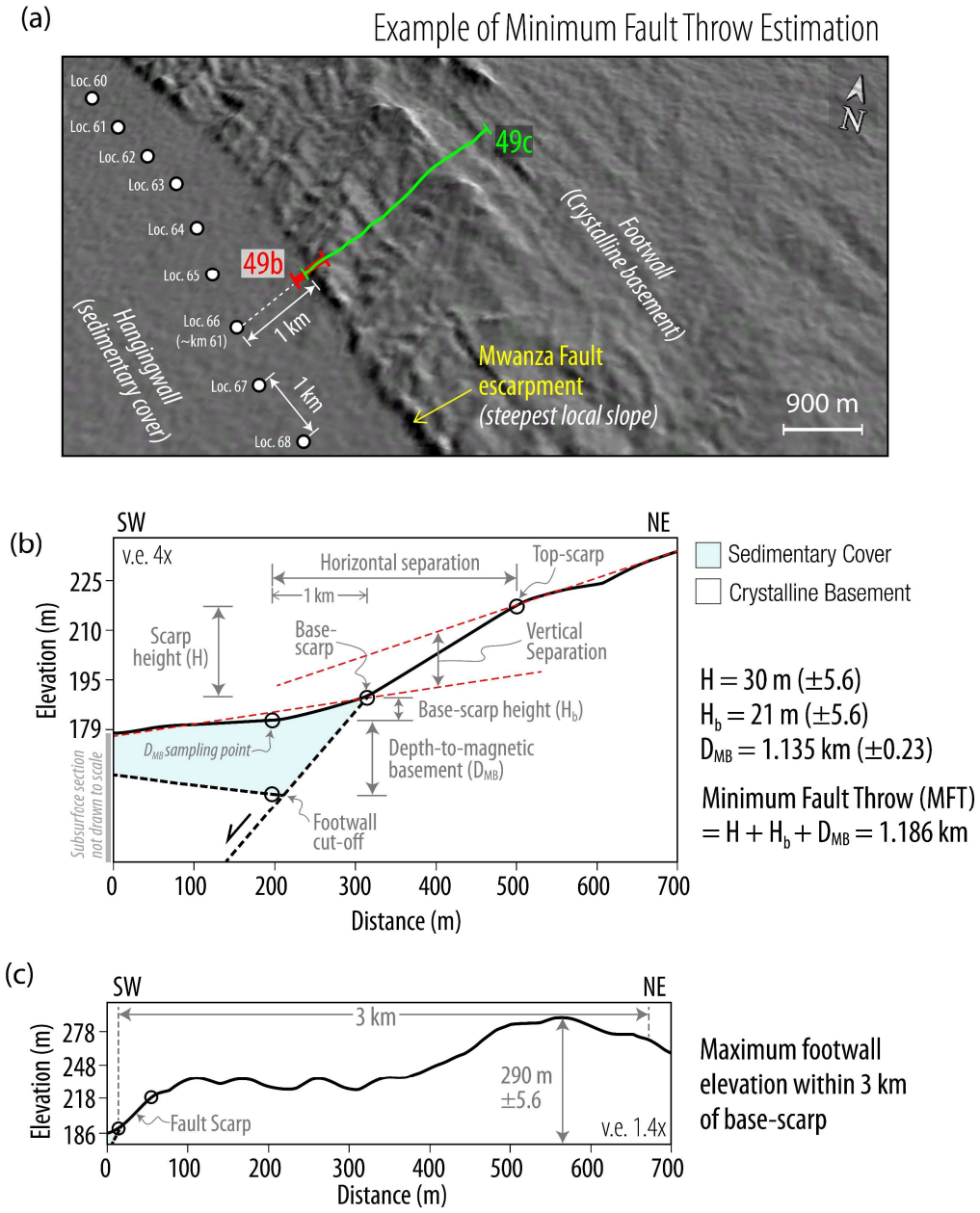

Figure 49. Minimum Top-Basement fault throw estimation. (a) Oblique-view of Shuttle Radar Topography Mission (SRTM) digital elevation model (DEM) hillshade map of a segment of the Mwanza rift-bounding fault, showing 1 km-spaced measurement locations used in this study. The red and green lines represent fault-perpendicular transects used for minimum fault throw estimation at the Location (Loc.) 66 measurement location. Note that the measurement locations follow the fault trend, but the location distance values represent straight-line distances between the locations. (b) Representative fault perpendicular topographic profile for Location 66 (see Figure 49a) showing the measurements obtained for the estimation of Minimum Fault Throw (MFT), and (c) maximum footwall elevation. The measurement of scarp height in Figure 49b is based on the convention of Caskey (1995).

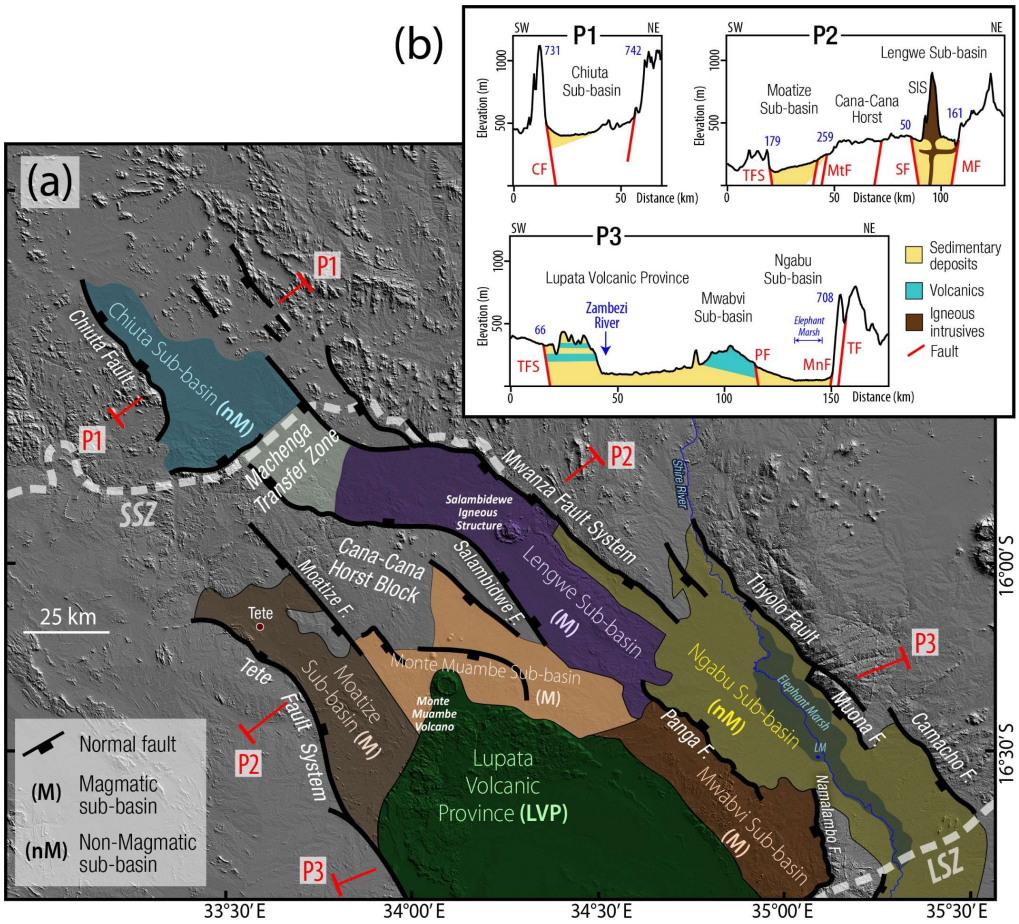
(b)
P1
SW
NE
731
742
Chiuta Sub-basin
Elevation (m)
1000
500
0
50
Distance (km)
CF
P2
Lengwe Sub-basin
Moatize Sub-basin
Cana-Cana Horst
SIS
161
179
259
50
TFS
MtF
SF
MF
100
P3
Ngabu Sub-basin
Lupata Volcanic Province
Mwabvi Sub-basin
Zambezi River
66
708
Elephant Marsh
PF
MnF
TF
150
Sedimentary deposits
Volcanics
Igneous intrusives
Fault
(a)
Chiuta Sub-basin (nM)
Chiuta Fault
SSZ
Machenga Transfer Zone
Mwanza Fault System
Shire River
Salambidewe Igneous Structure
Cana-Cana Horst Block
Salambidewe F.
Lengwe Sub-basin (M)
Thyolo Fault
Moatize F.
Tete
25 km
Monte Muambe Sub-basin (M)
Ngabu Sub-basin (nM)
Elephant Marsh
Muona F.
Camacho F.
Tete Fault System
Moatize Sub-basin (M)
Monte Muambe Volcano
Panga F.
LM
Namalambo F.
Lupata Volcanic Province (LVP)
Mwabvi Sub-basin (M)
LSZ
Normal fault
(M) Magmatic sub-basin
(nM) Non-Magmatic sub-basin
16°00′S
16°30′S
33°30′E
34°00′E
34°30′E
35°00′E
35°30′E
(c)
25 km
Chiuta Fault
Zambezi River
Machenga Transfer Zone
Zambezi Rift
Southern Malawi Rift
Zomba graben
Zomba
Blantyre
SDC
Shire River
Salambidewe Igneous Structure
Mwanza Fault
Cana-Cana Horst
Moatize F.
Salambidewe F.
Thyolo Fault
Phirilongwe River
MDC
Tete
Tete Fault System
Monte Muambe Caldera
Lupata Volcanic Province (LVP)
Panga F.
Muona F.
Camacho F.
Namalambo F.
Nsanje Horst
Exposed
Buried
Rift-bounding fault
Intrabasin/ minor fault
Exposed volcano/intrusion
Buried volcano/intrusion
Extent of volcanic deposits
Rift-axial
Off-Rift
Mafic dikes
15°00′S
15°30′S
16°00′S
16°30′S
33°30′E
34°00′E
34°30′E
35°00′E
35°30′E

Figure 50. New interpretation of the Shire Rift structure. (a) Map showing the Shire Rift extents and sub-basin compartmentalization based on fault scarp continuity and published distribution of the syn-rift sedimentary and volcaniclastic fill (Figure 46; Choubert et al., 1988). LM = Lake Mbenje, LSV = Lurio Shear Zone, SSZ = Sanangoe Shear Zone. (b) Along-trend rift-perpendicular topographic profiles showing the variation of rift morphology. Numbers in blue represent rift shoulder-to-basin axis elevation difference (in meters). CF = Chiuta Fault, MF = Mwanza Fault, MnF = Muona Fault, MtF = Moatize Fault, PF = Panga Fault, TF = Thyolo Fault, TFS = Tete Fault System. (c) Map showing the distribution of rift-related structural and tectono-thermal elements in the basin, consisting of those compiled from interpretations in this study and previous publications (Choubert et al., 1988; Castaing, 1991; Chisenga et al. 2018; Nyalugwe et al., 2019a). MDC = Mulata Dike Cluster, SDC = Salambidwe Dike Cluster.

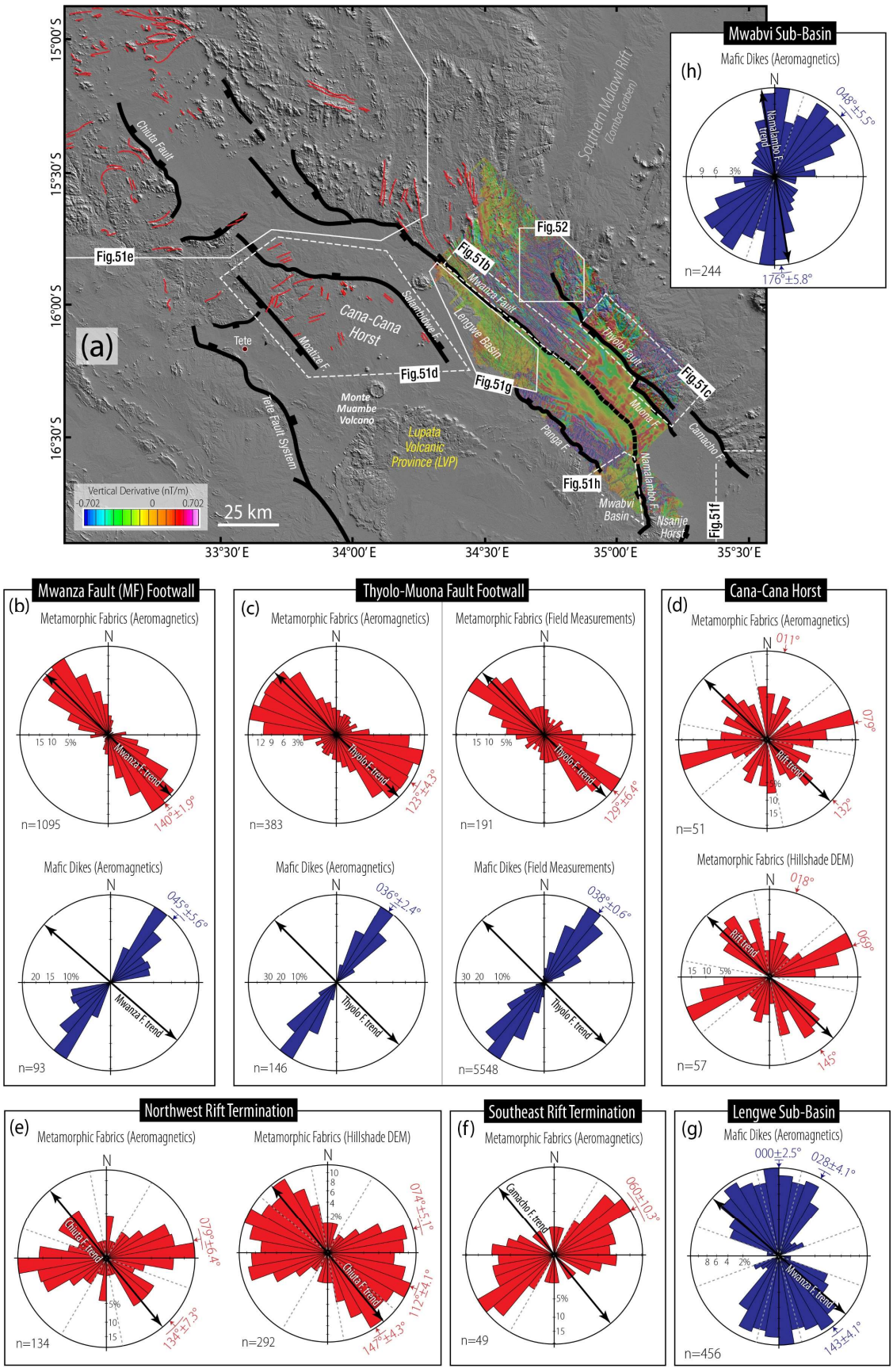
(a)
Chiuta Fault
Southern Malawi Rift (Zomba Graben)
Fig.52
Fig.51e
Fig.51b
Mwanza Fault
Cana-Cana Horst
Salambidwe F.
Lengwe Basin
Thyolo Fault
Fig.51c
Tete
Moatize F.
Fig.51d
Fig.51g
Monte Muambe Volcano
Tete Fault System
Lupata Volcanic Province (LVP)
Muona F.
Panga F.
Camacho F.
Fig.51h
Namalambo F.
Mwabvi Basin
Nsanje Horst
Fig.51f
Vertical Derivative (nT/m)
-0.702
0
0.702
25 km
15°00′S
15°30′S
16°00′S
16°30′S
33°30′E
34°00′E
34°30′E
35°00′E
35°30′E
Mwabvi Sub-Basin
(h)
Mafic Dikes (Aeromagnetics)
N
048°±5.5°
Namalambo F. trend
9 6 3%
n=244
176°±5.8°
Mwanza Fault (MF) Footwall
(b)
Metamorphic Fabrics (Aeromagnetics)
N
15 10 5%
Mwanza F. trend
140°±1.9°
n=1095
Mafic Dikes (Aeromagnetics)
N
045°±5.6°
20 15 10%
Mwanza F. trend
n=93
Thyolo-Muona Fault Footwall
(c)
Metamorphic Fabrics (Aeromagnetics)
N
12 9 6 3%
Thyolo F. trend
123°±4.3°
n=383
Metamorphic Fabrics (Field Measurements)
N
15 10 5%
Thyolo F. trend
129°±6.4°
n=191
Mafic Dikes (Aeromagnetics)
N
036°±2.4°
30 20 10%
Thyolo F. trend
n=146
Mafic Dikes (Field Measurements)
N
038°±0.6°
30 20 10%
Thyolo F. trend
n=5548
Cana-Cana Horst
(d)
Metamorphic Fabrics (Aeromagnetics)
N
011°
079°
Rift trend
5%
10
15
132°
n=51
Metamorphic Fabrics (Hillshade DEM)
N
018°
069°
Rift trend
15 10 5%
145°
n=57
Northwest Rift Termination
(e)
Metamorphic Fabrics (Aeromagnetics)
N
Chiuta F. trend
079°±6.4°
5%
10
15
134°±7.3°
n=134
Metamorphic Fabrics (Hillshade DEM)
N
10
8
6
4
2%
074°±5.1°
Chiuta F. trend
112°±4.1°
147°±4.3°
n=292
Southeast Rift Termination
(f)
Metamorphic Fabrics (Aeromagnetics)
N
Camacho F. trend
060°±10.2°
5%
10
15
n=49
Lengwe Sub-Basin
(g)
Mafic Dikes (Aeromagnetics)
000±2.5°
028±4.1°
8 6 4 2%
Mwanza F. trend
143±4.1°
n=456

Figure 51. Distribution of the inherited structural trends. (a) Shuttle Radar Topography Mission (SRTM) Hillshade DEM of the Shire Rift overlaid with vertical derivative map of the Malawi part of the rift, topographic trends of basement fabrics (red lines) at the NW termination of the rift, and sub-regions on which Figures 50b-50i are based. The major faults are delineated from the sub-aerial linear zones of abrupt increase in local slope in the SRTM hillshade maps (see Figure 49a). Dikes are mapped from the filtered aeromagnetic maps where they are represented by clusters of parallel discrete magnetic lineaments (see Figure 47e). (b - c) Azimuth-frequency distribution of basement metamorphic fabrics and mafic dikes along the footwall of (b) the Mwanza Fault, and (c) the Thyolo and Muona Faults; (d - f) Frequency-azimuth distribution of metamorphic fabrics within the Cana-Cana horst block (d), the NW (e) and the SE (f) rift terminations zones; (g - h) Frequency-azimuth distribution of mafic dikes in the Lengwe (g) and Mwabvi sub-basins (h). The field measurements of metamorphic fabrics and dikes shown in 6c include a combination of ground truthing (this study) and published (Habgood et al., 1973) field measurements. Black dashed lines represent frequency minima used for modal set grouping and calculation of circular vector mean for the modal sets. Along the rift shoulders, the dikes strike perpendicular to the rift and border-fault trend (Figures 51b-c), however, in the rift sub-basins, the dike sets largely show both rift/ border fault-parallel and rift/border fault-oblique trends.

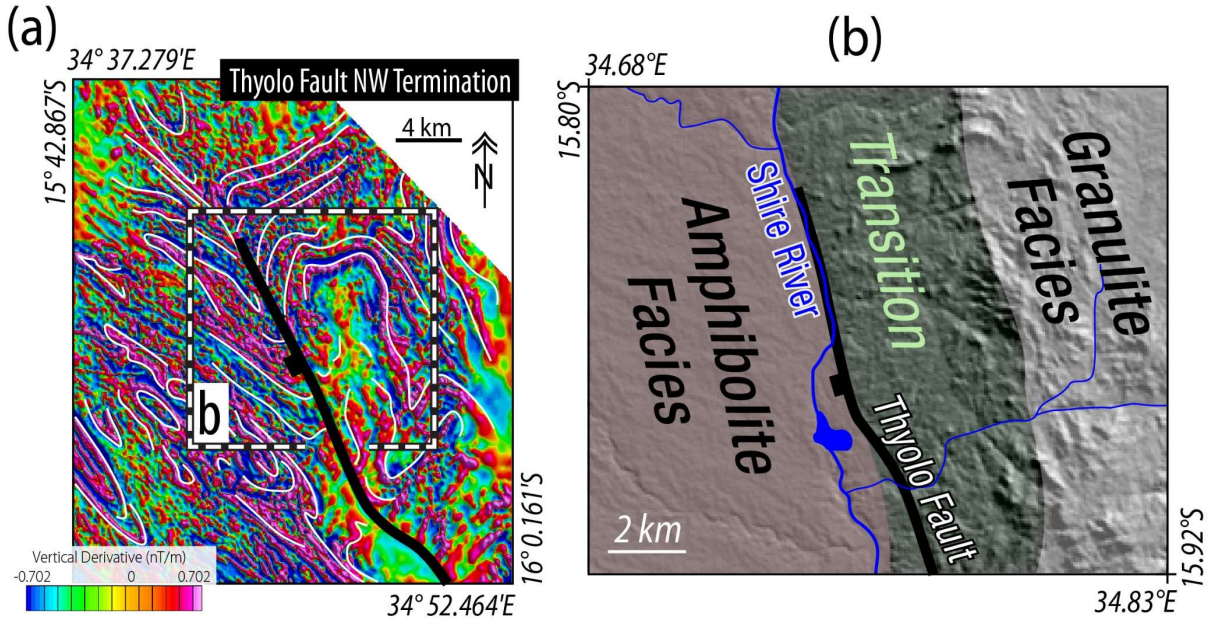

Figure 52. Basement metamorphic fabrics at the NW Tip of Thyolo Fault. (a) Filtered aeromagnetic map (subset of Fig. 3c) and (b) geologic map (after Morel, 1958) of the NW tip of the Thyolo fault, showing the collocation of the fault trace with an exhumed Precambrian shear zone. Figure 51a for the location of the maps.

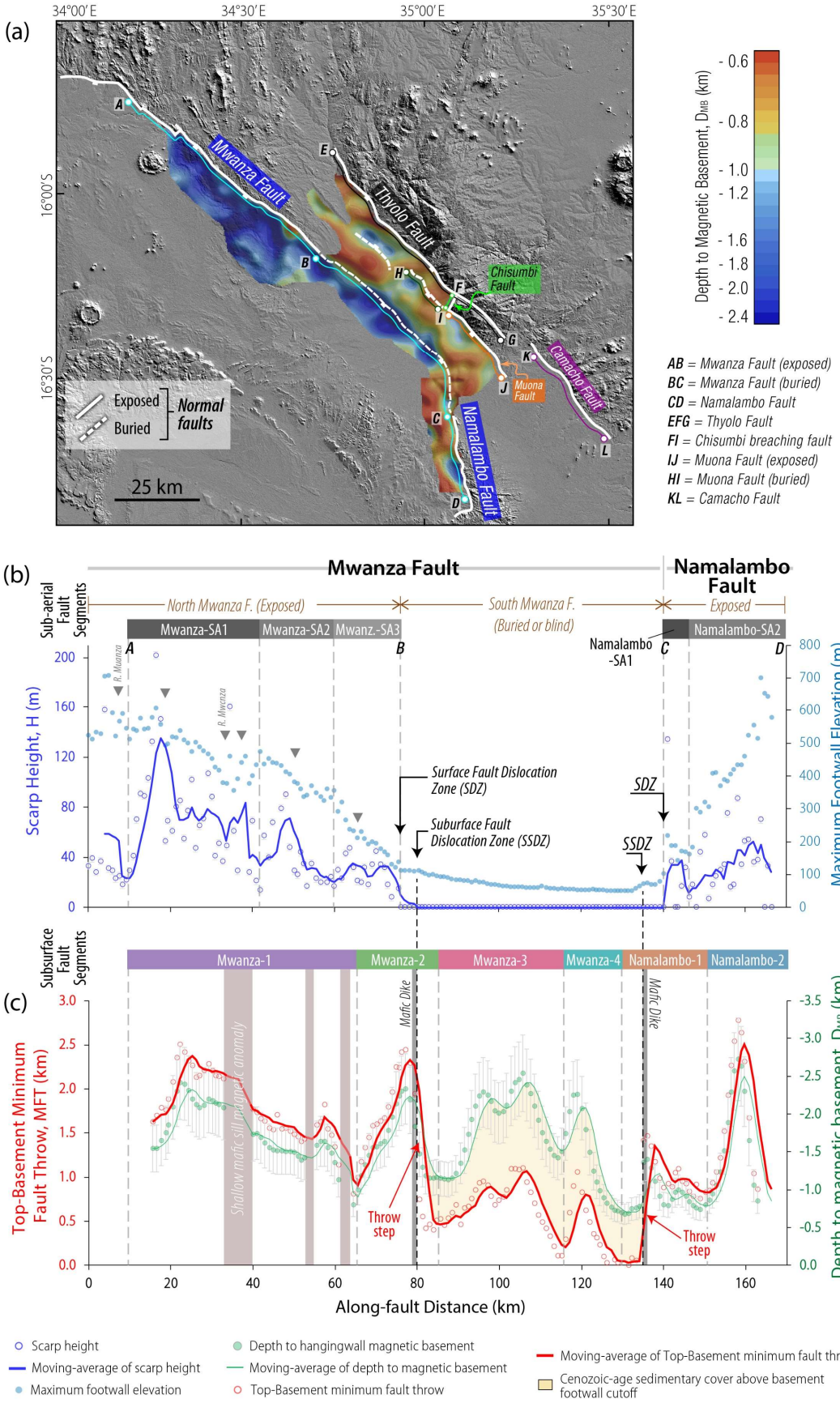
(a)
34°00′E
34°30′E
35°00′E
35°30′E
16°00′S
16°30′S
Mwanza Fault
Thyolo Fault
Chisumbi Fault
Muona Fault
Camacho Fault
Namalambo Fault
A
B
C
D
E
F
G
H
I
J
K
L
Exposed
Buried
Normal faults
25 km
Depth to Magnetic Basement, DMB (km)
- 0.6
- 0.8
- 1.0
- 1.2
- 1.6
- 1.8
- 2.0
- 2.4
AB = Mwanza Fault (exposed)
BC = Mwanza Fault (buried)
CD = Namalambo Fault
EFG = Thyolo Fault
FI = Chisumbi breaching fault
IJ = Muona Fault (exposed)
HI = Muona Fault (buried)
KL = Camacho Fault
(b)
Mwanza Fault
Namalambo Fault
Sub-aerial Fault Segments
North Mwanza F. (Exposed)
South Mwanza F. (Buried or blind)
Exposed
Mwanza-SA1
Mwanza-SA2
Mwanz.-SA3
Namalambo -SA1
Namalambo-SA2
R. Mwanza
R. Mwanza
Scarp Height, H (m)
Maximum Footwall Elevation (m)
Surface Fault Dislocation Zone (SDZ)
Suburface Fault Dislocation Zone (SSDZ)
SDZ
SSDZ
(c)
Subsurface Fault Segments
Mwanza-1
Mwanza-2
Mwanza-3
Mwanza-4
Namalambo-1
Namalambo-2
Mafic Dike
Mafic Dike
Shallow mafic sill magnetic anomaly
Top-Basement Minimum Fault Throw, MFT (km)
Depth to magnetic basement, DMB (km)
Throw step
Throw step
Along-fault Distance (km)
Scarp height
Moving-average of scarp height
Maximum footwall elevation
Depth to hangingwall magnetic basement
Moving-average of depth to magnetic basement
Top-Basement minimum fault throw
Moving-average of Top-Basement minimum fault throw
Cenozoic-age sedimentary cover above basement footwall cutoff

Figure 53. Sub-aerial and subsurface segmentation of the Mwanza – Namalambo border fault system. (a) Depth-to-magnetic basement map of the NE part of the Shire Rift (overlaid on SRTM hillshade DEM), calculated using the Source Parameter ImagingTM transform of the 1985 aeromagnetic grid (Figure 47a); (b) Distribution of fault scarp height and maximum footwall elevation along the sub-aerial exposures of the Mwanza – Namalambo fault system; (c) Distribution of the depth-to-magnetic basement (hangingwall) and the estimated Top-Basement minimum fault throw along the trend of the Mwanza – Namalambo fault system. SDZ (surface fault dislocation zone) marks the surface location basinward of which the fault scarp is not visible. SSDZ (subsurface fault dislocation zone) marks the subsurface transition between the buried and exposed segments. Note that the SSDZs are collocated with subtle gradients in the maximum footwall elevation profile. The error bars in 53c represent the standard ±20% accuracy associated with source depth estimates from aeromagnetic data (Gay, 2009).

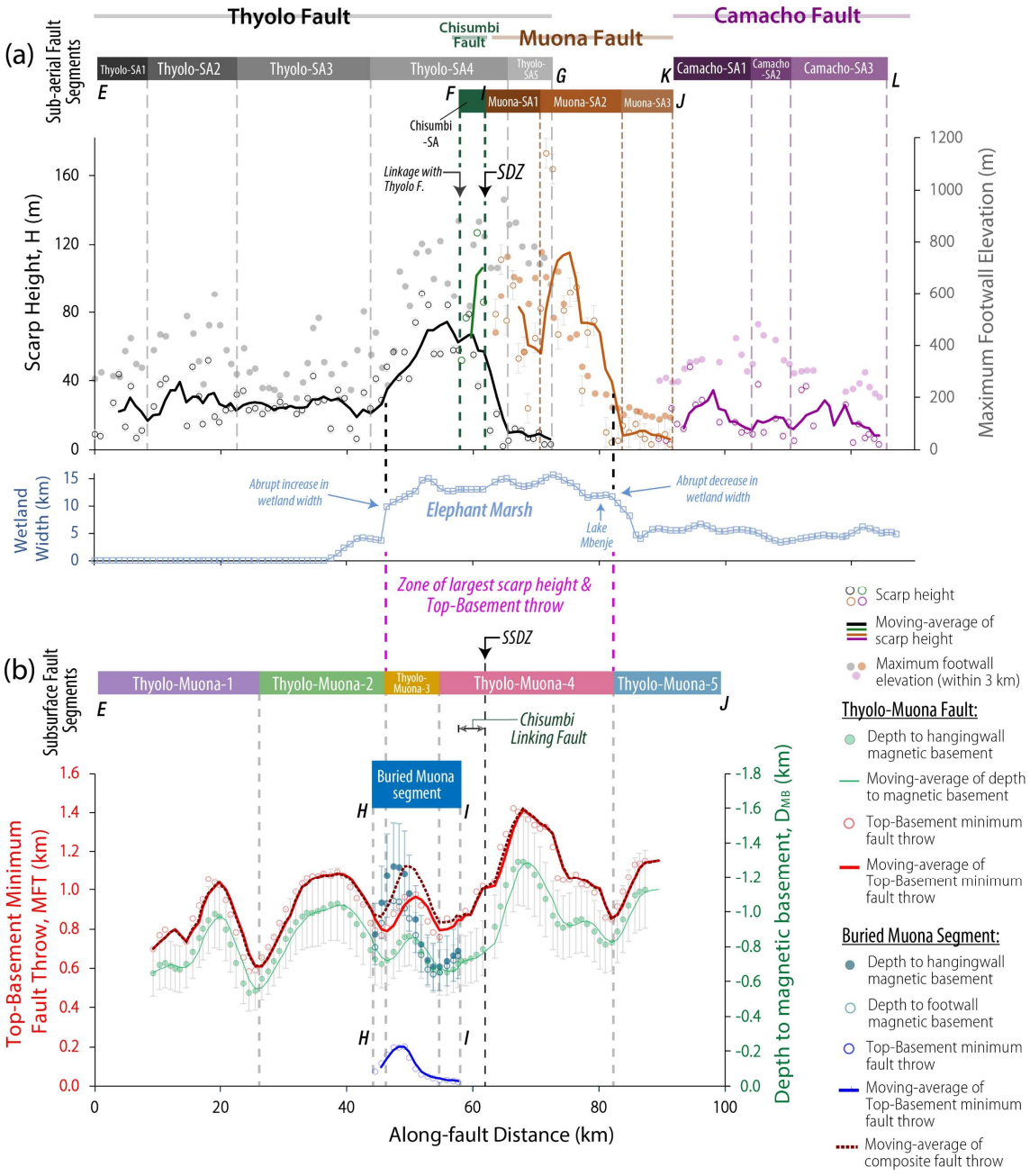

Figure 54. Sub-aerial and subsurface segmentation of the Thyolo-Muona-Camacho border fault system. (a) Distribution of fault scarp height and maximum footwall elevation along the sub-aerial exposures of the Thyolo, Chisumbi, Muona, and Camacho Faults. *Lower panel:* Plot of along-rift variation in the width of the Elephant Marsh (measured on 1 km spaced N-S profiles on Landsat Image), a >600 km^2 permanent wetland sitting on the hangingwall of the Thyolo-Muona Fault system (Ngabu sub-basin); see Figures 50a and 50b (profile P3) for location. (b) Distribution of the depth-to-magnetic basement (hangingwall) and the estimated Top-Basement minimum fault throw along the trend of the Thyolo-Muona fault system. SDZ = surface fault dislocation zone, SSDZ = subsurface fault dislocation zone. The error bars in 54b represent the standard ±20% accuracy associated with source depth estimates from aeromagnetic data (Gay, 2009).

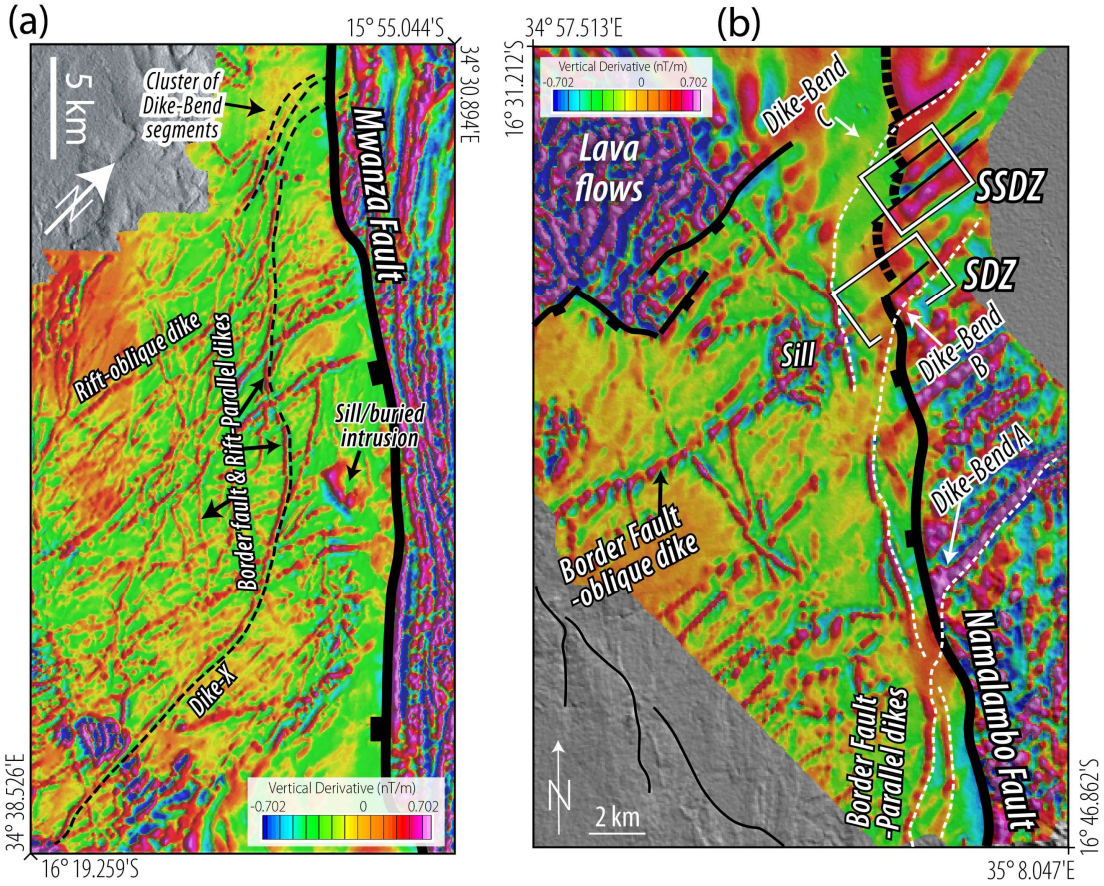

Figure 55. Phase-2 (Late Jurassic to Mid Cretaceous) Rifting: Igneous diking and inherited structures. (a) Filtered aeromagnetic grid overlaid on satellite digital elevation model (DEM) hillshade map of a part of the Lengwe sub-basin, showing the relationships between dike geometry and border fault trends. Black dotted lines track the trends of border fault-parallel dikes which deflect along-strike into Mwanza Fault-oblique trends. (b) Filtered aeromagnetic grid overlaid on satellite DEM hillshade map of a part of the Mwabvi sub-basin, showing the relationships between dike geometry and the dislocation zones along the Namalambo Fault. White dotted lines track the trends of border fault-parallel dikes which deflect along-strike into fault-oblique trends and extend across the dislocation zone of the Namalambo Fault. See Figure 56a for location of the two maps. SDZ = surface fault dislocation zone, SSDZ = subsurface fault dislocation zone.

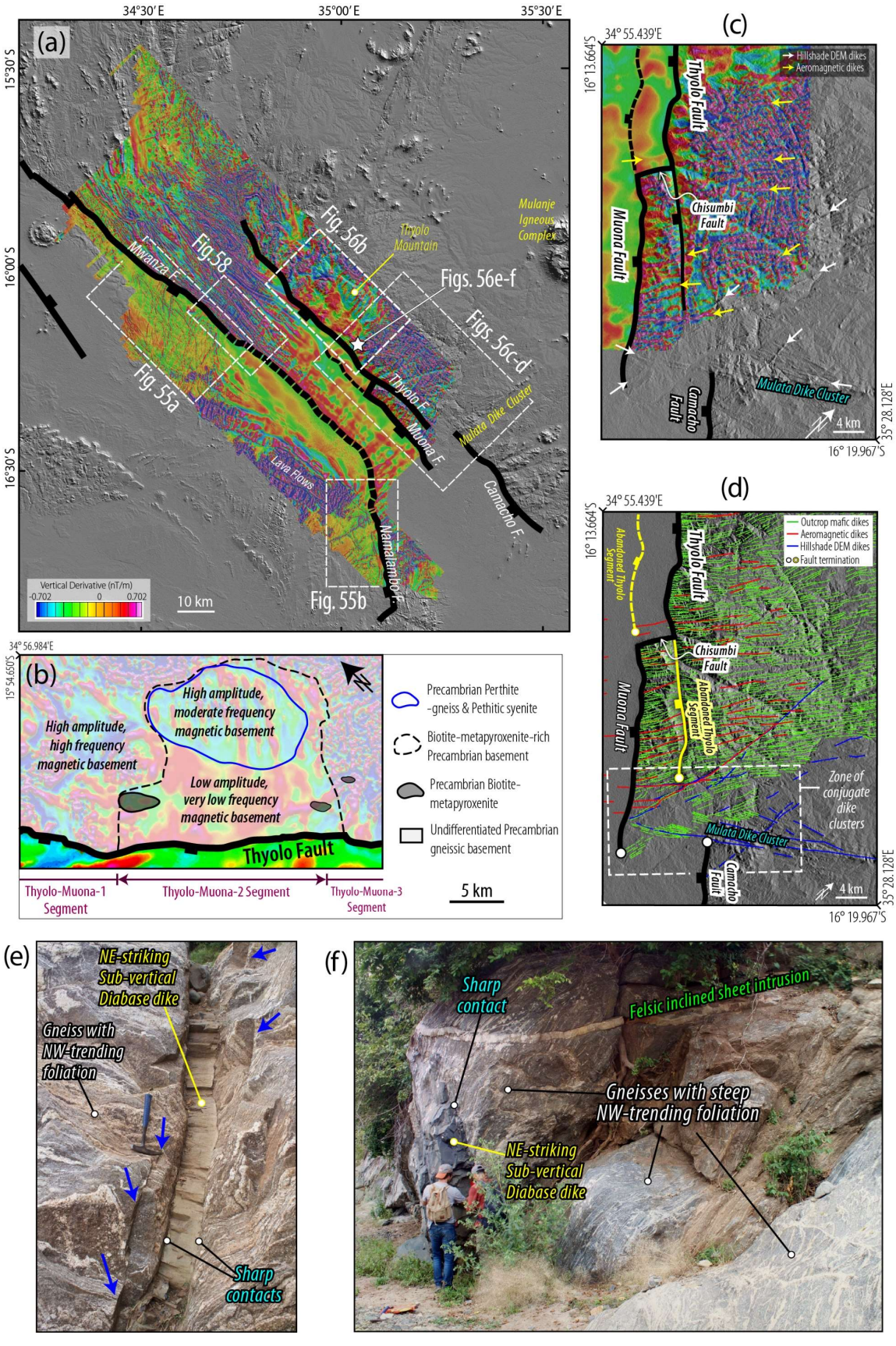
(a)
34°30′ E
35°00′ E
35°30′ E
15°30′S
16°00′S
16°30′S
Mulanje Igneous Complex
Thyolo Mountain
Fig. 56b
Figs. 56e-f
Figs. 56c-d
Fig.58
Mwanza F.
Fig. 55a
Thyolo F.
Muona F.
Mulata Dike Cluster
Lava Flows
Namalambo F.
Camacho F.
Fig. 55b
Vertical Derivative (nT/m)
-0.702
0
0.702
10 km
(c)
34° 55.439'E
16° 13.664'S
Hillshade DEM dikes
Aeromagnetic dikes
Thyolo Fault
Chisumbi Fault
Muona Fault
Camacho Fault
Mulata Dike Cluster
4 km
35° 28.128'E
16° 19.967'S
(d)
34° 55.439'E
16° 13.664'S
Outcrop mafic dikes
Aeromagnetic dikes
Hillshade DEM dikes
Fault termination
Abandoned Thyolo Segment
Thyolo Fault
Chisumbi Fault
Muona fault
Abandoned Thyolo Segment
Zone of conjugate dike clusters
Mulata Dike Cluster
Camacho Fault
4 km
35° 28.128'E
16° 19.967'S
34° 56.984'E
15° 54.650'S
(b)
High amplitude, moderate frequency magnetic basement
High amplitude, high frequency magnetic basement
Low amplitude, very low frequency magnetic basement
Thyolo Fault
Thyolo-Muona-1 Segment
Thyolo-Muona-2 Segment
Thyolo-Muona-3 Segment
Precambrian Perthite -gneiss & Pethitic syenite
Biotite-metapyroxenite-rich Precambrian basement
Precambrian Biotite-metapyroxenite
Undifferentiated Precambrian gneissic basement
5 km
(e)
NE-striking Sub-vertical Diabase dike
Gneiss with NW-trending foliation
Sharp contacts
(f)
Sharp contact
Felsic inclined sheet intrusion
Gneisses with steep NW-trending foliation
NE-striking Sub-vertical Diabase dike

Figure 56. Phase-3 (Cenozoic) Rifting: Influence of inherited structures on the establishment of new border fault segments. (a) Filtered aeromagnetic map of the Malawi part of the Shire Rift overlaid on Shuttle Radar Topography Mission (SRTM) Hillshade DEM; (b) Map showing relationships between the aeromagnetic basement structure and fault segmentation along the NW half of the Thyolo Fault, constrained by published field mapping from Habgood et al., 1973; (c) Filtered aeromagnetic map overlaid on SRTM hillshade DEM showing aeromagnetic dike lineaments (yellow arrows) and topographic expression of dikes (white arrows); (d) Map of same area as in Fig. 56c, showing the interpreted mafic dike aeromagnetic lineaments (red lines), SRTM hillshade dike lineaments (blue lines), and those from published field mapping (green lines; Habgood et al., 1963). (e – f) Field photographs along the footwall of Thyolo Fault (see white star in Fig. 56a for location) showing NE-trending, sub-vertical mafic dikes truncating NW-trending gneissic foliation in the host rock. Blue arrows indicate en echelon dike-parallel fractures clustering near the contact of the dike. See hammer in 56e and two people in 56f for scale.

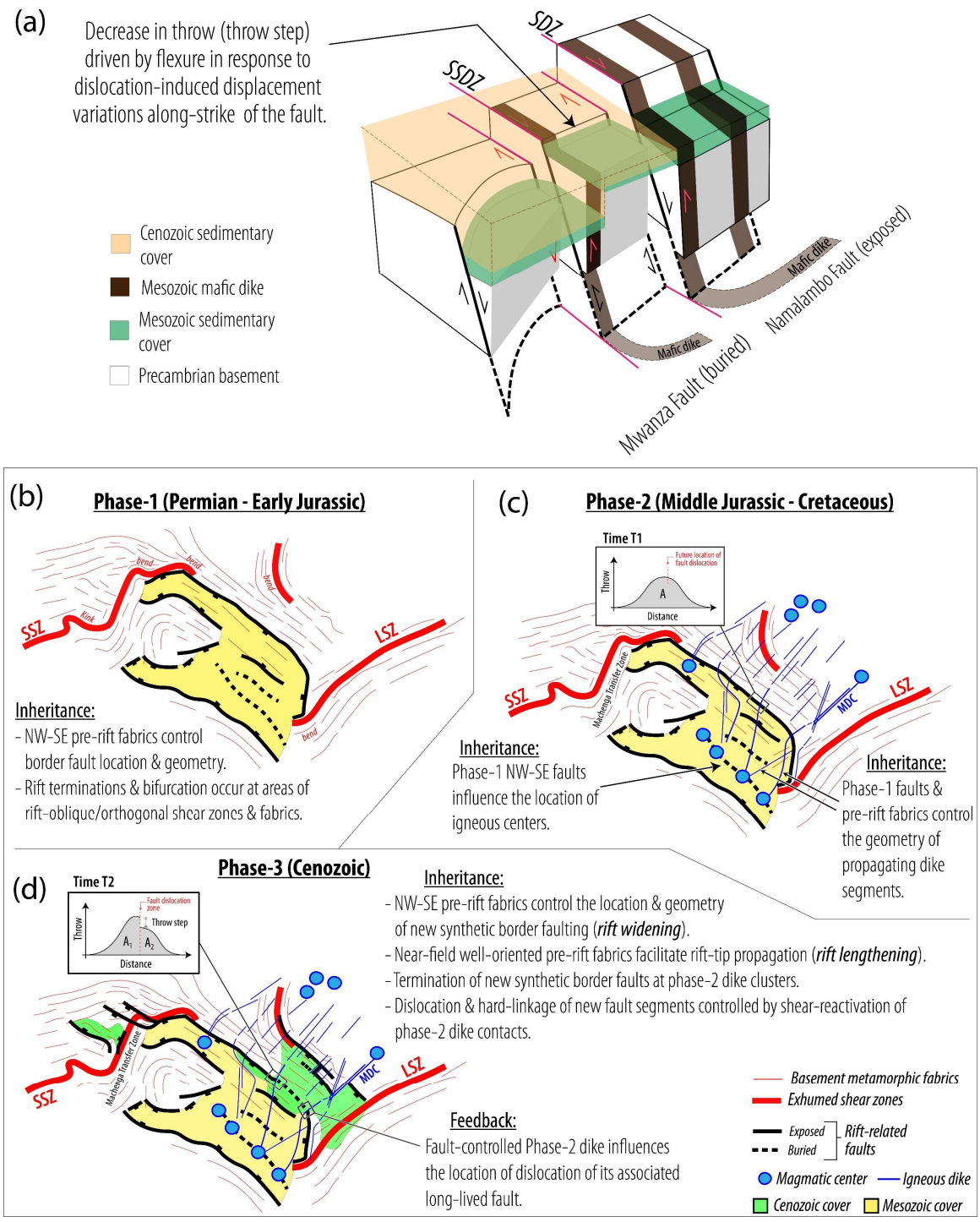

Figure 57. (a) 3-D cartoon showing the interpreted structure of the dike-influenced fault dislocation zones along the Mwanza-Namalambo and the Thyolo-Muona border faults. (b - d) Cartoons showing Continuous Structural Inheritance and the associated feedbacks observed in the multiple phases of early-rift extension in the Shire Rift. LSZ = Lurio Shear Zone, MDC = Mulata Dike Cluster, SSZ = Sanangoè Shear Zone.

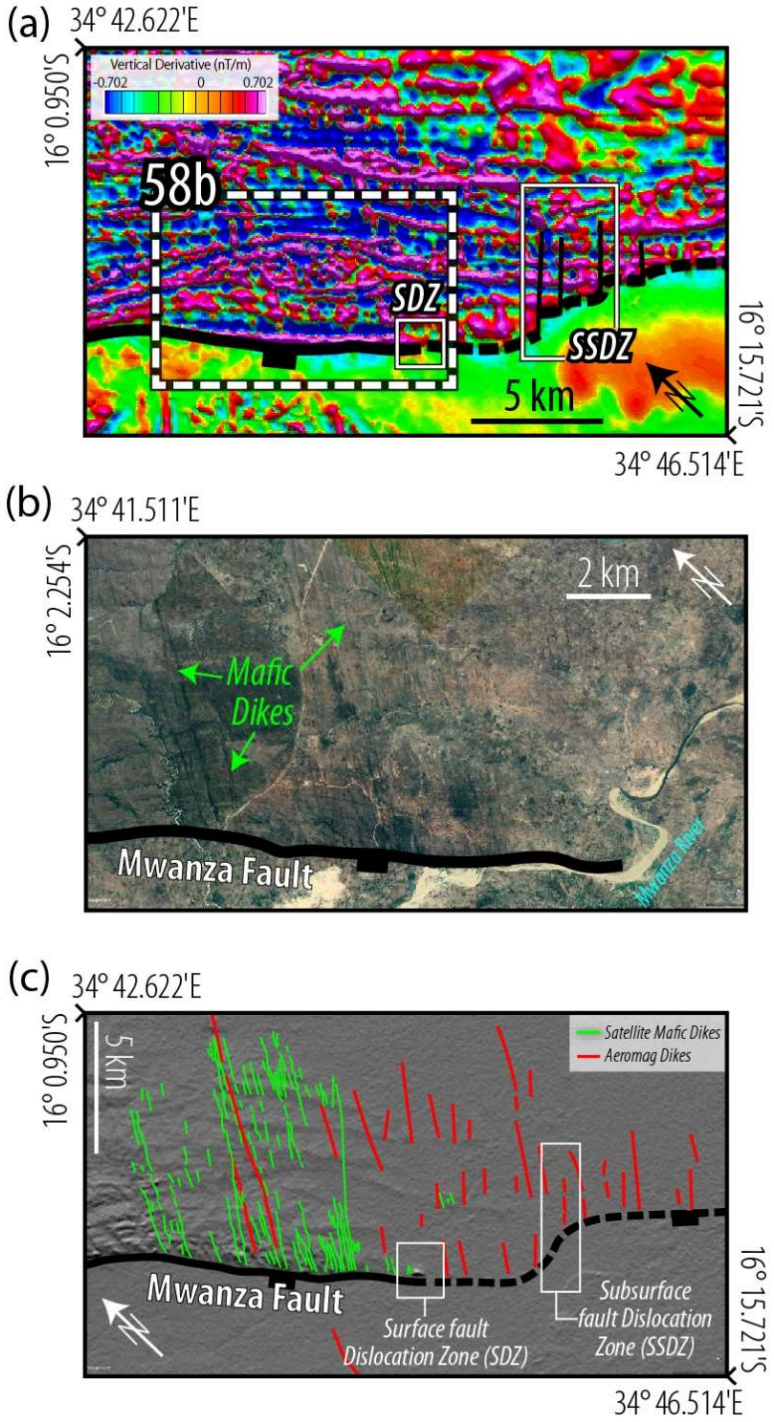

Figure 58. (a) Filtered aeromagnetic grid, (b) Satellite image (Google Earth©), and (c) interpretations, showing the relationships between dike geometry and dike-fault intersection locations, and the location of the dislocation zones along the Mwanza Fault. See Figure 56a for the location of the maps.

REFERENCES

Acocella, V., Faccenna, C., Funiciello, R. and Rossetti, F. (1999). Sand-box modelling of basement-controlled transfer zones in extensional domains. Terra Nova-Oxford, 11(4), 149-156.

Alvarez Naranjo, A. (2016). The role of pre-existing basement fabrics in the initiation of continental rifting: The Okavango Rift Zone, Botswana. Dissertation, Missouri University of Science and Technology, Rolla.

Arkani-Hamed, J. (1988). Differential reduction-to-the-pole of regional magnetic anomalies. Geophysics, 53(12), 1592–1600.

Arrowsmith, J. R., & Zielke, O. (2009). Tectonic geomorphology of the San Andreas Fault zone from high resolution topography: An example from the Cholame segment. Geomorphology, 113(1-2), 70-81.

Blakely, R. J., & Simpson, R. W. (1986). Approximating edges of source bodies from magnetic or gravity anomalies, Geophysics, v. 51, 1494-1498.

Barr, M. W. C., & Brown, M. A. (1987). Precambrian gabbro–anorthosite complexes, Tete Province, Mozambique. Geological Journal, 22(S2), 139-159.

Baranov, V. (1957). A new method for interpretation of aeromagnetic maps: Pseudo-gravimetric anomalies. Geophysics, 22(2), 359–382.

Bennett, J. D. (1989). Smaller Coal Basins in Africa Project - Final Report: Review of Lower Karoo coal basins and coal resource development in parts of central and southern Africa with particular reference to northern Malawi. British Geological Survey Technical Report WC/89/21.

Bingen, B., Jacobs, J., Viola, G., Henderson, I. H. C., Skår, Ø., Boyd, R., Thomas, R. J., Solli, A., Key, R. M., & Daudi, E. X. F. (2009). Geochronology of the Precambrian crust in the Mozambique belt in NE Mozambique, and implications for Gondwana assembly. Precambrian Research, 170(3-4), 231-255.

Bloomfield, K. (1958). The geology of the Port Herald area. Malawi Geological Survey Department Bulletin 9, Zomba.

Caskey, S. (1995). Geometric relations of dip slip to a faulted ground surface: New nomograms for estimating components of fault displacement, J. Struct. Geol. 17, 1197–1202

Castaing, C. (1991). Post-Pan-African tectonic evolution of South Malawi in relation to the Karroo and recent East African rift systems. Tectonophysics, 191(1-2), 55-73.

Chisenga, C., Dulanya, Z., & Jianguo, Y. (2019). The structural re-interpretation of the Lower Shire Basin in the Southern Malawi rift using gravity data. Journal of African Earth Sciences, 149, 280-290.

Choubert, G., Faure-Muret, A., Chanteux, P., Roche, G., Simpson, E. S. W., Shackleton, L., Ségoufin, J., Seguin, C., & Sougy, J. (1988). International geological map of Africa. Scale 1: 5 000 000, Commission for the Geological Map of the World (CGMW), Unesco, Paris.

Cooper, W. G. G., & Bloomfield, K. (1961). The geology of the Tambani-Salambidwe area. Malawi Geological Survey Department Bulletin 13, Zomba.

Corti, G. (2004). Centrifuge modelling of the influence of crustal fabrics on the development of transfer zones: insights into the mechanics of continental rifting architecture. Tectonophysics, 384(1-4), 191-208.

Corti, G. (2012). Evolution and characteristics of continental rifting: Analog modeling-inspired view and comparison with examples from the East African Rift System. Tectonophysics, 522, 1-33.

Corti, G., van Wijk, J., Cloetingh, S., & Morley, C. K. (2007). Tectonic inheritance and continental rift architecture: Numerical and analogue models of the East African Rift system. Tectonics, 26(6).

Daly, M. C., Chorowicz, J., & Fairhead, J. D. (1989). Rift basin evolution in Africa: the influence of reactivated steep basement shear zones. Geological Society, London, Special Publications, 44(1), 309-334.

Dawson, S. M., Laó-Dávila, D. A., Atekwana, E. A., & Abdelsalam, M. G. (2018). The influence of the Precambrian Mughese Shear Zone structures on strain accommodation in the northern Malawi Rift. Tectonophysics, 722, 53-68.

Delvaux, D. (1989). The Karoo to Recent rifting in the western branch of the East-African Rift System: A bibliographical synthesis. Mus. roy. Afr. centr., Tervuren (Belg.), Dépt. Géol. Min., Rapp. ann, 1990 (1991), 63-83.

Donath, F. A. (1961). Experimental study of shear failure in anisotropic rocks. Geological Society of America Bulletin, 72(6), 985-989.

Duffy, O. B., Bell, R .E., Jackson, C. A. L., Gawthorpe, R. L., & Whipp, P. S. (2015). Fault growth and interactions in a multiphase rift fault network: Horda Platform, Norwegian North Sea. Journal of Structural Geology, 80, 99-119.

Dutra, A. C., Marangoni, Y. R., & Trindade, R. I. (2014). Aeromagnetic and physical-chemical properties of some complexes from Goiás Alkaline Province. Brazilian Journal of Geology, 44(3), 361-373.

Engelkemeir, R. M., & Khan, S. D. (2008). Lidar mapping of faults in Houston, Texas, USA. Geosphere, 4(1), 170-182.

Fontijn, K., Delvaux, D., Ernst, G. G., Kervyn, M., Mbede, E., & Jacobs, P. (2010). Tectonic control over active volcanism at a range of scales: Case of the Rungwe Volcanic Province, SW Tanzania; and hazard implications. Journal of African Earth Sciences, 58(5), 764–777.

Fossen, H. (2010). Structural geology. Cambridge University Press, New York.

Fritz, H., Abdelsalam, M., Ali, K. A., Bingen, B., Collins, A. S., Fowler, A. R., et al. (2013). Orogen styles in the East African Orogen: A review of the Neoproterozoic to Cambrian tectonic evolution. Journal of African Earth Sciences, 86, 65–106.

Gay, S. P. Jr. (2009). Reactivation tectonics: The evidence and the consequences. Salt Lake City, UT: American Stereo Map Co.

Habgood, F. (1963). The geology of the country west of the Shire River between Chikwawa and Chiromo. Malawi Geological Survey Department Bulletin No. 14, Zomba.

Habgood, F., Holt, D. N., and Walshaw, R.D. (1973). The Geology of the Thyolo Area. Malawi Geological Survey Department Bulletin No. 22, Zomba.

Hargrove, U.S., Hanson, R.E., Martin, M.W., Blenkinsop, T.G., Bowring, S.A., Walker, N. and Munyanyiwa, H. (2003). Tectonic evolution of the Zambezi orogenic belt: geochronological, structural, and petrological constraints from northern Zimbabwe. Precambrian Research, 123(2-4), 159-186.

Heilman, E., Kolawole, F., Atekwana, E.A. and Mayle, M. (2019). Controls of Basement fabric on the Linkage of Rift Segments. Tectonics, 38(4), 1337-1366.

Heron, P. J., Peace, A. L., McCaffrey, K. J. W., Welford, J. K., Wilson, R., van Hunen, J., & Pysklywec, R. N. (2019). Segmentation of rifts through structural inheritance: Creation of the Davis Strait. Tectonics, 38(7), 2411-2430.

Hill, G. (1994). The role of the pre-rift structure in the architecture of the Dampier Basin area, North West Shelf, Australia. The APPEA Journal, 34(1), 602-613.

Hodge, M., Fagereng, Å., Biggs, J., & Mdala, H. (2018). Controls on early-rift geometry: new perspectives from the Bilila-Mtakataka fault, Malawi. Geophysical Research Letters, 45(9), 3896-3905.

Hornsby, K. T., Streig, A. R., Bennett, S. E., Chang, J. C., & Mahan, S. (2020). Neotectonic and Paleoseismic Analysis of the Northwest Extent of Holocene Surface Deformation along the Meers Fault, Oklahoma. Bulletin of the Seismological Society of America, 110(1), 49-66.

Katumwehe, A. B., Abdelsalam, M. G., & Atekwana, E.A., 2015. The role of pre-existing Precambrian structures in rift evolution: The Albertine and Rhino grabens, Uganda. Tectonophysics, 646, 117-129.

Kinabo, B. D., Atekwana, E. A., Hogan, J. P., Modisi, M. P., Wheaton, D. D., & Kampunzu, A. B. (2007). Early structural development of the Okavango rift zone, NW Botswana. Journal of African Earth Sciences, 48(2-3), 125–136.

Kinabo, B. D., Hogan, J. P., Atekwana, E. A., Abdelsalam, M. G., & Modisi, M. P. (2008). Fault growth and propagation during incipient continental rifting: Insights from a combined

aeromagnetic and Shuttle Radar Topography Mission digital elevation model investigation of the Okavango Rift Zone, northwest Botswana. Tectonics, 27(3).

Kirkpatrick, J. D., Bezerra, F. H. R., Shipton, Z. K., Do Nascimento, A. F., Pytharouli, S. I., Lunn, R. J., & Soden, A. M. (2013). Scale-dependent influence of pre-existing basement shear zones on rift faulting: a case study from NE Brazil. Journal of the Geological Society, 170(2), 237-247.

Kolawole, F., Atekwana, E. A., Laó-Dávila, D. A., Abdelsalam, M. G., Chindandali, P. R., Salima, J., & Kalindekafe, L. (2018). Active deformation of Malawi rift's north basin Hinge zone modulated by reactivation of preexisting Precambrian Shear zone fabric. Tectonics, 37(3), 683-704.

Kolawole, F., Phillips, T. B., Atekwana, E. A., & Jackson, C.-A.-L. (2019). Structural inheritance controls strain distribution during early continental rifting, rukwa rift. EGU General Assembly Conference Abstract EGU2019-1849 (vol. 21).

Kröner, A., Sacchi, R., Jaeckel, P., Costa, M. (1997). Kibaran magmatism and Pan-African granulite metamorphism in northern Mozambique: single zircon ages and regional implications. Journal of African Earth Sciences 25, 467–484.

Laó-Dávila, D. A., Al-Salmi, H. S., Abdelsalam, M. G., & Atekwana, E. A. (2015). Hierarchical segmentation of the Malawi Rift: The influence of inherited lithospheric heterogeneity and kinematics in the evolution of continental rifts. Tectonics, 34, 2399–2417.

Ma, G. Q., Du, X. J., Li, L. L., & Meng, L. S. (2012). Interpretation of magnetic anomalies by horizontal and vertical derivatives of the analytic signal. Applied Geophysics, 9(4), 468–474.

Mardia, K. V., & Jupp, P. E. (2009). Directional statistics. Vol. 494, John Wiley & Sons, West Sussex, England.

Manatschal, G., Lavier, L., & Chenin, P. (2015). The role of inheritance in structuring hyperextended rift systems: Some considerations based on observations and numerical modeling. Gondwana Research, 27(1), 140-164.

Morel, S. W. (1958). The geology of the Middle Shire area. Malawi Geological Survey Department Bulletin No. 10, Zomba.

Morley, C. K. (1999). Influence of preexisting fabrics on rift structure. In C. K. Morley (Ed.), Geoscience of Rift Systems—Evolution of East Africa, AAPG Studies in Geology (Vol. 44, 151–160).

Morley, C. K. (2010). Stress re-orientation along zones of weak fabrics in rifts: An explanation for pure extension in ‘oblique’ rift segments? Earth and Planetary Science Letters, 297(3-4), 667–673.

Muirhead, J. D., Wright, L. J., & Scholz, C.A. (2019). Rift evolution in regions of low magma input in East Africa. Earth and Planetary Science Letters, 506, 332-346.

Nelson, R. A., Patton, T. L., & Morley, C. K. (1992). Rift-segment interaction and its relation to hydrocarbon exploration in continental rift systems (1). AAPG bulletin, 76(8), 1153-1169.

Nyalugwe, V. N., Abdelsalam, M. G., Atekwana, E. A., Katumwehe, A., Mickus, K. L., Salima, J., Njinju, E. A., & Emishaw, L. (2019a). Lithospheric structure beneath the Cretaceous Chilwa Alkaline Province (CAP) in southern Malawi and northeastern Mozambique. Journal of Geophysical Research: Solid Earth, 124(11), 12224-12240.

Nyalugwe, V.; Abdelsalam, M.; Atekwana, E.; Katumwehe, A.; Mickus, K.; Salima, J.; Njinju, E. and L. Emishaw, (2019b). 2013 Total Magnetic Intensity (TMI) gridded aeromagnetic data of southern Malawi 34 45 E – 36 00 E and 14 45 S and 16 15 S (investigator Mohamed Abdelsalam). Interdisciplinary Earth Data Alliance (IEDA). doi:10.1594/IEDA/324860.

Oesterlen, P. M., & Blenkinsop, T. G. (1994). Extension directions and strain near the failed triple junction of the Zambezi and Luangwa Rift zones, southern Africa. Journal of African Earth Sciences, 18(2), 175-180.

Osagiede, E. E., Rotevatn, A., Gawthorpe, R., Kristensen, T. B., Jackson, C. A., & Marsh, N. (2020). Pre-existing intra-basement shear zones influence growth and geometry of non-colinear normal faults, western Utsira High–Heimdal Terrace, North Sea. Journal of Structural Geology, 130, 103908.

Phillips, T. B., Jackson, C. A., Bell, R. E., Duffy, O. B., & Fossen, H. (2016). Reactivation of intrabasement structures during rifting: A case study from offshore southern Norway. Journal of Structural Geology, 91, 54-73.

Phillips, T. B., Magee, C., Jackson, C. A. L., & Bell, R. E. (2018). Determining the three-dimensional geometry of a dike swarm and its impact on later rift geometry using seismic reflection data. Geology, 46(2), 119-122.

Phillips, T. B., Fazlikhani, H., Gawthorpe, R. L., Fossen, H., Jackson, C. A. L., Bell, R. E., Faleide, J. I., & Rotevatn, A. (2019). The Influence of Structural Inheritance and Multiphase Extension on Rift Development, the NorthernNorth Sea. Tectonics, 38.

Ragland, P. C., Hatcher Jr, R. D., & Whittington, D., 1983. Juxtaposed Mesozoic diabase dike sets from the Carolinas: A preliminary assessment. Geology, 11(7), 394-399.

Ranalli, G., & Yin, Z. M. (1990). Critical stress difference and orientation of faults in rocks with strength anisotropies: the two-dimensional case. Journal of Structural geology, 12(8), 1067-1071.

Rodriguez, E., Morris, C. S., & Belz, J. E. (2006). A global assessment of the SRTM performance. Photogrammetric Engineering & Remote Sensing, 72(3), 249-260.

Rotevatn, A., Kristensen, T., Ksienzyk, A., Wemmer, K., Henstra, G., Midtkandal, I., Grundvåg, S. A., Andresen, A. (2018). Structural inheritance and rapid rift-length establishment in a multiphase rift: the East Greenland rift system and its Caledonian orogenic ancestry. Tectonics 37, 1858–1875.

Ryan, W. B. F., S. M. Carbotte, J. Coplan, S. O'Hara, A. Melkonian, R. Arko, R. A. Weissel, V. Ferrini, A. Goodwillie, F. Nitsche, J. Bonczkowski, & Zemsky, R. (2009). Global Multi-Resolution Topography (GMRT) synthesis data set, Geochem. Geophys. Geosyst., 10, Q03014.

Sacchi, R., Cadoppi, P., & Costa, M. (2000). Pan-African reactivation of the Lurio segment of the Kibaran Belt system: a reappraisal from recent age determinations in northern Mozambique. Journal of African Earth Sciences, 30(3), 629-639.

Salem, A., Williams, S., Fairhead, J. D., Smith, R., & Ravat, D. (2007). Interpretation of magnetic data using tilt-angle derivatives. Geophysics, 73(1), L1–L10.

Shemang, E., & Molwalefhe, L. (2011). Geomorphic landforms and tectonism along the eastern margin of the Okavango Rift Zone, Northwestern Botswana, as deduced from geophysical data. New frontiers in tectonics research, general problems, sedimentary basins, and island arcs. Intechopen, Rijeka, 169-182.

Smets, B., Delvaux, D., Ross, K. A., Poppe, S., Kervyn, M., d'Oreye, N., & Kervyn, F. (2016). The role of inherited crustal structures and magmatism in the development of rift segments: Insights from the Kivu basin, western branch of the East African Rift. Tectonophysics, 683, 62-76.

Smith, R. S., Thurston, J. B., Dai, T. F., & MacLeod, I. N. (1998). iSPITM—The improved source parameter imaging method. Geophysical Prospecting, 46(2), 141–151.

Stamps, D.S., Saria, E. and Kreemer, C. (2018). A geodetic strain rate model for the East African Rift system. Scientific reports, 8(1), 1-8.

Thurston, J. B., & Smith, R. S. (1997). Automatic conversion of magnetic data to depth, dip, and susceptibility contrast using the SPI (TM) method. Geophysics, 62(3), 807-813.

Vasconcelos, D.L., Bezerra, F.H., Medeiros, W.E., de Castro, D.L., Clausen, O.R., Vital, H. and Oliveira, R.G., 2019. Basement fabric controls rift nucleation and postrift basin inversion in the continental margin of NE Brazil. Tectonophysics, 751, pp.23-40.

Versfelt, J.W. (2009), South Atlantic margin rift basin asymmetry and implications for pre-salt exploration. International Petroleum Technology Conference (IPTC) paper 13833, Doha, Qatar.

Wheeler, W. H., & Karson, J. A. (1989). Structure and kinematics of the Livingstone Mountains border fault zone, Nyasa (Malawi) Rift, southwestern Tanzania. Journal of African Earth Sciences (and the Middle East), 8(2–4), 393–413.

Wheeler, W. H., & Karson, J. A. (1994). Extension and subsidence adjacent to a" weak" continental transform: An example from the Rukwa rift, East Africa. Geology, 22(7), 625-628.

Williams, J. N., Fagereng, Å., Wedmore, L. N., Biggs, J., Mphepo, F., Dulanya, Z., Mdala, H., & Blenkinsop, T. (2019). How do variably striking faults reactivate during rifting? Insights from southern Malawi. Geochemistry, Geophysics, Geosystems, 20(7), 3588-3607.

Wedmore, L., Biggs, J., Williams, J., Fagereng, A., Dulanya, Z., Mphepo, F., & Mdala, H. (2019). Active fault scarps in southern Malawi and their implications for the distribution and evolution of strain in amagmatic continental rifts, version 1. https://eartharxiv.org/ujchx, Doi: 10.1029/2019TC005834.

Wedmore, L., Williams, J., Biggs, J., Fagereng, A., Mphepo, F., Dulanya, Z., Willoughby, J., Mdala, H., & Adams, B. (2020). Depth-dependent controls on structure, reactivation and geomorphology of the active Thyolo border fault, Malawi rift. Eartharxiv preprint, DOI: 10.31223/osf.io/4bs9x.

Woolley, A. R., Bevan, J. C., & Elliott, C. J. (1979). The Karroo dolerites of southern Malawi and their regional geochemical implications. Mineralogical Magazine, 43(328), 487-495.

Wright, L. J., Muirhead, J. D., & Scholz, C. A. (2020). Spatio-temporal variations in upper crustal extension across the different basement terranes of the Lake Tanganyika Rift, East Africa. Tectonics, p.e2019TC006019. https://doi.org/10.1029/2019TC006019

Youash, Y. (1969). Tension tests on layered rocks. Geological Society of America Bulletin, 80(2), 303-306.

CHAPTER 6

CONCLUSIONS AND RECOMMENDATIONS

In this dissertation, I have presented several pieces of evidence that suggest that the multiphase tectonic deformation of the earth's crust emplace systematically arranged planes of weakness that influence the patterns and styles of subsequent stress perturbations and strain accommodation, be it anthropogenic or tectonically induced. I show that the scales of this influence range from basin-scale to regional-scale.

The results presented in my dissertation, for the first time, demonstrate the controls of basement fabrics, fault structure and frictional stability on the production of widespread and sporadic basement-hosted seismicity in response to anthropogenic stress perturbation. Also, I show that multiphase deformation produces cumulative inheritance of structures, and that the influence of structural inheritance on strain accommodation is a continuous process through the cycles of crustal amalgamation and divergence. In summary, in both the environments of induced seismicity & active tectonics, inherited basement structures control the patterns of crustal deformation and strain release… ***Inherited Geological Structures Matter!!***

For future work, I identify the following as some of the outstanding following questions:

1.) In active tectonic settings, is the influence of structural inheritance temporal or is it sustained throughout the entire life cycle of a tectonic event?
2.) What is the influence of the fault structure at the basement-sedimentary interface (BSI) on the patterns of seismicity in areas of wastewater induced seismicity?

3.) Induced seismicity inherits the fracture networks along the reactivated pre-existing faults. The fault reactivation is associated with shear, dilation, and linkage (permeability enhancement) of the pre-existing fracture network. What are the coupling and feedback mechanisms (in spatio-temporal scales) between the interactions of inherited basement fault structure and persistent fluid injection-induced seismicity?

4.) What brittle deformation mechanism of crystalline rocks allows for the contemporaneous development of shear fractures that are bounded by dense saturation of parallel or sub-parallel tensile fractures?

5.) How does the depth of emplacement of inherited structures influence the styles of strain release and localization of deformation during subsequent anthropogenic or tectonic crustal stress perturbations?

6.) What is the depth distribution and age(s) of emplacement of the mafic sheet intrusions that have been observed in various parts of the Granite-Rhyolite Provinces of the U.S. Mid-Continent? What insights can mineral fracture fill provide on the timing of fluid movement along the basement fractures and the relationships with major tectonic events?

7.) Mafic sheet intrusions also impose a structural fabric on the igneous basement and have contacts that represent density contrast boundaries. Therefore, there is a need to address the question of if the intrusions have any influence(s) on the localization and patterns of seismicity (anthropogenic or tectonic) in the continental crust?

APPENDICES

APPENDIX 1

THE FRACTURE-DEFINED STRUCTURAL FABRIC OF THE PRECAMBRIAN IGNEOUS BASEMENT OF THE U.S. MID-CONTINENT

ABSTRACT

Tectonic events often emplace structures in the earth's crust which become planes of weakness that are inherited by subsequent geological events leading to the reactivation of the earlier structures. Here, I examine the dominant trends of brittle deformation in the Mesoproterozoic Granite-Rhyolite Provinces of the U.S. Mid-Continent which extend northeastwards from West Texas to Michigan. This basement, which covers a region of ~1 billion km^2, is exposed only in a few areas and is buried in most places. I combine structural data of the crystalline basement from the outcrops, seismicity patterns, and published 3-D seismic reflection fault data across the region. My results show the prominence of NE-SW and NW-SE (with minor N-S and E-W) trends in the Mesoproterozoic basement. I suggest that these prominent trends define the structural fabric and planes of weakness of the Mid-Continent Precambrian basement that were reactivated during the Phanerozoic rifting and basin inversion tectonic events that affected the Mid-Continent region. Furthermore, I suggest the inheritance of this regional-scale structural fabric by anthropogenic stress perturbations facilitates the production of widespread regional-scale induced seismicity.

INTRODUCTION

The Mesoproterozoic igneous basement of the United States Mid-Continent is defined by two major provinces of granitic and rhyolitic igneous rocks, known as the Granite-Rhyolite Provinces of Central U.S. (Whitmeyer and Karlstrom, 2007; Bickford et al., 2015). The provinces include the 1.5-1.44 Ga Eastern Granite-Rhyolite Province (EGR) and the 1.4-1.34 Ga Southern Granite-Rhyolite Province (SGR) (Figure A1). The EGR extends across south Michigan, western Ohio, Indiana, Illinois, west Tennessee, eastern and southern Missouri, and northeastern Arkansas. The SGR underlies central Arkansas, Oklahoma, southern Kansas, Texas Panhandle and west Texas. This basement, which covers a region of ~1 billion km^2, is exposed only in four areas (one in west Texas, two in Oklahoma and one in SE Missouri) and but occurs as subcrop in most places.

Post-emplacement of the EGR and SGR provinces, the Mid-Continent experienced two major episodes of continental extension, one in the 1.1 Ga during which the N-S-trending Mid-Continent Rift system (MCR) developed, and the other in Late Proterozoic to Cambrian (Figure A1). The later is associated with the Southern Oklahoma Aulacogen (SOA), Reelfoot Rift, Rough Creek Graben, Rome Trough, Wabash Valley Fault Zone, and the Fort Wayne Rift (Figure A1). These rift basins, some of which were magmatic, did not successfully develop into oceanic basins, thus are classified as failed rifts (Keller and Stephenson, 2007). In the Late Paleozoic (Mississippian to Pennsylvanian), the region experienced widespread contraction associated with the Appalachian Orogeny, leading to the inversion of the rift basins and reactivation of older structures.

In recent times, widespread earthquakes dominate the region, attributable to increased unconventional hydrocarbon exploration and subsurface wastewater disposal in the region (Ellsworth, 2013). This induced seismicity is characterized by strike-slip reactivation of pre-

existing fractures in the Precambrian basement, largely the igneous rocks of the Granite-Rhyolite Province (Schoenball and Ellsworth, 2017; Kolawole et al., 2019).

The goal of this study is to (1.) define the dominant trends of fracture-related structural weakness that characterize the EGR-SGR igneous province, and (2.) explore the relationships between these trends and the Phanerozoic stress perturbations (both tectonic and anthropogenic) across the U.S. Mid-Continent region. Our analysis reveals that prominent NE-SW and NW-SE (with minor N-S and E-W) trends characterize the fracture-defined structural fabric of the Mesoproterozoic basement. We suggest that these prominent trends were reactivated during the Phanerozoic rifting, thus influencing the rift geometries. We also argue that these trends, being favorably-oriented to the current stress field, is controlling the widespread pattern of recent induced seismicity across the region.

DATA & METHODS

Outcrop Fracture Mapping

In the outcrops of the EGR and SGR basement rocks, we map fracture systems in the field and in satellite images (Google Earth©). We perform the field mapping of fractures in basement outcrops in southern Oklahoma (Mill Creek area, Arbuckle Uplift) and northeastern Oklahoma (Spavinaw area, Ozark Uplift) (Figure A1). In the southern Oklahoma outcrops, we complement field data with satellite fracture mapping. In the basement outcrops of the Ozark Uplift, southeast Missouri (St. Francois Mountains), we characterize the fracture systems using the satellite images. For all the fracture mapping in satellite images, we manually digitize the visible penetrative fracture traces (i.e. non-exfoliation related). We calculate the frequency-azimuth distribution of the mapped fracture segments. For all the plots, we calculate the circular vector mean and 95% confidence

interval for the modal sets using the method of Mardia and Jupp (2009). All frequency-azimuth plots presented in this study are area-weighted.

Seismicity Cluster Mapping

To characterize structural trends in the subcrops of the EGR-SGR basement rocks, we obtain catalogs of recorded seismicity epicenters in the Central Oklahoma and Kansas sub-region, as well as the Missouri through Michigan sub-region (Figure A1). For the Oklahoma-Kansas sub-region, we utilize published relocated earthquake catalogs from Schoenball and Ellsworth (2017) and Kolawole et al. (2019), both providing events that cover the 2010-2017 period. The relocated events provide excellent linear clusters (map-view) that define the traces of the reactivated fault segments.

Whereas for the Missouri through Michigan sub-region, we utilize the public-domain earthquake catalogs from U.S. Geological survey (events spanning the 1875 to 2020 period) and University of Memphis Center for Earthquake Research (CERI) earthquake catalog (events spanning the 1974 to 2019 period). Although the USGS and CERI datasets are not relocated, the combined records provide reliable definition of the overall trends of the large clusters. In addition to the USGS and CERI catalogs, we obtain relocated earthquakes from the Ozarks-Illinois-Indiana-Kentucky (OIINK) catalog (Yang et al., 2014). Also, we map the trends of well-located microseismicity clusters in the central part of the Illinois basin that were recorded during the Illinois Basin – Decatur Project (IBDP) and published in Will et al. (2016) and McBride et al. (2018).

We manually digitize the lineaments delineated by earthquake clusters across the extents of the EGR-SGR (Figure A1). Following the technique of Kolawole et al. (2019) and Fielding et al.

(2017), we only digitize linear clusters that consist of at least three events within an 8 km distance. However, we exclude areas of intense rifting where large seismicity clusters occur (e.g., RR, RG and RT in Figure A1) so as not to bias the structural data. We calculate the frequency-azimuth distribution of the mapped seismicity cluster lineaments. For all the plots, we calculate the circular vector mean and 95% confidence interval for the modal sets using the method of Mardia and Jupp (2009).

3-D Seismic Reflection Data

To complement structural data from seismicity clusters in the basement of the Oklahoma-southern Kansas sub-region, we obtain published measurements of fault trends interpreted on the basement-sedimentary interface in 3-D seismic reflection datasets. These published measurements cover parts of central Oklahoma (Patel, 2020), and northern Oklahoma (Machado, 2019; Firkins, 2020).

RESULTS AND DISCUSSION

General Characteristics of the Basement Fractures at all the Scales of Observation

In the outcrops of the basement in southern Oklahoma, we observe two broad patterns of fracturing that show associations with the texture of the granite. Areas of finer-grained granites (e.g., Figure A2a) generally exhibit sparse, widely spaced (>1 m mean spacing) fracturing, with discrete linear zones of intense damage and tight fracture clustering (<8 cm mean spacing) which partially control the local drainage system. The coarser-grained granites generally show pervasive fracturing with multiple trends of overprinted sets (e.g., Figure A2b). In both the southern and northeastern Oklahoma, the fractures generally display sub-vertical geometries, and tensile features such as rough surfaces, en-echelon segmentation, with limited evidence of shear displacements (e.g.,

Figures A2c-f). Also, in the published seismic datasets, the basement-rooting faults are sub-vertical and may show upward splay up-dip, or sidewall splays along-strike (Kolawole et al., 2019, 2020).

Dominant Structural Trends in the Granite-Rhyolite Provinces of the U.S. Mid Continent

In southern Oklahoma, both the satellite and field mapping of fractures in the exposed basement show a dominance of NE-SW (234°±3.7 and 241°±2.0) and NW-SE (308°±3.6 and 314°±5.2) trends (Figure A3a). However, the field outcrop data (Figure A3b) shows a secondary N-S trend (355°±5.88). Whereas, in the central Oklahoma to southern Kansas sub-region, the liner clusters of seismicity (reactivated fault traces; Figure A3c) also show a dominance of NE-SW (239°±2.8) and NW-SE (296°±3.5) trends. Also, within the central and northern Oklahoma sub-regions, interpreted Top-Basement fault zones (Figure A3d) show three dominant trends which include the NE-SW trend (226°±6.6), a WNW-ESE trend (285°±7.8), and a N-S trend (180°±5.8). Interestingly, outcrop fractures in northeastern Oklahoma (Figure A3e) show a prominence of a NNW-SSE trend (342°±10.3) and the NE-SW trend (233°±9.3), with the NW-SE trend (299°±0.5) occurring as a very minor set. Fracture systems in the basement outcrops of southeast Missouri (Figure A3f) show a dominance of the NE-SW (239°±2.3) and NW-SE (299°±1.9) trends. Whereas, the linear seismicity clusters extending northeastwards from eastern Missouri through southern Michigan (Figure A3g) show a dominance of the NE-SW (222°±13.2) and NW-SE (321°±14.67) trends, with a very minor ~E-W set (281°±6.76).

The clusters of the mean trends suggest that across the extents of the EGR-SGR Provinces, the NE-SW and NW-SE structural trends of discontinuity surfaces dominate the rocks (Figure A4). In addition to these dominant trends, minor trends of ~N-S and ~E-W structures occur in the rocks (Figure A4). Observations of contact relationships between the fracture sets in the exposures of

the basement in Oklahoma and southeast Missouri show that the NE-SW and NW-SE sets are mutually cross-cutting. In areas where offset relationship is apparent, we observe that pegmatite dikes striking along any of the two trends are offset by fractures of the conjugate trend (e.g., see Chapter 2). In other places, the fractures form conjugate patterns without any observable offset (e.g., Figure A5). However, in the Oklahoma outcrops, the N-S fractures appear to either offset, overprint, or terminate at the prominent NE and NW sets (e.g., Figures A5 and A6). Therefore, we interpret that the NE-SW and NW-SE structural trends that dominate the EGR-SGR are coeval whereas the ~N-S and ~E-W are likely younger.

Furthermore, the Cambrian rifting events in southern Oklahoma is associated with voluminous emplacement of granitic rocks which show excellent outcrop exposures in the Southern Oklahoma Aulacogen (Keller and Stephenson, 2007; Chase, 2019). Unlike the Precambrian granite structures, the Cambrian granite fractures show a dominant E-W trend (272°±6.2) and a minor ~N-S trend (192°±11.5) (Figure A7). Thus, the dominant structural trends in the Cambrian granites are consistent with the minor structural trends that are observable in the Precambrian granites (Figure A4). In addition, the diabase dikes in the southern Oklahoma Precambrian basement outcrops dominantly trend NW-SE (Denison, 1995), parallel to one of the dominant fracture trends. Geochronological investigation of the diabase dikes suggests Proterozoic to Cambrian ages. Therefore, we infer that the prominent NW-SE and NE-SW structural trends of the Precambrian EGR-SGR provinces are possibly of Mesoproterozoic age, and pre-date the E-W and N-S structural trends.

Implications for the Late Proterozoic and Phanerozoic Crustal Deformation, and Recent Seismicity in the Central and Eastern U.S. Region

The NW-SE and NE-SW fracture-defined trends of the EGR-SGR represent a prominent structural weakness in the Precambrian basement. The trend of the Cambrian rift basins in the region (Figure A1) are parallel to the NW-SE and NE-SW structural trends that dominate the EGR-SGR Precambrian basement within which the rifts developed. Furthermore, the NE-SW trend of the Late Paleozoic contractional belts bounding the granitic provinces to the south (e.g., Ouachita Belt in Figure A1) trends parallel to one of the delineated basement fracture trends. This indicates the control of the Precambrian basement fabrics on the development of the southeast boundary of the U.S. Mid-Continent.

Additionally, two minor trends, ~N-S (NNW & NNE) and ~E-W (WNW and ENE) are observable in the structural data (Figures A4a-b). The first-order plan-view geometry of the 1.1 Ga Mid Continent Rift is NNE to N-S-trending and is parallel to the one of the minor structural trends in the Granite-Rhyolite Province (Figure A1). It is apparent that the extents of the Mid-Continent rift indicate that most of its length is located outboard of the Granite-Rhyolite Provinces (Figure A1). Thus, it is likely that the minor structural trends in the granitic rocks of the Granite-Rhyolite Province may have been emplaced by the Post- Mesoproterozoic tectonic events that affected the region.

In Chapter 2, I showed that the widespread induced seismicity of Oklahoma represents the seismogenic reactivation of the NE- and NW-trending structural fabrics in the Precambrian basement. However, the analysis in the current study extends this analysis and demonstrate that the consistency of seismicity patterns with the Precambrian basement fabrics is regional in scale. Therefore, I suggest the inheritance of this regional-scale structural fabric by anthropogenic stress perturbations facilitates the production of widespread regional-scale induced seismicity.

CONCLUSIONS

We explored the fracture systems in the Mesoproterozoic granite-rhyolite provinces of the central-eastern United states and show that prominent NE-SW and NW-SE (with minor N-S and E-W) trends characterize the structural fabric of the basement. We suggest that these prominent trends were reactivated during the Phanerozoic rifting, thus influencing the rift geometries. Also, we argue that these trends, being favorably-oriented to the current stress field, is controlling the widespread pattern of recent induced seismicity across the Central U.S. region. Thus, these prominent structural trends represent inherent weaknesses in the Mesoproterozoic igneous basement of the U.S. Mid-Continent that facilitates the current regional-spread induced seismicity.

APPENDIX 1 FIGURES

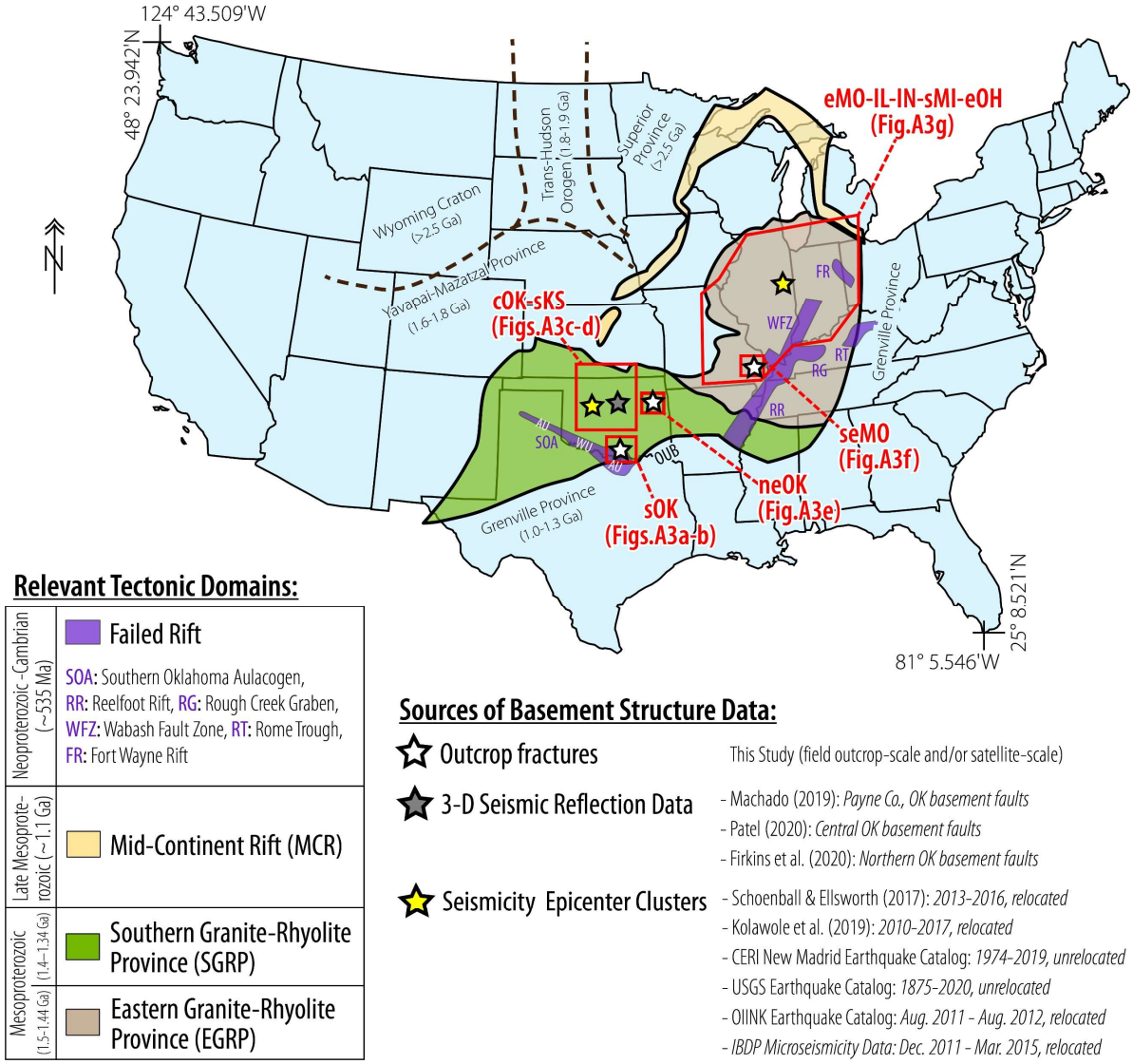

Figure A1. Major Precambrian tectonic domains of the Central-Eastern United States (CEUS), modified after Keller and Stephenson (2007), Soreghan and Soreghan (2013), and Bickford et al. (2015). The red polygons indicate the sampling locations of structural data shown in Figure 2. sOK = southern Oklahoma (Mill Creek area), cOK-sKS = central Oklahoma & southern Kansas, neOK = northeast Oklahoma (Spavinaw area), seMO = southeast Missouri (St. Francois Mountains), eMO-IL-IN-sMI-eOH = eastern Missouri, Illinois (Illinois Basin), Indiana, southern Michigan, & eastern Ohio, OUB = Ouachita Fold & Thrust Belt, WU = Wichita Uplift. Earthquake catalogues: CERI: Center for Earthquake Research & Information; IBDP: Illinois Basin – Decatur Project; OIINK = Ozarks-Illinois-Indiana-Kentucky Catalog; USGS = United States Geological Survey.

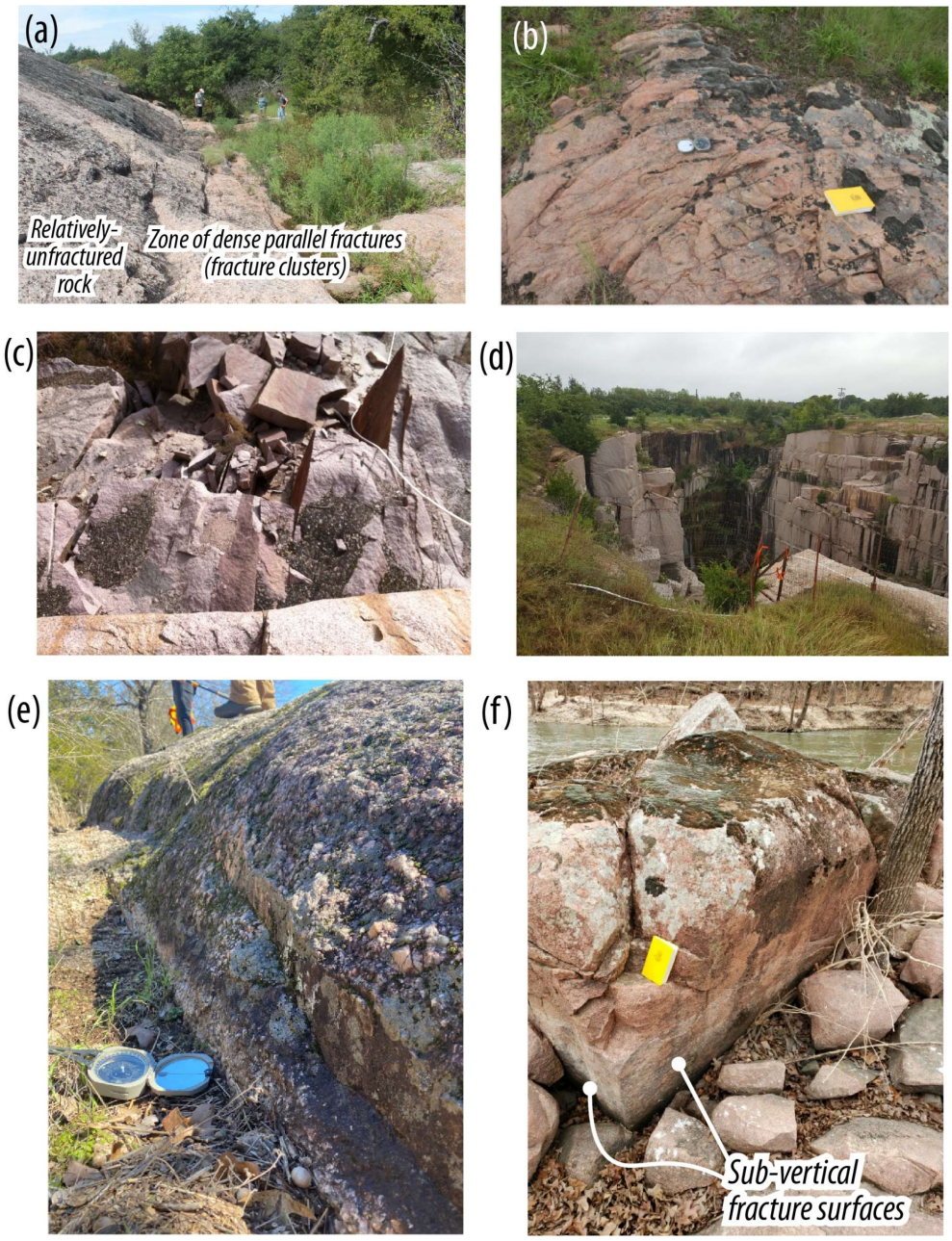

Figure A2. (a) Outcrop (Tishomingo Granite) in southern Oklahoma showing isolated zone of dense fracture clustering within a relatively unfractured rock. (b) Outcrop (Blue River Granite) in southern Oklahoma showing densely fractured rocks that characterize majority of the outcrops of the Blue River Granite. Photographs of the (c - e) Troy and (e) Tishomingo granites showing the sub-vertical geometry of the fractures in southern Oklahoma. The Photograph in A2e is courtesy of Connor Mears. (f) Photograph of the Spavinaw granite outcrop in northeastern Oklahoma, showing the sub-vertical geometry of the fractures.

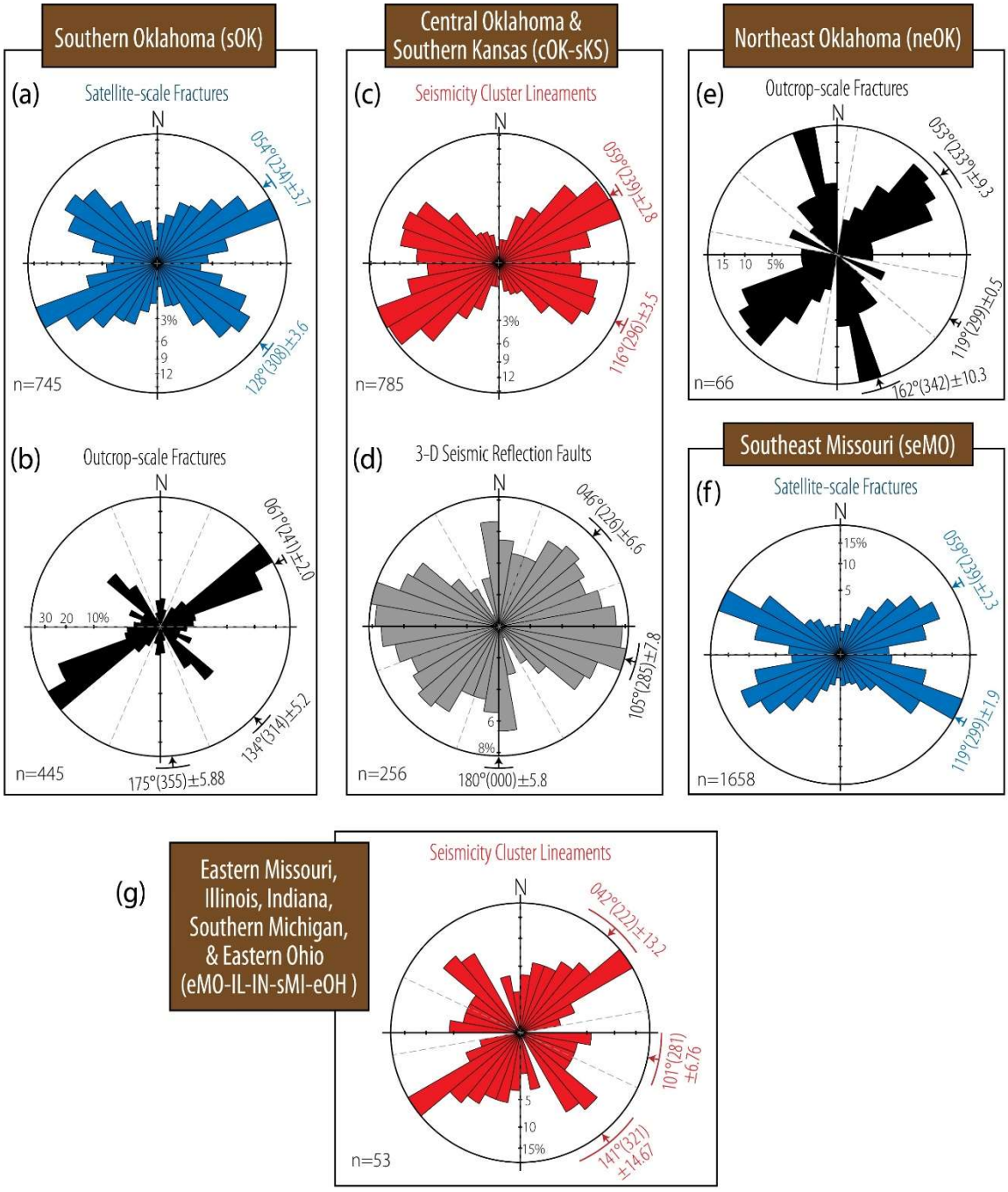

Figure A3. Area-weighted frequency-azimuth distribution of faults and fractures in different parts of the granite-rhyolite provinces of central-eastern United States (CEUS). The arrows on the rose diagrams represent circular vector mean trend of modal sets and the 95% confidence intervals, calculated using the method of Mardia and Jupp (2009). Black dashed lines represent frequency minima used for modal set grouping and calculation of circular vector mean for the modal sets.

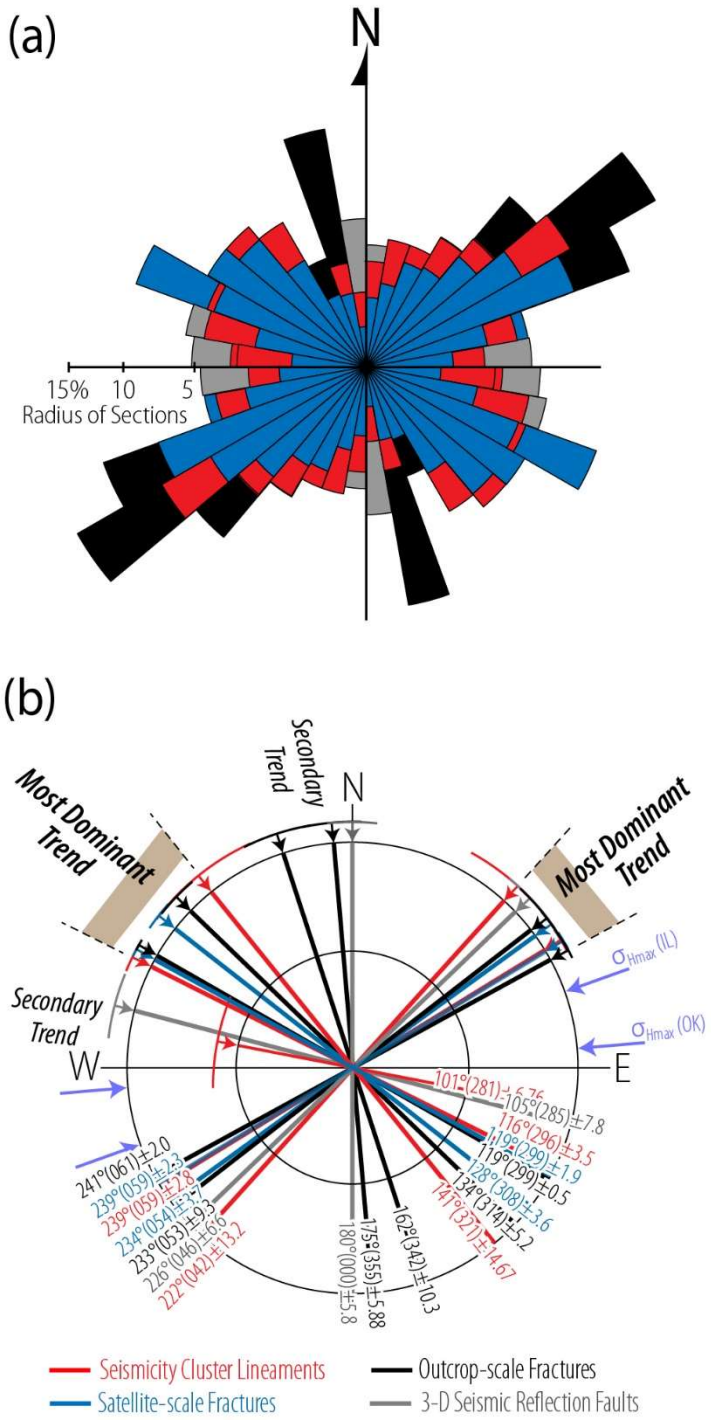

Figure A4. Summary rose diagrams showing the dominant structural fabric of the granite-rhyolite provinces of the central-eastern United States. (a) Stacked overlay of the fracture distributions at each of the sampling locations (shown in Figure A3). (b) Stacked overlay of the mean trends of the dominant structural trends at the sampling locations (the mean trends are also shown in Figure A3). σ_{Hmax} (IL) = Regional maximum principal horizontal stress orientation for the Illinois Basin,

σ_{Hmax} (OK) = Regional maximum principal horizontal stress orientation for the Anadarko Basin (Zoback and Zoback, 1991; Alt and Zoback, 2017; Heidbach et al., 2018).

Figure A5. Outcrop of the Mesoproterozoic granitic basement in Mill Creek area of southern Oklahoma (see location in Figure A1) showing an intersection zone of the dominant fracture trends in the rocks.

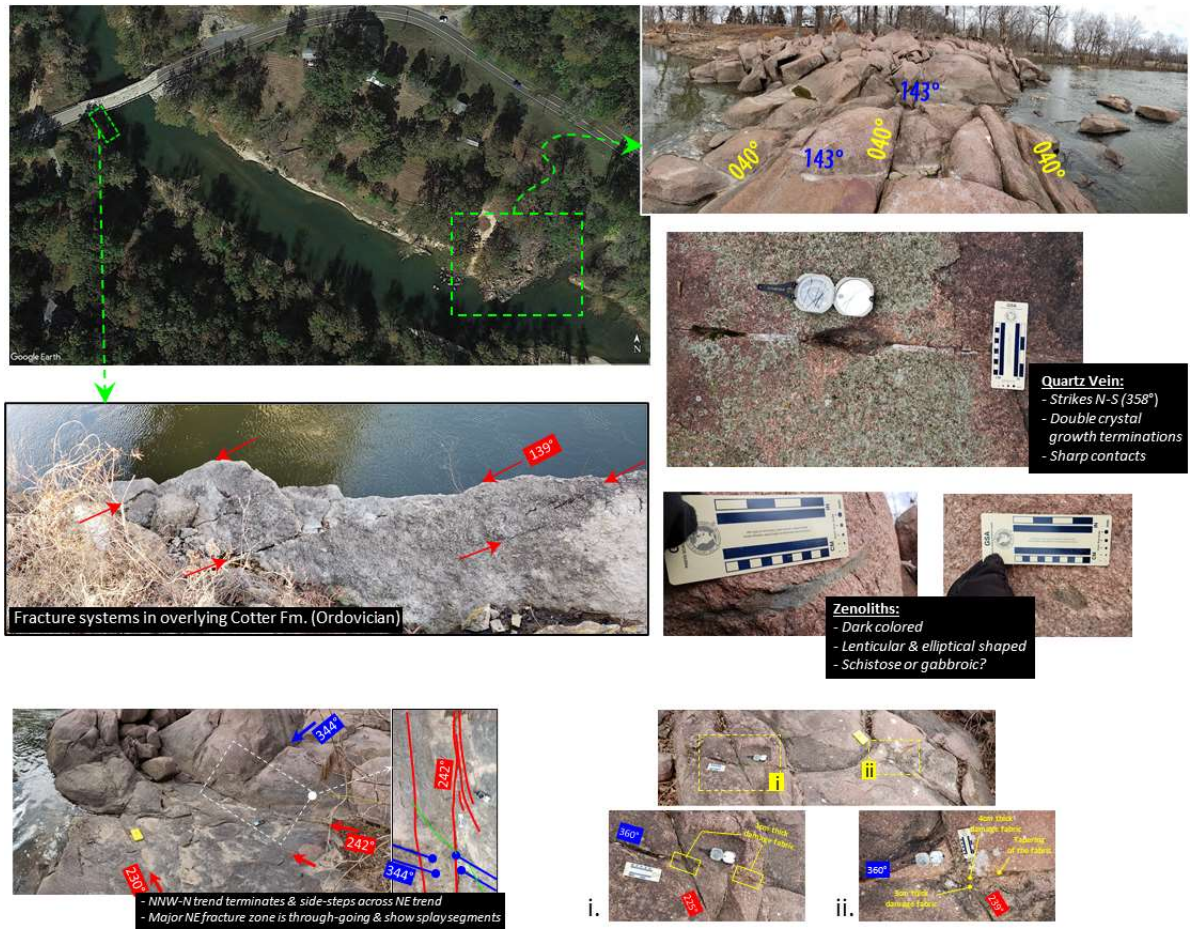

Figure A6. Map and photographs of the fracture systems in the outcrop of the Mesoproterozoic granite in Spavinaw area of NE Oklahoma (see location in Figure A1).

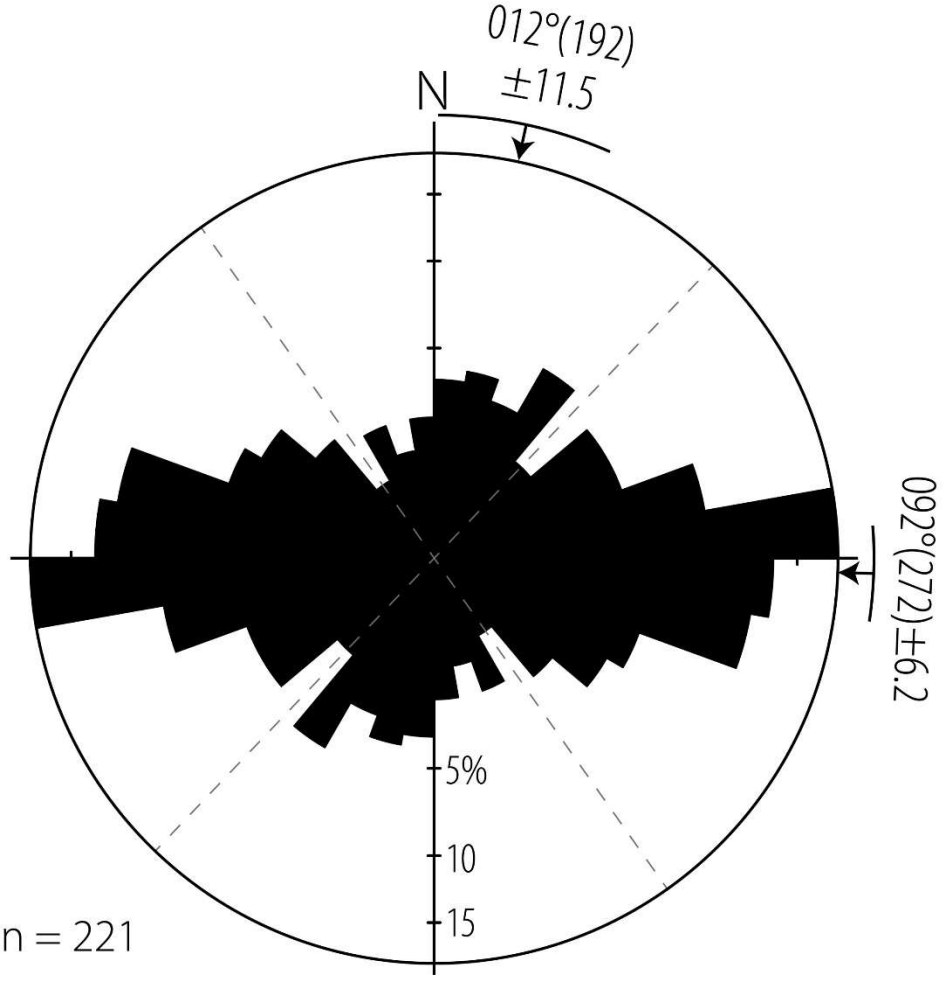

Figure A7. Frequency-azimuth distribution of satellite-scale fractures in the Cambrian granitic outcrops of the Wichita Uplift (see WU in Figure A1). The distribution shows dominant E-W trend with a secondary NNE-SSW set. Fracture data and interpretation are from Chase (2019).

REFERENCES

Alt, R. C., & Zoback, M. D. (2017). In Situ Stress and Active Faulting in OklahomaIn Situ Stress and Active Faulting in Oklahoma. Bulletin of the Seismological Society of America, 107(1), 216-228.

Bickford, M. E., Van Schmus, W. R., Karlstrom, K. E., Mueller, P. A., & Kamenov, G. D. (2015). Mesoproterozoic-trans-Laurentian magmatism: A synthesis of continent-wide age distributions, new SIMS U–Pb ages, zircon saturation temperatures, and Hf and Nd isotopic compositions. Precambrian Research, 265, 286-312.

Chase, B. (2019). High Resolution Geophysical Imaging Reveals Major Faults in the Southern Oklahoma Aulacogen: Implications for Mid-Continent Seismic Hazards, Masters Thesis, Oklahoma State University.

Denison, R. E. (1995). Significance of air-photograph linears in the basement rocks of the Arbuckle Mountains: Oklahoma Geological Survey Circular 97, 119-131.

Ellsworth, W. L. (2013). Injection-induced earthquakes. Science, 341(6142), 1225942.

Fielding, E .J., Sangha, S. S., Bekaert, D. P., Samsonov, S. V., & Chang, J. C. (2017). Surface deformation of north-central Oklahoma related to the 2016 M w 5.8 Pawnee earthquake from SAR interferometry time series. Seismological Research Letters, 88(4), 971-982.

Firkins, M., Kolawole, F., Marfurt, K. J., & Carpenter, B. M. (2020). Attribute Assisted Characterization of Basement Faulting and the Associated Sedimentary Sequence Deformation in North-Central Oklahoma. Interpretation.

Heidbach, O., Rajabi, M., Cui, X., Fuchs, K., Müller, B., Reinecker, J., Reiter, K., Tingay, M., Wenzel, F., Xie, F., & Ziegler, M. O. (2018). The World Stress Map database release 2016: Crustal stress pattern across scales. Tectonophysics, 744, 484-498.

Keller, G. and Stephenson, R. A. (2007). The southern Oklahoma and Dniepr-Donets aulacogens: a comparative analysis. Memoirs of the Geological Society of London, 200, 127-143.

Machado, A. G. (2019). Characterization of Arbuckle-Basement System with a focus on Seismic Attributes Image of Igneous Intrusions and Seismic Resolution, Payne County, Northern Oklahoma. PhD dissertation, University of Oklahoma.

McBride, J. H., William Keach II, R., Leetaru, H. E., & Smith, K. M. (2018). Visualizing Precambrian basement tectonics beneath a carbon capture and storage site, Illinois Basin. Interpretation, 6(2), T257-T270.

Patel, S. (2020) Geophysical Characterization of Resource Plays. PhD dissertation, University of Oklahoma.

Schoenball, M., & Ellsworth, W. L. (2017). Waveform-relocated earthquake catalog for Oklahoma and southern Kansas illuminates the regional fault network. Seismol. Res. Lett. 88, 1252–1258.

Soreghan, G. S., & Soreghan, M. J. (2013). Tracing Clastic Delivery to the Permian Delaware Basin, U.S.A. Implications for Paleogeography and Circulation in Westernmost Equatorial Pangea. Journal of Sedimentary Research, 83 (9), 786–802.

Will, R., El-Kaseeh, G., Jaques, P., Carney, M., Greenberg, S., & Finley, R. (2016). Microseismic data acquisition, processing, and event characterization at the Illinois Basin–Decatur Project. International Journal of Greenhouse Gas Control, 54, 404-420.

Whitmeyer, S. J., & Karlstrom, K. E. (2007). Tectonic model for the Proterozoic growth of North America. Geosphere, 3(4), 220-259.

Yang, X., Pavlis, G. L., Hamburger, M. W., Sherrill, E., Gilbert, H., Marshak, S., Rupp, J., & Larson, T. H. (2014). Seismicity of the Ste. Genevieve seismic zone based on observations from the EarthScope OIINK flexible array. Seismological Research Letters, 85(6), 1285-1294.

Zoback, M. L., & Zoback, M. D. (1989). Tectonic stress field of the continental United States. Geophysical framework of the continental United States: Geological Society of America Memoir, 172, 523-539.

APPENDIX 2

SEISMIC RUPTURE AT COLLOCATED FAULT-INTERSECTION AND FAULTED BASEMENT CONTACT: THE 2016 MW5.1 FAIRVIEW EARTHQUAKE, OKLAHOMA

Key Points:

• The 2016 Mw5.1 Fairview earthquake localized at the intersection of critically-oriented basement faults

• The aftershocks delineate a fault trace aligns with the contact of aeromagnetic and gravity anomaly in the basement, interpreted as an igneous intrusion

• Observations in the outcrops of the basement show localization of fracturing that follow the contacts of granitic intrusions

• Collocation of the intersection of critically-oriented faults and faulted contacts are stress concentrators, enabling the localization of seismogenic fault rupture

SUMMARY

In Central Oklahoma, the variability in the locations of major (Mw >5) earthquakes from high-volume injection wells and depths of events indicate that seismicity is controlled by pre-existing geologic conditions within the crystalline basement. Therefore, to better characterize the seismic hazards in the state of Oklahoma, it is important to identify basement structures that are potentially susceptible to seismogenic reactivation. Here, I investigate the control of pre-existing geologic structures, such as intra-basement faults and lithologic contacts on the localization of the 2016 Mw ≤5.1 Fairview earthquake (Figure A8). This event has been attributed to wastewater injection in the area (Yeck et al., 2016; Goebel et al., 2017). I utilize mathematically filtered aeromagnetic and gravity grids, relocated earthquake data, and field analogues to analyze the relationships between

basement deformation and the seismicity. My results show that the aftershocks of the earthquake delineate two previously unmapped fault lineaments consisting of a primary NE-trending cluster and a minor ENE- to E-W-trending minor cluster. The epicenter of the main shock is collocated with the intersection of the two faults. In addition, the primary cluster aligns with- and trends parallel to the contact of an elongate collocated magnetic (Figures A9a-d) and gravity (Figures A10a-d) anomaly in the crystalline basement. The regional gravity map shows that the Fairview earthquakes trend parallel to a regional-scale NE-trending gravity anomaly (Figure A11).

Further, observations of deformations in the outcrops of the igneous basement in southern Oklahoma show outcrop-scale evidence of localization of relatively more persistent brittle deformation along the contact between fine- and coarse-grained granite intrusions (Figure A12). The preferential localization of the brittle deformation suggests that lithologic contacts are density contrast boundaries that may concentrate stresses. This is consistent with previous studies that demonstrated that geologic structures such as mechanical contrast contacts are zones at which the refraction and/or rotation of stress trajectories may occur, allowing for the nucleation of brittle deformation (e.g., Sengupta, 1998, McConaughy and Engelder, 2001). In addition, analyses of an induced seismicity cluster in eastern Texas shows that local structural complexity, such as the intersection zone of multiple fractures is more likely to localize higher levels of stress concentration with highest stress drop (Chen et al. 2019).

Therefore, I interpret that the primary cluster represents a fault segment that was originally controlled by planes of basement mechanical contrast defined by the contact of an intrusion, thus representing a faulted basement contact. Both the earthquake lineaments and contact of the interpreted intrusion are well-oriented for reactivation in the current stress field (Figure A13a). Thus, I suggest that the localization of the Fairview earthquake event may have been influenced

by the collocation of stress concentrating structures defined by both the fault intersection and basement contact (Figure A13b).

APPENDIX 2 FIGURES

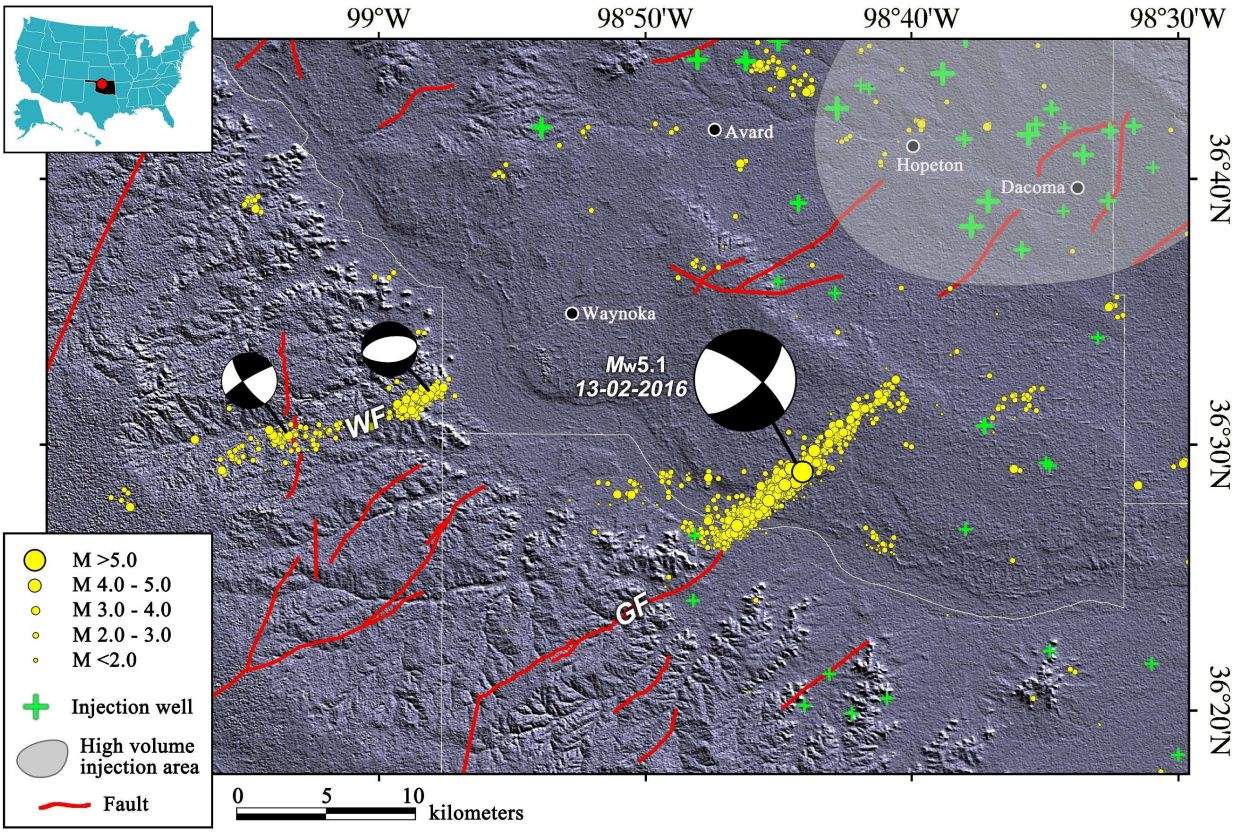

Figure A8. Digital elevation model (DEM) hillshade made showing injection well locations, previously mapped faults (red lines), and the seismicity cluster of the Mw5.1 Fairview earthquake and those of the nearby Mw4 Woodward earthquake.

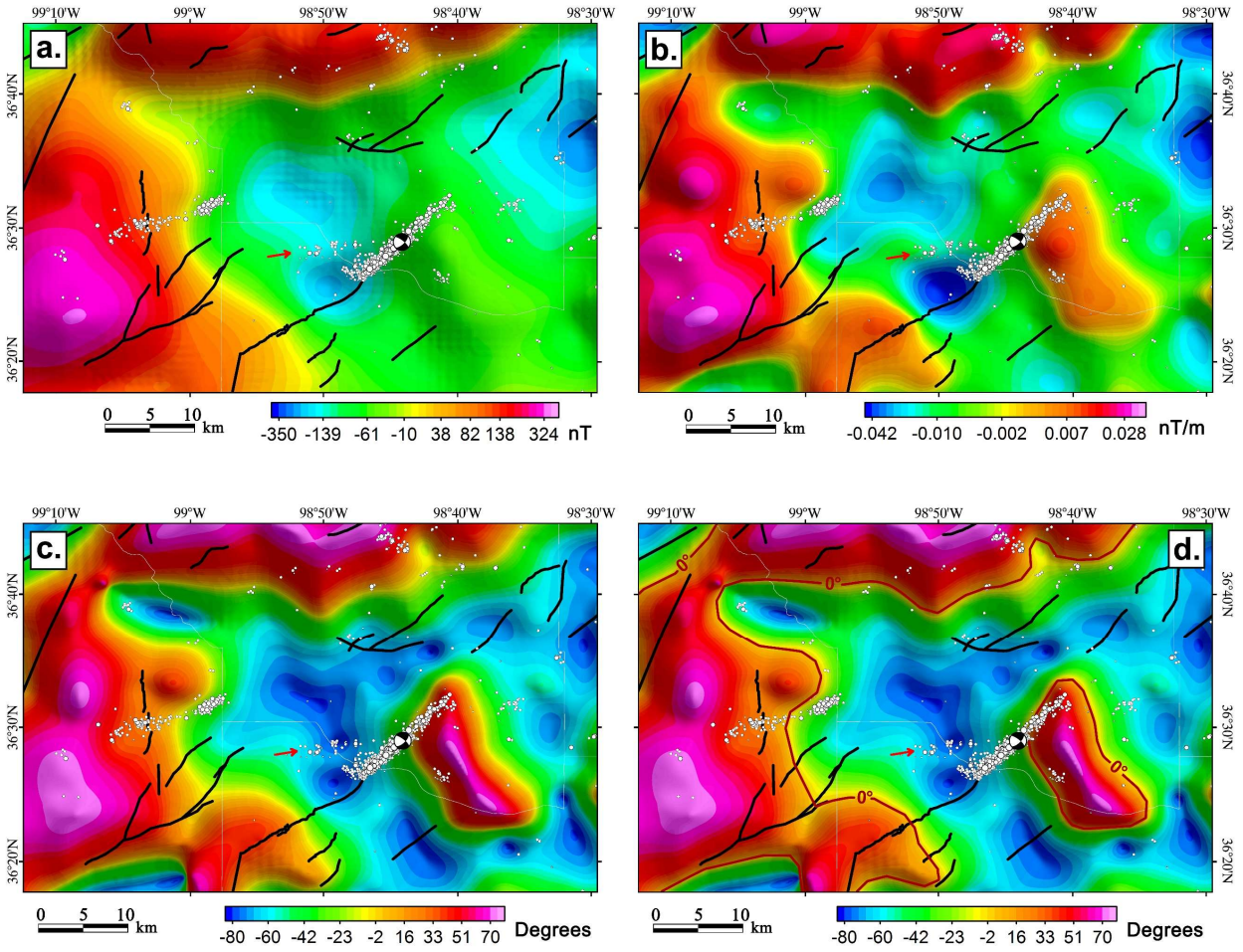

Figure A9. (a) Total magnetic intensity of the pole-reduced aeromagnetic grid of the Fairview earthquake region. (b) Vertical derivative, (c) tilt derivative, and (d) tilt derivative overlaid with the 0°-tilt derivative contour of the pole-reduced grid. The red arrow in each of the maps point at an ENE-trending seismicity cluster that delineates a subsidiary fault to the main NE-trending cluster.

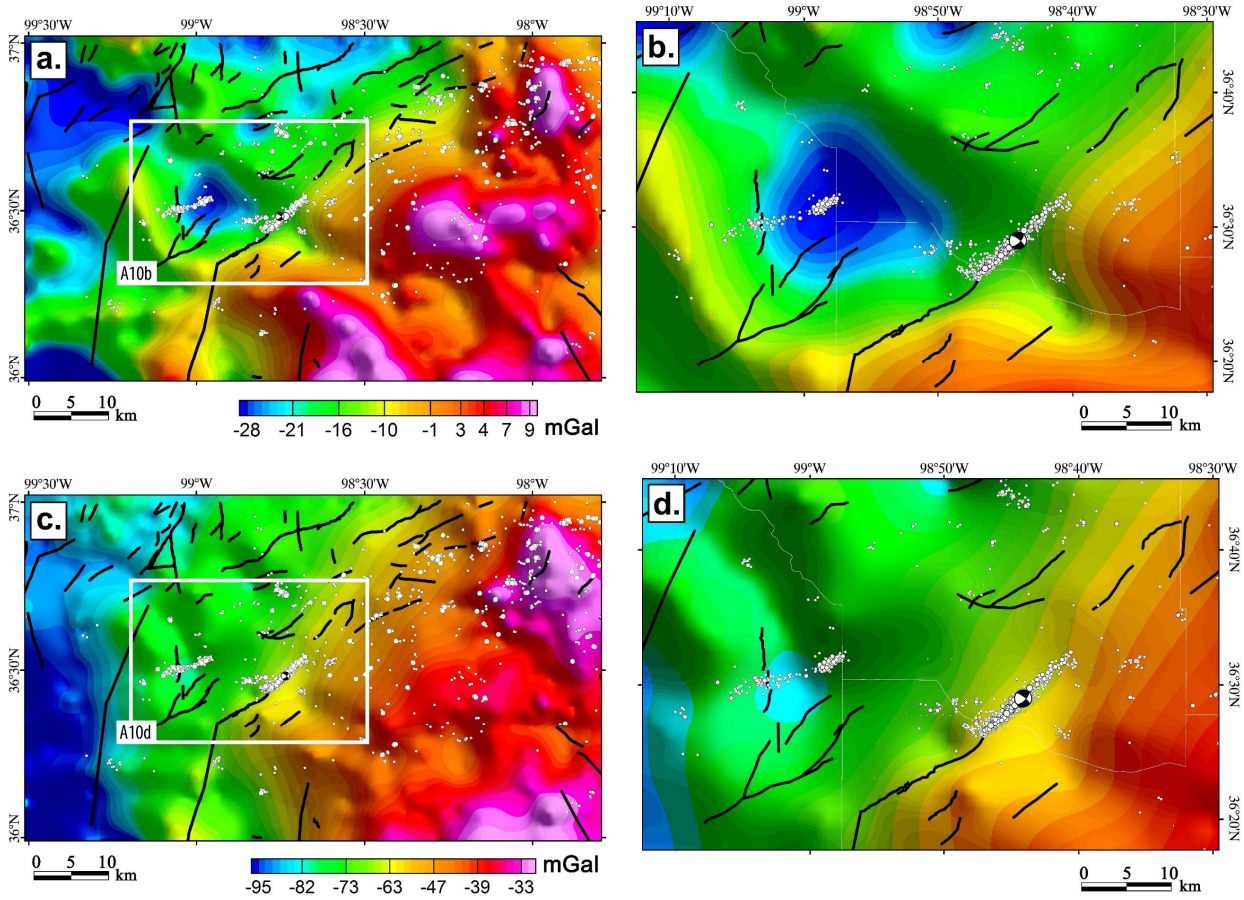

Figure A10. (a - b) The Free Air gravity anomaly grid of the Fairview earthquake region. (c - d) The Bouguer gravity anomaly grid of the Fairview earthquake region.

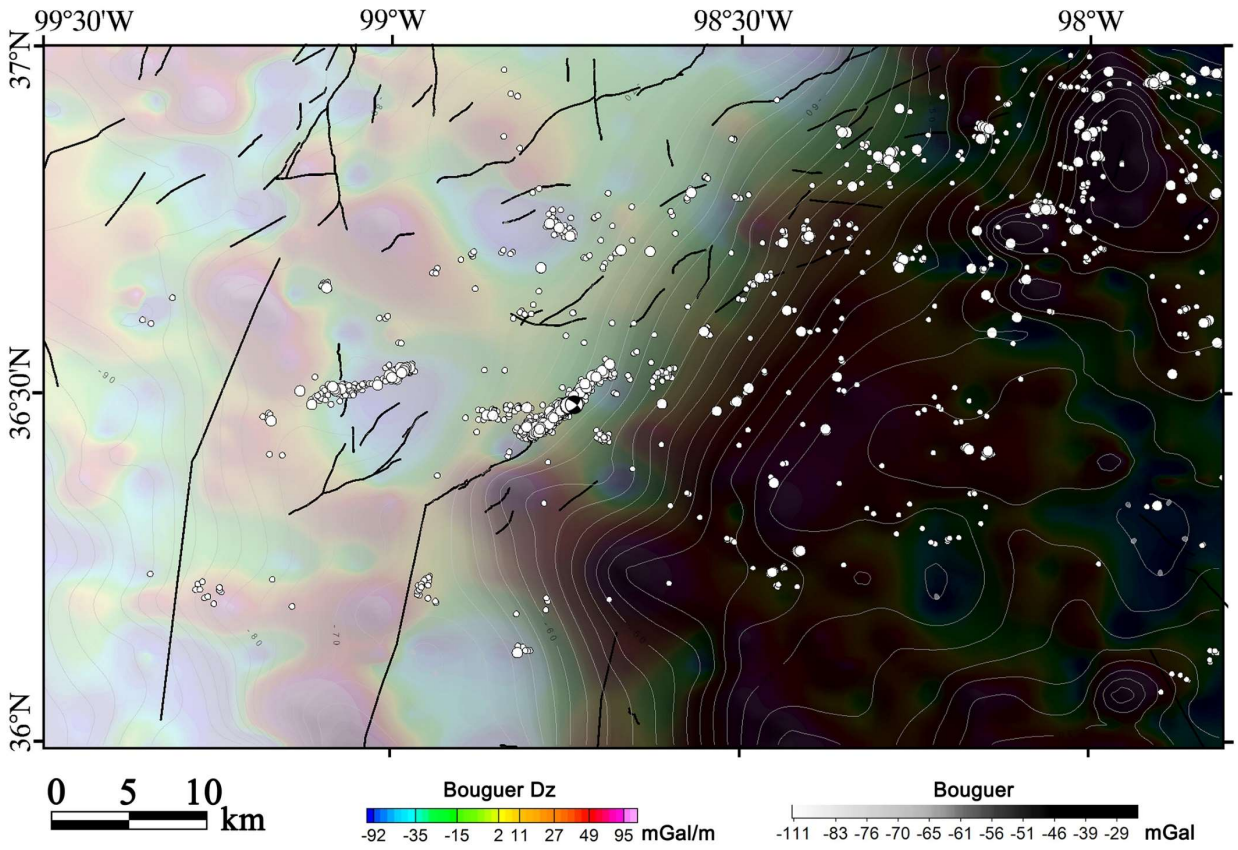

Figure A11. Regional gravity maps overlaid with previously mapped faults and recent seismicity, showing that the Fairview earthquake and surrounding seismicity trend parallel to a regional-scale NE-trending gravity anomaly (Figure A11).

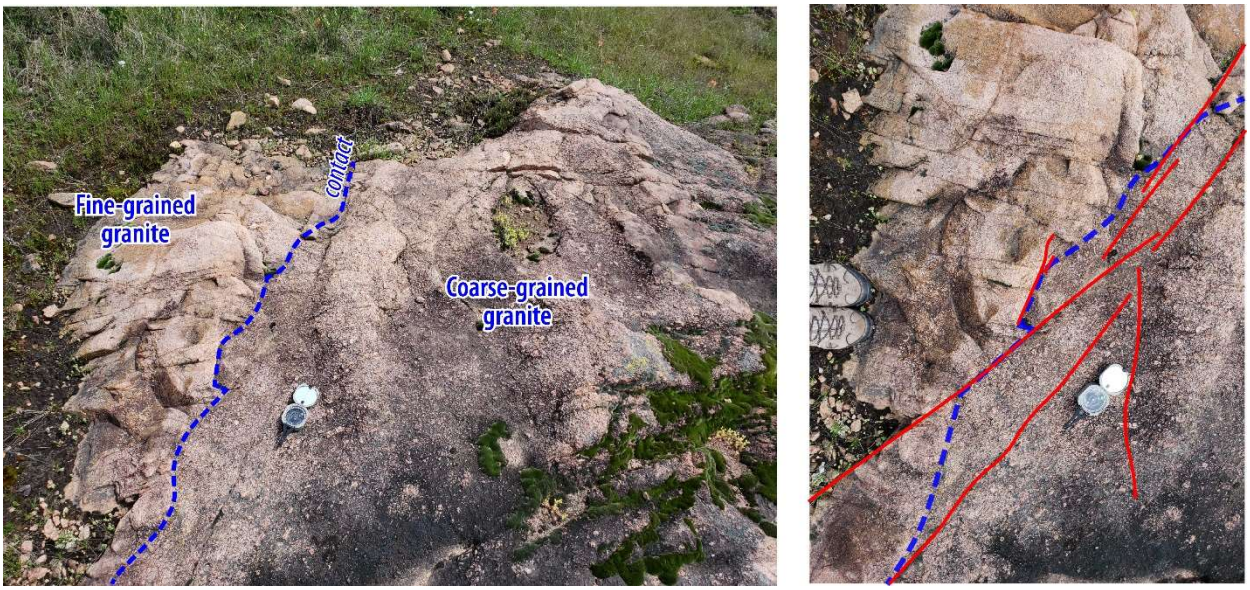

Figure A12. Brittle deformation in the outcrops of the igneous basement (Blue River Granite) in southern Oklahoma. the fractures oriented perpendicular to the contact are shorter (less persistent) than the fractures extending along the contacts of the two basement lithologies (red lines). The photographs show an outcrop-scale evidence for the localization of relatively more persistent brittle deformation along the contact between fine- and coarse-grained granite intrusions

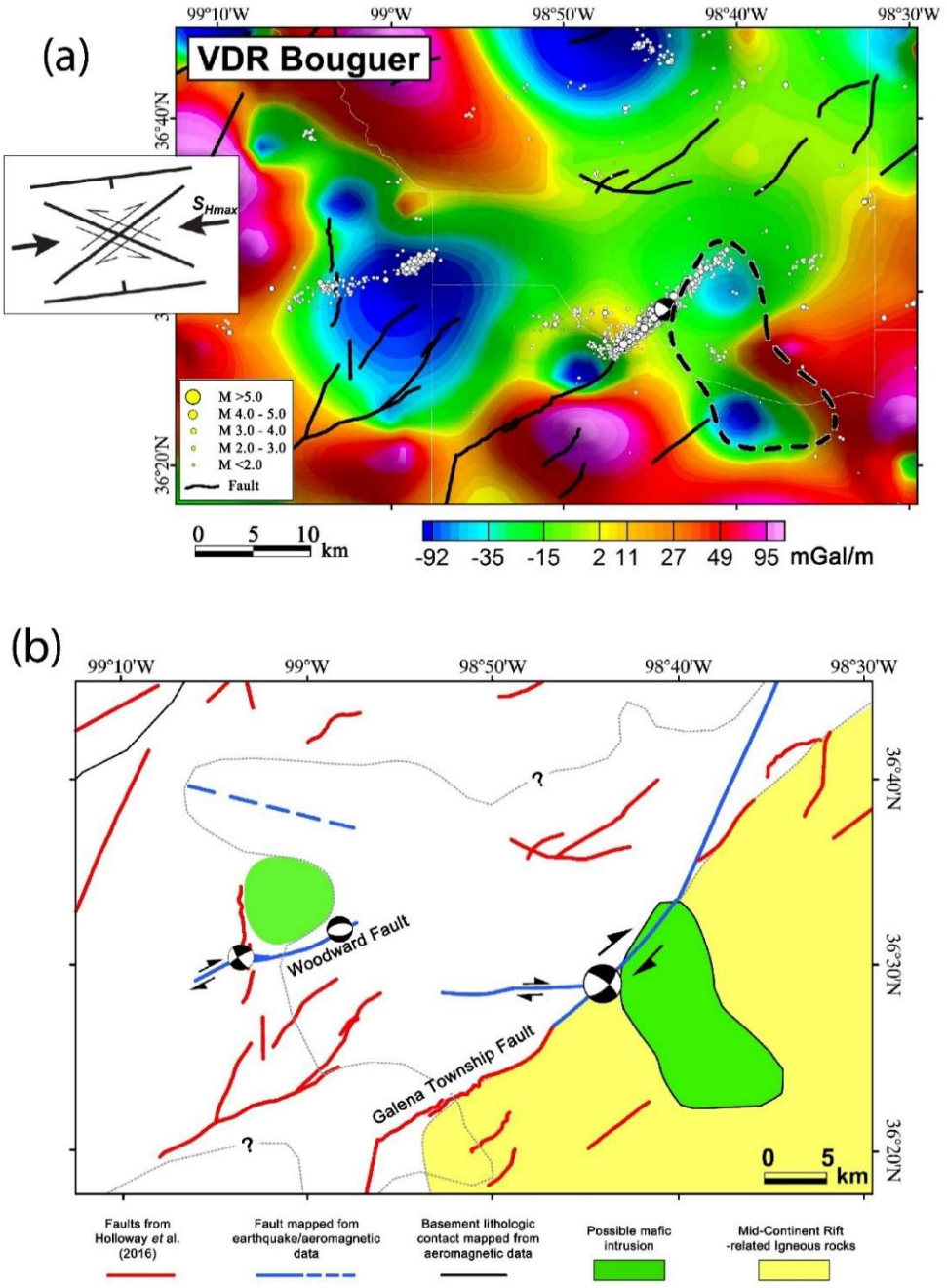

Figure A13. (a) The vertical derivative of the Bouguer gravity anomaly grid of the Fairview earthquake region overlaid with known faults (black lines) and outline of the aeromagnetic anomaly that is collocated with the earthquake. The stress field orientation (inset) is from Alt and Zoback (2017). (b) Interpretation of the Figure A13a.

REFERENCES

Alt, R. C., & Zoback, M. D. (2017). In Situ Stress and Active Faulting in Oklahoma. Bulletin of the Seismological Society of America, v. 107, 1–13.

Chen, X., Pennington, C., Ng, R., Nakata, N., & Zhang, J. (2019). September. Source parameter analysis of microseismicity during hydraulic fracture: Pinning stress distributions within fracture zone. In SEG International Exposition and Annual Meeting. Society of Exploration Geophysicists.

Goebel, T. H. W., Weingarten, M., Chen, X., Haffener, J., & Brodsky, E. E. (2017). The 2016 Mw5.1 Fairview, Oklahoma earthquakes: Evidence for long-range poroelastic triggering at> 40 km from fluid disposal wells. Earth and Planetary Science Letters, 472, 50-61.

McConaughy, D. T., & Engelder, T., 2001. Joint initiation in bedded clastic rocks. Journal of Structural Geology, 23(2-3), 203-221.

Sengupta, S. (1998). Influence of geological structures on in-situ stresses. Doctoral dissertation, Indian Institute of Technology, Delhi, India.

Yeck, W. L., Weingarten, M., Benz, H. M., McNamara, D. E., Bergman, E. A., Herrmann, R. B., Rubinstein, J. L., & Earle, P. S. (2016). Far-field pressurization likely caused one of the largest injection induced earthquakes by reactivating a large preexisting basement fault structure. Geophysical Research Letters, 43(19), 10-198.

APPENDIX 3

PATTERNS OF MAFIC SHEET INTRUSIONS IN FRACTURED GRANITE, MILL CREEK, SOUTHERN OKLAHOMA

SUMMARY

The primary goal of this study is to assess the relationships between mafic (diabase) sheet intrusions (tabular dikes and sills) and the fracture systems in granitic basement. The patterns of sheet intrusions and associated fracture surfaces may provide insight into the structure of the host rock prior to the emplacement of the intrusions (e.g., Baer and Beyth, 1994; Stephens et al., 2017). I anticipate that a better understanding of these relationships will provide insight into the influence of pre-existing planes of weaknesses on the emplacement of upper crustal magmatism within the crystalline basement. I perform this study in the exposures of the Mesoproterozoic Troy Granite in the Mill Creek area of Southern Oklahoma (Figure A14a). The dikes dominantly strike ~300° and form topographic ridges delineated by isolated vegetative tree growth (Figure A14b; Denison, 1995). The age of the emplacement of the intrusions is controversial as geochronological investigations suggest Precambrian age (Denison, 1995) and Cambrian age (Lidiak et al., 2014).

However, the structural deformation within the granite is excellently exposed in open pit excavations at the Martin Marietta Quarry (Figure A14b). The results of this study will also provide insight into the brittle structure of the Oklahoma basement that were inherited by the Phanerozoic tectonic events in the region. At the Martin Marietta Quarry, two sites are of interest, the South and North Pits (Figure A14b). In the South Pit (Figures A15a-f), there exists a pervasive occurrence of fractures with minor occurrence of diabase intrusions, whereas the North Pit reveals a pervasive occurrence of both fracturing and diabase intrusions.

I summarize my observations below:

• The geometries of diabase sills and dikes show patterns that suggest interactions with pre-existing fractures:

1) All the observed dikes and sills exhibit sharp contacts with the host granitic rocks (e.g., Figures A15e).

2) Dip-slip shear fracture pattern along a dike, defined by a system of intruded and unintruded splay fractures (Figures A15b to A16e). Contrasting geometries of the splay fractures and as well as relative sill occurrence in the bounding blocks of a steeply dipping mafic dike, illustrate Reidel patterns that suggest that the dike possibly intruded a pre-existing reverse fault.

3) In the South Pit where mafic intrusions are less pervasive, sills do not exhibit well-developed breaching of sill bridges (Figure A15f).

4.) In the North Pit where fracturing and sheet intrusions are pervasive (Figures A16a and 16b), sills are relatively thicker than those of the South Pit, and commonly show step geometries across sub-vertical dikes and fractures (Figures A16c and 16d). Where approaching sill segments do not show interactions with sub-vertical fractures or dikes, they show broken bridge geometries (Figure A16e).

5.) Unintruded fractures in the South Pit show stepped patterns defined by sub-horizontal (and dipping) fractures that terminate at or step across sub-vertical fractures (Figures A17a to 17c). The shear reactivation of pre-existing sub-vertical fractures allow for magma dilation within interconnecting sub-horizontal fractures (Baer and Beyth, 1994; Stephens et al., 2017).

6.) I observe slickenlines on a sample from the contact of one of the diabase dikes in the North Pit (Figure A18), suggesting that the contact of the dike has accommodated shear reactivation after the dike has cooled.

Overall, the observed geometries of the diabase sheet intrusions show patterns that suggest interactions with pre-existing fractures in the Troy granite. Thus, I suggest that the diabase dikes and sills were emplaced in a pre-fractured granitic basement, and that the inherited patterns of fracturing influenced the emplacement of the mafic intrusions. Further, the possible shear reactivation of the dike contacts (likely associated with the Phanerozoic tectonic events) suggest that the dike contacts represent a density contrast boundary where tectonic stresses mat preferentially localize.

APPENDIX 3 FIGURES

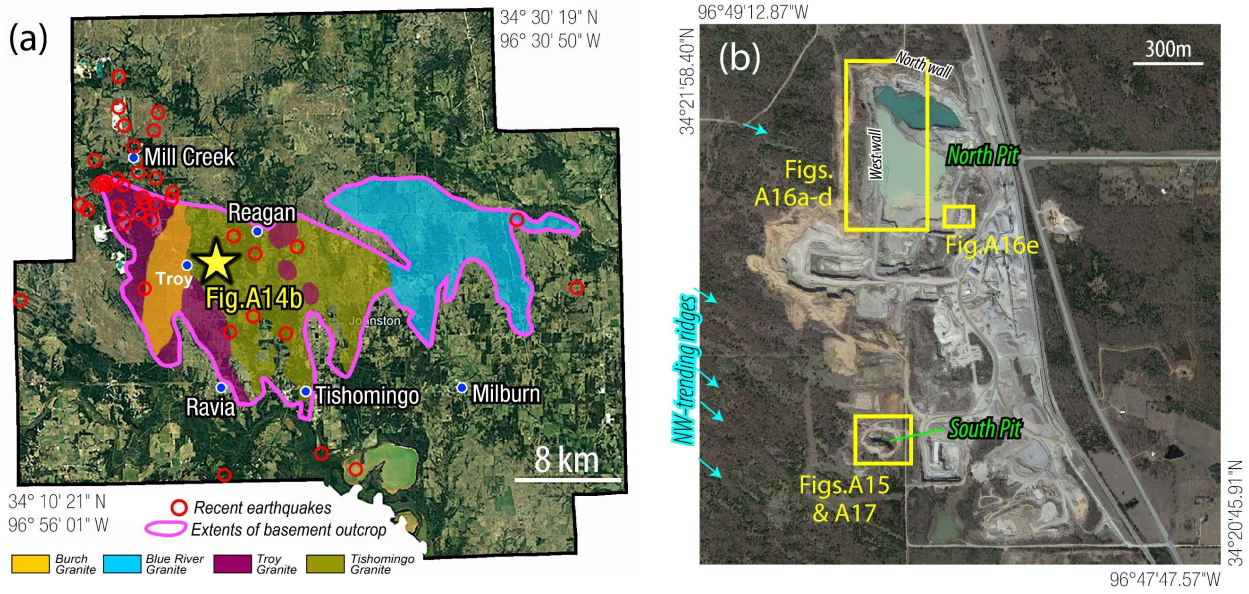

Figure A14. (a) Google Earth© satellite image of the Johnston County, southern Oklahoma, showing the Precambrian granite basement exposures and location of the study area, Martin Marietta Quarry Mill Creek, Southern Oklahoma (yellow star). (modified after Lidiak et al., 2014). (b) Google Earth© satellite image of the Martin Marietta Quarry showing the study sites.

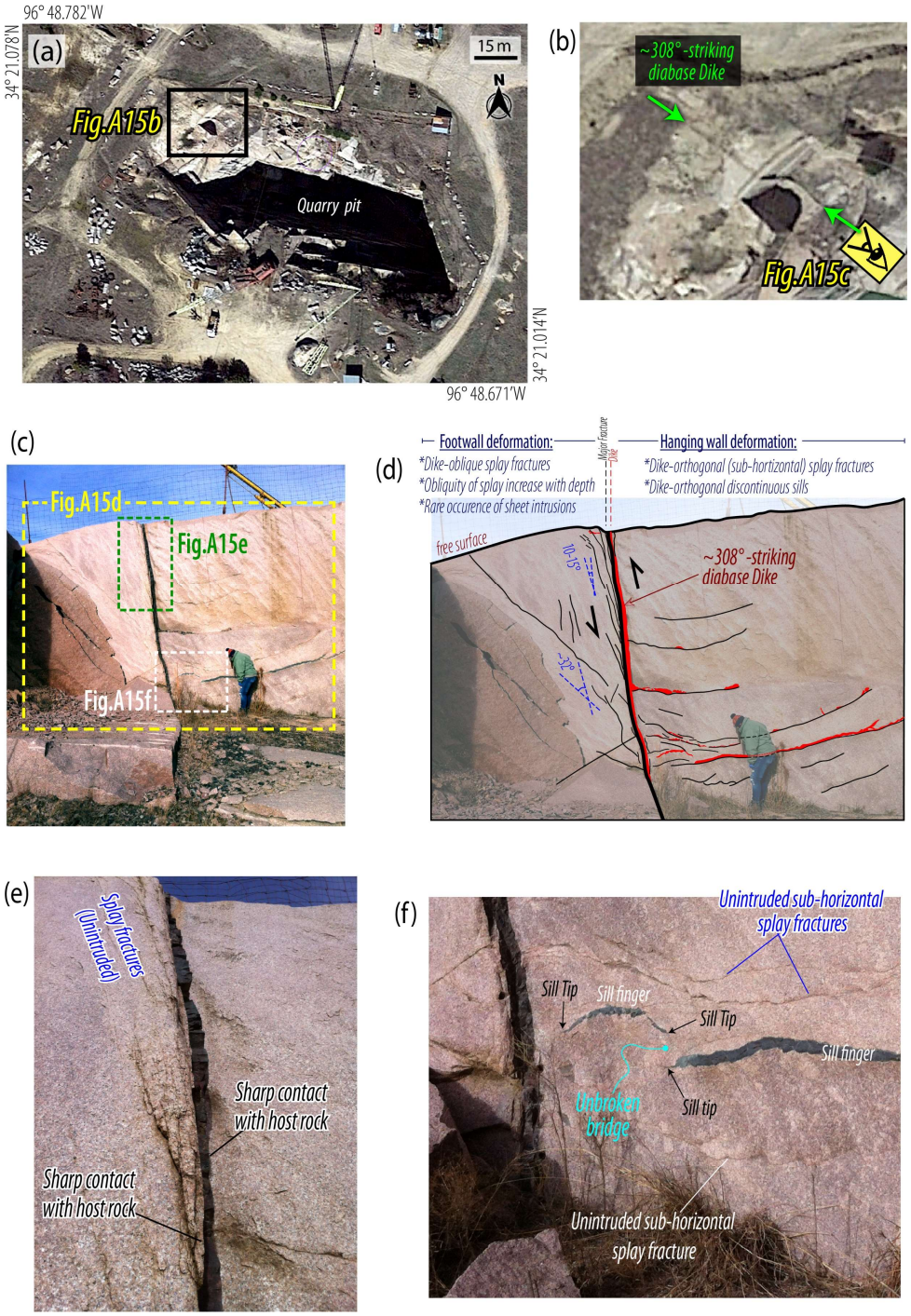

Figure A15. (a) Google Earth© satellite image of the south pit (see location in Fig. A3-1b). (b) Satellite image of the map-view trace of the NW-trending dike shown in Figures c to e. (f) Sill intrusion into the splay fractures of the NW-trending dike.

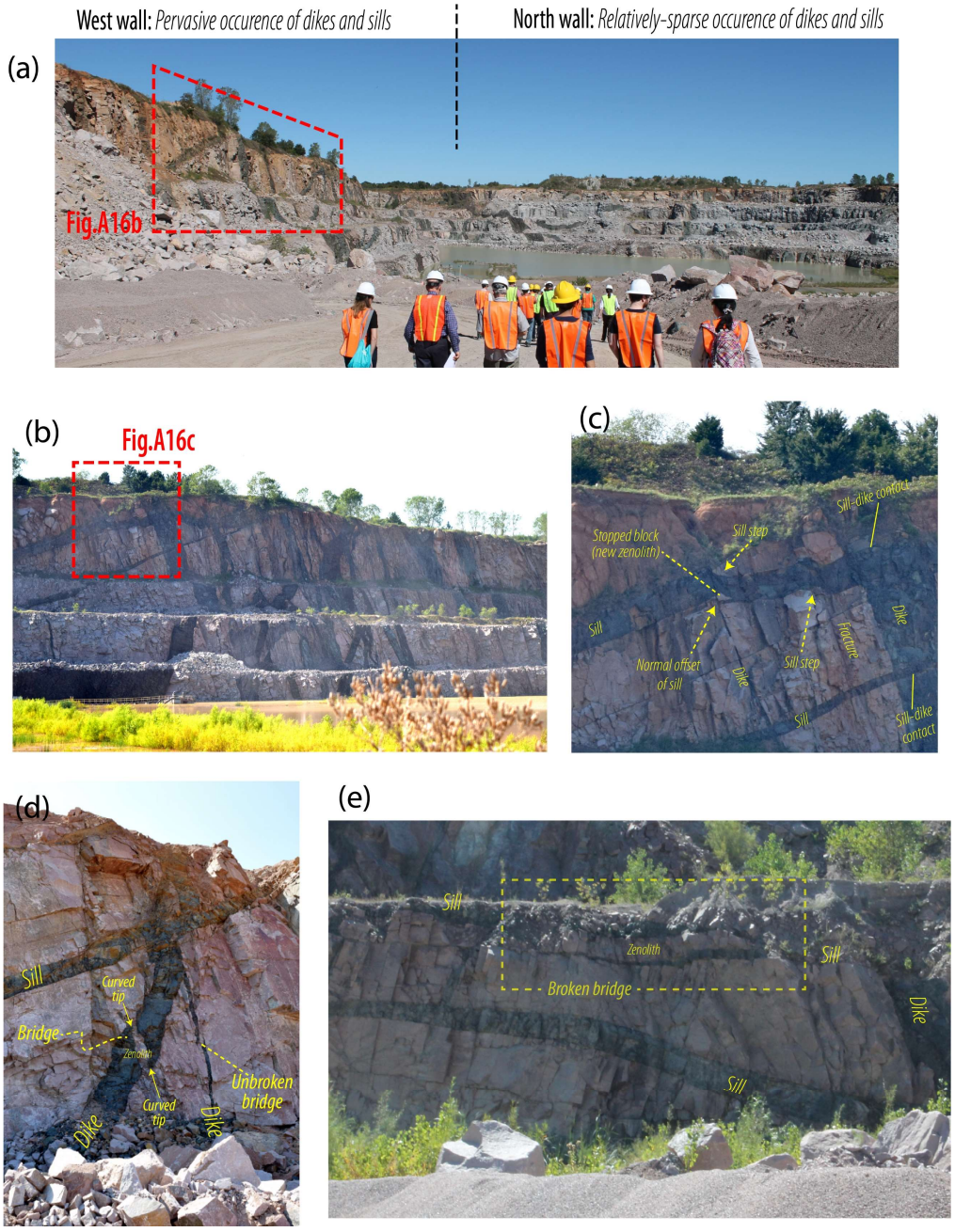

Figure A16. (a) Landscape photograph of the North Pit showing the apparent difference in the pervasiveness of the mafic intrusions on the North and West walls of the pit. I interpret this to indicate that the North wall is longitudinal to the strike of the dikes, whereas, the West wall represents a dip-section. (b – e) Photographs of (b) the West wall.

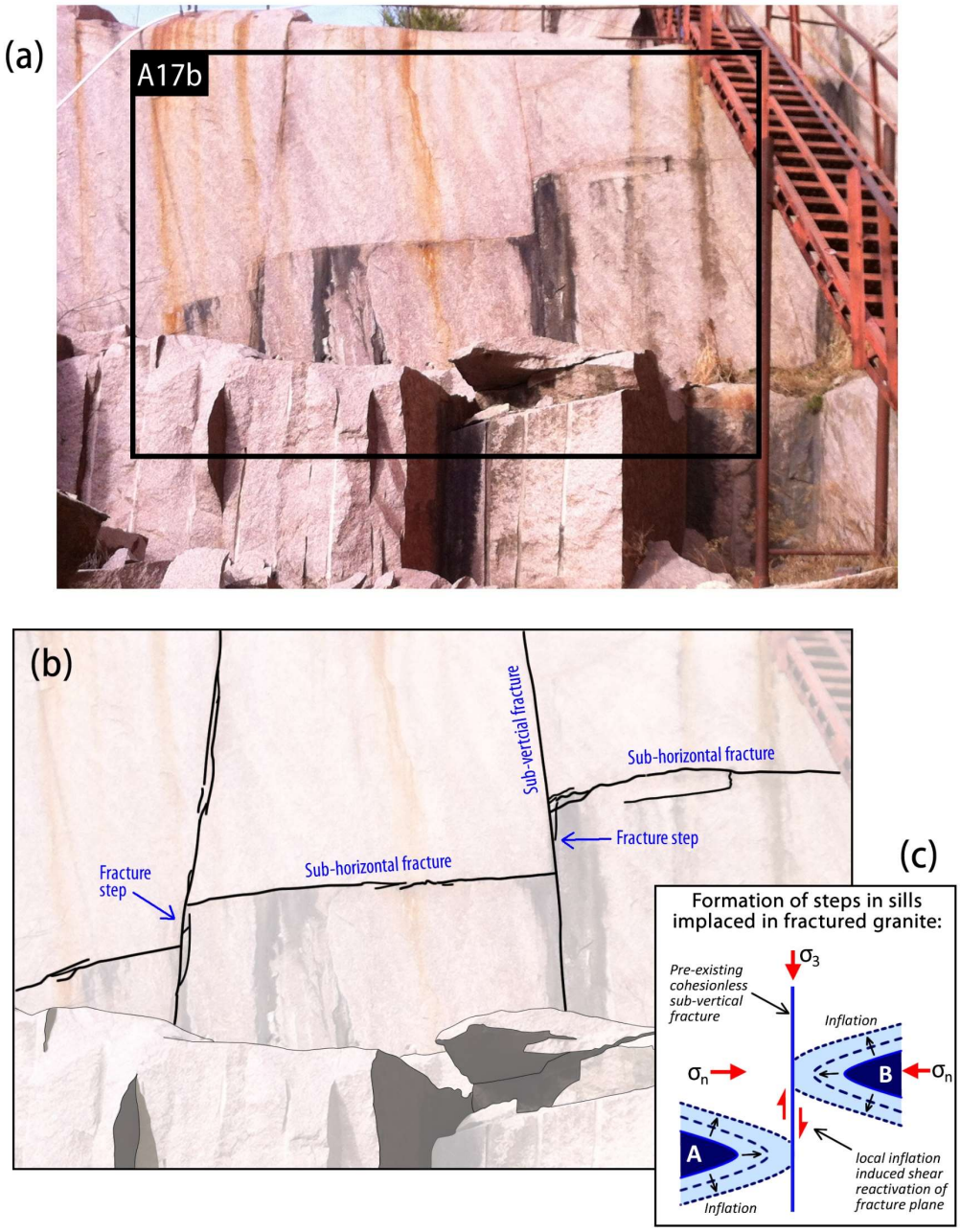

Figure A17. (a - b) Photograph of stepped fracture network in the granitic rocks. The fractures are not intruded by diabase, thus possibly representing the pre-existing fracture patterns (cross-section view) in the basement. (c) Schematic illustrating how steps form in mafic sills intruding fracture granite basement, modified after Baer and Beyth (1994) and Stephens et al. (2017).

Figure A18. Photograph showing slickenside on a sample from the contact of one of the diabase dikes in the North Pit.

REFERENCES

Baer, G., Beyth, M., & Reches, Z. E. (1994). Dikes emplaced into fractured basement, Timna igneous complex, Israel. Journal of Geophysical Research: Solid Earth, 99, 24039-24050.

Denison, R. E. (1995). Significance of air-photograph linears in the basement rocks of the Arbuckle Mountains. Circular-Oklahoma Geological Survey, 97, 119-131.

Lidiak, E. G., Denison, R. E., & Stern, R. J. (2014). Cambrian (?) Mill Creek Diabase Dike Swarm, Eastern Arbuckles: A Glimpse of Cambrian Rifting in the Southern Oklahoma Aulacogen. Oklahoma Geological Survey Guidebook 38, 105-122.

Stephens, T. L., Walker, R. J., Healy, D., Bubeck, A., England, R. W., & McCaffrey, K. J. (2017). Igneous sills record far-field and near-field stress interactions during volcano construction: Isle of Mull, Scotland. Earth and Planetary Science Letters, 478, 159-174.

APPENDIX 4

TABLE 6**.** Vertical separation (Vsep) measurements along Fault F1

**no data = seismic data gap, poor seismic data quality, or difficulty of identifying deformation of the target fault*

Measurement Location	L1	L2	L3	L4	L5	L6	L7	L8	L9	L10
Along-strike Distance on Fault F1 (km)	0.0	1.7	3.8	5.7	7.6	9.7	11.7	13.8	15.7	17.8
Top-Basement Vertical Separation (m)	90.6	96.1	53.2	41.8	26.7	21.7	0.0	3.3	13.8	13.0
Depth to mid-offset of Top-Basement (m)	2880.4	2933.7	3032.8	3048.0	3121.2	3115.1	No offset	3206.5	3368.0	3432.0
Top-Arbuckle Vertical Separation (m)	66.7	84.5	53.5	43.8	12.3	40.6	0.0	6.2	12.3	21.3
Depth to mid-offset of Top-Arbuckle (m)	2476.5	2461.3	2529.8	2560.3	2603.0	2627.4	No offset	2731.0	2785.9	2877.3
Top-Hunton Vertical Separation (m)	50.8	57.4	39.2	35.5	7.0	18.3	0.0	2.0	7.6	14.0
Depth to mid-offset of Top-Hunton (m)	2194.6	2222.0	2209.8	2225.0	2255.5	2273.8	No offset	2340.9	2363.7	2435.4
Mississippian Reflector	44.5	46.2	13.8	22.2	7.6	17.9	0.0	1.1	7.6	10.9
Depth to mid-offset of Mississippian Reflector (m)	2057.4	2066.5	2087.9	2090.9	2116.8	2121.4	No offset	2118.4	2240.3	2249.4
Top-Chester Vertical Separation (m)	41.6	38.8	8.9	23.6	11.1	10.1	0.0	0	5.3	6.0

Depth to mid-offset of Top-Chester (m)	1882.1	1905.0	1920.2	1944.6	1966.0	1988.8	No offset	No offset	2066.5	2087.9
Pennsylvanian Reflector Vertical Separation (m)	27.4	18.2	6.9	13.4	4.5	9.5	0.0	0	No data	2.5
Depth to mid-offset of Pennsylvanian Reflector (m)	1600.2	1745.0	1539.2	1554.5	1745.0	1731.3	No offset	No offset	No data	1996.4

APPENDIX 5

TABLE 7. Vertical separation (Vsep) measurements along Fault F2

**no data = seismic data gap, poor seismic data quality, or difficulty of identifying deformation of the target fault*

Measurement Location	L1	L2	L3	L4	L5	L6	L7
Along-strike Distance on Fault F1 (km)	0.0	1.6	4.1	6.1	7.7	9.8	12.0
Top-Basement Vertical Separation (m)	30.6	27.2	no data	30.6	21.4	25.0	0.0
Depth to mid-offset of Top-Basement (m)	2935.2	2980.9	no data	3093.7	3151.6	3185.2	No offset
Top-Arbuckle Vertical Separation (m)	30.4	25.8	no data	27.8	17.1	17.5	0.0
Depth to mid-offset of Top-Arbuckle (m)	2438.4	2465.8	no data	2560.3	2615.2	2639.6	No offset
Top-Hunton Vertical Separation (m)	26.7	17.5	no data	15.2	13.4	11.6	0.0
Depth to mid-offset of Top-Hunton (m)	2148.8	2145.8	no data	2240.3	2267.7	2289.0	No offset
Mississippian Reflector Vertical Separation (m)	14.3	9.0	no data	12.5	5.8	4.8	0.0
Depth to mid-offset of Mississippian Reflector (m)	2049.8	2072.6	no data	2110.7	2188.5	2145.8	No offset
Top-Chester Vertical Separation (m)	no data	8.2	no data	10.0	12.4	no data	0.0

Depth to mid-offset of Top-Chester (m)		1905.0	no data	1962.9	2060.4	no data	No offset
Pennsylvanian Reflector Vertical Separation (m)	8.3	5.0	no data	6.5	9.4	no data	0.0
Depth to mid-offset of Pennsylvanian Reflector (m)	1600.2	1740.4	no data	1569.7	1737.4	no data	No offset